

B-6

Yu. A. Izrael' and E. D. Stukin

THE GAMMA EMISSION OF RADIOACTIVE FALLOUT

DTIC QUALITY INSPECTED 4

Reproduced From
Best Available Copy

20000912 033

TRANSLATED FROM RUSSIAN

Published for the U.S. Atomic Energy Commission
and the National Science Foundation, Washington, D.C.
by the Israel Program for Scientific Translations

DISTRIBUTION STATEMENT A
Approved for Public Release
Distribution Unlimited

Yu. A. Izrael' and E. D. Stukin

THE GAMMA EMISSION OF RADIOACTIVE FALLOUT

(Gamma-izluchenie radioaktivnykh vypadenii)

Atomizdat
Moskva 1967

Translated from Russian

Israel Program for Scientific Translations
Jerusalem 1970

TT 70-50008
AEC-tr-7100
UC-41

Published Pursuant to an Agreement with
THE U.S. ATOMIC ENERGY COMMISSION
and
THE NATIONAL SCIENCE FOUNDATION, WASHINGTON, D.C.

Copyright © 1970
Israel Program for Scientific Translations Ltd.
IPST Cat. No. 5658
UDC 539.166.3: 539.1.03

Translated and Edited by Ron Hardin

Printed in Jerusalem by Keter Press
Binding: Weiner Bindery Ltd. Jerusalem

Available from the
U.S. DEPARTMENT OF COMMERCE
Clearinghouse for Federal Scientific and Technical Information
Springfield, Va. 22151

TABLE OF CONTENTS

| | |
|--|-----|
| PREFACE | v |
| Chapter I. PRODUCTION OF RADIOACTIVE FALLOUT | 1 |
| 1. Characteristics of radioactive products of a nuclear explosion | 1 |
| 2. Fallout of nuclear-explosion products in a region | 16 |
| 3. Fractionation of nuclear-explosion products and isotopic composition of radioactive fallout..... | 26 |
| 4. Gamma emission of radioactive products falling out in a region .. | 37 |
| Chapter II. GAMMA FIELDS OF SOURCES SIMULATING FALLOUT- CONTAMINATED LOCALITIES | 47 |
| 5. General information. Definitions | 47 |
| 6. Gamma field of isotropic point source | 49 |
| 7. Gamma field of isotropic plane source. Dose rate and emission density..... | 57 |
| 8. Spectral and angular distributions of gamma emission from isotropic plane source | 63 |
| 9. Gamma field of three-dimensional source | 67 |
| 10. Gamma field of artificial model of fallout | 71 |
| 11. Interpretation of experimental data obtained with artificial model.. | 81 |
| Chapter III. GAMMA FIELDS OVER CONTAMINATED REGIONS | 88 |
| 12. Effect of actual underlying surface | 88 |
| 13. Effects of vegetation and weather conditions | 101 |
| 14. Determination of surface density of contamination according to measured gamma-ray dose rate | 108 |
| 15. Determination of surface density of contamination by individual isotopes, according to gamma emission in air..... | 119 |
| APPENDIX | 126 |
| REFERENCES | 141 |
| SUBJECT INDEX | 149 |

FROM THE SOVIET PUBLISHER

The gamma emission of a radioactive fallout determines, to a considerable extent, the radiation hazard of the fallout. Thus gamma-emission studies will indicate the contamination of an area. This book discusses the production of radioactive fallout as a result of a nuclear explosion and gives the characteristics of the gamma-emitting products, taking into account fractionation of the fission products.

The gamma field in the air over a plane isotropic source is calculated; the dose rates, intensities, and spectral-angular distributions of the gamma emission in the air above artificial models of contaminated areas are given, for primary emitter energies from 0.32 to 1.69 Mev. The influence of actual conditions (roughness of terrain, ground which is not air-equivalent, presence of vegetation, weather conditions) on the gamma-emission field is shown. And finally, some methodological questions related to air surveys of the gamma emission of a contaminated area are discussed.

This book should be of interest to physicists, engineers, geophysicists, and doctors studying the propagation of nuclear-explosion products, radioactive fallout, and the harmful effects of fallout. Some of the data may prove to be useful in geophysical surveying, for accurate calculations of the radioactive-fallout background. The book includes 28 tables, 223 bibliographic references, and 71 figures.

PREFACE

The radioactive fallout caused by nuclear explosions or by industrial radioactive emanations (for example, in case of an accident) has drawn the attention of many investigators, because of the danger to public health presented by such fallout. The Moscow Agreement forbidding the testing of nuclear weapons in the atmosphere, in outer space, and underwater (1963) resulted in a sharp decrease in the intensity of radioactive fallout, but did not reduce this intensity to zero.

Fallout of radioactive products creates fields of nuclear radiation. The most dangerous of these fields is the gamma-emission field, which requires especially careful study. Such studies give us information on the gamma-ray emitters and on their distribution. The results of such investigations enable us to get an idea of the propagation of radioactive products and of the conditions under which the products form, and thus give direct information on the source of contamination. Consequently, it is possible to work out a scheme for predicting radioactive fallout and the radiation fields which accompany it.

In both Soviet and non-Soviet literature monographs have been published which discuss the propagation and fallout of radioactive products /1-3/, radioactive pollution of the environment /4/, and shelter from radioactive fallout /5, 6/. The gamma emission accompanying an atomic blast is considered by Leipunskii in /7/, and data from studies of a nuclear explosion are also included in monograph /8/. Finally, a great deal of work has been done on the propagation of gamma radiation in matter (for instance, see /9, 10/).

However, the information on the gamma emission of radioactive fallout which is available in the literature (in periodicals from different fields of study) is only fragmentary although some data are given in the above-mentioned monograph by Leipunskii.

In the present work an attempt will be made to consider in detail various questions related to the gamma emission of radioactive fallout. Data on the gamma emission of the radioactive products formed during nuclear explosions will be presented; the gamma-emission field in the fallout region will be analyzed; the effects of natural conditions on this field will be considered; and the study of radioactive contamination on the basis of measurements of the gamma-emission characteristics will be discussed. The instruments and methods used to measure the gamma emission will not be described, since very complete studies both of dosimetry /11, 12/ and of spectrometry /13-15/ exist. Also, the biological consequences of exposure to gamma radiation will not be considered in this monograph.

Chapter I gives the basic characteristics of the radioactive products appearing after nuclear explosions, both due to the fission itself and as a

result of activation of elements of the environment by neutrons from the explosion. The main physicochemical processes occurring after the explosion are discussed, as well as the propagation of the products and their fallout in the region. Data from observations of the gamma emission of fallout products are cited.

In Chapter II gamma-emission fields in the air over idealized sources are described; the sources simulate regions contaminated by fallout. Results of measurements of the dose rate, and of the intensity and spectral-angular distribution of gamma emission in the air over sections of the region, are given. These sections were contaminated artificially with Cr⁵¹, Sb¹²⁴, and Co⁶⁰ isotopes ($E = 0.32, 0.60, 1.17, 1.33$, and 1.69 Mev).

The gamma-emission field in the air over a contaminated locality is described in Chapter III, and the effects on this field of actual cases of a solid underlying surface (ground), microrelief, vegetation cover, and weather conditions are indicated. Results of calculations and simulation experiments are presented. In Sections 14 and 15 of Chapter III we consider how to determine the basic characteristics of the contamination of a region (contamination density, isotopic composition, dose rate at earth's surface) from measurements of the gamma-field parameters made at a distance (for example, from an aircraft). Correction factors taking into account the effects of different conditions are given, as well as the instrument errors during measurement. The data of these two sections may be used in air surveys of the gamma emission from regions contaminated by radioactive isotopes.

The main subject of the book is the gamma emission of the radioactive fallout resulting from nuclear explosions. However, most of the conclusions and physical data pertain as well to the contamination caused by industrial radioactive emanations.

It is to be hoped that this book will be of use to physicists, engineers, geophysicists, and doctors studying the propagation of nuclear-explosion products and radioactive industrial emanations, and that it will be of aid in studies of the harmful effects of these, of the penetrating power of the fallout gamma emission, and of the corresponding means of radiation protection. Certain of the data may be of interest to specialists in the physics of radiation protection, and also to geophysicists seeking a correct evaluation of the background of radioactive fallout.

Sections 2, 3, 5—9 and 12—14 were written by Yu. A. Izrael', and Sections 4, 10, and 15 and the Appendix were written by E. D. Stukin. Sections 1 and 11 were written jointly by the two authors. The authors wish to thank Prof. O. I. Leipunskii, A. F. Yakovlev, and A. S. Volkov for reading through the manuscript and offering valuable remarks, and they also wish to thank L. V. Gerasimova and G. S. Chirkova for their assistance in preparing the manuscript for printing.

Chapter I

PRODUCTION OF RADIOACTIVE FALLOUT

1. Characteristics of radioactive products of a nuclear explosion

Radioactive fallout is caused by the deposition of radioactive products from the atmosphere onto the earth's surface. Nuclear explosions are the most important source of radioactive pollution of the atmosphere.

Nuclear explosions are based on nuclear reactions. There are differences between the explosions of atomic bombs, thermonuclear bombs, and bombs characterized by successive "fission-fusion-fission" reactions /16-17/. An atomic bomb /17, 18/ involves a chain fission reaction in heavy fissionable nuclei (such as U²³⁵ or Pu²³⁹). The first atomic bombs (the so-called nominal bombs) possessed the power of 20 kilotons (kt) of trinitrotoluene (TNT), that is, they released energies equivalent to that released by the explosion of 20,000 tons of TNT. The application of various techniques makes it possible to vary the power of an atomic bomb considerably. The strengths of the atomic bombs set off prior to 1963 varied from 0.001 kt to hundreds of kt of TNT /19-22/.

When a 1-kt atomic bomb goes off, $1.45 \cdot 10^{23}$ fission events take place and an energy of $4.19 \cdot 10^{19}$ ergs is released /7, 8/. During each fission event an average of 2.5 (for U²³⁵) or 3.0 (for Pu²³⁹) neutrons are liberated; the average energy of these neutrons is about 2.0 Mev and their most probable energy is 0.8 Mev /23/. In addition, about 20 more Mev are released, of which 7.2 to 8.4 Mev are in the form of instantaneous gamma emission /7, 8/ and about 13 Mev are in the form of beta and gamma emission of the fission products /8, 24/.

In a thermonuclear or hydrogen bomb /18, 25-27/ the fusion of light nuclei is utilized to liberate a large amount of energy. The following reaction between deuterium and tritium was used in the thermonuclear explosion set off by the USA in November 1952 /28/:



In this reaction a neutron carries off an energy of about 14 Mev.

However, if reaction (1) is used, the problem arises of how to obtain a mixture density high enough to ensure an effective thermonuclear reaction. High rates of the fusion reaction will require a high initial temperature (more than 10 million degrees Celsius) /26, 27/. The explosion of an ordinary atomic bomb is used as a "trigger" to create the initial temperature required for a thermonuclear bomb. Therefore, the explosion of a thermonuclear bomb follows a "fission-fusion" pattern.

When lithium deuteride Li^6D /18, 28/ is used as the fuel, an important role in the development of the thermonuclear process may be played by nuclear reaction ${}_3\text{Li}^6 + {}_1\text{n}, {}_2\text{T}^3 + {}_2\text{He}^4$, in which the tritium taking part in the subsequent reaction is formed. For example, in certain thermonuclear devices detonated by the Americans in spring 1954, this reaction was used and it was unnecessary to introduce tritium from outside /28/.

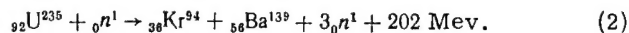
The reactions taking place in atomic and thermonuclear bombs are self-sustaining, and, once they have begun, will continue without any input of energy or neutrons from outside (provided the quantity of material is sufficient). In some fissionable heavy elements, like U^{238} and Th^{232} , it is impossible to obtain a self-sustaining reaction, since for these elements the capture sections for neutrons possessing energies of the fission spectrum are small, in comparison with the scattering cross section, while the threshold of the fission reaction is too high. Moreover, for neutron energies of the order of 1 Mev, (n, γ) reactions take place concurrently with the fission, and these have cross sections comparable to the section for the fission reaction. However, these elements fission comparatively easily, under the influence of fast neutrons entering from outside (fission threshold of $\text{U}^{238} \cong 1$ Mev /28–30/).

The inclusion of U^{238} in the envelope of a thermonuclear bomb enhances its effects considerably, since the surplus neutrons are then used to split the U^{238} . An explosive device consisting of a thermonuclear bomb (with an atomic trigger) encased in a U^{238} envelope is known as a "fission-fusion-fission" bomb. The possibility of using this scheme for a bomb was first mentioned in 1955 /31–35/. In such a bomb about 80% of all the energy released comes from the fission of U^{238} by fast neutrons /31/.

The power of a thermonuclear bomb or a "fission-fusion-fission" bomb may vary over a wide range: from hundreds of thousands to tens of millions of tons of TNT /20–22/. Only two long-lived radioactive isotopes are produced during thermonuclear reactions: H^3 and, possibly, Be^7 /18, 36–38/. Tritium, large quantities of which are produced in a thermonuclear explosion, is not a gamma emitter, and the cutoff of its beta spectrum is 18 kev. Therefore, the biological hazard of tritium is not great, although so far it has been insufficiently studied.

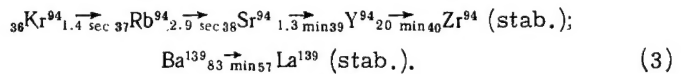
Consequently, regardless of the ratio between the total energy of the explosion and the energy released by the atomic trigger, the products of the fission of heavy nuclei play the main role in the radioactive contamination of the atmosphere and the locality. The only exceptions are explosions of very "clean" bombs near the earth or underground, when isotopes produced by neutron activation of elements of the ground material (rocks) may make a substantial contribution to the gamma-ray activity /39–41/.

The characteristics of a mixture of fission products from heavy nuclei will be considered in detail below. As a rule, two massive fragments and an average of 2.5 to 3.0 neutrons are produced when a heavy nucleus fissions /23/. For example



The fragments which are produced are in general unstable and, before reaching a stable state, each of them undergoes an average of three

successive beta transformations (the average number of beta decays for the two primary fragments is 5.4 /16/). For example, the fragments produced as a result of reaction (2) follow the following pattern of beta decay:



In all, more than 100 unstable primary isotopes are produced during fission, having half-lives from fractions of a second to many years.

The probability that a given nucleus or nuclear chain will be created during a fission event is known as the fission-product yield. In accordance with the terminology adopted in /30/, let us differentiate between the independent and cumulative yields of fragment isotopes. The independent yield of a given isotope is the probability that it will be formed directly in the fission process. The cumulative yield is the sum of the independent yields of the isotope in question and of all its predecessors along the chain which produce this isotope when they decay.

The cumulative yield of the last member of a radioactive chain is usually called the total yield of the given chain, since it indicates the probability that a fragment with the corresponding atomic number will be produced. The curve showing the total yields of the fission products as a function of atomic number is a familiar distribution curve having two maxima (double-humped curve). The curve has this shape because, during fission, fragments with atomic weight near 95 and 139 are the most probable, while the probability of a symmetrical splitting is low.

It has been shown /29, 30, 42/ that a fission process may produce three fragments rather than two, but a double cleavage is 500 to 1000 times more likely than a triple one. The most common third fragment, by the way, is an α particle.

While considering the rules governing the fission of heavy nuclei, we should mention that with an increase in the mass of the fissionable nucleus the peak of the curve showing the distribution of light fragments shifts monotonically toward higher masses. For fissionable nuclei from thorium to plutonium, however, the distribution peak for heavy fragments shows practically no shift /29, 43/. This is because there is a maximum of heavy fragments of nuclei with a magic number of neutrons or protons on the left side of the distribution curve /29, 43/.

Another important rule is that the probability of a symmetrical fission rises sharply with an increase in the energy of the neutrons bombarding the fissionable isotope. For example, the yield of a mass chain with an atomic weight of 111, when U^{235} is bombarded with 14-Mev neutrons, increases by a factor of more than 15, in comparison with bombardment by fission neutrons. In this case, the mass distributions of the light and heavy fragments become wider /43/.

Quite comprehensive data on the yields of different isotopes, for fission of heavy nuclei by neutrons with various energies, have been collected in /30/, which combines the results of studies made between 1939 and 1962.

The first description of the change with time in the composition of a mixture of fission products was that of Way and Wigner /44/. They

represented the time change in mixture activity by the empirical formula

$$A(t) = A_0 t^{-n}, \quad (4)$$

where A_0 and $A(t)$ are the activities of the mixture of products at times $t = 1$ and t , respectively. Coefficient n in formula (4) may vary somewhat with time, its average value being $n \approx 1.2$.

On the basis of known fission yields and decay schemes for various isotopes, it was possible to compute the decay rate for a mixture of products of instantaneous fission of U^{233} , U^{235} , and Pu^{239} , as well as the activity of each radioactive isotope /45–48/. The mixture of fission products was taken to be the sum of the individual fission products; the contribution of the conversion electrons was not taken into account.

In /45, 46/ data on the time variation in the activity of individual isotopes were presented in graphical form, which is not always convenient for use. Reference /49/ gives the activities of individual isotopes for ages from 1 hour to 100 years for five kinds of fission ($U_{n_{ther}}^{235}$, $U_{n_{fiss}}^{235}$, $Pu_{n_{fiss}}^{239}$, $U_{n_{fiss}}^{238}$, and $U_{n_{14 \text{ Mev}}}^{238}$). These data are tabulated in units of disintegrations per minute for 10^4 fissions.

Our tables were compiled using the data of /47, 48/ on the isotope yields during fission, and the decay chains were borrowed from /50/. More accurate half-lives (1962) for individual isotopes were also used for the calculations. Table 1 shows the beta activity of all the fragments together as a function of mixture age, calculated using data from the tables in /49/. The fragment mixture which should be produced in an explosion (fission of U^{235} and Pu^{239} by fission-spectrum neutrons) equivalent to 1 kt is considered. The accuracy of the results in this table depends mainly on the reliability of the data used for the calculations.

Table 2 shows a comparison between the cumulative yields given in /48/ and data published after 1958 in journals /30/. The discrepancies between the two sets of data are also given in the table, in percent. It follows from Table 2 that for the fission of $U_{n_{ther}}^{235}$ the new data for the isotopes making

the main contribution to the activity of a fragment mixture at least two days old are in good agreement with the values taken in /48/. However, for the reactions $U_{n_{fiss}}^{235}$ and $Pu_{n_{fiss}}^{239}$ the deviation from the data in /48/ is greater,

and for some isotopes the yields differ by a factor of two. Assuming that the data in /30/ are more reliable, it is to be expected that the time dependence of the beta activity of a mixture of fragment [fission] products, and also the absolute number of beta decays for a specified number of fissions, may differ from the data in Table 1 by 10 to 20%, or by even more than this for some mixture ages and fission types.

The time variation of the mixture composition, for the products of fission of U^{235} by thermal neutrons ($U_{n_{ther}}^{235}$), according to the data of /40–42, 44/, shows a good fit with the experimental data. For $U_{n_{ther}}^{235}$ the deviation of theoretical values from experimental values, obtained in laboratory

measurements of the activity of a mixture of fission products during the course of a year /51/, did not exceed 20 to 30%.

TABLE 1. Beta and gamma activities of fission products, as functions of time elapsed after 1-kt explosion

| Mixture age | Beta activity, disint/sec | | Gamma activity, Mev/sec | | | |
|-------------|------------------------------------|-------------------------------------|--|------------------------------------|---|-------------------------------------|
| | $U_{n \text{ fiss}}^{235}$ /49/ | $Pu_{n \text{ fiss}}^{239}$ /49/ | $U_{n \text{ fiss}}^{235}$ /present work/ | $U_{n \text{ fiss}}^{235}$ /48/ | $Pu_{n \text{ fiss}}^{239}$ /present work/ | $Pu_{n \text{ fiss}}^{239}$ /48/ |
| 1 hr | $1.6 \cdot 10^{19}$ | $1.47 \cdot 10^{19}$ | $1.73 \cdot 10^{19}$ | $1.65 \cdot 10^{19}$ | $1.46 \cdot 10^{19}$ | $1.44 \cdot 10^{19}$ |
| 2 hr | $6.6 \cdot 10^{18}$ | $5.92 \cdot 10^{18}$ | $6.94 \cdot 10^{18}$ | $7.72 \cdot 10^{18}$ | $5.93 \cdot 10^{18}$ | $6.62 \cdot 10^{18}$ |
| 5 hr | $2.23 \cdot 10^{18}$ | $1.93 \cdot 10^{18}$ | $1.77 \cdot 10^{18}$ | $2.03 \cdot 10^{18}$ | $1.44 \cdot 10^{18}$ | $1.7 \cdot 10^{18}$ |
| 10 hr | $1.09 \cdot 10^{18}$ | $1.0 \cdot 10^{18}$ | $6.96 \cdot 10^{17}$ | $7.6 \cdot 10^{17}$ | $5.95 \cdot 10^{17}$ | $6.88 \cdot 10^{17}$ |
| 1 day | $4.16 \cdot 10^{17}$ | $4.2 \cdot 10^{17}$ | $2.38 \cdot 10^{17}$ | $2.53 \cdot 10^{17}$ | $2.21 \cdot 10^{17}$ | $2.45 \cdot 10^{17}$ |
| 2 days | $1.73 \cdot 10^{17}$ | $1.93 \cdot 10^{17}$ | $9.31 \cdot 10^{16}$ | $9.7 \cdot 10^{16}$ | $9.49 \cdot 10^{16}$ | $1.02 \cdot 10^{17}$ |
| 5 " | $6.14 \cdot 10^{16}$ | $7.42 \cdot 10^{16}$ | $3.25 \cdot 10^{16}$ | $3.12 \cdot 10^{16}$ | $3.91 \cdot 10^{16}$ | $3.65 \cdot 10^{16}$ |
| 10 " | $3.05 \cdot 10^{16}$ | $3.24 \cdot 10^{16}$ | $1.65 \cdot 10^{16}$ | $1.56 \cdot 10^{16}$ | $1.74 \cdot 10^{16}$ | $1.7 \cdot 10^{16}$ |
| 20 " | $1.49 \cdot 10^{16}$ | $1.43 \cdot 10^{16}$ | $7.65 \cdot 10^{15}$ | — | $7.33 \cdot 10^{15}$ | — |
| 30 " | $9.44 \cdot 10^{15}$ | $8.72 \cdot 10^{15}$ | $4.65 \cdot 10^{15}$ | $4.45 \cdot 10^{15}$ | $4.32 \cdot 10^{15}$ | $4.14 \cdot 10^{15}$ |
| 70 " | $3.65 \cdot 10^{15}$ | $3.26 \cdot 10^{15}$ | $1.42 \cdot 10^{15}$ | — | $1.3 \cdot 10^{15}$ | — |
| 100 " | — | — | — | $8.97 \cdot 10^{14}$ | — | $8.05 \cdot 10^{14}$ |
| 150 " | $1.46 \cdot 10^{15}$ | $1.39 \cdot 10^{15}$ | $5.41 \cdot 10^{14}$ | — | $4.84 \cdot 10^{14}$ | — |
| 1 year | $3.24 \cdot 10^{14}$ | $4.33 \cdot 10^{14}$ | $6.87 \cdot 10^{13}$ | $6.38 \cdot 10^{13}$ | $7.68 \cdot 10^{13}$ | $7.22 \cdot 10^{13}$ |
| 1.5 years | $1.72 \cdot 10^{14}$ | $2.65 \cdot 10^{14}$ | $1.65 \cdot 10^{13}$ | — | $2.97 \cdot 10^{13}$ | — |
| 2 " | $1.16 \cdot 10^{14}$ | $1.83 \cdot 10^{14}$ | $7.8 \cdot 10^{12}$ | — | $1.83 \cdot 10^{13}$ | — |
| 3 " | $6.6 \cdot 10^{13}$ | $9.9 \cdot 10^{13}$ | $4.85 \cdot 10^{12}$ | $5.18 \cdot 10^{12}$ | $1.04 \cdot 10^{13}$ | $1.05 \cdot 10^{13}$ |
| 5 " | $3.22 \cdot 10^{13}$ | $3.65 \cdot 10^{13}$ | $4.57 \cdot 10^{12}$ | — | $5.05 \cdot 10^{12}$ | — |
| 10 " | $1.65 \cdot 10^{13}$ | $1.25 \cdot 10^{13}$ | $2.85 \cdot 10^{12}$ | $3.09 \cdot 10^{12}$ | $2.9 \cdot 10^{12}$ | $3.14 \cdot 10^{12}$ |
| 15 " | $1.27 \cdot 10^{13}$ | $9.27 \cdot 10^{12}$ | $2.52 \cdot 10^{12}$ | — | $2.49 \cdot 10^{12}$ | — |
| 30 " | $8.33 \cdot 10^{12}$ | $5.79 \cdot 10^{12}$ | $1.77 \cdot 10^{12}$ | $1.84 \cdot 10^{12}$ | $1.76 \cdot 10^{12}$ | $1.82 \cdot 10^{12}$ |

It is a good deal more complicated to calculate the gamma emission of a mixture of fission products from an explosion. Aside from the reasons given above, the fact that not enough is known about the decay schemes introduces new errors. The gamma-emission characteristics for 125 isotopes /49/ are given in the Appendix. The reliability of the data cited for each individual isotope is also considered. These data for the gamma emission of isotopes, together with data from /49/ on the beta activity of fission products during different time intervals after an explosion, were used to calculate the integral characteristics of a mixture of fission products as gamma emitters.

Figure 1, and also Table 1, show the calculated dependence of the gamma-emission intensity on time (mixture age), for a mixture of the accumulated products of a kiloton atomic explosion. Two types of fission are considered: $U_{n \text{ fiss}}^{235}$ and $Pu_{n \text{ fiss}}^{239}$. A comparison of the curves shows that for mixture ages

from 1 hour to 1 year the gamma-emission intensities for the two types of fission differ by less than 20%. For ages of around 2 years, however, the two sets of data differ by more than twice as much. This is explained by the considerable difference between the Ru^{106} yields for the two types of fission considered. The deviation between two curves may turn out to be less if the Ru^{106} fission yields given in /30/ are taken into account (see Table 2).

TABLE 2. Comparison of cumulative yields of certain fragment isotopes (experimental data)

| Isotope | $U_{n_{\text{ther}}}^{235}$ | | | $U_{n_{\text{fiss}}}^{235}$ | | | $Pu_{n_{\text{fiss}}}^{239}$ | | |
|-------------|-----------------------------|-----------------|----------------|-----------------------------|--------------------|----------------|------------------------------|-------------------|----------------|
| | /48/ | /30/ | Discrepancy, % | /48/ | /30/ | Discrepancy, % | /48/ | /30/ | Discrepancy, % |
| Sr^{89} | 4.79 | 4.79 | <2 | 4.15 | 4.4 ± 0.4 | 20 | 1.44 | 1.8 ± 0.2 | 25 |
| | | 4.8 | | | 5.6 ± 0.4 | | | | |
| Sr^{90} | 5.74 | 5.77 | <2 | 4.38 | 5.0 | 14 | 2.23 | 2.2 | <2 |
| | | 5.9 | | | | | | | |
| Zr^{85} | 6.4 | 6.2 | <2 | 6.72 | 5.85 ± 0.55 | <2 | 5.12 | 5.6 | 6.5 |
| | | 6.4 | | | 7.7 ± 0.6 | | | | |
| Zr^{97} | 6.2 | 5.9 | 2.4 | 6.51 | 6.55 ± 0.70 | <2 | 5.05 | 5.3 ± 0.5 | 3 |
| | | 6.2 | | | | | | 5.2 | |
| Mo^{99} | 6.1 | 6.06 | <2 | 6.1 | 6.1 | <2 | 5.73 | 5.9 | <2 |
| | | 6.1 | | | 5.9 ± 0.4 | | | 5.5 ± 0.4 | |
| | | 6.14 ± 0.16 | | | 6.4 ± 0.4 | | | 5.9 ± 0.6 | |
| Ru^{103} | 2.9 | 3.0 | <2 | 3.97 | 3.75 ± 0.55 | 13 | 6.25 | 6.0 ± 0.7 | 6.4 |
| | | 2.9 | | | 3.2 ± 0.6 | | | 5.7 ± 1.0 | |
| Ru^{108} | 0.38 | 0.38 | <2 | 0.47 | 1.19 ± 0.14 | Factor of 2 | 6.17 | 4.8 ± 0.6 | 24 |
| | | | | | 0.71 ± 0.12 | | | 4.6 ± 0.8 | |
| Rh^{105} | 0.9 | 0.9 | <2 | 1.02 | 1.45 ± 0.15 | 42 | 4.68 | — | — |
| Pd^{109} | 0.028 | 0.030 | 3.6 | 0.11 | 0.146 | 32 | 1.65 | 1.9 | 15 |
| | | 0.028 | | | | | | | |
| Pd^{112} | 0.011 | 0.010 | <2 | 0.043 | 0.041 | 5 | 0.17 | 0.14 | 18 |
| | | 0.011 | | | 0.035 ± 0.007 | | | | |
| Ag^{111} | 0.018 | 0.019 | <2 | 0.06 | 0.031 ± 0.002 | 23 | 0.48 | 0.55 ± 0.06 | 4.2 |
| | | 0.018 | | | 0.071 | | | 0.45 ± 0.03 | |
| Cd^{113m} | 0.0009 | 0.0007 | 22 | 0.0043 | 0.0022 | Factor of 2 | 0.0066 | — | — |
| | | 0.00071 | | | | | | | |
| Cd^{116} | 0.0091 | 0.0097 | 12 | 0.041 | 0.0304 ± 0.006 | 27 | 0.066 | 0.069 | 23 |
| | | 0.011 | | | 0.022 ± 0.002 | | | 0.09 ± 0.01 | |
| | | 0.0098 | | | 0.038 | | | 0.098 ± 0.008 | |
| | | | | | | | | 0.067 | |
| Te^{129m} | 0.22 | 0.35 | 55 | 0.19 | 0.55 ± 0.06 | Factor of 2.9 | 0.43 | 0.45 ± 0.09 | 4.7 |
| | | 0.34 | | | | | | | |
| Te^{132} | 4.37 | 4.7 | 4.1 | 4.44 | 5.35 ± 0.50 | 20 | 6.32 | 3.5 ± 1.0 | 45 |
| | | 4.4 | | | | | | | |
| Cs^{137} | 6.15 | 5.9 | 2.3 | 6.18 | 6.87 ± 0.17 | 6.5 | 6.14 | 6.6 | 13 |
| | | 6.81 | | | 6.3 | | | 7.45 ± 0.20 | |
| | | 6.15 | | | | | | 6.8 | |
| Ba^{140} | 6.33 | 6.32 | <2 | 5.79 | 5.0 ± 0.4 | 5 | 4.95 | 5.4 ± 0.5 | 3 |
| | | 6.3 | | | 6.0 ± 0.5 | | | 5.0 | |
| | | 6.35 | | | | | | 4.9 ± 0.4 | |
| Ce^{141} | 6.0 | 6.0 | <2 | 5.29 | 6.1 ± 0.6 | 15 | 4.65 | — | — |
| | | 6.0 | | | | | | | |
| Ce^{144} | 5.39 | 6.0 | 11 | 4.76 | 5.33 | 7.8 | 3.66 | — | — |
| | | 6.1 | | | 5.1 | | | | |
| | | 6.0 | | | 5.0 | | | | |
| Nd^{147} | 2.38 | 2.7 | 9.2 | 3.24 | 2.5 | 26 | 2.52 | — | — |
| | | 2.6 | | | 2.4 | | | | |
| | | 2.6 | | | 2.3 | | | | |
| Pm^{149} | 1.13 | 1.3 | 15 | 1.17 | 1.3 | 5 | 1.88 | — | — |
| | | | | | 1.3 | | | | |
| | | | | | 1.1 | | | | |
| Sm^{153} | 0.15 | 0.15 | <2 | 0.14 | 0.18 ± 0.01 | 36 | 0.48 | 0.48 | <2 |
| | | 0.14 | | | 0.19 ± 0.021 | | | | |
| Eu^{158} | 0.013 | 0.014 | <2 | 0.013 | 0.023 | 85 | 0.08 | — | — |
| | | 0.013 | | | 0.023 | | | | |
| | | | | | 0.025 | | | | |

* Mean discrepancies are given.

As the Appendix shows, for 31 of the 125 isotopes so little is known about the decay schemes that the absolute quantum yields cannot be determined. This pertains mainly to short-lived isotopes. Consequently, for small mixture ages these isotopes may make a substantial contribution to the total intensity, whereas for a 24-hour-old mixture their contribution will be less than 4%, provided the sum of the isotopes with unknown decay schemes is assumed to have the same mean energies and average quantum yield as the sum of the isotopes with known decay schemes.

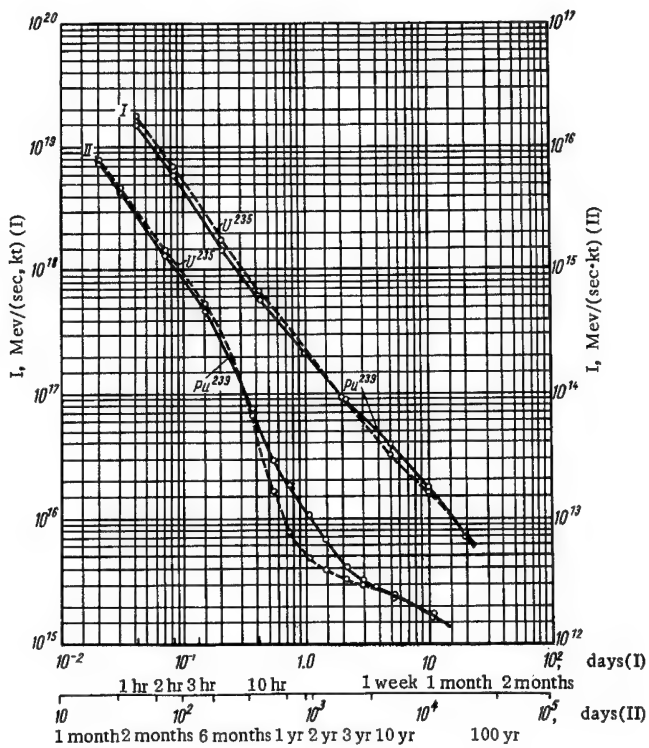


FIGURE 1. Gamma-emission intensity of sum of fission products of kiloton atomic explosion as function of time (mixture age) for two types of fission ($U_{n_{\text{fiss}}}^{235}$ and $Pu_{n_{\text{fiss}}}^{239}$).

The sections of the curves in Figure 1 for ages from 1 to 24 hours were constructed on the basis of these assumptions. It should be noted that for the $Pu_{n_{\text{fiss}}}^{239}$ mixture the contribution of these isotopes to the intensity at an age of 1 hour amounts to about 40% of the total intensity.

If we assume that the gamma-emission intensity diminishes according to some power law analogous to the law describing the decrease in total beta activity, then this variation can be represented by the formula

$$\frac{I}{I_0} = \left(\frac{T_0}{T} \right)^n \quad (5)$$

and, taking $T_0 = 1$ hour, we can find exponent n for different ages. Table 3 lists some values for n for the two types of fission considered.

TABLE 3. Values of exponent n in formula (5) for different ages of mixture of fission products for Pu^{239} and U^{235}

| Age | $\text{Pu}_{\text{n fiss}}^{239}$ | $\text{U}_{\text{n fiss}}^{235}$ | Age | $\text{Pu}_{\text{n fiss}}^{239}$ | $\text{U}_{\text{n fiss}}^{235}$ |
|-------|-----------------------------------|----------------------------------|----------|-----------------------------------|----------------------------------|
| 2 hr | 1.31 | 1.32 | 5 days | 1.24 | 1.31 |
| 5 hr | 1.43 | 1.43 | 20 days | 1.23 | 1.25 |
| 10 hr | 1.39 | 1.40 | 70 days | 1.26 | 1.27 |
| 1 day | 1.32 | 1.35 | 150 days | 1.26 | 1.27 |
| | | | 1 year | 1.34 | 1.37 |

For the sake of the subsequent discussion, it will be convenient to evaluate the contribution (to the total activity) of the long-lived radioactive isotopes of the inert gases and the products of their decay. Table 4 shows this contribution in percent of the total beta activity of the mixture, for the $\text{Pu}_{\text{n fiss}}^{239}$ reaction.

TABLE 4.

| Age | 1 hr | 2 hr | 5 hr | 10 hr | 1 day | 2 days | 5 days | 10 days | 20 days | 30 days |
|-----------------|------|------|------|-------|-------|--------|--------|---------|---------|---------|
| Contribution, % | 14 | 13 | 11 | 14 | 17 | 12 | 11 | 13 | 8 | 3.5 |

Because of the significant contribution of the volatile component, exponent n in formula (5) may have values somewhat different from those shown in Table 3, at least for fission products with ages up to 20 days. The ratio between the volatile and bound components of the iodine isotopes (I^{134} , I^{135} , I^{133} , and I^{131}) may affect the value of exponent n .

On the basis of the tables in /49/ and the Appendix, we calculated the numerical intensity of gamma-ray quanta, as a time function expressed in quanta per second per kt of fission (Table 5). This function can be described by a law almost identical to that for the energy intensity:

$$\frac{N_\gamma}{N_{\nu_0}} = \left(\frac{T_0}{T} \right)^n. \quad (6)$$

The value of the exponent in formulas (4) through (6) depends slightly on whether we consider the time variation of the total beta activity or the time variation of the numerical and energetic gamma-emission intensities of the mixture of fission products.

TABLE 5. Numerical gamma-emission intensity for mixture of fragment isotopes, as function of mixture age, quanta/(sec·kt)

| Mixture age | $U_{n_{\text{fiss}}}^{235}$ | $Pu_{n_{\text{fiss}}}^{239}$ | Mixture age | $U_{n_{\text{fiss}}}^{235}$ | $Pu_{n_{\text{fiss}}}^{239}$ |
|-------------|-----------------------------|------------------------------|-------------|-----------------------------|------------------------------|
| 1 hr | $1.9 \cdot 10^{19}$ | $1.7 \cdot 10^{19}$ | 70 days | $2.23 \cdot 10^{15}$ | $2.16 \cdot 10^{15}$ |
| 2 hr | $7.63 \cdot 10^{18}$ | $6.93 \cdot 10^{18}$ | 150 days | $8.22 \cdot 10^{14}$ | $7.75 \cdot 10^{14}$ |
| 5 hr | $2.05 \cdot 10^{18}$ | $1.82 \cdot 10^{18}$ | 1 year | $1.1 \cdot 10^{14}$ | $1.29 \cdot 10^{14}$ |
| 10 hr | $9.36 \cdot 10^{17}$ | $8.81 \cdot 10^{17}$ | 1.5 years | $3.4 \cdot 10^{13}$ | $5.71 \cdot 10^{13}$ |
| 1 day | $4.08 \cdot 10^{17}$ | $4.05 \cdot 10^{17}$ | 2 years | $1.87 \cdot 10^{13}$ | $3.69 \cdot 10^{13}$ |
| 2 days | $1.83 \cdot 10^{17}$ | $1.97 \cdot 10^{17}$ | 3 years | $1.06 \cdot 10^{13}$ | $2.06 \cdot 10^{13}$ |
| 5 days | $6.7 \cdot 10^{16}$ | $8.3 \cdot 10^{16}$ | 5 years | $7.87 \cdot 10^{12}$ | $9.15 \cdot 10^{12}$ |
| 10 days | $3.01 \cdot 10^{16}$ | $3.37 \cdot 10^{16}$ | 10 years | $4.39 \cdot 10^{12}$ | $4.58 \cdot 10^{12}$ |
| 20 days | $1.2 \cdot 10^{16}$ | $1.22 \cdot 10^{16}$ | 15 years | $3.82 \cdot 10^{12}$ | $3.82 \cdot 10^{12}$ |
| 30 days | $6.94 \cdot 10^{15}$ | $6.81 \cdot 10^{15}$ | 30 years | $2.68 \cdot 10^{12}$ | $2.66 \cdot 10^{12}$ |

For the calculations we often also have to know such quantities as the average energy E_{av} of the gamma-ray quanta (in Mev per quantum), the average quantum yield ν (gamma-ray quanta per disintegration), and the average gamma-emission yield (Mev per disintegration), all corresponding to the sum of the fragments of a given age. Figure 2 shows the first two of these as functions of mixture age, for two types of fission: $U_{n_{\text{fiss}}}^{235}$ (solid curves) and $Pu_{n_{\text{fiss}}}^{239}$ (dashed curves). For mixtures of all ages the data were calculated taking into account only those isotopes whose decay schemes were known (see Appendix).

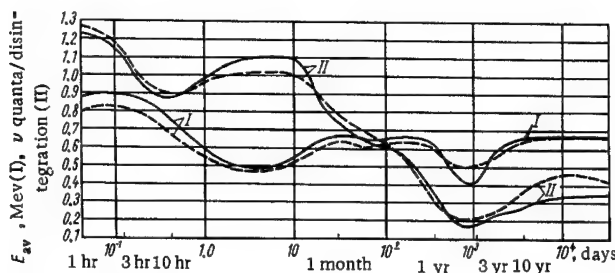


FIGURE 2. Average energy E_{av} and average quantum yield ν of gamma emission for sum of fission products, as functions of mixture age. Solid curves pertain to $U_{n_{\text{fiss}}}^{235}$ and dashed curves to $Pu_{n_{\text{fiss}}}^{239}$.

It is evident from Figure 2 that the average gamma-emission energy of a fragment mixture does not exceed 0.9 Mev (the maximum value of 0.9 Mev is attained about 2 hours after fission). Minimum values of the energy (about 0.4 Mev) are attained at ages of 2 to 5 days and 2 to 3 years. The time-variation curves of the average energy for the two types of fission do not on the whole differ significantly from one another.

The average quantum yield of the mixture varies over a quite wide range as the mixture ages: whereas this yield is about 1.25 for $T = 1$ hour, for ages up to around 2 years it is of the order of 0.2 quantum/disintegration.

In addition to the integral characteristics for a mixture of fission products, we also computed the differential gamma-emission spectra (the so-called line spectra) for the fission of U^{238} by 14-Mev neutrons. The range of mixture ages studied was from 2 days to 1 year.

The choice of the $U_{14\text{ Mev}}^{238}$ fission reaction was dictated by the fact that for neutron energies of 14 Mev the probability of a symmetrical fission is sharply increased. Consequently, the isotopes whose lines may appear in the line spectra for the $U_{14\text{ Mev}}^{238}$ reaction will not show up in the spectra for other fission reactions.

All the spectra which were calculated are shown in Figures 3 through 6. Two energy ranges were considered: from 0 to 400 kev (second range, "soft" radiation) and from 0 to 2000 kev (first range, "hard" radiation). These ranges correspond approximately to the energies at which it is convenient to study the spectra of the fission products experimentally. In plotting Figures 3 through 6, the energies of the gamma-emission lines were rounded off to the nearest kev in the second range and to the nearest 5 kev in the first range.

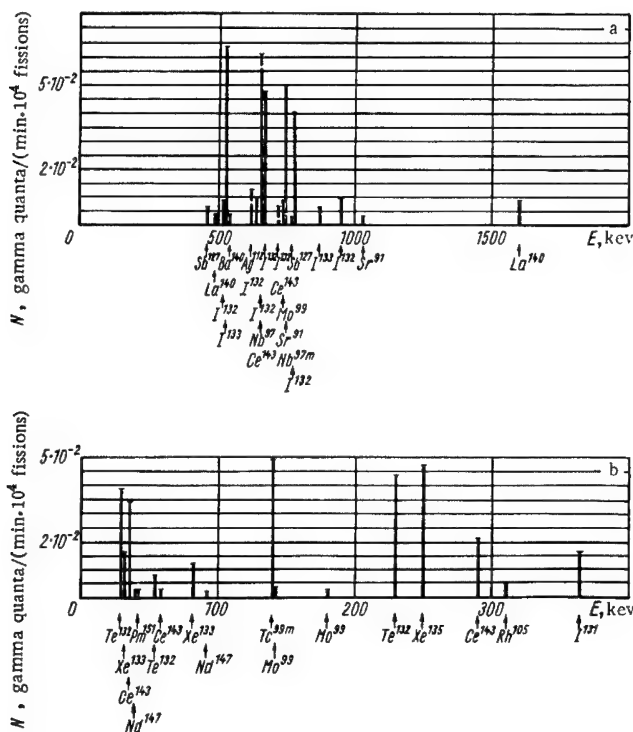


FIGURE 3. Line spectrum of gamma emission for mixture of fission products 2 days old, in energy ranges from 0 to 2000 kev (a) and 0 to 400 kev (b).

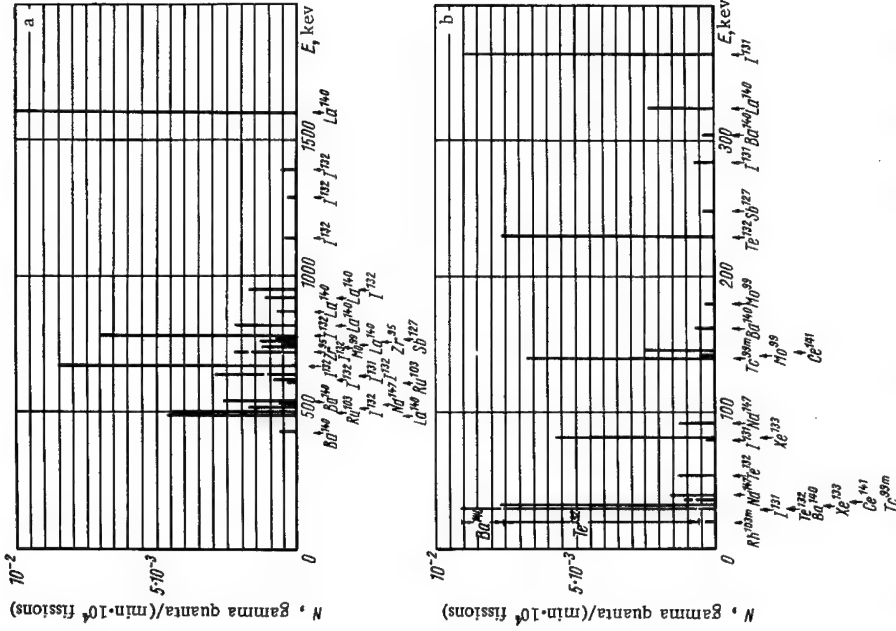


FIGURE 4. Line spectrum of gamma emission for mixture of fission products 10 days old, in energy ranges from 0 to 200 kev (a) and 0 to 400 kev (b).

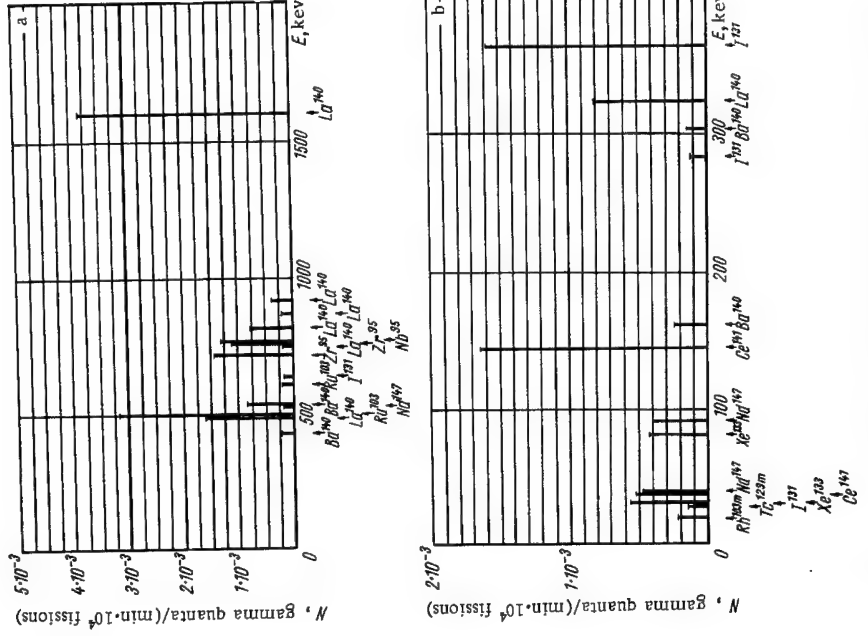


FIGURE 5. Line spectrum of gamma emission for mixture of fission products 30 days old, in energy ranges from 0 to 2000 kev (a) and 0 to 400 kev (b).

The integral characteristics of a mixture of fission products and the differential gamma-emission spectra were calculated in /45–48, 52–54/. The most complete of such data are those given in /47, 48/. While comparing the results of those studies with the calculations made in the present section, it should be kept in mind that /48/ was published back in 1960; thus the data used in it for the fission-product yields, half-lives, and isotope decay schemes were published before the middle of 1958 and are frequently unreliable. In addition to the results of our calculations, Table 1 also included the gamma-emission intensities (gamma activities) obtained in /48/ for a mixture of fission products. In view of the good fit between these results, it is to be assumed that a further improvement of the data for the half-lives and isotope decay schemes will not alter significantly the figures given in Table 1.

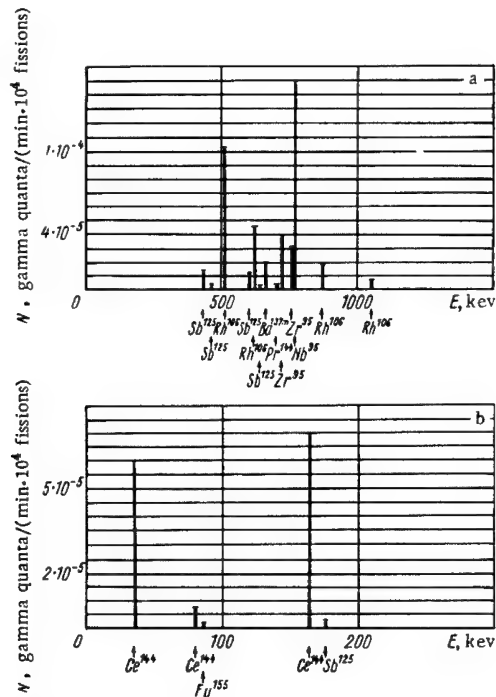
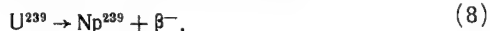
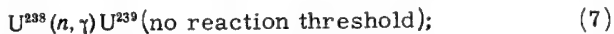


FIGURE 6. Line spectrum of gamma emission for mixture of fission products 1 year old, in energy ranges from 0 to 2000 kev (a) and 0 to 400 kev (b).

So far we have considered only the fission products of a nuclear explosion. However, an explosion (especially a thermonuclear one) may generate a considerable amount of activity as a result of interactions of neutrons with nuclei of the environment and with the structural elements of the bomb itself. Here the amount of activity created depends on the number of neutrons generated, the composition of the environment, the structural material of the bomb, and also the energy range and spatial distribution of the neutrons.

The various isotopes of the activity induced by the neutron flux can be divided into three groups: 1) isotopes produced by the action of the neutrons of the explosion on the elements of the charge itself; 2) isotopes produced by the action of neutrons on the structural elements of the bomb; 3) isotopes produced by the interaction between neutrons leaving the bomb envelope and elements of the environment (air, water, earth, etc.).

The most important isotopes in the first group are Np^{239} ($T_{1/2} = 2.3$ days) and U^{237} ($T_{1/2} = 6.7$ days) /55, 56/. Isotope Np^{239} , which has an average gamma-emission energy of about 0.14 Mev, is formed in the reaction



Isotope U^{237} , which has an average gamma-emission energy of about 0.1 Mev, is formed when U^{238} is bombarded with strictly high-energy neutrons, in the reaction



(reaction threshold about 5.9 Mev /57/).

We see from reactions (7) through (9) that a necessary condition for the presence of Np^{239} and U^{237} in the explosion products is the presence of a certain amount of U^{238} in the charge. Therefore, when an atomic bomb containing U^{235} (with an admixture of U^{238}) explodes, a certain amount of Np^{239} may be produced, but the isotope U^{237} appears in negligible quantities only, due to the high reaction threshold of (9). When a thermonuclear bomb explodes, considerably more neutrons per unit energy are released than in the case of an atomic bomb /17, 23/; accordingly, more activity is induced by the neutron flux as well. For such bombs elements with higher atomic numbers may appear, due to the action of the intense neutron flux on the fissionable materials in the bomb /58–60/. However, if U^{238} is added to the envelope of a thermonuclear bomb to enhance the force of the explosion, forming a "fission-fusion-fission" bomb, isotopes Np^{239} and U^{237} will be produced in very substantial quantities /55, 56/. For example, the Np^{239} content (in terms of activity) of the radioactive products of such a bomb, 3 or 4 days after the explosion, may amount to 50 to 65% of the total activity /56, 61/.

The presence of considerable amounts of radioactive isotope U^{237} in the explosion products is an unambiguous indication that a thermonuclear reaction took place, since this isotope is formed from U^{238} in a reaction having a threshold of about 5.9 Mev. The presence of U^{237} in the explosion products was first pointed out in /62, 63/. These studies described the results of a radiochemical and radiometric analysis of the particles which fell upon certain Japanese fishing boats (the so-called "Bikini ashes") after the "Bravo" explosion at Bikini Atoll on 1 March 1954.

Due to the presence of a considerable number of radioactive isotopes Np^{239} and U^{237} in the debris of a "fission-fusion-fission" bomb, the characteristics of the explosion products in this case differ significantly from those of a mixture of fission fragments for the $\text{U}^{235}_{\text{n,ther}}$ reaction.

A small amount of isotope U^{240} is also produced during the explosion of a "fission-fusion-fission" bomb /48, 64/, when U^{238} nuclei manage to pick up two neutrons. Minute amounts of the transuranic elements Es^{255} and Fm^{255} are also formed /58–60/. In this case a U^{238} nucleus must capture 17 neutrons.

According to available data /19–22/, all the powerful bombs set off before 1958 were bombs which operated on the "fission-fusion-fission" principle. During this period not a single explosion of a "clean" thermonuclear bomb of high power was reported. Different data give the following ratios of the fission-product yields for "fission-fusion-fission" bombs and atomic bombs (per unit of power): 0.5 /65/; 0.66 /56/; 0.8 /16/.

The total power of all the nuclear-weapon tests in the world during the period from 1945 through 1958 amounted to about 170 Mt /23, 65/ (of this, about 92 Mt came from fission explosions). Therefore, the yield ratio for the explosions during these years may be assumed to be approximately 0.5. The total power of the nuclear weapons tests from 1959 through 1962 was 510 Mt, of which fission reactions accounted for 190 Mt; thus, for this period the above-indicated coefficient dropped to about 0.37 /21, 22/.

The activity induced by interactions between neutrons and the structural elements of a bomb (second group of induced-activity isotopes) may be relatively great. Moreover, it is clear that the spectrum of the neutrons inside the bomb will be quite hard, especially for a thermonuclear explosion. Consequently, ($n, 2n$) reactions, which have a comparatively high threshold, make a significant contribution to the neutron interaction.

Considerable material has been collected on those isotopes of the induced activity which may belong to the second group. Some of these isotopes are: Co⁶⁰ /60–72/; Co⁵⁷, Co⁵⁸ /70/; Fe⁵⁹ /41, 73/; Fe⁵⁵ /79/; Mn⁵⁴ /40, 41, 66, 74–78/; Zn⁶⁵ /68, 72/; Y⁸⁸ /40/; W¹⁸⁵, W¹⁸¹, W¹⁸⁷, Re¹⁸⁸ /39, 40, 80, 82, 83/, and two isomers of Rh¹⁰² /40, 76, 81, 84, 85/. In the "Hardtack" series of American tests, isotopes of tungsten and rhodium were produced as a result of activation of elements especially included in the bomb envelope; these isotopes were used to differentiate between the products of individual explosions. There have also been reports of the use of isotopes Sb¹²⁴, Cd¹⁰⁹, and Cd^{113m} as "tracers" /86–89/.

The isotopes of the third group are produced by interactions between neutrons leaving the bomb envelope and elements of the environment. The latter elements may be: air, for atmospheric explosions; water, for underwater and above-water explosions; the structural elements of the tower, for tower explosions; and ground material, for explosions near, on, and under the earth.

As a rule, a slight amount of induced activity is produced when the neutrons interact with air atoms. One or two hours after the explosion this activity amounts to less than one percent of the total fragment activity (the short-lived isotope A⁴¹ and a small amount of long-lived C¹⁴) /23, 36, 90–94/.

The large amount of activity induced during explosions near the earth or water can be attributed to interactions between neutrons and the elements of the underlying surface (ground or water). Calculations /7, 41, 95/ show that the following elements play a substantial role in creating this induced activity: aluminum, silicon, sodium, manganese, iron, and cobalt (in the ground); and chlorine, sodium, magnesium, and bromine (in sea water).

The activity induced in the material of the underlying surface, $\sigma(t)$ disintegrations/(sec·cm³), at a time t after the exposure, is given by the relation

$$\sigma(t) = \rho \prod_i \sum_j 10^{-24} \alpha_j N_i \sigma_{\alpha_j} \lambda_j e^{-\lambda_j t}, \quad (10)$$

and the gamma activity (amount of gamma emission in Mev/(sec·cm³)) is given by the relation

$$\sigma_y(t) = \rho \Pi \sum_i 10^{-24} \alpha_j N_i \sigma_{aj} E_j \lambda_j e^{-\lambda_j t}. \quad (10a)$$

Here ρ is the density of the material of the underlying surface in g/cm³, Π is the flux of slow neutrons at the activation point for the entire exposure time (in neutrons/cm²), α_j is the j th-isotope portion of a mixture of isotopes of the i th element, N_i is the number of atoms of the i th element in a gram of material of the underlying surface, σ_{aj} is the microscopic activation cross section for the j th isotope (in barns), λ_j is the decay constant of the isotope produced during activation of the j th isotope (in sec⁻¹), and E_j is the total gamma-emission energy of the decay of a radioactive isotope produced as a result of activation of the j th isotope of the i th element (in Mev/disintegration).

Let us designate as f the specific activity per gram of underlying-surface material exposed to unit neutron flux (neutron/cm²) at a time t ; f is measured in (disintegration/sec·g)). Analogously, F is the specific gamma activity (amount of energy emitted in the form of gamma radiation by one gram of material exposed to unit neutron flux), measured in Mev/(sec·g). Let us calculate:

$$f(t) = \frac{\sigma(t)}{\rho \Pi}; \quad F(t) = \frac{\sigma_y(t)}{\rho \Pi}.$$

Figure 7 shows the curves of $f(t)$ and $F(t)$ for ground of average* composition for $0.03 \leq t \leq 500$ hr. The time variations of the activities of individual isotopes contributing most to the total specific activity f (for ground) are also plotted. As the figure shows, the induced activity of the ground (gamma activity) is determined mainly by the following radioactive isotopes:

- Al²⁸ — from 0 to 15 min;
- Mn⁵⁶ and Na²⁴ — from 15 min to 200 hr;
- Fe⁵⁹ — after 300 hr.

From 100 to 300 days after the explosion, radioactive isotope Co⁶⁰ begins to make a significant contribution to the induced activity /40, 41/.

Since the chemical content may vary from soil type to soil type, the specific activity f and gamma activity F induced in the material constituting the underlying surface may differ from the values plotted in Figure 7. Table 6 lists the chemical compositions of the most common types of soil (in percent by weight for dry soil) /96/.

The second part of Table 6 lists the calculated correction factors $k_i(t)$ for the curves in Figure 7, for various soils and for 3 time intervals. Here,

$$k_i(t) = \frac{f_i(t)}{f_{av}(t)},$$

where $f_i(t)$ corresponds to the i th type of soil and $f_{av}(t)$ is the average composition of the earth's crust.

* Here, average composition refers to soil composition averaged over the surface layer of the entire earth /96/.

TABLE 6. Correction factors for determining induced activity in various types of soils

| Soil type | Content, % | | | | Correction factors | | |
|--|------------|------|------|------|--------------------|-----------|---------|
| | Si | Al | Fe | Na | 0—15 min | 10—200 hr | >200 hr |
| Chernozem | 20.7 | 8.37 | 3.16 | 0.58 | 1.12 | 0.22 | 0.75 |
| Podzolic | 32.5 | 7.93 | 2.16 | 1.90 | 1.06 | 0.8 | 0.52 |
| Highly podzolized loamy | 36.1 | 4.19 | 1.93 | 1.26 | 0.6 | 0.53 | 0.48 |
| Desert-steppe sierozem | 27.9 | 5.92 | 3.64 | 1.86 | 0.8 | 0.77 | 0.87 |
| Dark chestnut brown | 30.8 | 7.88 | 3.06 | 0.83 | 1.06 | 0.35 | 0.73 |
| Desert zone | 32.0 | 6.90 | 2.2 | 1.3 | 0.93 | 0.54 | 0.52 |
| Tundra | — | 1.30 | — | 2.0 | 0.18 | 0.84 | — |
| Average composition of earth's crust . | 26.0 | 7.45 | 4.2 | 2.4 | 1.0 | 1.0 | 1.0 |

As the table shows, the specific activity (or gamma activity) does not vary much from soil type to soil type: by a factor of no more than 1.5 to 2.0, on the average. Other isotopes may also appear for certain soils: Ca⁴⁵ (for an explosion on a coral atoll), S³⁵ /62/, etc., but such cases are not typical. Fallout samples and air samples collected in the atmospheric layer near the earth indicate that induced activity is present. Aside from isotopes Co⁶⁰, Fe⁵⁹, and Fe⁵⁵, which belong to the third group of induced-activity isotopes, the following have also been reported: Sc⁴⁶ /40, 69, 72/, Na²⁴ /39/, Cs¹³⁴, Eu¹⁵², and Eu¹⁵⁴ /69/. These may also be placed in the third group.

It should be mentioned that only a small part of the neutrons absorbed by the ground go to activate the ground elements. This part is determined by the ratio of the sum of the effective activation cross sections to the sum of the effective capture cross sections for neutrons in soil. For the average composition of elements in the earth's crust (dry soil) this ratio is about 0.15 /7/; with an increase in moisture content this ratio will decrease.

The salinity of seawater is practically the same everywhere in the world; in the open ocean it is about 35 g per kg of water /97/. Thus the content of the most important ions is comparatively uniform. For example, 1 kg of seawater includes: 10.7 g of Na⁺, 1.3 g of Mg²⁺, and 19.3 g of Cl⁻. Consequently, Cl³⁸ (for up to about 2 hours) and Na²⁴ should contribute most to the induced activity after an explosion at sea.

2. Fallout of nuclear-explosion products in a region

A nuclear explosion results in the liberation of an enormous amount of energy, over a short time interval and within a limited volume. For instance, the energy density of the radiation from a nuclear explosion may be as much as 10¹⁶ erg/cm³ /8/.

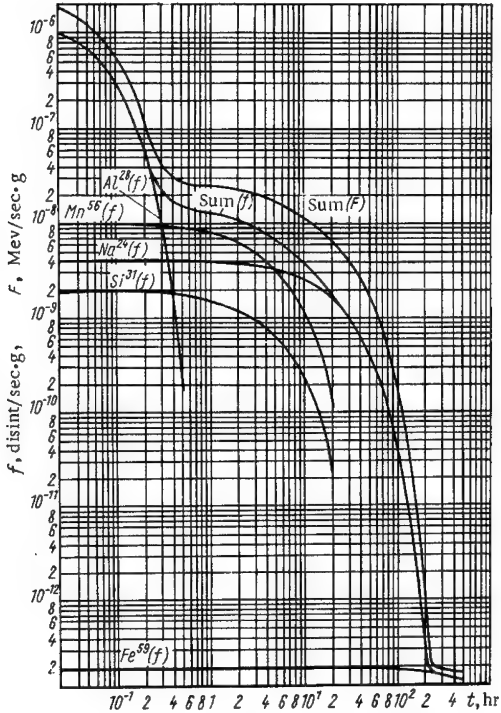


FIGURE 7. Time variation of induced activity of ground exposed to unit neutron flux.

At the same time, temperatures of several million degrees and pressures of hundreds of thousands of atmospheres are developed (for a blast of nominal strength), so that the debris of the bomb becomes vaporized (and the fission fragments as well). In an atmospheric explosion the air adjacent to the blast point becomes greatly heated, producing a brightly luminous fireball having an approximately uniform temperature distribution throughout /18/. Due to the intense radiation and dispersion of matter, the fireball begins to grow larger. Adiabatic expansion and the consequent drawing in of air from the surroundings into the outer layers of the ball produce a continual reduction of the fireball temperature. However, the effective temperature of the luminous (that is, visible) surface, after dropping to about 2000°K (the temperature at the surface of a shock wave moving away from the isothermal ball), then begins to increase once again. This happens because the shock-wave front cools and becomes transparent to the radiation of the isothermal ball /8/. The temperature of the visible outer surface of the ball rises until it equals the temperature inside it (about 7500°K) and then diminishes monotonically.

The time variation of the fireball temperature $T(t)$, if we consider just the cooling (after T_0 has been reached) due to radiation, is given by the formula

$$T(t) = T_0 e^{-t/3 \sqrt{W/20}}, \quad (11)$$

where $T_0 \approx 7500^\circ\text{K}$, the temperature at the time of the second maximum, is practically independent of the strength W of the explosion in kt; and t is the time after the explosion in seconds /2/.

The maximum size (diameter) $D(\text{m})$ of the fireball for an atmospheric explosion /8/ is

$$D = 67W^{0.4}. \quad (12)$$

The variations of the relative mass, relative mean volume, and average temperature of the fireball was computed by Storebö /98/ for various rates of intake of air from the surroundings and mixing with this air (for an atmospheric explosion).

If the explosion is set off near an underlying surface (land or water), at a height $h \leq D/2$, then the fireball will pick up a considerable amount of material from the underlying surface. Some of the matter pulled up into the fireball will become vaporized (more than 4 tons of soil per kiloton pulled up, for a surface test) /8/. Most of it, however, will melt (several hundred tons per kiloton of soil /99/), producing an enormous quantity of liquid (molten) particles, on which the radioactive explosion products will later condense during cooling.

Right after it is formed, the fireball starts to move upward at a velocity of 75 to 100 m/sec, due to the buoyant force caused by the difference in densities inside and outside the fireball. As it ascends and cools, the fireball changes shape: condensation of bomb material and atmospheric moisture (or moisture drawn up from below) begins; the ball becomes toroidal in shape and intensive circulation takes place, with an upward flow in the center regions and a downward flow out toward the edges /100/. At the same time, a radioactive cloud is formed, which rises for several minutes, until the density inside it equals the density of the surroundings, after which the cloud stabilizes /100/. During this time the cloud ascends to an altitude of several kilometers (for a kiloton blast) or to somewhere above the tropopause (for a megaton blast).

As the cloud's velocity of ascent decreases, an ever-increasing number of radioactive particles fall out onto the earth's surface. These descending particles constitute the so-called radioactive fallout, which continues even after stabilization of the cloud. The radioactive particles may be produced either as a result of condensation and subsequent coagulation of the fission products and the vaporized bomb material, or else as a result of their condensation on molten particles of the ground drawn up into the fireball and cloud /101/.

The formation of radioactive particles in the fireball and cloud of an atmospheric explosion has been described in detail by Stewart /102/, Freiling /103/, Storebö /98/, and Lavrenchik /2/.

Two theories of particle formation are compared in /103/. According to the first theory, the particles form as a result of condensation, and the distribution of particles according to size is exponential. According to the second theory /102/, the particles form as a result of simultaneous condensation and coagulation, and the size distribution of particles is described by a logarithmic normal curve. Experimental data verify the importance of the coagulation process in the particle formation accompanying an atmospheric blast /101/, although neither of the distribution curves constructed on the basis of these theories contradicts the experimental results /103/.

In /2/ both diffusion and molecular-kinetic mechanisms of particle growth were considered. It was demonstrated that for diffusion condensation $r(t) \approx t^{1/4}$, for molecular-kinetic condensation $r(t) \approx t$, and in the coagulation process /102/ $r(t) \approx t^{1/2}$ (where r is the particle radius and t is the time).

The particles produced during atmospheric explosions are, as a rule, smaller than 10 microns in diameter, the average size being 0.01 micron (for a 20-kt explosion) /102/. For more powerful explosions the average particle size will be even less.

When material from the underlying layer (ground) is drawn up into the fireball, as is the case for an explosion on the earth, a large number of radioactive particles are produced due to condensation of vaporized radioactive products on molten soil particles. In a tower explosion, when a smaller amount of material (from the ground and from the tower itself) is picked up by the fireball, in comparison with a surface explosion, the coagulation mechanism of particle formation predominates; the average size of these particles for a nominal explosion is 0.1 micron /102/.

Large fallout particles are produced during a surface explosion due to interactions between condensing bomb material present in the fireball in a gaseous state and material from the earth's surface which has been drawn up into the ball (or into the radioactive cloud). A considerable amount of the unvaporized (partially molten) soil material is thereby mixed over the volume of the fireball. If the fireball is large, this mixing can hardly be uniform.

For a surface explosion the particles are of a glassy material produced when silicate minerals of the soil melt. There are two kinds of such particles: transparent spherical particles which are yellowish-green in color, and opaque particles of irregular shape (angular particles), produced in the peripheral regions of the fireball by fusion of mineral grains of soil (both kinds of particles have diameters up to 2 or 3 mm /101/).

In the spherical particles the radioactive products are distributed more or less uniformly over the volume or in a thick volume layer. For the large angular particles the radioactive products are distributed in a thin surface layer, and there is a tendency to diffuse somewhat into the interior.

The spherical particles probably form close to the center of the explosion (they are heated to higher temperatures), while the very fine particles form during the immediate condensation of the vaporizing material. However, since the concentration of individual [fission] fragments is lower by far than the concentration of matter drawn up into the fireball, the fragments will in general be deposited onto soil particles, and there will be only a small number of these fine particles.

The beginning of the condensation of radioactive explosion products (first period) may be considered to be the start of the radioactive-particle

formation. After solidification of the particles (for surface explosions this takes place at the melting point t_m of the principal components of the material of the underlying surface; for soil t_m ranges from 1100 to 1700°C), condensation of the volatile explosion products proceeds on the surfaces of these particles (second period), until they leave the cloud under the influence of gravitational forces.

The number of different elements remaining in the cloud at each moment and not deposited onto particles will equal the number required for saturation of the cloud at the given temperature /99/. While the cloud is still ascending, the largest radioactive particles start to leave the cloud and then to fall out onto the earth's surface. The finer particles continue rising with the cloud /1/ and possess lower rates of fall, so that they are deposited onto the earth's surface at a considerably greater distance from the site of the explosion.

The radioactive fallout from a nuclear explosion can be divided up into the following categories (see, for example, /104/).

1. Restricted or local fallout, in a region immediately adjacent to the site of the explosion (the first tens or hundreds of kilometers away), according to the wind direction. The region of this fallout is often called the wake of the radioactive cloud /105/. The local fallout is produced mainly as a result of gravitational precipitation of large particles ("dry" fallout), which form principally during surface nuclear explosions.

The best criterion for determining the local fallout is one involving the maximum particle size, since very large particles are not found beyond the local fallout. In /100/ this maximum size is taken as 50 microns.

For a surface explosion, according to different estimates, up to 40 to 80% /1, 2/ of the total residual radioactivity is deposited in the local-fallout region. For tower explosions (at heights of 150 to 200m, for explosive forces from 10 to 40kt) this percentage will be from 10 to 20%, and for aerostatic explosions (at heights of about 200m, for forces from 10 to 70kt), which are essentially atmospheric explosions, it will be from 0.1 to 2% /106/.

2. Intermediate fallout, extending out to several thousand kilometers from the site of the explosion. This fallout retains the characteristics of the particular synoptic conditions obtaining at the time of the explosion /2/.

3. Global [world-wide] fallout, lasting for weeks, months, and even several years after the explosion. It consists mainly of radioactive products cast up into the stratosphere, the particle sizes being from 2 to 5 microns (or less). These radioactive aerosols fall from the stratosphere into the troposphere via cracks in the tropopause, as a result of turbulence in the jet streams /104/. In 80 to 90% of the cases, these aerosols are carried to the earth's surface by the precipitation of moisture, that is, the radioactivity is in effect washed out of the troposphere /85/.*

The local fallout attending surface and underground nuclear explosions (with ejection of earth) is the most dangerous type, from the point of view of the creation of areas having high radiation levels /8, 107/. However, if the frequency of nuclear-weapon testing is high, then the intermediate and global fallouts also become a hazard, since, even though their intensities may be low, they spread out to great distances from the explosion site and may fall into densely populated regions.

* [These three types of fallout are sometimes called local, tropospheric, and stratospheric fallout.]

In the following we consider some possible schemes for describing the local fallout in terms of known explosion parameters and meteorological characteristics. Such a scheme can be constructed by making a mathematical model of the fallout /8/.

It is possible to predict the contamination zones even if only a minimum of information is available concerning the strength of the explosion and the structure of the wind. This is done either by constructing idealized fallout diagrams or by selecting simulation models of the fallout on the basis of experimental data or mathematical modeling /8/.

To construct a mathematical model of the fallout, it is first necessary to select a function describing the distribution of radioactive products in a stabilized explosion cloud, for particles of different sizes and for different fallout heights, as a function of the settling velocity in the direction of the mean wind (averaged over the height).

Various functions have been suggested for the distribution according to particle size, on the basis of experimental results. In most cases these functions may be represented by a logarithmic-normal law, for surface /108/, underground /99, 100/, and atmospheric /102/ explosions. Exponential functions may also be used for atmospheric explosions /103/.

The propagation of a contaminant coming from a transient point source was studied, the fall velocities v of the particles being nonuniform. The following distribution, in the form of a two-parameter function (v -distribution), was suggested /109/:

$$N(v) = \frac{a^{n+1}}{\Gamma(n+1)} v^n e^{-av}. \quad (13)$$

It is typical that the activity distribution according to particle sizes, for a given type of explosion, is practically independent of the strength of the blast /108/. However, it is greatly influenced by the type of material forming the underlying surface /100/ (for surface and underground explosions).

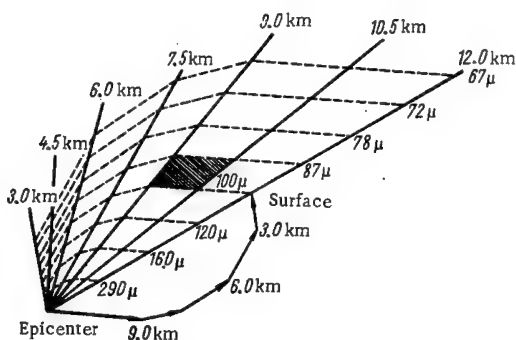


FIGURE 8. Distribution of particles precipitated onto earth's surface from various heights.

When constructing a mathematical model, it is convenient to consider the propagation of a polydisperse contaminant from a point source /109/, a vertical line source /1, 110/, and a volume source /100, 108/. Clearly, the line source and three-dimensional source can be treated as combinations of point sources. The results obtained using the mathematical models will be discussed below.

Figure 8 shows the distributions for particles of different sizes, precipitated onto the earth's surface from a vertical line source at various heights /110/. The radial and dashed lines show, respectively, the geometric loci of the points to which particles of different sizes fall from a specified height and the loci of points to which particles of a specified size fall from different heights. The line with the arrows is a projection of the trajectory for the fall of a 100 micron particle from a height of 12 km. The shaded area indicates the location of particles 87 to 100 microns in size, falling from heights of 9 to 10.5 km. In the diagrams of the local fallout /100, 110/ the effect of eddy diffusion is not taken into account; it was suggested in /1/ that the calculated fallout area should be increased by 1/7 because of diffusion. It was demonstrated theoretically in /109/ that for the propagation of a sufficiently nonuniform contaminant it is not necessary to take into account the turbulent dispersion either along the vertical or in the direction of the wind. The region is determined in which the error introduced by such a simplification will be negligible.

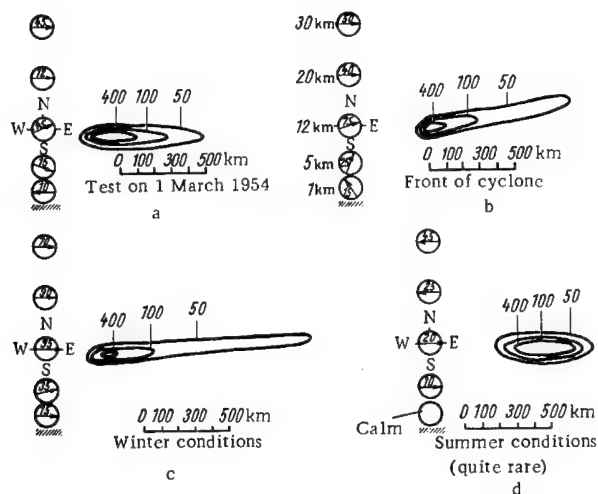


FIGURE 9. Isodose contours (in roentgens) for first 96 hours, in wake of powerful surface nuclear explosion, for different wind conditions. Wind direction and velocity (km/hr) are shown to left of sketches, for different heights (km).

Figure 9a shows isolines of the doses for the first 96 hours after the "Bravo" explosion at Bikini Atoll on 1 March 1954; the wind conditions

for this blast are also shown. The other three sketches present some results of isoline calculations for this same case, but with different wind conditions.

The model of local fallout from a three-dimensional source /100/ postulates a stabilized mushroom cloud; the calculations are based on an assumed distribution of fallout particles within this cloud. In general the amount of fallout can be computed by following the motion of groups of radioactivity-carrying particles in the atmosphere, from the time of particle formation after the blast until deposition on the earth. For the calculations the particles were divided into classes according to size.

The effect of the height of ascent of the cloud on particle motion was taken into account. Also, the gravitational fallout of a particle was considered, together with the effect of wind velocity on its horizontal motion. Data on particle trajectories and on the distribution of particle activity as a function of particle size enable us to make numerical calculations either of the specific activity settling onto a locality or of the dose rate at a given point in the wake.

At any moment after the beginning of fallout the vertical (with respect to the earth) particle velocity will be

$$v = v_1 - v_2, \quad (14)$$

where v_1 is the velocity of particle ascent due to upward motion of the air in the cloud, and v_2 is the velocity of gravitational settling of a particle.

Large particles attain their maximum height and fall when smaller ones are still ascending. The height z of particle ascent at a time t is found by integrating the particle velocity with respect to time:

$$z = \int_{t_0}^t (v_1 - v_2) dt + z_0, \quad (15)$$

where t_0 is the time of particle formation, and z_0 is the particle height at this time. For the calculation the integral in (15) is approximated by a finite-difference equation, the integration time interval being divided into n smaller intervals. Therefore, we can write

$$z = \sum_{i=0}^{n-1} (v_{1i} - v_{2i}) \Delta t_i + z_0, \quad (16)$$

where v_{1i} and v_{2i} are the average velocities of ascent and descent, respectively, of the particles for the time interval Δt_i . After the cloud has reached its maximum height, $v_{1i} = 0$.

To determine the height z_u of the upper edge of the cloud and the height z_l of its lower edge, let us use the empirical formulas of /100/. The force W of the blast is from 0.01 to 20,000kt, and atmospheric conditions are typical for the middle and tropical latitudes:

$$z_u = 230\sqrt[4]{Wt^2}; \quad (17)$$

$$z_l = 100\sqrt[4]{Wt^2}. \quad (18)$$

Here z is the height in meters, W is the force of the blast in kt, and t is the time in seconds.

The time t_m for ascent of the cloud to its maximum height (its stabilization) is taken to be 6 minutes /100/. For forces exceeding 100kt, t_m may be determined /100/ using the empirical formula

$$t_m = 510 - 34 \ln W, \quad (19)$$

where t_m is the time in seconds. For explosions of greater force this time will be less than 6 minutes. For instance, for a 20-metagon bomb $t_m \approx 180$ sec.

Data on the ascent velocities of particles in the cloud are given in /100/. The terminal velocities of particles in still air are determined on the basis of Stokes' law /108/.

The horizontal motion is assumed to be a result of wind action. It is true that some particle dispersion may be caused by eddy diffusion, but this is neglected in the calculations of local fallout in /100/. Additional horizontal motion is caused by the expansion of the cloud prior to stabilization. The maximum horizontal particle displacement H during the time it takes to rise from a height z_0 to the maximum height z_m plus the time of fall to the level of the earth z_e may be expressed as the sum of the two corresponding horizontal movements:

$$H = \sum_{z=z_0}^{z_m} \frac{w\Delta z}{v_1-v_2} + \sum_{z=z_m}^{z_e} \frac{w\Delta z}{v_2-v_1}, \quad (20)$$

where w is the wind velocity and Δz is the thickness of the altitude layer.

A dynamic model (D -model) of local fallout based on Anderson's theory /100/ has been suggested. In this model the cloud is assumed to consist of 100 superposed circular cylinders, each of the cylinders corresponding to one class (according to size) of radioactive particle (in other words, the entire particle distribution is divided into 100 intervals). The particles of a given class are assumed to be shifted uniformly over the cylinder. Each cylinder is in turn divided into a number of disks (from 7 to 230), depending on the force of the explosion. The trajectory of a particle whose size corresponds to the particle class for the given cylinder is taken as the trajectory of each disk in air. Consequently, the cylinders corresponding to different classes of radioactive particles will slowly separate from one another. Cylinders representing large particles do not ascend to great heights and fall rapidly. Those representing small particles will go up higher and descend more slowly.

The distribution of activity as a function of particle size is given by the formula

$$F = \frac{1}{\sigma \sqrt{2\pi}} \int_{\beta_1}^{\beta_2} e^{-\frac{(\beta-\bar{\beta})^2}{2\sigma^2}} d\beta, \quad (21)$$

where F is the portion of the activity associated with the class of particles having sizes from d_1 to d_2 , while $\beta_1 = \lg d_1$, $\beta_2 = \lg d_2$, and $\beta = \lg d$. For

cohesive soil from the state of Nevada $\bar{\beta} = 2.053$ and $\sigma = 0.732$, and for coral $\bar{\beta} = 2.209$ and $\sigma = 0.424$.

The number of particles of a given size (or with specified fall velocities) settling onto some part of the earth's surface was converted to values of the dose rate P using experimental data /100, 110/. In /100/ this relation is expressed by the following empirical formula, which takes into account the irregularity of the earth's surface:

$$P = \frac{11FA}{NS}, \quad (22)$$

where P is the dose rate in r/hr at a height of 1 meter, 1 hour after the explosion; F is given by formula (21); A is the total residual radioactivity (curies) 1 hour after the explosion (this falls over the entire near wake of the explosion; it is $8.5 \cdot 10^8 \delta$ curies/kt for a gamma-emission energy of 0.7 Mev/disint, δ being the portion of the activity falling out in the wake /7/); N is the number of disks used to represent the class of particles with sizes from d_1 to d_2 ; and S is the area of the earth's surface in m^2 covered by the radioactivity contained in the disk. The total dose rate is determined by adding together the dose rates for all the disks covering the given point.

In /100/ the experimental fallout pattern obtained for the "Jangle-U" underground test was shown to agree with the pattern calculated on the basis of the D -model for an hour after the blast. A good fit is observed between the basic isolines in this case.

The method suggested in /108/ for calculating the local fallout is similar to the D -model described above. However, in this case the vertical component of the particle velocity during ascent was not taken into account.

Intermediate fallout and global fallout are more difficult to describe and predict than local fallout. The reason for this is that a considerably larger number of factors, many of which have not been adequately studied, affect the formation of intermediate and global fallouts. For example, in the case of intermediate fallout, it is necessary to know: the variability of the wind, the effect of removal of radioactivity from the troposphere by precipitation washing, the role of eddy diffusion in scattering the cloud, etc.

For global fallout it is necessary to take into account the stratospheric circulation, exchange processes between stratosphere and troposphere, and the means by which finely divided aerosols are removed from the troposphere. The formation and prediction of global fallout are described in detail in /2/. The global fallout (according to data on the concentrations of air near the earth and on the density of surface contamination) is most intensive in the latitude bands $25 - 50^\circ N$ and $20 - 30^\circ S$, irrespective of where the tests were carried out /2, 85/.

The radioactive fallout (local as well as global) causes surface contamination of a locality. Gradually, as a result of various processes, radioactive products begin to penetrate into the soil (ground); they may be carried by particles, washed off the surfaces of the particles, or produced when the particles disintegrate. Thus the entire volume of the upper layer (to a depth of several centimeters) of soil becomes contaminated. According to different data, the upper layer (5 to 6 cm deep) contains 80 to 95% of the activity, for both local /56/ and global /4/ fallout.

3. Fractionation of nuclear-explosion products and isotopic composition of radioactive fallout

Radioactive fallout is a result of complex nuclear, physicochemical, and geophysical processes. Figure 10 gives a schematic representation of the various processes leading to radioactive fallout /103/. The horizontal scale of the diagram (time scale) is divided into explosion, condensation, and fallout phases; the vertical scale is divided into nuclear and physicochemical processes. Dashed lines indicate processes taking place only in the case of surface explosions. This diagram enables us to understand the interaction of the different processes taking place during fallout formation.

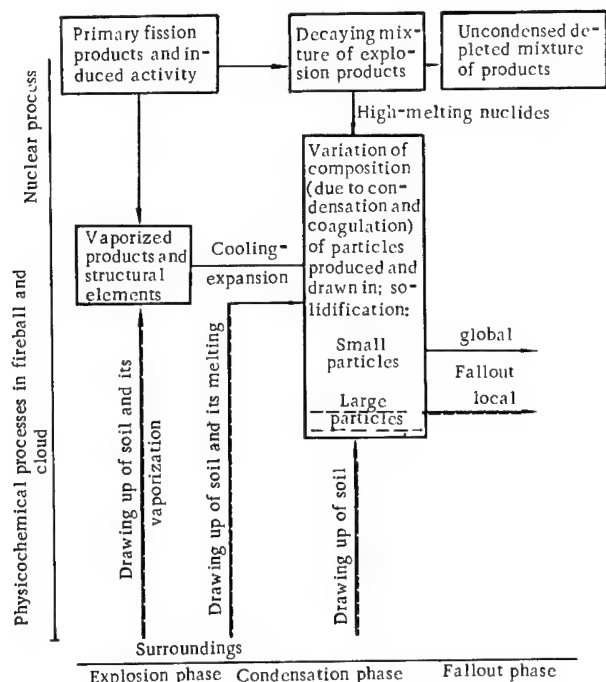


FIGURE 10. Diagram of processes leading to radioactive fallout.

The complex aggregate of physicochemical processes observed after the radioactive products have formed (as a result of nuclear reactions) has a significant effect on the isotopic composition of the radioactive fallout (global and local). These processes change the ratios in which the isotopes are produced for some given kind of fission, that is, they lead to fractionation of the radioactive products. An understanding of fractionation is exceptionally important in order to determine the contamination of a region by individual isotopes (according to the radiation field or the total activity) and the hazard associated with the penetration of isotope into an organism.

The fractionation of the products of a nuclear explosion may be characterized by the following coefficient /111/:

$$f_{i-j}(r) = \frac{n_i(t, r)_e}{n_j(t, r)_e} : \frac{n_i(t)_t}{n_j(t)_t}, \quad (23)$$

where $n_i(t, r)_e$ and $n_j(t, r)_e$ are the experimentally determined activities (or numbers of nuclei) of isotopes belonging to the i th and j th mass chains, respectively, in a particle (or group of particles) of dimension r at a time t after the explosion; and $n_i(t)_t/n_j(t)_t$ is the theoretical ratio of the activities (or numbers of nuclei) of these same isotopes at the same time.

Some values of f_{i-95} for radioactive particles collected in the fallout on Japan in 1961–1962 are given in /112, 113/. * For particles around 10 microns in size, the values of f_{103-95} fluctuate about zero, that is, in these particles Ru¹⁰³ is practically absent. The values of $f_{(141+144)-95}$ lie between 0.25 and 0.7, which shows good agreement with the data of /111/ for particles sampled in 1957–1958 in the air over Sweden; moreover, these values do not contradict the data in /114/ for particles sampled in the Moscow region in autumn 1962.

A number of studies /112–120/ which have appeared in recent years indicate that, for the large radioactive particles in local and global fallout, the ratio of the number of Ru¹⁰³ nuclei to the number of Zr⁹⁵+Nb⁹⁵ nuclei is considerably lower than the theoretical value. Moreover, in some gamma-emission spectra of the particles, the line around 0.5 Mev corresponding to the Ru¹⁰³ isotope (Ba¹⁴⁰ and La¹⁴⁰) is completely missing. Finally, it is noteworthy that the fine particles are richer (in comparison with the large particles) in such isotopes as Sr⁸⁹, Ba¹⁴⁰ /101, 121/, and Sr⁹⁰ /122/.

The foregoing results are consequences of fractionation of the radioactive nuclei produced during nuclear explosions. The term "fractionation" designates such a change in the composition of a mixture of radioactive nuclei (during different stages following the nuclear explosion) that the aggregate of these nuclei in a given sample becomes nonrepresentative, in comparison with the explosion products taken as a whole (at the same time) /123/.

Fractionation of radioactive nuclei begins during the condensation of vaporized material containing fission products and induced activity. It is caused by a selective capture of individual isotopes of the liquid phase at the moment when the radioactive particles are produced. The explanation of this is that, at different stages of particle formation, nuclides of the same mass chain (isobars) may exist successively in the guise of different elements, due to radioactive decay.

In order to evaluate the effect of fractionation quantitatively, it is necessary to know what times after the explosion correspond to the different stages of particle formation. The time t_i at which the temperature of the fireball reaches the melting points of the soil material (surface explosion) and the basic structural material of the bomb (atmospheric explosion) may be considered to be the moment of solidification of the particles. In surface explosions, when the most abundant constituents of the material drawn up

* In this case f_{i-95} is the coefficient of fractionation for long-lived isotopes belonging to the i th mass chain, relative to the isotope sum Zr⁹⁵+Nb⁹⁵.

into the fireball are silicon compounds (SiO_2), the minimum melting (solidification) temperature for the particles is 1100°C . In this case /100/

$$t_i \approx 0.67 \sqrt{W} \text{ sec}, \quad (24)$$

where W is the force of the blast in kt. Analogously, for the maximum melting temperatures of these substances (1700°C),

$$t_i \approx 0.58 \sqrt{W} \text{ sec.} \quad (25)$$

Particles leaving the radioactive cloud before solidifying will be stripped of all their volatile elements (in comparison with the high-melting elements). If a particle remains in the cloud after solidification, the condensation of volatile elements onto its surface proceeds, as the condensation temperatures of these elements are reached.

The fact that there are many different types of particles as well as different particle sizes complicates the study of fractionation considerably: For example, if angular particles capture radioactive products in cooler parts of the fireball and at later periods, in comparison with spherical particles, then we can assume that they will be richer in radioactive isotopes having volatile parents. Large spherical particles, on the other hand, contain less Ba^{140} and Sr^{89} /101/ (as compared with Mo^{99} and Np^{239}) than particles of irregular shape.

Some experimental results on fractionation during surface explosions of great (megaton) force are given in /121/, along with attempts to evaluate this phenomenon quantitatively. Zr^{95} and Sr^{89} were chosen as reference nuclei in the analysis of the results. These isotopes were selected for two reasons: 1) the ratio of these isotopes is a sensitive indication of fractionation, since there is a comparatively long-lived volatile isotope (Kr^{89} , with $T_{1/2} = 3.2 \text{ min}$) in the chain with a mass number of 89, whereas in the chain with a mass number of 95 there are practically no volatile parents; 2) elements with mass numbers of 89 and 95 have substantial fission yields and also isotopes Sr^{89} and Zr^{95} have quite long half-lives, so that these isotopes should be present in most of the samples.

The value of f_{95-89} was found to vary by a factor of 5 for different samples for a megaton blast at the surface of a deep bay, by a factor of 20 for an explosion of less than a megaton at the surface of a deep bay, by a factor of 12 for a megaton surface explosion in low water, and by a factor of 100 for an explosion at the surface of a coral atoll. The quantity f_{i-j} is a complex function of the type and force of the explosion, the nature of the material making up the underlying surface, the place and time of sampling, and the sizes and shapes of the radioactive particles in the sample.

The values of f_{i-j} for different samples (particles) for a given explosion fluctuate over a considerable range. Thus the fractionation of an isotope with respect to some other reference isotope such as Zr^{95} can be determined by correlating the values of f_{i-89} and f_{95-89} . The slope of the correlation curve characterizes the fractionation coefficient of the given isotope i relative to Zr^{95} in this region (for the given explosion).

The method of least squares is used to find the tangents to the curves for logarithmic correlation for different isotopes. The samples are from

contaminated areas in the vicinity of surface explosions of megaton bombs. Table 7 lists some values of these tangents /121/. It should be noted that the slopes of the curves vary slightly depending on the environment.

TABLE 7. Tangents to curves of logarithmic correlation, for various isotopes

| Isotope | $\tan \alpha$ | Isotope | $\tan \alpha$ |
|-------------------|---------------|-------------------|---------------|
| Sr ⁹⁰ | 0.32 | Ba ¹⁴⁰ | 0.43 |
| Mo ⁹⁹ | 1.11 | Ce ¹⁴⁴ | 0.94 |
| Te ¹³² | 0.60 | U ²³⁷ | 1.04 |
| Cs ¹³⁷ | -0.06 | Np ²³⁹ | 1.05 |

Consequently, the experimental results in the table are a clear indication that fractionation greatly affects the presence of volatile parents in the decay chain. Reference /121/ gives $\tan \alpha$ for various isotopes as a function of the square root of the fraction F_i of high-melting elements already condensed at the moment of particle solidification (in the mass chains to which these isotopes belong). It turns out that this relation is expressed by a straight line (within the limits of experimental error), that is, it may be described by the formula

$$\lg f_{i-89} = \sqrt{F_i} \lg f_{95-89}. \quad (26)$$

The experimental values of $\tan \alpha = \frac{\lg f_{i-89}}{\lg f_{95-89}}$ listed in Table 7 were used /121/ to derive formula (26), and in the calculations of F_i it was assumed that the halogens, the inert gases, the alkali metals, and tellurium (or their oxides) are volatile. The quantity F_i was calculated at a time 35 seconds after the explosion (for $W \approx 3$ Mt). For less powerful explosions the effect of fractionation is more pronounced.

As noted above, the main parameter used to evaluate the fractionation is F_i , the fraction of high-melting elements in the mass chain at the moment of particle solidification, the oxides of which (or the elements themselves) have boiling points higher than the melting (solidification) point of the basic constituent of the underlying surface (ground).

$F_i(t_i)$ may be calculated as a function of the solidification time for the particles, which in turn is a function of the force W of the explosion and the solidification temperature, for each mass chain of the radioactive transformations /123/. This calculation is made on the basis of the known (or computed) individual fission yields and half-lives for all the members of the chains, together with the boiling points of the oxides of the elements in the form of which the isobars appear successively in the given mass chain. As a first approximation it may be assumed that the temperature is the same at all points inside the fireball at the time of cooling, and also that the explosion products are distributed uniformly throughout the entire fireball. For each chain of radioactive transformations, a calculation is made of the number of products which will be present, by the time the solidification point for the particles is reached, in the form of elements whose oxides are volatile at this temperature. In addition, a calculation is made of the number of isotopes which will be present in the form of

elements whose oxides have boiling points higher than the selected temperature and may thus condense and be picked up by the particles being formed.

The oxides are considered rather than the elements themselves, since the probability that oxides will form is obviously quite high, given a high enough temperature and an excess of oxygen (although sometimes decomposition of oxides also occurs). Elements with oxide boiling points (if the oxides decompose, then the boiling points of the elements themselves are considered) lower than the solidification point of the particles should be assumed to be volatile elements, that is, elements which are not picked up by the particles as they form. At temperatures from 1100 to 1700°C the volatile elements may include inert gases (Kr, Xe), halogens (I, Br), alkaline elements (Rb, Cs), and also arsenic, selenium, cadmium, indium, and ruthenium.

The nonvolatile elements, which are picked up by particles at their formation, will be elements which have oxide boiling points higher than 1100 to 1700°C; gallium, germanium, strontium, yttrium, zirconium, niobium, rhodium, palladium, silver, tin, barium, lanthanum, cerium, praseodymium, samarium, europium, gadolinium, and terbium.

Isotopes of tellurium, antimony, and technetium may be considered to be volatile elements too, but the behavior of these isotopes in the described processes is more complex. For example, the condensation temperatures of oxides of antimony and technetium are higher than, but close to, the temperatures taken for particle formation (1100 to 1700°C).

Actually, the penetration of fission products into particles does not occur instantaneously, but rather over a period of time which depends on the elasticity of the vapors of the fragment elements (because of the small and variable concentration). Accordingly, the above elements are probably intermediate between the high-melting and volatile elements. Therefore, in analogous calculations in /99, 121/, tellurium was included in the volatile elements. Tin* has been thought to be a volatile element, and molybdenum sometimes behaves like a high-melting element. However, since there is no experimental confirmation of this, tin will be considered to be a high-melting element for our calculations, and molybdenum will not be considered at all, due to the complexity of its behavior.

The independent yields of separate members of the chains were determined using /123/ a method suggested in /124/. The authors of these works assume that the distribution of independent yields among members of a chain, as a function of the charge, obeys Gauss's law:

$$p(Z) = (c\pi)^{-1/2} \exp[-(Z - Z_p)^2/c]. \quad (27)$$

Here $p(Z)$ is the independent fission yield of a nucleus with charge Z (the yield of the whole mass chain is taken as 1); $c \approx 2(\sigma^2 + \frac{1}{12})$, where σ^2 is the variance, assumed to be the same for all chains ($\sigma = 0.62 \pm 0.06$, so that $c = 0.94 \pm 0.15$); and Z_p is some effective value of the charge, corresponding to the peak of the Gaussian curve. Values for Z_p are given in /124/. Using these values, the independent yields for all members of the chains with

* And palladium and silver as well.

mass numbers of 78–105 and 128–156 were calculated. These yields show good agreement with the experimental values.

Figure 11 shows the results of the calculations of F_i ; the solidification time t_i for the particles is plotted on the abscissa axis, along with the force of the explosion, for melting points of 1100 and 1700°C, and F_i is plotted on the ordinate axis.

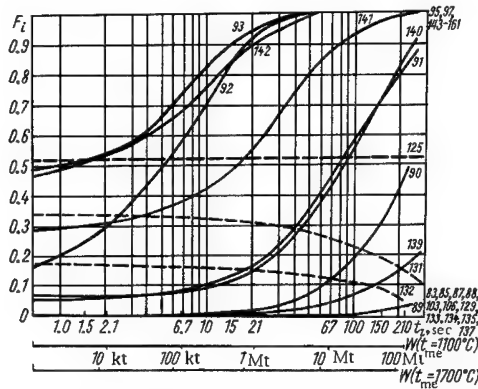


FIGURE 11. Fraction of high-melting elements in mass chain at time of particle solidification, as function of force of explosion. Numbers near curves indicate numbers of mass chains.

The values of F_i computed for the two melting temperatures differ by no more than 5%. These values are not affected by a variation in the force of the explosion for nuclides belonging to chains with the following mass numbers: 83, 85, 87, 88, 95, 97, 103, 106, 129, 133, 134, 135, 137, 143–161. There is almost no change for the range of W from 1 to 500 kt for nuclides with mass numbers of 89, 90, 131, 132, and 139. The values of F_i are most sensitive to variations in the force of the blast (for W from 1 kt to 3–5 Mt) for nuclides with mass numbers of 92, 93, 141, and 142. In the range of W from 1 to 100 Mt this is true for nuclides with mass numbers of 90, 91, 140, and 141.

For purposes of comparison, Figure 11 also includes some curves of $F_i(t_i)$ for chains in which there are no long-lived gamma emitters.* However, a knowledge of F_i does not give us the value of the fractionation coefficient, it just indicates the part of a long-lived isotope belonging to the i th mass chain. This isotope may ultimately enter into the large particles making up the local fallout (assuming that only a small amount of total activity exists on the surfaces of the large particles).

Let us assume that the isotopes of high-melting elements (or their oxides), having entered into liquid particles, become distributed relatively uniformly throughout the particles /101/. Let us also assume that the

* For isotopes having a tin isotope as a parent, the F_i curves are dashed.

isotopes of volatile elements condense on the surfaces of heavy particles. It is then possible to calculate $f_{i-j}(r)$ as a function of particle size (this was suggested by us in /125/) and thus to determine the fractionation coefficient for products falling out at different distances from the explosion. The indicated mechanism of radioactive-particle production will be predominant if a great number of comparatively large inactive liquid particles (more than 10 to 20 microns in diameter) are present in the fireball, and if the fission products condense onto them; this is the case for surface explosions /101, 121/.

In an atmospheric explosion particle formation takes place as a result of condensation of vaporized bomb material and coagulation of the submicronic particles produced thereby /2, 98, 102/. An analogous method may be used to determine f_{i-j} for fused particles of spherical shape greater than 2 microns in size. Thus, for spherical fused particles:

$$\begin{aligned} \frac{n_i(t, r)_e}{n_j(t, r)_e} &= \frac{N_i(t, r)_e}{N_j(t, r)_e} = \frac{N_i^v(t, r)_e + N_i^s(t, r)_e}{N_j^v(t, r)_e + N_j^s(t, r)_e} = \\ &= \frac{\frac{n_i(t)_t F_i}{n_j(t)_t F_j} + \frac{n_i(t)_t (1 - F_i) N^s(t, r)_e \sum_k n_k(t)_t F_k}{N_j^v(t, r)_e \sum_k n_k(t)_t (1 - F_k)}}{1 + \frac{(1 - F_j) N^s(t, r)_e \sum_k n_k(t)_t F_k}{F_j N^v(t, r)_e \sum_k n_k(t)_t (1 - F_k)}}, \quad (28) \end{aligned}$$

since it is evident that

$$N_i^v(t, r)_e = \frac{n_i(t)_t F_i}{\sum_k n_k(t)_t F_k} N^v(t, r)_e$$

and

$$N_i^s(t, r)_e = \frac{n_i(t)_t (1 - F_i)}{\sum_k n_k(t)_t (1 - F_k)} N^s(t, r)_e.$$

Here $N_i(t, r)_e$, $N_i^v(t, r)_e$, and $N_i^s(t, r)_e$ are the probability density functions for the total, volume, and surface activities of the i th isotope (or of the combined isotope mixture, for $N(t, r)_e$, $N^v(t, r)_e$, and $N^s(t, r)_e$). These are functions of the particle radius r and the time t . Function $n_i(t)_t$ is the activity of the i th isotope produced during the explosion, at a time t (calculated theoretically); $n_i(t, r)_e$ is the experimentally determined activity of the i th isotope in the particle. F_i is the fraction of the elements in the i th mass chain of elements which have condensed by the moment when particle solidification takes place /121/, and k is the number of mass chains whose isotopes make a substantial contribution to the total activity at the time t .

An isotope having high-melting predecessors (most frequently it is Zr⁹⁵) is usually taken to be the isotope belonging to the j th mass chain (the reference isotope for determining fractionation of the isotope in the i th mass chain) /111, 121/. Therefore, when using formulas (23) and (28) to

determine f_{t-95} , we can set $F_j = 1$, so that

$$f_{t-95} = F_i + (1 - F_i) \frac{N^s(t, r)_e \sum_k Y_k \lambda_k e^{-\lambda_k t} F_k}{N^v(t, r)_e \sum_k Y_k \lambda_k e^{-\lambda_k t} (1 - F_k)}, \quad (29)$$

since

$$\frac{\sum_k n_k(t)_i F_k}{\sum_k n_k(t)_i (1 - F_k)} = \frac{\sum_k Y_k \lambda_k e^{-\lambda_k t} F_k}{\sum_k Y_k \lambda_k e^{-\lambda_k t} (1 - F_k)},$$

where Y is the cumulative yield of the k th mass chain during fission.

As (29) shows, f_{t-95} is a function of the particle size, the force (F_i) /121/, the kind of fission Y_i /49/, the type of explosion, and the nature of the ground constituting the underlying surface. This follows from the fact that function $N(t, r)_e$ is different for underground, surface, and atmospheric explosions /99, 100, 103/, and also for different kinds of ground /99/. With respect to the particle size, the probability density function for the total activity will obviously be

$$N(t, r)_e = N^v(t, r)_e + N^s(t, r)_e, \quad (30)$$

from which

$$\frac{N^s(t, r)_e}{N^v(t, r)_e} = \frac{N(t, r)_e}{N^v(t, r)_e} - 1. \quad (31)$$

Function $N(t, r)_e$ is known for different types of explosions /99, 100, 103, 108/. As noted above, this distribution may be expressed by a logarithmic-normal curve, by an exponential function, or in the form of the two-parameter function used in /109/ to represent the probability density function of a polydisperse contaminant with respect to the particle fall velocities. Let us set

$$\int_0^\infty N(t, r)_e dr = Q(t),$$

where $Q(t)$ is the total amount of activity produced during the explosion, at a time t .

Let us assume that thermodynamic equilibrium exists and let us apply the Raoult law to the process of particle formation in the fireball /99/. It may then be assumed that the volume and surface concentrations of radioactive isotopes in the just-formed particles of different sizes (for $r \geq 2 \mu$), present in the cloud for a time sufficient to complete condensation of the fragment elements in these particles, are constant (that is, σ_v and σ_s are constant). Accordingly,

$$\frac{N^s(t, r)_e}{N^v(t, r)_e} = \frac{3\sigma_s}{\sigma_v r} = \frac{\alpha}{r}, \quad (32)$$

where α is a constant.*

* For some large radioactive particles the activity is distributed over a thick external volume layer /101/, rather than uniformly throughout the volume. Thus it is to be assumed that the condition of thermodynamic equilibrium is not always satisfied completely. In this case N^s/N^v will depend less on r .

The value of F_i can be calculated approximately if the force of the blast is known /121, 123/, if $N(t, r)_e$ is selected for the case in question /8, 99, 100, 103, 108/ and if Y_i is known for the given type of fission /49/. The main problem when determining f_{i-j} is to find the constant α . From formulas (31) and (32) we obtain

$$N^v(t, r)_e = \frac{rN(t, r)_e}{r + \alpha}. \quad (33)$$

The value of α may be found, for example, from an equation indicating that practically all the isotopes of elements boiling at temperatures higher than the solidification point for the material of the particles fall into these particles:

$$\int_0^\infty N^v(t, r)_e dr = \frac{\sum_k Y_k \lambda_k e^{-\lambda_k t} F_k}{\sum_k Y_k \lambda_k e^{-\lambda_k t}} \int_0^\infty N(t, r)_e dr. \quad (34)$$

The foregoing formulas can be used to calculate $f_{i-95}(r)$ for various W and $N(t, r)_e$. Let us find $f_{i-95}(r)$ for $W = 1 \text{ kt}$ and 1 Mt (surface explosion) and for $t_{av} = 1100$ and 1700°C . The values of F_i for this case are taken from Figure 11. The data for $N(t, r)_e$ are taken from /8/. Figure 12 shows the function $1/Q(t) \times N(t, r)_e$ in the form of a histogram (curve 2). The probability density function $N(t, r)_e$ for a fresh fallout (after days or weeks) is assumed to be practically independent of time /8, 99, 100, 103, 108/.

The curve for $1/Q(t) N(t, r)_e$ shown in Figure 12 (curve 1) can be represented approximately by the formula

$$\frac{1}{Q(t)} N(t, r)_e = \frac{a^{n+1}}{\Gamma(n+1)} r^n e^{-ar}, \quad (35)$$

where $n = 2$ and $a = 0.06$ /125/. Now, from formulas (33) through (35), we obtain

$$\frac{1}{2} \{0.06a + (0.06a)^3 e^{0.06a} [-Ei(-0.06a)] - (0.06a)^2\} = 1 - \frac{\sum_k Y_k \lambda_k e^{-\lambda_k t} F_k}{\sum_k Y_k \lambda_k e^{-\lambda_k t}}. \quad (36)$$

The values of F_i computed above can be used to determine the fraction η of the total radioactivity of the products released during the explosion for a time t , referred (according to the previously indicated criterion) to the high-melting elements:

$$\eta = \frac{\sum_k Y_k \lambda_k e^{-\lambda_k t} F_k}{\sum_k Y_k \lambda_k e^{-\lambda_k t}}. \quad (37)$$

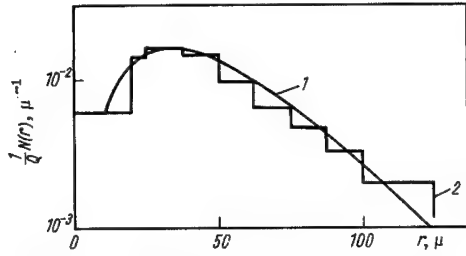


FIGURE 12. Probability density function of total activity for surface explosion, in terms of sizes of carrier particles.

Table 8 lists some values of η for various t and W . The type of fission is assumed to be the same for all the explosions (1 kt, 1 Mt, and 100 Mt).

TABLE 8. Fraction of activity of high-melting products in total activity of fragment products of explosion

| t | $W = 1 \text{ kt}$ | $W = 1 \text{ Mt}$ | $W = 100 \text{ Mt}$ |
|---------|--------------------|--------------------|----------------------|
| 1 day | 0.37 | 0.44 | 0.51 |
| 20 days | 0.38 | 0.44 | — |

When the calculated values are substituted into (36) and the latter is solved graphically, it is easy to show that for $W = 1 \text{ kt}$, $a \approx 80$ microns, while for $W = 1 \text{ Mt}$, $a \approx 60$ microns (a has the same units as r). It should be noted that for $r = a$ the distribution curves for $N^s(t, r)_e$ and $N^v(t, r)_e$ will intersect.

Figure 13 shows some curves for $f_{i-95}(r)$ for $W = 1 \text{ kt}$ and $t_{me} = 1100$ and 1700°C (at these temperatures the values of $f_{i-95}(r)$ differ from one another by less than 5%, for $r \geq 20$ microns); the data selected above for $N(t, r)_e$ were used to plot the curves, together with the calculated values of a . The function $f_{i-95}(r)$ was calculated for the mass chains containing the most important gamma emitters right after the explosion.

It is clear from Figure 13 that the values of f_{i-95} which differ most from unity are those for $i = 103, 106, 137$; on the other hand, for $i = 97$ and 144, $f_{i-95} = 1.0$. All the f_{i-95} curves intersect for the values

$$r = \frac{\sum_k n_k F_k}{\sum_k n_k (1 - F_k)} a.$$

The f_{i-95} curve corresponding to $i = 92$ is the most sensitive to variations in the force of the explosion.

The $f_{i-95}(r)$ functions determined using the method described above are independent of time, that is, they are also valid for fallouts which are not fresh.

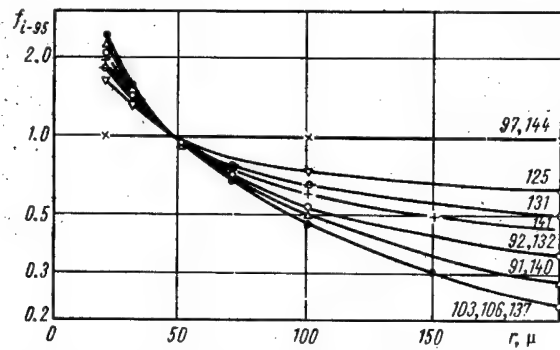


FIGURE 13. Dependence of the fractionation coefficients on the particle size for an explosive power $W = 1 \text{ kt}$ ($t_{mc} = 1100 - 1700^\circ\text{C}$). The numbers on the curves correspond to the number of mass chains.

Fractionation of the radioactive products does not cease after the radioactive particles fall out of the cloud. The subsequent fractionation can be attributed to the influence of meteorological (mainly before particles land in the region) and geochemical (in the region) processes. For example, according to /112/, at the beginning of a rain there are products in the rain samples which have undergone more fractionation than the average for rain samples (fractionation due to a washing out of larger particles). Fractionation as a result of the washing out of particles of different origins is described in /126/. The reduction of the $\text{Ba}^{140}/\text{Sr}^{90}$ ratio can be attributed to a selective washing out of Ba^{140} of tropospheric origin.

Fractionation caused by washing out from the atmosphere of larger particles from the windward side of a mountain range is described in /127, 128/. The fractionation of radioactive nuclei in the products falling onto a region, due to their different susceptibilities to washing out and their different mobilities in the soil of the local-fallout region, is described in /56/. Radioactive nuclei having inert gases as predecessors turn successively into alkaline and alkali-earth elements, after the first and second beta decays. These products, which are concentrated on the surfaces of the fallout particles, are readily soluble /121/. Consequently, fission products having volatile parents are subjected to washing out more than fission products having high-melting parents are.

The probability density function $N_i^s(t, r)_e$ obtained above enables us to determine the activity of the i th isotope, which is present on the surfaces of particles of a given size and is primarily subjected to washing away from the particles under natural conditions. If the substance constituting the base material of the particles (for example, SiO_2) is practically insoluble in water and weak acids, then a knowledge of $N_i^s(t, r)_e$ makes it possible to determine the biological availability as a function of particle size.

The concept of the biological availability of radioactive explosion products was introduced in /129/. The biological availability of an isotope is the relative accumulation of this isotope (from the radioactive explosion particles) by a biological system, divided by the relative accumulation of

the isotope from a mixture. According to /129/, the biological availability of Sr⁹⁰ in particles from a tower explosion or other type of explosion is practically equal to the fraction of Sr⁹⁰ which is soluble in one normal solution (1N) of HCl, that is, it is almost the same as the fraction of Sr⁹⁰ deposited on the particle surfaces after solidification of the particles (isotope diffusion from inside a particle to the outside is practically excluded). Therefore, the maximum value of the (coefficient of) biological availability for the i th isotope may be assumed to be quantitatively equal to the fraction of this isotope present on the surfaces of particles of a given size (that is, the isotopes deposited after particle solidification), provided the basic substance making up the particles is essentially insoluble in water or in weak acids:

$$\begin{aligned}
 b_i(r) &= \frac{N_i^s(t,r)_e}{N_i^s(t,r)_e + N_i^v(t,r)_e} = \\
 &= \left(1 + \frac{F_i N^v(t,r)_e \sum_k Y_k \lambda_k e^{-\lambda_k t} (1 - F_k)}{(1 - F_i) N^s(t,r)_e \sum_k Y_k \lambda_k e^{-\lambda_k t} F_k} \right)^{-1} = \\
 &= \left(1 + \frac{F_i N^v(t,r)_e (1 - \eta)}{(1 - F_i) N^s(t,r)_e \eta} \right)^{-1}. \quad (38)
 \end{aligned}$$

The meager, very disconnected, material /106, 129–133/ containing information on the coefficients of biological availability, and on the washing off of various isotopes from particles by water or by weak acids, in general verifies formula (38) /125/. For example, the Sr⁹⁰ in large particles is more soluble than the accumulated fission products. The solubility of the accumulated products in such particles is low /106, 129, 131/, and the fraction of the soluble part is less for these particles than for small particles (for surface and tower explosions /106/). The solubility in particles from very powerful explosions is the least /106, 129/. There was less than 2% activity, enclosed in particles, present on the surfaces of vitrified globules more than 50 microns in size which were gathered in the state of Nevada /131, 132/.

4. Gamma emission of radioactive products falling out in a region

Several hundred nuclear explosions were set off throughout the world between 1945 and 1966. These explosions were carried out under various conditions. For example, of 298 announced explosions by the USA between 1945 and 1962, 67 were on or near the earth, 78 were set off in the atmosphere at altitudes of more than 500 meters, 98 were underground explosions, and 11 were set off in the stratosphere or in space /21, 133/. Most of these explosions caused radioactive contamination of the earth's surface.

Propagation through the atmosphere precedes the fallout of radioactive products onto the earth's surface. The time between the formation of the radioactive products and the fallout of these products from their

carrier-particles onto the earth's surface depends greatly on the height at which the explosion products were thrown out and also on the sizes of the carrier-particles themselves (that is, on the settling velocities of these particles). The particle sizes depend on the explosion conditions: for nuclear explosions on, near, or under the earth (with ejection of earth), the average particle size is considerably greater than for the other types of explosions. In view of the large range of fallout times onto the earth's surface, one of the most important characteristics of a radioactive fallout is its "age." For products originating in the same explosion, the age of the fallout refers to the time elapsed from the moment of the blast until the moment of age determination (for example, until the moment the products are collected or, in some cases, until the moment the analysis is carried out). However, it is possible to collect a sample of radioactive products for which most of the activity comes from the debris of an individual explosion, if the sampling station is located a comparatively small distance (up to a few thousand km) away from the explosion site along the travel line of the air masses, or else when isolated test explosions are set off.

In all other cases a sample will contain a mixture of debris from several explosions, as well as radioactive material from the global fallout. The products are characterized by some average (effective) age, as determined by the ratio of the activities of two or more isotopes, an extrapolation of this ratio being made back to the initial moment. Studies of highly active hot particles have been given considerable attention by many investigators /134-137/. The radioactive products present in each such particle certainly all come from the same explosion. However, the isotopes in them undergo fractionation (see Section 3), and so the ratios of their activities may differ markedly from the theoretical values.

In cases where an "artificial plane table" is used as a sampling technique, that is, where samples of soil or vegetation are gathered for analysis, it should be kept in mind that artificial radioactive debris from explosions has been accumulating in nature since the year 1945. Accordingly, as a result of various migration processes, radioactive products have penetrated into the ground, with the result that some months after contamination plane emission sources were turned into volume sources.

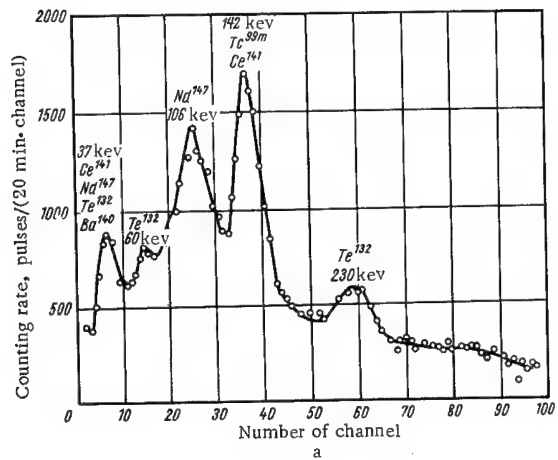
Scintillation gamma-ray spectrometry is a promising tool for studying the gamma emission of radioactive fallout. This technique tells us directly what the isotopic compositions of the main gamma emitters are, together with their relative contributions, and it also indicates the total gamma activity of the given specimen (sample). The shape of the gamma-emission spectrum of a fallout sample is determined primarily by the following factors: the age of the products in the sample, the relative contributions of fresh and global products, and the contribution of isotopes of the neutron-induced activity.

Using theoretically computed line spectra (see Section 1), the age of the fragment products in the sample can be evaluated approximately. There are some factors which should be taken into account when comparing the theoretical and experimental spectra:

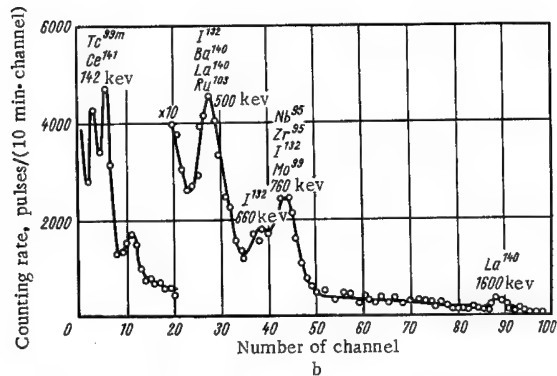
- 1) the theoretically computed spectra can be used only when considering debris from a single explosion or series of explosions, the duration of which is small in comparison with the age of the products;

2) the experimental spectra differ from theoretical spectra of the same age, in that there is fractionation of the fission products and a contribution by induced-activity isotopes;

3) fallout spectra for fission products in which it would be possible to identify peaks corresponding to radioactive isotopes of the noble gases (for example, Xe^{135} or Xe^{133}) are not described in the literature.



a



b

FIGURE 14. Gamma-emission spectrum of sample about 10 days old (in two energy ranges, a and b).

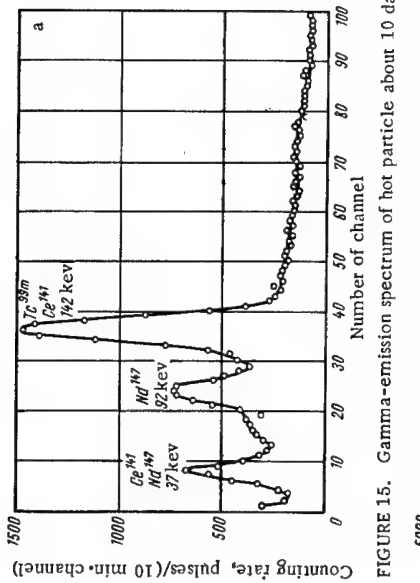
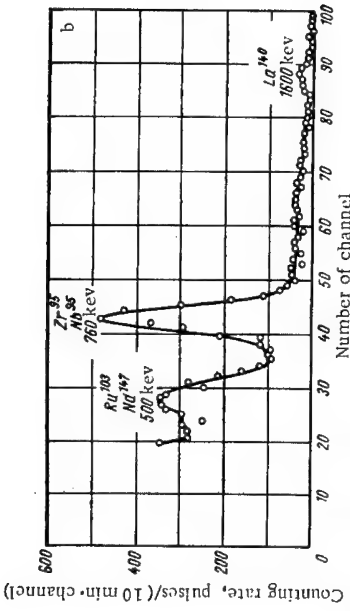


FIGURE 15. Gamma-emission spectrum of hot particle about 10 days old (in two energy ranges, a and b).



WILHELM EICHENBERG

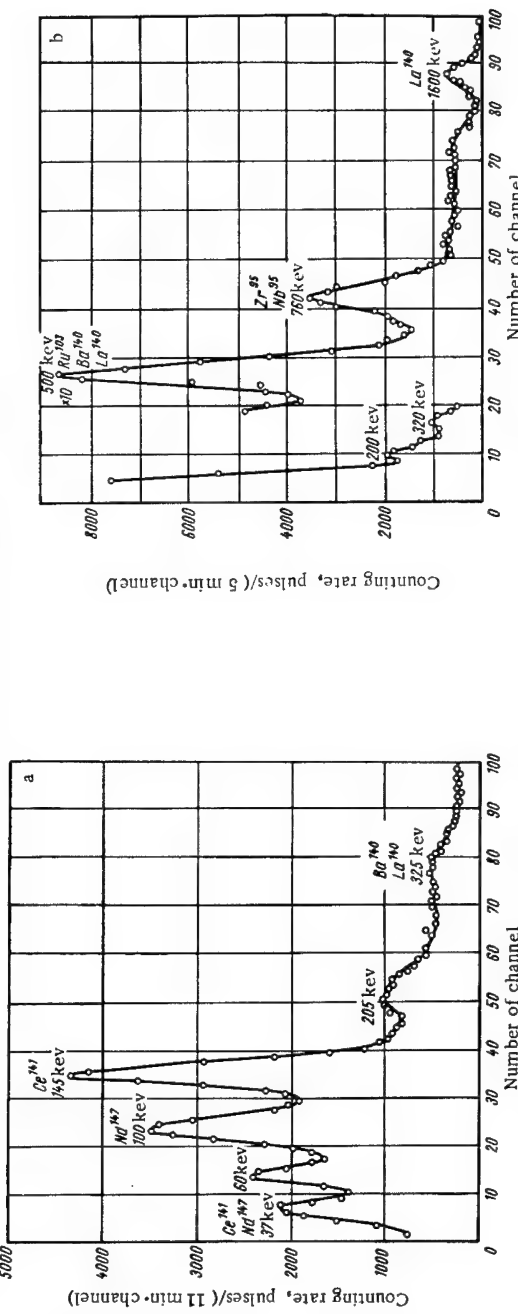


FIGURE 16. Gamma-emission spectrum of sample about one month old (in two energy ranges, a and b).

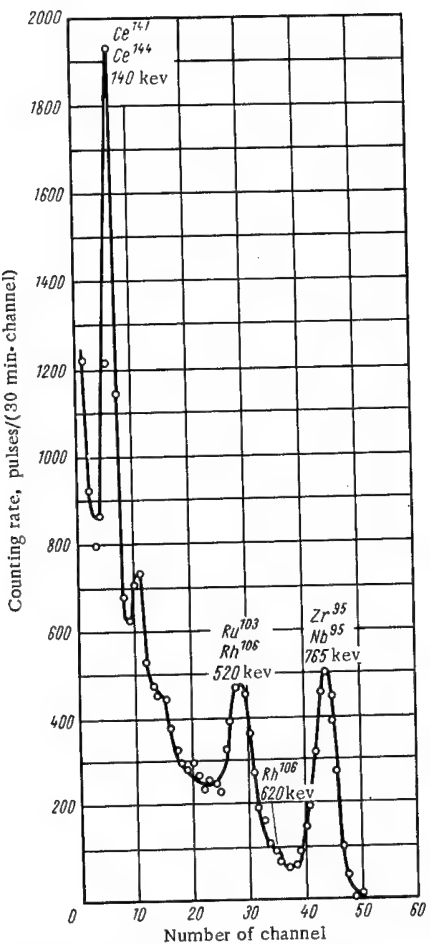


FIGURE 17. Gamma-emission spectrum of sample about seven months old.

The peak at 145 kev corresponds to the emission of Ce¹⁴¹. Anomalously low peaks at 500 and 1600 kev are a characteristic feature of the gamma-emission spectrum for a hot particle of this age. This indicates that the particle is depleted of such isotopes as Ba¹⁴⁰ and Ru¹⁰³, which agrees with the results obtained in Section 3. Other investigators /112-115, 134-136/ have obtained similar results for the differences between the gamma-emission spectra of filtered samples and hot particles. The peaks at 60, 100, and 205 kev (see Figure 16) are apparently associated with the emission of U²³⁷. Figure 17 shows the gamma-emission spectrum of a sample with a tentative age of seven months; the same was obtained with a filter from the atmospheric layer near the earth.

Let us now consider some spectra of radioactive explosion products which were obtained experimentally. The gamma-emission spectra for some relatively fresh products (global fallout) collected in the summer of 1962 are shown in Figure 14, for two energy ranges. The age of these products (on the basis of a comparison with the calculated spectra of Section 1) can be set at about 10 days. The products were collected from the atmospheric layer near the earth by a filter-ventilating apparatus. A comparison with the line spectrum in Figure 4 shows a satisfactory convergence of the overall character of the spectra. The absence of the peak at 364 kev (I^{131}) is due to calcination of the sample at 500°C. The spectrum was obtained using a spectrometer with an NaI(Tl) crystal 30×15 mm in size. The peak at about 106 kev is apparently due to the contribution of Np²³⁹ and Nd¹⁴⁷; a considerable part of the peak at 230 kev is probably also due to Np²³⁹ ($E_{\gamma} = 228$ kev). The gamma-emission spectrum of a hot particle taken from this same filter is presented in Figure 15; this curve shows a definite depletion of isotopes I¹³¹ (364 kev), Te¹³² (230 kev), and La¹⁴⁰ (1600 kev). It is assumed that the age of the particles is the same as the age of the products in the sample as a whole.

Figure 16 shows the gamma-emission spectra of a sample about one month old, collected in the filter.

The peak at 145 kev corresponds to the emission of Ce¹⁴¹. Anomalously low peaks at 500 and 1600 kev are a characteristic feature of the gamma-emission spectrum for a hot particle of this age. This indicates that the particle is depleted of such isotopes as Ba¹⁴⁰ and Ru¹⁰³, which agrees with the results obtained in Section 3. Other investigators /112-115, 134-136/ have obtained similar results for the differences between the gamma-emission spectra of filtered samples and hot particles. The peaks at 60, 100, and 205 kev (see Figure 16) are apparently associated with the emission of U²³⁷. Figure 17 shows the gamma-emission spectrum of a sample with a tentative age of seven months; the same was obtained with a filter from the atmospheric layer near the earth.

A gamma-emission spectrum for nuclear-explosion products 1.7 years old is plotted in Figure 18 (spectrometer with NaI (Tl) crystal 40×40 mm in size). It is natural to assume that during the subsequent radioactive decay the 660-kev peak ($\text{Cs}^{137} \rightarrow \text{Ba}^{137m}$) will be more pronounced in the spectrum, whereas the 765-kev peak ($\text{Zr}^{95} \rightarrow \text{Nb}^{95}$) will disappear. Figure 19 shows the gamma-emission spectra for hot particles of different ages /136/.

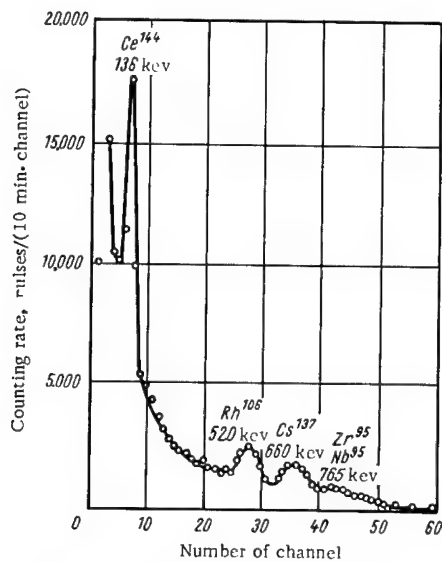


FIGURE 18. Gamma-emission spectrum of sample 1.7 years old.

As already noted in Section 1, in some cases isotopes from activity induced by neutrons in elements of the exploding device or in elements of the soil (for explosions on, near, or under the earth) may contribute substantially to the gamma emission of a fallout sample for a nuclear explosion.

Figure 20 shows gamma-emission spectra for some fallout samples collected several kilometers from the epicenter of an underground nuclear explosion accompanied by the ejection of earth /133/. The explosion was the "Sedan" test, set off on 6 July 1962 at a Nevada proving ground in the USA. Spectra of nuclear debris about two days old were obtained with a spectrometer having an NaI (Tl) crystal 102×102 mm in size. Simple calculations (with a correction for spectrometer efficiency) indicate that two days after the explosion the contribution of W^{187} to the total beta activity amounted to 60%, while that of Na^{24} was 1.2%. The fission products were evaluated in terms of the 1.60-Mev peak (La^{140}); the contribution of W^{187} was evaluated in terms of the peaks at 0.48 and 0.69 Mev; that of Na^{24} was evaluated in terms of the peaks at 2.75 and 1.38 Mev. The mixture of fission products was found to be slightly fractionated /39/. As much as 90% of the gamma emission of the fallout from this explosion (as judged by the

number of gamma-ray quanta), at an age of 167 days, was due to tungsten isotopes (mainly W¹⁸¹) /40/.

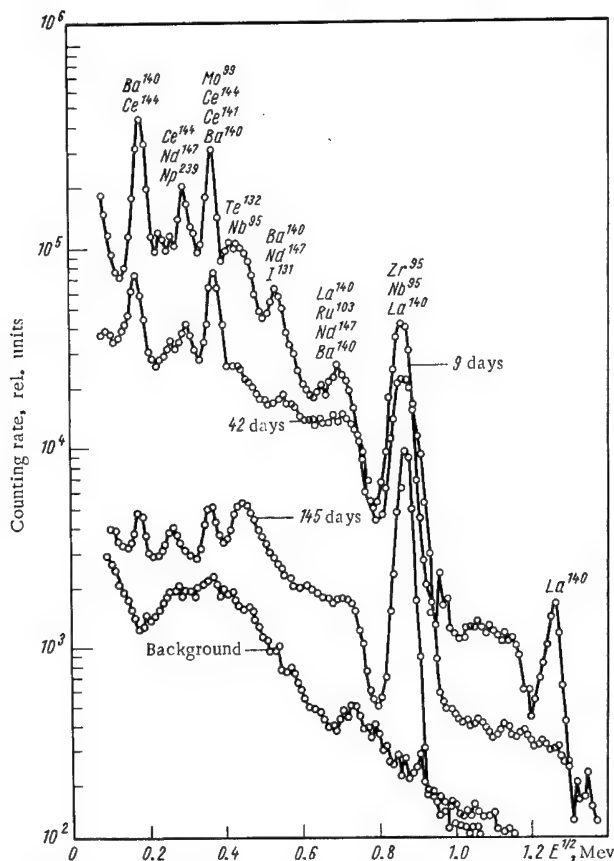


FIGURE 19. Gamma-emission spectra of hot particles of different ages /136/ (9.42 days and 145 days).

A gamma-emission spectrum cited in /78/ may also serve to illustrate the contribution of the induced radioactivity. This spectrum was that of a sample of pasture vegetation collected in 1963. Along with the 1460-kev peak corresponding to the natural emitter K⁴⁰ and the peaks at 662 (Ba^{137m}), 520 (Rh¹⁰⁶), 430 (Sb¹²⁵), and 140 (Ce¹⁴⁴) kev corresponding to fission products, this spectrum also contained a definite peak at about 840 kev, which was attributed to the emission of Mn⁵⁴, an isotope of the induced activity.

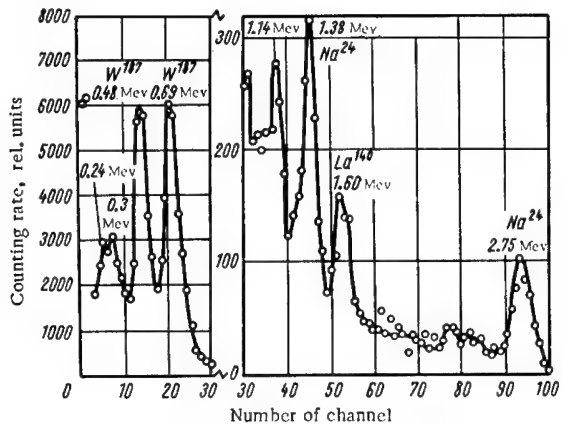


FIGURE 20. Gamma-emission spectra of sample collected near epicenter of American "Sedan" test (age of sample about two days).

According to the data of /133/, the combined power of all the bombs (fission reaction only) detonated up to and including 1958 amounted to around 92 Mt, of which 52 Mt were from the years up to and including 1956. A steady radioactive contamination of the soil of the world was produced as a consequence of these explosions. Late in the summer of 1961, just before the beginning of a new series of tests in that year, a study was made of the isotopic composition and distribution of gamma emitters in the soil of the Moscow, Ryazan, and Leningrad regions of the Soviet Union. This study showed that there had been a lasting accumulation of radioactive products by the soil, mainly in its upper layer (to 5 or 6 cm).

TABLE 9. Penetration coefficients for various soil types

| Area | Brief description of soil and area | Penetration coefficient, cm^2/g |
|------|---|---|
| I | Dark-gray forest soil, loamy | 1.15 |
| II | Chernozem, podsolized, loamy | 0.77 |
| III | Soddy, highly podsolized soil, with texture similar to that of light loam | 1.35 |
| IV | Peaty soil | 6.7 |
| V | Soddy gley soil, found in floodplains, with texture similar to that of average loam | 2.3 |
| VI | Soddy, highly podsolized, sandy loam | 1.14 |
| VII | Soddy gley soil, with texture similar to that of heavy loam found in floodplains | 1.79 |
| VIII | Soddy sandy soil | 0.29 |

By means of a standard sampler 582 cm² in area, several block samples of soil 10 cm thick were obtained; these blocks were then sliced, using a special device, into layers 0.5 cm thick. After being divided into layers and dried out at a temperature of 150°C, the soil was carefully quartered and measurements were made using a scintillation gamma-ray spectrometer. The spectrometer had a sensing unit with an NaI (Tl) crystal 70×50 mm in size (11% resolution for the 662-kev line) and an AI-100-1 pulse analyzer. The measurements were carried out in specially shaped cells, surrounding the crystal in front and on the side. A steel chamber with walls approximately 15 cm thick served to shield the sample from background radiation. Specimens of 11 types of soil were studied.

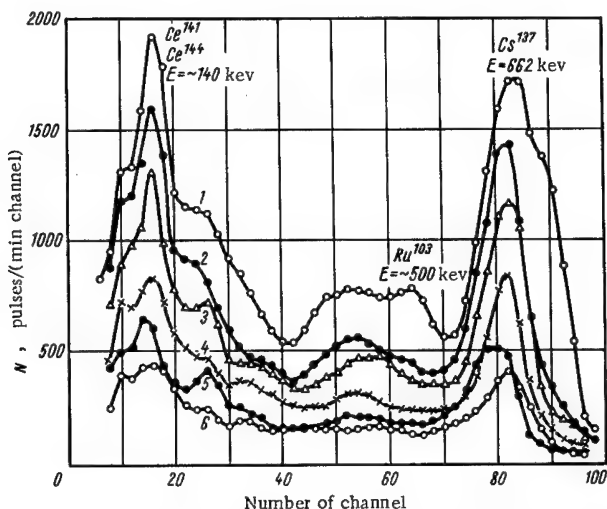


FIGURE 21. Gamma-emission spectra of samples from successive half-centimeter soil layers (curve 1 corresponds to upper layer, curve 2 to 0.5–1.0 cm layer, etc.).

The gamma-emission spectra of six successive soil layers (each one 0.5 cm thick) from different depths are shown in Figure 21. Inspection of the figure shows that the spectral composition of the gamma emitters is represented primarily by the isotopes Cs¹³⁷ → Ba^{137m} and Ce¹⁴⁴ → Pr¹⁴⁴. The slight distortion of the 662-kev peak on curve 1 (for the surface layer) is due to incipient fresh fallout from autumn 1961. The activity of natural emitters in the ground was taken into account by a comparison measurement of a relatively deep soil layer (the tenth or twelfth layer), to which fission products had not penetrated.

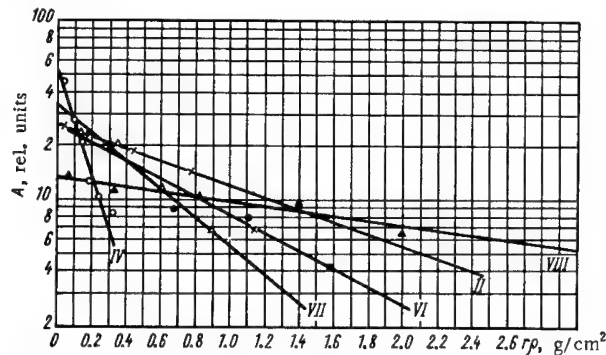


FIGURE 22. Penetration of Cs^{137} isotope of global fallout in various soils of central region of Soviet Union (numerals at curves correspond to areas and soil types listed in Table 9).

The results of the spectrometer measurements were used to calculate the penetration coefficients m of isotope $\text{Cs}^{137} \rightarrow \text{Ba}^{137m}$ for different types of soil, according to the formula

$$A(r) = A_0 e^{-mr\rho},$$

where $A(r)$ and A_0 are the specific activities of Cs^{137} at a depth of r cm and in the surface layer, and ρ is the soil density. The penetration coefficients obtained for several soil types studied are listed in Table 9. Figure 22 shows the variation with depth into the earth of the specific activity of Cs^{137} for some of the soil types in Table 9.

Chapter II

GAMMA FIELDS OF SOURCES SIMULATING FALLOUT- CONTAMINATED LOCALITIES

5. General information. Definitions

When gamma radiation passes through matter, the gamma-ray quanta may interact with: A) atomic electrons, B) nuclear particles (nucleons), C) electric fields surrounding charged particles (nuclei and electrons), and D) meson fields surrounding nucleons. As a result of these interactions, the following may take place: a) total absorption, b) elastic (coherent) gamma-ray scattering, and c) inelastic (incoherent) gamma-ray scattering.

Each of interactions A through D may lead to any of end results a through c. Thus there are 12 possible elementary processes /138/. Let us consider the main processes of gamma-ray interaction with matter for the energy range corresponding to the emission of radioactive products from a nuclear explosion (fission products and induced activity); this range is from 0.05 to 4.8 Mev /47/.* These processes are: Aa) the photoelectric effect, Ac) Compton scattering, and Ca) electron-positron pair production. The effects of coherent (Rayleigh) scattering by bound electrons (process Ab) on the energy distribution of the gamma emission are minor in the energy range considered here. The remaining processes play only a negligible role in interactions between gamma radiation of the given energies and matter /138/, and thus may be neglected.

A narrow beam of monoenergetic gamma-ray quanta incident upon a uniform absorber will be attenuated according to the exponential law:

$$N = N_0 e^{-\mu r} = N_0 e^{-n\sigma_0 r}, \quad (39)$$

where N_0 and N are the number of quanta in the beam before and after passing through an absorber r cm thick, and σ_0 is the total atomic cross section characterizing the exit of gamma-ray quanta from a narrow beam. This cross section is the sum of the photoelectric-effect section τ , the Compton-scattering cross section σ_s , the absorption cross section σ_a , and the pair-production cross section χ :

$$\sigma_0 = \tau + \sigma_s + \sigma_a + \chi.$$

In (39) $\mu = n\sigma_0$ is the linear coefficient of gamma-ray attenuation for the given medium (measured in cm^{-1} , if σ_0 is in cm^2 and n is the number of atoms of absorber per cm^3).

* According to the data of /139/, the upper limit for the gamma-emission energies of fission products is 5.4 Mev.

As gamma-ray quanta from a radioactive fallout propagate, they are as a rule attenuated and absorbed in an air-equivalent medium. Consequently, just gamma-ray interactions in such a medium will be considered below. The linear coefficients of attenuation μ and absorption of gamma-ray energy $\mu_a = \mu - n\sigma_s$ as functions of energy for air are given in /7, 140/, and in other works.

A gamma-ray flux in a system consisting of a well-collimated point source and detector is a typical example of a narrow beam. A gamma-ray flux spreading outward from an isotropic point (uncollimated) source is a typical example of a wide beam. The attenuation of a wide beam does not obey an exponential law, and thus differs from the attenuation of a narrow beam. A wide beam of gamma rays which is singly or repeatedly scattered may come back into the flux incident upon the radiation detector. Therefore, the gamma-ray attenuation (due to interactions with matter) will be somewhat less for a wide beam than for a narrow beam, because of the accumulation of secondary (scattered) radiation. The probability of gamma-ray scattering is especially high in air-equivalent media. Consequently, when gamma-ray attenuation in an air-equivalent medium is considered, the secondary (scattered) radiation must be taken into account, and also its distribution with respect to energy and direction.

Let us now define the basic quantities which will be required in this analysis /9/. The function

$$J'(\mathbf{r}, \Omega, E) = EN(\mathbf{r}, \Omega, E) \quad (40)$$

is known as the spectral-angular distribution (or distribution function), with respect to energy and direction at a point \mathbf{r} , for a flux of gamma-ray energy. Here $J'(\mathbf{r}, \Omega, E)d\Omega dE$ is the gamma-emission energy in the interval from E to $E+dE$ for radiation passing through unit area in an element of solid angle $d\Omega$ about the direction Ω , and $N(\mathbf{r}, \Omega, E)$ is the corresponding distribution function for the number of gamma-ray quanta.

The quantity

$$J_0(\mathbf{r}, E) = \int_{4\pi} J'(\mathbf{r}, \Omega, E) d\Omega \quad (41)$$

is the gamma-ray energy flux through unit area in all directions (in a unit energy interval);

$$J(\mathbf{r}) = \int_E J_0(\mathbf{r}, E) dE \quad (42)$$

is the (energetic) gamma-ray intensity; and

$$P(\mathbf{r}) = \int_E \mu_a(E) J_0(\mathbf{r}, E) dE \quad (43)$$

is the dose rate of the gamma emission at point \mathbf{r} , where $\mu_a(E)$ is the linear coefficient of absorption in air of gamma rays with an energy E .

The factor taking into account accumulation of energy of scattered radiation for a wide beam (energy-accumulation factor) will depend on the initial gamma-ray energy E_0 , the distance from the source, and the

constitution and geometry of the absorbing medium. This factor may be defined /140/ as:

$$B_E(r) = \frac{\int_{E_0}^E J_0(r, E) dE}{\int_{E_0}^E J_0^0(r, E) dE}, \quad (44)$$

where $J_0^0(r, E)$ is the unscattered part of the energy flux at point r .

In the following, reference will be made to the factors B , taking into account repeated scattering in an infinite homogeneous air-equivalent medium. When determining the dose rate P of the gamma emission, and taking into account the accumulation of secondary radiation, the following dosage accumulation factor B_d /141/ is used instead of B_E :

$$B_d(r) = \frac{\int_{E_0}^E \mu_a(E) J_0(r, E) dE}{\int_{E_0}^E \mu_a(E) J_0^0(r, E) dE}. \quad (45)$$

The function describing the distribution of gamma-ray quanta is known /9/ to satisfy the kinetic equation of the radiation-transfer equation. Because of the complexity of the kinetic equation, an accurate analytical solution is possible only in individual cases, for example, for high energies of the primary quanta (several Mev), for penetration of the gamma radiation to very great depths, or for certain other special cases, when the kinetic equation can be integrated analytically. The greatest number of results have been obtained for repeated scattering of gamma radiation in infinite homogeneous media and with simple source geometries, by solving the kinetic equation numerically using the method of moments /141/. In recent years the Monte-Carlo method and the method of random trials have also been applied to the problem of repeated gamma-ray scattering, even for complex source geometries /10, 142/.

Methods of calculating the gamma-quantum distribution function, for different media and for various source geometries and energies, have been widely studied; some Soviet studies of this subject are /9, 143, 144/.

6. Gamma field of isotropic point source

The gamma emission of a radioactive fallout may be a hazard if the fall-out contaminates the environment. Therefore, it will be advisable to consider the gamma field which exists under such conditions. As mentioned above, a fallout results in either a surface contamination of the locality or else contamination of a thin upper layer of the soil. In the former case the gamma field is similar to the field around an isotropic plane source, and in the latter case it is similar to the field produced when plane sources are superimposed. The gamma field of an isotropic plane source may in turn be represented as a superposition of the gamma fields of isotropic point sources located in a plane.

For an isotropic point source the overall gamma-ray attenuation factor includes attenuation according to an inverse-square law. This factor may be represented as

$$B(r) e^{-\mu r} (4\pi r^2)^{-1}.$$

Accordingly, the dose rate P for an isotropic point source of gamma radiation may be written as

$$P(r) = \frac{kavE\mu_a(E)}{4\pi r^2} B_d(r) e^{-\mu r}, \quad (46)$$

where r is the distance from the source to the measuring point; k is a constant which depends on the units used; a is the activity of the source in disintegrations per second; v is the number of gamma-ray quanta of energy E per disintegration; μ is the linear attenuation coefficient for gamma radiation of energy E ; $\mu_a(E) = n\sigma_a$ is the linear coefficient of energy absorption; and $B_d(r)$ is the dosage accumulation factor. If P is in r/hr , E is in Mev, μ and μ_a are in cm^{-1} , and r is in cm, then for an air-equivalent medium $k = 5.09 \cdot 10^{-2} \text{ r/hr per Mev}/(\text{cm}^3 \cdot \text{sec}) / 145$.

Values of the dosage accumulation factor for an infinite homogeneous air-equivalent medium will be given below. An aqueous medium is usually taken as the air-equivalent medium in the calculations and experiments. Water is a very satisfactory air equivalent, since the interaction cross sections of water and air, calculated for an electron, differ by no more than 1 or 2% in the energy range from 0.01 to 3.0 Mev /138/.

Table 10 lists some values of the dosage accumulation factor $B_d / 139, 141/$. These values were obtained by solving the radiation-transfer equation using the method of moments (in the energy range from 0.255 to 2.0 Mev, the depth of penetration into matter varied from 1 to 20 mean free paths). For energies of 0.09 and 0.16 Mev /146/ the values of B_d were obtained by extrapolating the values of B_d given in the tables in /139/. For most of the subsequent calculations it will suffice to know the values of B_d for depths up to 7 mean free paths for gamma rays.

Some experimental and calculated values of B_d for an aqueous medium are given in Figure 23 for comparison /9, 147—152/. The solid curves show the calculated data, obtained by interpolating values given in /141/. The data points show the experimental results.

TABLE 10. Dosage factors B_d for water

| E, Mev | μr | 0 | 1 | 2 | 4 | 7 | 10 | 15 | 20 |
|-----------------|---------|------|------|------|------|------|------|------|----|
| 0.09 | 1.0 | 3.56 | 8.86 | 31.6 | 121 | 305 | 990 | — | — |
| 0.16 | 1.0 | 3.34 | 8.14 | 27.8 | 93.4 | 231 | 693 | — | — |
| 0.225 | 1.0 | 3.09 | 7.14 | 23.0 | 72.9 | 166 | 456 | 982 | — |
| 0.5 | 1.0 | 2.52 | 5.14 | 14.3 | 38.8 | 77.6 | 178 | 334 | — |
| 1.0 | 1.0 | 2.13 | 3.71 | 7.68 | 16.2 | 27.1 | 50.4 | 82.2 | — |
| 3.0 | 1.0 | 1.69 | 2.42 | 3.91 | 6.23 | 8.63 | 12.8 | 17.0 | — |

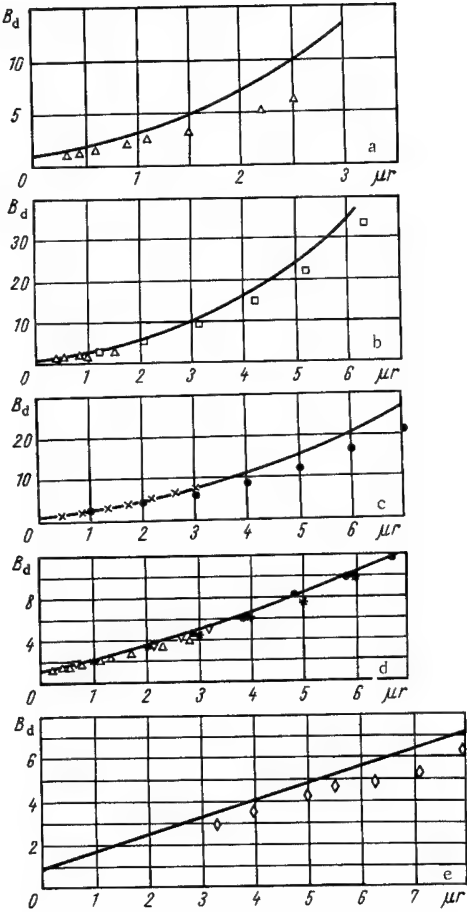


FIGURE 23. Comparison between calculated and experimental values of dosage accumulation factor for water.

the calculated values lie somewhat above the experimental ones.

The comparatively meager experimental data on the propagation of the gamma emission of Co^{60} in an air medium are also given in Figure 23d /153-155/ (here, data obtained near the interface were corrected using a factor taking into account the presence of this interface /156/). The figure shows that, as was to be expected, the values of B_d for an air medium show a good fit with the values of B_d calculated for water.

As noted above, to solve practical problems it is convenient to have analytical expressions for the dosage accumulation factors. Many different means of approximating B_d using approximation formulas have been suggested in the literature /141, 157/. The majority of these give an approximation for the experimental values of B_d which is too rough, or they specify a range of applicability (energetic and dimensional) which is

Inspection of the figure shows that, for the energy corresponding to the gamma emission Hg^{203} ($E = 0.28 \text{ Mev}$, Figure 23a), the experimental values lie somewhat below the calculated ones (below 2.5 means free paths μ_r , the difference is 20 to 35%) /148/. For the gamma emission of Au^{198} /148, 151/ ($E = 0.41 \text{ Mev}$, Figure 23b) and Cs^{137} /147, 149/ ($E = 0.66 \text{ Mev}$, Figure 23c), the experimental points are also below the calculated data (from 2.5 to 6 or 7 mean free paths, the difference is 5 to 14%). For Co^{60} /9, 148, 150, 155/ ($E_{av} = 1.25 \text{ Mev}$, Figure 23d) the experimental values practically coincide with the calculated ones (in one place the experimental values are slightly lower). The experimental data for the gamma emission of Na^{24} ($E = 2.76 \text{ Mev}$, Figure 23e) also lie somewhat below the calculated values (10 to 15% below $8\mu_r$) /152/.

A study of Figure 23 leads to the following general conclusion: the calculated values of the dosage accumulation factor show a satisfactory fit with the experimental data for energies from 0.41 to 2.76 Mev, for propagation depths in water up to 6 or 8 mean free paths (to within 5 to 15%, which is within the accuracy limits of the calculations). For 0.28 Mev the deviation is greater. In all cases

very limited and does not correspond to the range of interest for the analytical expression of B_d .

A very common expression for the accumulation factor, one which is convenient for practical calculations, was suggested in /140, 141/. This function applies to any medium and to wide ranges of energy and penetration depth. It is represented as a sum of exponential terms:

$$B_d(r, E) = \sum_{i=1}^n A_i e^{-\alpha_i \mu r}, \quad (47)$$

where A_i and α_i are constants calculated for different media and gamma-emission energies. In practice the sum of the first two terms is sufficient /141/:

$$B_d(r, E) = A_1 e^{-\alpha_1 \mu r} + A_2 e^{-\alpha_2 \mu r}, \quad (48)$$

where $A_2 = 1 - A_1$. Values of A_1 , α_1 and α_2 for different media and energies have been tabulated /140, 141/. The main disadvantage of the above formula is its inaccuracy at small gamma-ray penetration depths $0 \leq \mu r \leq 2.0$.

There is another approximation for the dosage accumulation factor B_d which is accurate in the energy range from 0.5 to 2.0 Mev. This is the formula suggested in /158/:

$$B_d(r, E) = 1 + \mu r + \frac{(\mu r)^2}{7E^{2.4}}. \quad (49)$$

The disadvantage of (49) is that it is somewhat unwieldy for the solution of various problems. However, formula (49) possesses two advantages over (48): it is considerably more accurate in the range $0 \leq \mu r \leq 2.0$, and tabulated or graphical data need not be resorted to when it is used (the gamma-emission energy enters into (49) in an explicit form).

Figure 24 shows the deviations (in percent) of the values of B_d calculated using (48) and (49) (curves 1 and 2, respectively) for gamma-emission energies of 0.5 Mev, 1.0 Mev, and 2.0 Mev (Figure 24, a, b, and c). The deviations plotted are with respect to the values in Table 10. For $\mu r = 2$ (Figure 24c) the accuracies of (48) and (49) are about the same, while for $\mu r < 2$ the accuracy of (49) is considerably higher.

In view of the lack of information on the values of B_d for low μr and the great importance of this range of distances, let us consider this particular problem in more detail. In Figure 25, a, b the dosage accumulation factors are plotted for the energies corresponding to the gamma emissions of Cs^{137} ($E = 0.66$ Mev) and Co^{60} ($E_{av} = 1.25$ Mev), for depths of travel away from the source from 0 to $2.2 \mu r$. The data points in the figure indicate experimental values of B_d for Cs^{137} /149/ and Co^{60} /148, 150/. The values of B_d calculated using formulas (48) and (49) are plotted as curves 1 and curves 2, respectively. Curves 3 were obtained by interpolating the calculated values in Table 10. Figure 25b also shows some values of B_d for $E = 1.28$ Mev, obtained using the Monte-Carlo method /156/ (with an indication of the calculation errors).

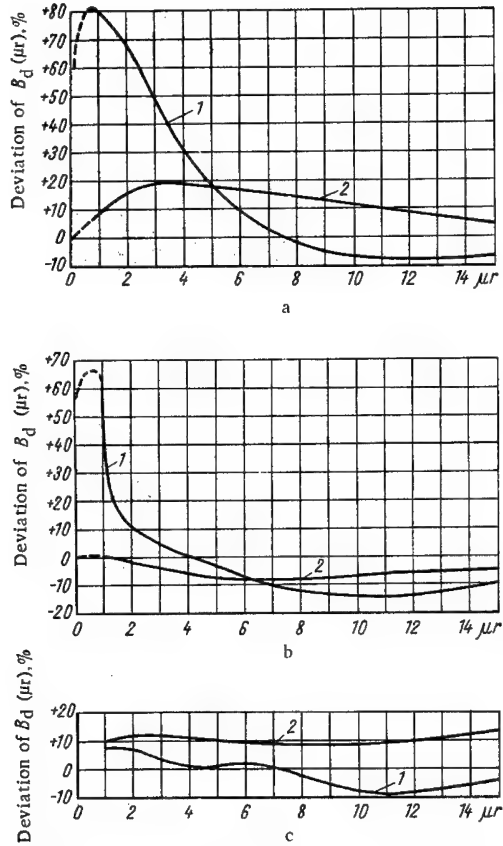


FIGURE 24. Deviation of values of B_d , approximated using formulas (48) (curve 1) and (49) (curve 2), from tabulated values, for gamma-emission energies of 0.5 Mev (a), 1.0 Mev (b), and 2.0 Mev (c).

It is evident from Figure 25 that the calculated values agree satisfactorily with the experimental data in the range $0 \leq \mu r \leq 2.0$, for $E = 0.66$ and 1.25 Mev. The approximation curves from formula (49) show a good fit with the calculated and experimental values. The curves corresponding to formula (48), however, are not satisfactory in the ranges considered. In the following, the approximation represented by formula (49) will be used, provided it does not make the calculations unduly complex.

In some cases it is necessary to know the spectral-angular characteristics of the field of a point source. The results of calculations using the method of moments or the Monte-Carlo method may be used to find these. Some examples of calculated angular dosage distributions for an isotropic point source are given in /6/ for water, concrete, sources of Co^{60} and Cs^{137} , and one-hour-old fission products. The spectral characteristics of the emission field of such a source in an aqueous (i.e., air-equivalent)

medium were given in /139—141/. Data on the spectral-angular characteristics were also quoted in /9/. The characteristics for values of μr and E for which no calculations have been made may be found by interpolation /159/.

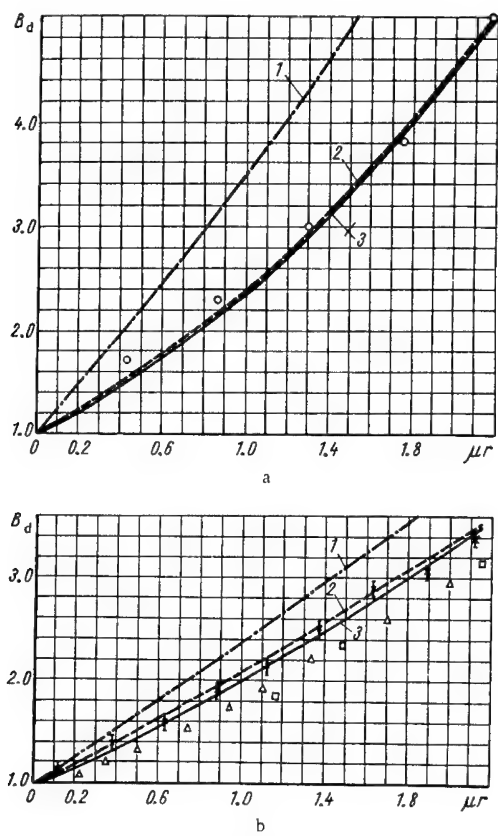


FIGURE 25. Values of dosage accumulation factor for water ($\mu r \leq 2.2$).

Geophysical problems usually involve emission sources which are located at boundaries between two phases (water and air, ground and air). Thus it will be useful to consider the effect which the density and atomic number of the material of the underlying surface has upon the gamma-emission field of an isotropic point source.

Above an interface between two phases consisting of substances with different densities and low atomic numbers Z , the gamma-emission intensity (dose rate) of a point source (measured close to the source, where $\mu r < 1$) will be higher than for a homogeneous medium. The emission intensity is measured in the layer of lower density (for water-air interfaces /9/ and ground-air interfaces /153, 156/). The higher intensity is due to

increased backscattering from the denser phase. For $\mu r \gg 1$ the dose rate P is less than for the corresponding distances in a homogeneous medium.

If the atomic number Z of the underlying-surface material is high, then a considerable portion of the scattered radiation will be absorbed in this material, and the resulting emission intensity will be less than for a homogeneous medium. Reference /156/ gives the results of some calculations, using the Monte-Carlo method, of correction factors K_u taking into account the effects of underlying surfaces consisting of materials with high densities and various atomic numbers.

The correction factors are defined as a ratio between two quantities: the dose rate from a source located at the interface between an air medium and an underlying surface, and the dose rate from a source located in a homogeneous air medium. Thus

$$K_u(Z, E, \rho, R, l, h) = \frac{dP_{\text{und}}}{dP_0}, \quad (50)$$

where Z is the atomic number of the underlying-surface material, E is the energy of the primary gamma emission, ρ is the density of the underlying-surface material, h and l are, respectively, the height of the detector and the height of the source above the interface plane, R is the distance between their projections onto this plane, dP_{und} is the dose rate from a point source with an underlying surface present, and dP_0 is the dose rate in the absence of such a surface.

Correction factor $K_u(Z, E, \rho, R, l, h)$ is a function of the atomic number Z and density ρ of the underlying-surface material, the gamma-emission energy E of the source, the heights l and h of source and detector above the interface planes, and the distance R between the projections of source and detector onto this plane.

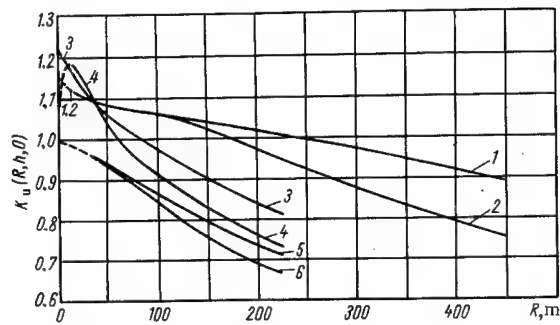


FIGURE 26. Curves of dose-rate correction factors for homogeneous medium in presence of interface, for various detector heights h , distance R , and atomic numbers Z . Curve 1) $h = 100$ m; 2) $h = 50$ m; 3) $h = 10$ m; 4) $h = 1$ m, for $Z = Z_{H_2O}$. Curve 5) $h = 10$ m; 6) $h = 1$ m, for $Z \gg Z_{H_2O}$.

Coefficient $K_n(R, h, l=0)$ is plotted in Figure 26 for the interface between air and a dense medium, for $E = 1.28 \text{ Mev}$ /156/, $l = 0$, $R \leq 450 \text{ m}$, $h = 1$ to 100 m , and low $Z(Z=Z_{H_2O})$ in curves 1 through 4, and for $h = 1$ and 10 m for a totally absorbing medium ($Z \gg Z_{H_2O}$) in curves 5 and 6. The density ρ is equal to the density of water in all cases.

Figure 26 shows that, as a rule, K_u decreases with an increase in R for practically any Z or h . For low Z the initial values of K are greater than unity, while for high Z this factor is always less than unity. The underlying surface has the greatest effect on the intensity variation at small heights.

The calculated values of K_u given in /156/ for low Z have been verified experimentally /153—155/; these pertain to the energy of Co^{60} ($E_{av} = 1.25 \text{ Mev}$). In /160/ the values of K_u for the gamma emission of Au^{198} ($E = 0.411 \text{ Mev}$) and low Z were determined experimentally. Table 11 lists some experimental values of K_u for $E = 0.411$ and 1.25 Mev for different values of μR (l and h are 1 m , and the interface is between ground and air). It is clear from the table that as E varies from 0.411 to 1.25 Mev the change in K_u is insignificant (within the limits of experimental error, since the values of K_u for $E = 1.25 \text{ Mev}$ obtained by different investigators vary more from one another than the values of K_u for $E = 0.411 \text{ Mev}$ vary from any of them).

TABLE 11. Values of K_u for ground-air and water-air interfaces

| μR | $E = 0.411 \text{ Mev}$ /160/ | $E = 1.25 \text{ Mev}$ /153, 154/ | $E = 1.28 \text{ Mev}$ /156/ |
|---------|----------------------------------|--------------------------------------|---------------------------------|
| 1.0 | 0.91 | 0.93 | 0.86 |
| 2.0 | 0.75 | 0.72 | 0.76 |
| 3.0 | 0.65 | 0.59 | 0.67 |
| 4.0 | 0.59 | 0.50 | 0.62 |
| 5.0 | 0.53 | 0.44 | 0.58 |
| 6.0 | 0.50 | 0.40 | 0.55 |

In addition, Table 11 lists some calculated values of K_u for a water-air interface for $E = 1.28 \text{ Mev}$ /156/. These values are practically identical to the experimental values obtained for the ground-air interface. Consequently, the values of K_u calculated for $E = 1.28 \text{ Mev}$ (Figure 26) for the ground-air interface and for other, lower energies can be used without introducing any significant error. Some experimental data on the angular distribution of the dose rate from an isotropic point source (Co^{60}), at a ground-air interface, are given in /153/.

Analytical expressions for correction factor K_u , for interface of air-equivalent media, are given in /161/, together with expressions for the angular distribution of the dose from an isotropic point source.

7. Gamma field of isotropic plane source. Dose rate and emission density

Let us now consider the basic characteristics of the gamma-emission field of an isotropic plane source. The source is assumed to be in an infinite homogeneous air-equivalent medium having a constant surface density of contamination. This source may be, for example, an infinitesimally thin film, covered uniformly with a gamma emitter and located in an infinite air medium.

First, it will be convenient to consider the integrated characteristics: the dose rate and the intensity of unscattered gamma radiation above the source. The dose rate P at an observation point above an isotropic plane source (film) is found by integrating, over the entire plane, the contributions dP of source elements located in this plane. Let us take as our source element an elementary area dS , covered with a monochromatic gamma emitter having a surface concentration σ (here and in the following, σ will be expressed in units of energy, for example, Mev/(cm²·sec)). The dose rate dP at a distance r from the area element will then be

$$dP(r, E) = \frac{k\sigma_a dS}{4\pi r^2} e^{-\mu r} B_d(r, E), \quad (51)$$

where E is the energy of the primary gamma emission, k is a constant depending on the measurement units used, σ_a and μ are linear coefficients of gamma-ray absorption and attenuation in air, and $B_d(r, E)$ is the dosage factor taking into account the contribution of the scattered gamma radiation to the total dose rate. In the following calculations, the analytical expression for $B_d(r, E)$ given in formula (49) will be used.

Let us set $dS=rdrd\varphi$ and integrate over φ from 0 to 2π and over r from h to r_0 . We now obtain the following expression for the dose rate $P(h)_{R_0}$ from an area of radius $R_0=\sqrt{r_0^2-h^2}$ measured at a point having a height h above the center of the emitting area:

$$\begin{aligned} P(h)_{R_0} = & \frac{k\sigma_a}{2} \left[E_1(\mu h) - E_1\left(\mu \sqrt{R_0^2 + h^2}\right) + \right. \\ & + \frac{e^{-\mu h}}{7E^{2.4}} (1 + 7E^{2.4} + \mu h) - \frac{e^{-\mu \sqrt{R_0^2 + h^2}}}{7E^{2.4}} (1 + \\ & \left. + 7E^{2.4} + \mu \sqrt{R_0^2 + h^2}) \right]. \end{aligned} \quad (52)$$

For an area with an infinite radius ($R_0=\infty$), equation (52) simplifies to

$$P(h)_\infty = \frac{k\sigma_a}{2} \left[E_1(\mu h) + \frac{e^{-\mu h}}{7E^{2.4}} (1 + 7E^{2.4} + \mu h) \right]. \quad (53)$$

In formulas (52) and (53), $E_1(x)=-Ei(-x)$ is an integral exponential function.

If the dosage factor is expressed by formula (48), then the dose rate above an infinite plane source can be written as /162/

$$P(h) = \frac{k\sigma_a}{2} \sum_{i=1}^2 A_i E_1(\mu_i h), \quad (54)$$

where $\mu_i = (1 + \alpha_i)\mu$, and $A_2 = 1 - A_1$.

Formulas (53) and (54) can be rewritten more concisely as

$$P(h) = \frac{k\sigma}{2} |\sigma_a G(h)|, \quad (55)$$

where

$$G(h) = \int_h^\infty \frac{e^{-\mu r} B_d(r, E)}{r} dr. \quad (56)$$

Figure 27 shows the percent deviations of the values of $G(h)$ obtained using the approximate dosage factors from formula (48) (curve 1) and formula (49) (curve 2), as compared with the values of $G(h)$ obtained by numerical integration of the known tabulated values of the dosage factor /139/ according to formula (56). The energies considered were from 0.5 to 2.0 Mev.

It is clear from Figure 27, a and b, that for an air-equivalent medium formula (49) provides a considerably better approximation than (48) does, for energies from 0.5 to 1.0 Mev and for $1 \leq h \leq 300$ m. For energies above 1.0 Mev (Figure 27c) the approximations of the dosage factor using formulas (48) and (49) are about equally accurate.

TABLE 12. Values of $K_{H=100}$ (h) for various energies

| E , Mev \ h , m | 1.0 | 5.0 | 25 | 100 |
|---------------------|------|------|------|-----|
| 0.09 | 6.66 | 5.10 | 3.03 | 1.0 |
| 0.16 | 5.98 | 4.53 | 2.76 | 1.0 |
| 0.255 | 5.68 | 4.07 | 2.57 | 1.0 |
| 0.5 | 5.86 | 4.06 | 2.48 | 1.0 |
| 1.0 | 6.03 | 3.95 | 2.39 | 1.0 |
| 2.0 | 5.38 | 3.62 | 2.25 | 1.0 |

(continued)

| E , Mev \ h , m | 200 | 300 | 500 | 1000 |
|---------------------|----------------------|----------------------|----------------------|----------------------|
| 0.09 | $2.16 \cdot 10^{-1}$ | $4.72 \cdot 10^{-2}$ | — | — |
| 0.16 | $2.80 \cdot 10^{-1}$ | $7.62 \cdot 10^{-2}$ | — | — |
| 0.255 | $3.26 \cdot 10^{-1}$ | — | $9.43 \cdot 10^{-3}$ | $1.69 \cdot 10^{-5}$ |
| 0.5 | $3.75 \cdot 10^{-1}$ | — | $2.17 \cdot 10^{-2}$ | $1.43 \cdot 10^{-4}$ |
| 1.0 | $4.12 \cdot 10^{-1}$ | — | $4.06 \cdot 10^{-2}$ | $8.28 \cdot 10^{-4}$ |
| 2.0 | $4.66 \cdot 10^{-1}$ | — | $7.17 \cdot 10^{-1}$ | $3.96 \cdot 10^{-3}$ |

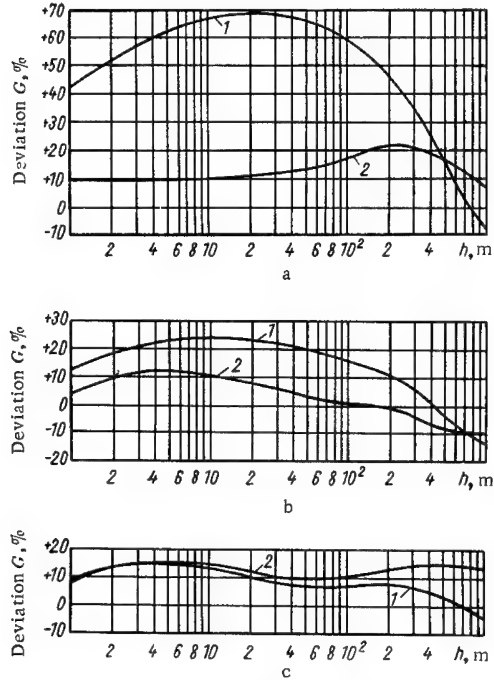


FIGURE 27. Deviations of values of $G(h)$ approximated using (48) (curve 1) and (49) (curve 2), as compared with tabulated values, for energies of 0.5 Mev (a), 1.0 Mev (b), and 2.0 Mev (c).

The values of $G(h)/G(H = 100 \text{ m}) \equiv K_{H=100}(h)$ obtained by numerical integration using formula (56) are listed in Table 12 (for h from 1 to 1000 m and for E_γ from 0.09 to 2.0 Mev).

TABLE 13. Averaged values of height conversion factors $K_H(h)$

| h, m | 1 | 10 | 25 | 50 | 100 | 200 |
|---------------|-----|------|------|------|------|------|
| $K_1(h)$ | 1 | 0.57 | 0.41 | 0.29 | 0.17 | 0.07 |
| $K_{100}(h)$ | 5.8 | 3.3 | 2.4 | 1.7 | 1.0 | 0.40 |

Table 13 gives some values of the height factors $K_H(h)$ for $H = 1$ and 100 m, averaged over the energy range from 0.255 to 2.0 Mev.

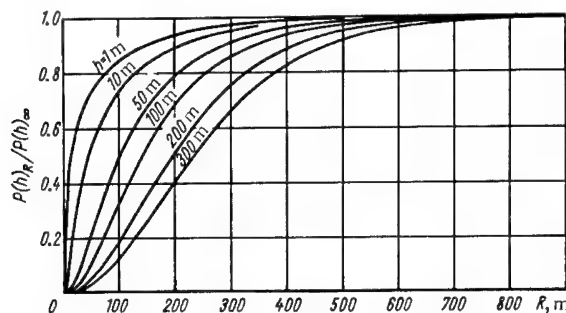
Finally, Table 14 lists some values of B_d^s for different values of E and $\mu h / 9$, for water and for $R_0 = \infty$ (plane source).

Curves for $P(h)_R/P(h)_\infty$ as a function of the test-area radius R for various heights h have been plotted in Figure 28. The energy in this case is 0.7 Mev, the average gamma-emission energy for the products of an atomic explosion.

TABLE 14. Values of dosage factors for isotropic plane source

| E_1, Mev | 1 | 2 | 4 | 7 | 10 | 15 |
|-------------------|------|------|------|------|------|------|
| 0.5 | 4.74 | 8.71 | 20.6 | 50.3 | 94.5 | 205 |
| 1.0 | 3.34 | 5.24 | 9.98 | 19.8 | 31.9 | 56.8 |
| 2.0 | 2.57 | 3.60 | 5.87 | 9.78 | 13.9 | 21.3 |
| 3.0 | 2.23 | 3.03 | 4.55 | 7.00 | 9.52 | 13.9 |

Using formulas (52) and (53) it is possible to determine the fraction α , of the total dose rate from an area of infinite radius, contributed by an area with any radius R . The radii of areas contributing equal portions of the total dose rate at an observation point less than $h = 200\text{ m}$ high will depend slightly on the primary energy of the gamma emission. These radii will not differ by more than 20% in the energy range $0.5 \leq E \leq 1.5\text{ Mev}$, for $\alpha \leq 0.8$.

FIGURE 28. Ratio $P(h)_R/P(h)_\infty$ as a function of the test-area radius R for various heights and for $E = 0.7\text{ Mev}$.

At energies from 0.5 to 2.5 Mev and for contaminated areas with radii greater than 500 m, formula (53), derived for an area of infinite radius, can be used in practice for heights up to $h = 200\text{ m}$. The errors introduced by using this approximation will not exceed 10%.

If the plane is covered with a mixture of n monochromatic gamma emitters, the dose rate $P_\Sigma(h)$ at a height h above the source will be

$$P_\Sigma(h) = \frac{k\sigma_\Sigma}{2} \sum_{j=1}^n q_j \sigma_{aj} \left[E_1(\mu_j h) + \frac{e^{-\mu_j h}}{7E_j^{2.4}} (1 + 7E_j^{2.4} + \mu_j h) \right]. \quad (57)$$

where σ_Σ is the density of contamination by the mixture, in $\text{Mev}/(\text{cm}^2 \cdot \text{sec})$; q_j is the fraction of the total gamma-ray energy (emitted by the contaminated

surface) contributed by gamma-ray quanta of energy E_j ; and σ_{aj} and μ_j are, respectively, the linear coefficients of energy absorption and attenuation, in air, for gamma radiation of energy E_j .

TABLE 15. Dose rate at height of 1 m above surface with contamination density of 100 mcuries /km²

| Radioactive isotopes | σ , Mev/(cm ² ·sec)* | Calculated dose rate, μ r/hr | | | |
|--|--|----------------------------------|-------|------|-------|
| | | /163/ | /164/ | /9/ | /165/ |
| Zr ⁹⁵ + Nb ⁹⁵ | 0.28 | 1.40 | 0.93 | 1.30 | 1.30 |
| Ru ¹⁰³ | 0.164 | 0.83 | 0.62 | 0.90 | 0.90 |
| Ru ¹⁰⁶ (Rh ¹⁰⁶) | 0.070 | 0.35 | 0.25 | 0.33 | 0.31 |
| Cs ¹³⁷ + Ba ^{137m} | 0.20 | 1.00 | 0.74 | 1.05 | 1.05 |

* Values of σ calculated using data in /7, 166/.

The material in this section pertains to contamination by a monochromatic emitter; however, it is easy to extend it to include contamination by a mixture of different emitters as well.

Table 15 lists some calculated dose rates 1 m above an isotropic plane source covered with radioactive isotopes, the latter being very spread out due to global fallout (surface concentration of emitters equal to 100 mcuries/km² /163/). For comparison, the dose rates for these same conditions, quoted in /164, 165/ or computed using the formulas of other investigators /9/, are also listed in the table. The agreement between the values calculated in /9, 165/ and those calculated by us /163/ was found to be good (the data in /164/ are apparently erroneous).

When calculating the dose rate P using formulas (53) and (54), coefficient

k may be taken to be $5.09 \cdot 10^{-2} \frac{r}{hr} / \frac{\text{Mev}}{\text{cm}^3 \cdot \text{sec}}$, provided P is in r/hr, σ in Mev/(cm²·sec), and σ_a in cm⁻¹ /145/.

Now let us assume that n layers of absorbing material, each having a thickness h_i , lie between the isotropic plane source and the observation point. The different layers have the same atomic composition but different attenuation coefficients μ_i . In this case formula (55) becomes

$$P(h) = \frac{k\sigma}{2} \left[\sigma_a G \left(\sum_{i=1}^n \mu_i h_i \right) \right], \quad (58)$$

that is, for a stratified medium the dose rate $P(h)$ does not depend on the vertical linear dimensions of the absorbing layers /167/, but only on the integral $\int_0^h \rho(h) dh$, where $\rho(h)$ is the varying density of the stratified medium (according to height). Thus we can write

$$P(h) = \frac{k\sigma}{2} \left[\sigma_a G \left(\left\{ \frac{\mu}{P} \right\}_0^h \rho(h) dh \right) \right], \quad (59)$$

where $\{\mu/\rho\}_0$ is the mass coefficient of attenuation for a medium with the given atomic composition.

The intensity of the unscattered gamma radiation above an isotropic plane source covered with a monochromatic emitter will be

$$J(h)_\infty = \frac{\sigma E_1(\mu h)}{2}. \quad (60)$$

Hence

$$\sigma = 2\mu \int_0^\infty J(h)_\infty dh. \quad (61)$$

Let us consider further the effect which a dense underlying surface (that is, an interface between two substances of different density) has upon the gamma-emission field of an isotropic plane source. The dose rate for a plane source, taking into account an underlying surface, can be found by integrating (over the entire plane) the equation

$$dP_{\text{und}} = dP_0 K_u,$$

where dP_{und} and dP_0 are the dose rates from an area element of the source, in the presence of the underlying surface and in its absence. Here K_u is the correction factor for the dose rate from an isotropic point source situated at the interface between two media (see Section 6).

This relation was integrated numerically to determine P_{und} , using the values of $K_u / 156$ for low Z , equal to Z_{eff} for water. Figure 29 shows the curves of $P(h)_R/P(h)_\infty$ for an isotropic plane source and an energy $E = 1.25$ Mev, in the presence of an underlying surface (solid curves) and without an underlying surface (dashed curves). The underlying surface is found to have some effect on the dose rate above an emitting disk, especially for low h . However, the distortion of the curves for a homogeneous medium, due to the presence of the underlying surface, does not exceed 15%. For high h , this effect is considerably less.

The dose rates for an infinite plane source providing uniform contamination are practically the same, with or without an underlying surface:

$$\int_S dP_{\text{und}} = \int_S dP_0$$

(with an accuracy up to 2 or 3% for numerical integration). This same result follows automatically from /167/ for stratified media (with equal Z for both substances).

If the contamination is nonuniform, the dose rates above a plane source may differ somewhat, depending on whether or not there is an underlying surface. However, for actual contamination gradients this difference will be only slight.

Using the data in Table 15, it is not difficult to calculate the dose rate from a mixture of fission products (global fallout) at a height of 1 m. The amount of fallout (from a nuclear explosion) onto the locality was taken from /168/. For an average strip (40–50°N) of the Soviet Union, the composition of the gamma-emitting products was: $\text{Ca}^{144} + \text{Pr}^{144}$,

630 mcuries/km²; Sb¹²⁵, 47 mcuries/km²; Ru¹⁰⁶ + Rh¹⁰⁶, 410 mcuries/km²; Cs¹³⁷, 95 mcuries/km²; and Zr⁹⁵ + Nb⁹⁵, 550 mcuries/km² (on 1 July 1963). Calculations according to the scheme indicated above give a fallout-caused dose rate of 11.5 μ/hr . Taking into account some penetration of isotopes into the soil, as well as the effect of the microrelief, this figure drops to 7 or 8 μ/hr .

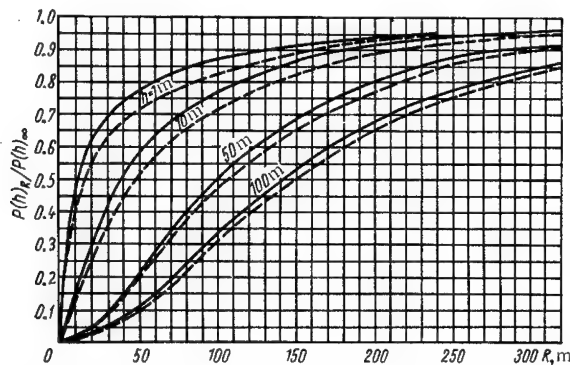


FIGURE 29. Ratio $P(h)_R / P(h)_{\infty}$ for $E = 1.25$ Mev as function of distance, with (solid curves) and without (dashed curves) underlying surface.

8. Spectral and angular distributions of gamma emission from isotropic plane source

In the previous section we considered the dose rate and the gamma-emission intensity. These characteristics of the gamma-emission field were found by integrating the distribution function $F(\mu_0 h, E_0, E, \omega)$ for the emission of an isotropic plane source, with respect to direction ω and energy E ($\omega = \cos \theta^*$). By integrating the above function with respect to only one variable, it is easy to obtain either the spectral or the angular distribution of the emission:

$$J_1(\mu_0 h, E_0, E) = \int_{-1}^{+1} F(\mu_0 h, E_0, E, \omega) d\omega; \quad (62)$$

$$I_1(\mu_0 h, E_0, E) = \mu_a(E) J_1(\mu_0 h, E_0, E); \quad (63)$$

$$J_2(\mu_0 h, E_0, \omega) = \int_0^{E_0} F(\mu_0 h, E_0, E, \omega) dE; \quad (64)$$

$$I_2(\mu_0 h, E_0, \omega) = \int_0^{E_0} \mu_a(E) F(\mu_0 h, E_0, E, \omega) dE, \quad (65)$$

* Here θ is the angle between the normal to the source plane and the direction of an area element dS (from the observation point).

where J_1 and I_1 are the spectral distributions of the intensity or dose rate, and J_2 and I_2 are the angular distributions of the intensity or dose rate (for the gamma emission of an isotropic plane source).

The integration of (62) through (65) may be carried out over any limits (E_1, E_2) and (ω_1, ω_2). It is very important in practice to know the spectral and angular distributions, first of all in order to determine the biological hazard at any point, and secondly in order to determine many properties of the source over the emission field. Let us now consider briefly the comparatively small amount of existing material on the spectral and angular distributions of the gamma emission of an isotropic plane source, in air or water. Some of the data are calculated and some are experimental.

The angular distribution was obtained /169/ by the method of moments for $E_0 = 1$ Mev and for the range from 0.477 to 0.864 Mev. The curves for $\mu_0 h = 1$ are shown in Figure 30 (for a surface density of 1 quantum/(cm²·sec)).

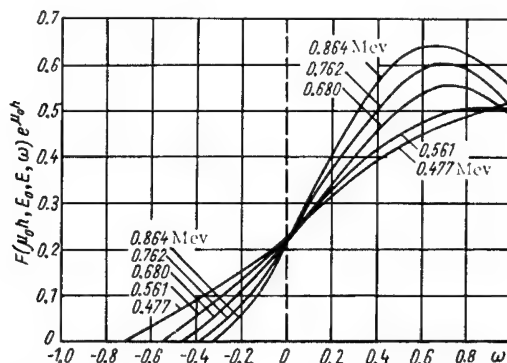


FIGURE 30. Angular distribution of gamma quanta above isotropic plane source, for $\mu_0 h = 1$ and $E = 1$ Mev.

The spectral-angular function F for scattered radiation from an isotropic plane source (Cs^{137} , with $E_0 = 0.66$ Mev) for $\mu_0 h$ from 0.5 to 2 was given in /170/. The spectral gamma-ray distribution in an air medium over an isotropic plane source can be obtained quite easily by integrating the spectral function for an isotropic point source (same medium) over the entire plane. Spectral intensity distributions over a plane, obtained in this way, were studied in /171, 172/.

Some calculated differential spectra of the gamma radiation over a plane, uniformly covered with fission products of various ages, are given in /173, 174/. Data on the angular distribution of the dose rate for emission from a plane source are given in /6/. Figure 31 shows this distribution $I(h, \omega)$ in air at different heights above a source contaminated with fission products 1.12 hr old. The function was so normalized that

$$\int_{-1}^{+1} I(h = 1m, \omega) d\omega = 1.$$

The above function can be used to calculate any dosage characteristics for a plane source.

Figure 32 shows the variations of $L(\mu_0 h, \Omega)$, the portion of the dose rate contributed by the radiation arriving at the measuring point within a solid angle $\Omega = 1 - \cos \alpha$, where α is the half-angle of opening of the cone from which the observations are made (at different heights). The curves of $L(\mu_0 h, \Omega)$ reach unity only for $\Omega = 2$. The distribution of gamma-ray quanta according to energy and direction in the air over a region of radioactive fallout was discussed in /174, 175/.

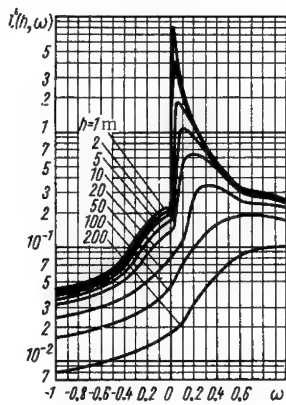


FIGURE 31. Angular dose-rate distribution for gamma emission of isotropic plane source.

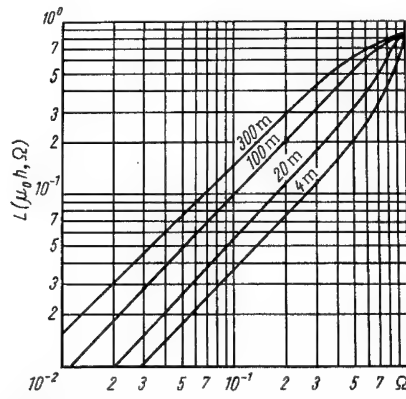


FIGURE 32. Portion of dose rate above plane source recorded in solid angle Ω (relative to total dose rate recorded by isotropic detector).

Some studies include experimentally obtained spectral-angular distributions of the gamma emission, in addition to the calculated data. Differential energy spectra of the gamma radiation over an artificial model [simulation] of an isotropic plane source are given in /176, 177/. The model consisted of an arrangement of point sources of gamma emission (Cs^{137} , $E = 0.66$ Mev or Co^{60} , $E_{av} = 1.25$ Mev) on the earth's surface. In Sections 10 and 11, the results of our simulation experiments will be discussed in detail (some preliminary data from these experiments were presented in /177/). Data on the spectral-angular distributions of the gamma emission for Cr^{51} ($E = 0.32$ Mev), Sb^{124} ($E_1 = 0.603$ Mev, $E_2 = 1.69$ Mev, $E_3 = 2.09$ Mev), and Co^{60} ($E_1 = 1.17$ Mev, $E_2 = 1.33$ Mev) will also be given.

The differential energy spectrum of the gamma emission over an isotropic plane Co^{60} source is given in /178/. This spectrum was calculated using experimental data obtained in spectroscopic measurements of the emission of a point Co^{60} source.

Data on the spectral-angular distributions have also been obtained by measuring the gamma radiation over sites contaminated by nuclear explosions /171, 179, 180/. Figure 33 shows this distribution at a height of 1 m over the region contaminated during the American "Teapot" test of 1955 /179/. The contributions to the dose rate

made by radiations of different rigidities, for the "Bravo" test of 1954 /171/, are shown in Figure 34. The vertical dashed lines in Figures 33 and 34 indicate the contributions of individual isotopes (in percent of total photon flux) to the gamma emission of the fallout for these explosions; these were determined by analyzing fallout samples collected at the site.

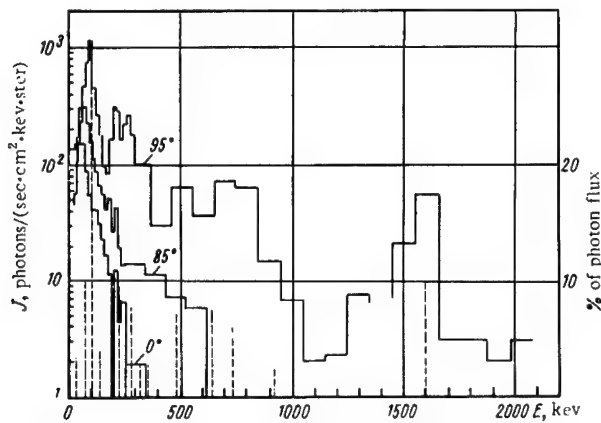


FIGURE 33. Spectral-angular distribution of gamma-ray quanta at height of 1 m above site contaminated during "Teapot" test /179/. Angles next to spectra are reckoned from vertical line directed toward zenith.

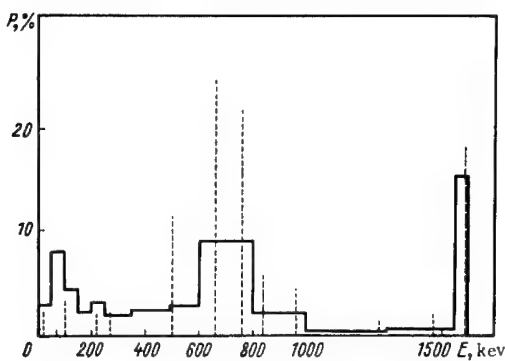


FIGURE 34. Contributions to dose rate of radiations of different rigidities, at height of 1 m above site contaminated during "Bravo" test.

Some gamma-emission spectra taken at different angles to the horizon are given in /180/. This emission was over a site contaminated during the "Small Boy" test in 1962.

9. Gamma field of three-dimensional source

Let us consider a volume element with a volume contamination $\sigma_v(z)$, enclosed between planes z and $z+dz$, in an emitting, absorbing medium 2 (Figure 35). The dose rate from this source element, measured at point C in absorbing medium 1, is assumed to be the same as the dose rate for an infinite isotropic plane source with a surface contamination

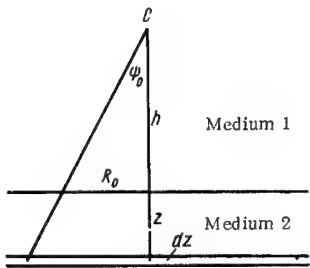


FIGURE 35. Positions of observation point and emitting-absorbing media, for derivation of formula for three-dimensional source.

the attenuation coefficient for the given initial gamma-emission energy is

$$\int_0^r \mu(r) dr = (\mu r)_{\text{eff}}. \quad (67)$$

Uniform contamination is considered, so that

$$\sigma_v(z) = \text{const.}$$

In an absorbing medium the dose rate from an infinite emitting-absorbing layer (half-space), for example, the dose rate in air over uniformly contaminated water or land, is

$$\begin{aligned} P^v(h, \psi_0 = \pi/2, z = \infty) &= \frac{k\sigma_0\sigma_a}{2\mu_0} \left[E_2(\mu h) + \right. \\ &+ \left(1 + \frac{1}{7E^{2.4}} \right) e^{-\mu h} + \frac{e^{-\mu h}}{7E^{2.4}} (1 + \mu h) \Big] = \\ &= \frac{k\sigma_0\sigma_a}{2\mu_0} \left[E_2(\mu h) + e^{-\mu h} \left(1 + \frac{2 + \mu h}{7E^{2.4}} \right) \right], \end{aligned} \quad (68)$$

where h is the height of the measuring point above the emitting medium, ψ_0 is the angle subtended by the emitting layer at the observation point (for a half-space, $\psi_0 = \pi/2$), k is a constant depending on the choice of units, σ_a is the linear coefficient of absorption of gamma-ray energy in air, μ_0 and μ are the linear coefficients of attenuation (medium 2 in Figure 35) and absorption (medium 1), respectively, and $E_2(x) = e^{-x} - xE_1(x)$ is the tabulated King function /146/.

Analogously, it is not difficult to obtain formulas giving

$$P^v(h, \psi_0, z_0) \text{ for } \psi_0 < \pi/2 \text{ and } z < \infty.$$

For $\psi_0 = \pi/2$, up to heights of 200 m in the air, about 95% of the dose rate from an infinite dense emitting layer (water or land) can be attributed to the emission from a surface layer only about six mean free paths (for gamma rays) thick, that is, for $z \approx 6\mu r$. For water this layer will be 70 to 80 cm thick, and for land it is 30 to 40 cm thick (at $E = 1.0$ Mev).

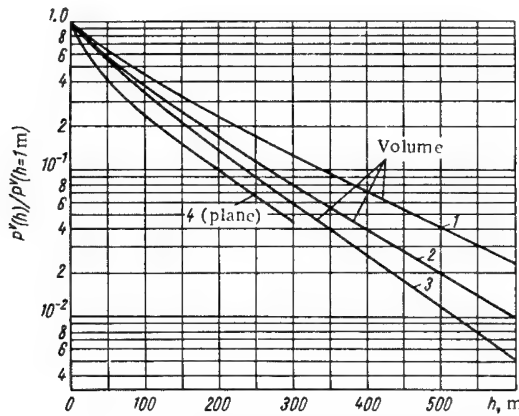


FIGURE 36. Variation of dose rate with height above volume emission source.

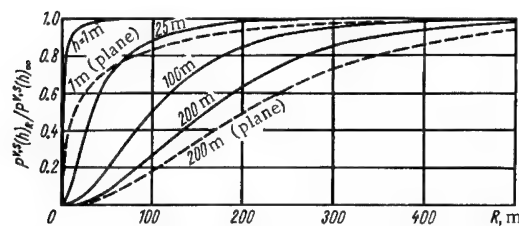


FIGURE 37. Ratio $P^{v,S}(h)_R/P^{v,S}(h)_\infty$ as function of radius R , for volume emission source (solid curves) and plane source (dashed curve).

Figure 36 shows the variation with height of the gamma-ray dose rate $P^v(h)/P^v(h = 1 \text{ m})$, calculated using formula (68). The source is water contaminated uniformly with: Na^{24} isotopes ($E_1 = 1.38 \text{ Mev}$, $E_2 = 2.76 \text{ Mev}$), curve 1; Co^{60} or Fe^{59} isotopes ($E_{av} \approx 1.2 \text{ Mev}$), curve 2; and a gamma emitter with an energy of 0.8 Mev, curve 3. The figure also gives the curve for an isotropic plane source (curve 4), for comparison.

Whereas the dose rate P^v above a three-dimensional source is a function of the source density (since μ_0 enters into formula (68)), the shape of the height curve does not depend on this density. Accordingly, the shapes of the height curves for contaminated ground with different densities will be the same as the shape of the height curve for contaminated water (on condition that the contamination has the same gamma-emission composition).

Figure 37 shows $P^v(h)_R/P^v(h)_\infty$ as a function of the radius R for a three-dimensional source with a layer thickness of more than $6 \mu r$ for different heights and for a gamma-emission energy of 1.0 Mev (solid curves). The curves of $P^s(h)_R/P^s(h)_\infty$ for a plane source ($h = 1$ and 200 m) are also shown in this figure (dashed curves).

A comparison of the above curves indicates that the effective radius of activity of a three-dimensional source is considerably less than the activity radius for a surface source, especially at low measuring heights.

If the point of observation is at the interface between the emitting and absorbing media (that is, if $h = 0$), then it follows from (68) that

$$P^v = \frac{k\sigma_v \sigma_a}{\mu_0} \left(1 + \frac{1}{7E^{2.4}} \right), \quad (69)$$

where $k = 5.09 \cdot 10^{-2} \frac{r}{\text{hr}} / \frac{\text{Mev}}{\text{cm}^3 \cdot \text{sec}} / 145$. For any air-equivalent medium the quantity $\frac{\sigma_a}{\mu} (1 + \frac{1}{7E^{2.4}})$ is practically constant over a wide range of energies and is equal to about 0.5. Accordingly, formula (69) simplifies to

$$P^v = \frac{k\sigma_v}{2} \frac{\mu}{\mu_0}. \quad (70)$$

If the contamination of the layer is nonuniform (with respect to z), the dose rate above the layer can also be determined by integrating the dose rate from the infinite number of plane sources constituting the three-dimensional source. However, in this case the concentration of the radioactive contamination of these sources does not vary continuously.

Let us consider the case which is most important in practice, namely volume contamination for which the activity diminishes exponentially with depth:

$$\sigma_v(z) = \sigma_{v_0} e^{-mz}, \quad (71)$$

where σ_{v_0} is the volume concentration of the surface layer, and m is a constant characterizing the rate of decrease of concentration with depth.

As mentioned previously, such a source is created some weeks (months) after radioactive products fall out onto a region, as a result of their penetration into the soil. For different soils and times after fallout, m may range from 0.3 to 6 cm²/g (see Section 4). In this case (for $\psi_0 = \pi/2$)

$$P^v(h) = \frac{k\sigma_{v_0} \sigma_a}{2m} \left\{ E_1(\mu h) - e^{(\beta-1)\mu h} E_1(\beta\mu h) + \right. \\ \left. + \frac{\beta-1}{\beta} e^{-\mu h} \left[1 + \frac{1}{7E^{2.4}} \left(1 + \mu h + \frac{1}{\beta} \right) \right] \right\}, \quad (72)$$

where $\beta = 1 + \frac{m}{\mu_0}$ and all the other symbols are as previously.

The intensity of the unscattered gamma emission in air from a layer of infinite thickness and size (half-space with constant concentration σ_{v_0} at a height h) is equal to the emission intensity of a plane directional source with a surface concentration of contamination equal to $\sigma_0 \cos \theta$, where

$\sigma_0 = \frac{\sigma_{v_0}}{\mu_0}$ (here μ_0 is the linear coefficient in the emitting medium), and θ is the angle between the normal to the surface and the direction of the emitting surface element /181/:

$$J(h) = \frac{\sigma_{v_0}}{2\mu_0} E_2(\mu h) \quad (73)$$

μ being the linear attenuation coefficient in air.

For volume contamination, with an activity that diminishes exponentially with depth, the intensity of the unscattered radiation can be expressed as

$$J^*(h) = \frac{\sigma_{v_0}}{2m} [E_1(\mu h) - e^{(\beta-1)\mu h} E_1(\beta\mu h)]. \quad (74)$$

Now it is easy to obtain the spectral and angular distributions for an infinite three-dimensional source, by integrating the analogous distribution for an isotropic plane source with respect to z . Figure 38 shows a differential spectrum obtained in this way, for the gamma emission in air at a height of 25 m above a three-dimensional source (land or water) having radioactive Na²⁴ isotopes uniformly distributed throughout it ($E_1 = 1.38$ Mev, $E_2 = 2.76$ Mev). Some spectra above a three-dimensional source, also obtained in this way, are given in /172/, for various heights and gamma-emission lines.

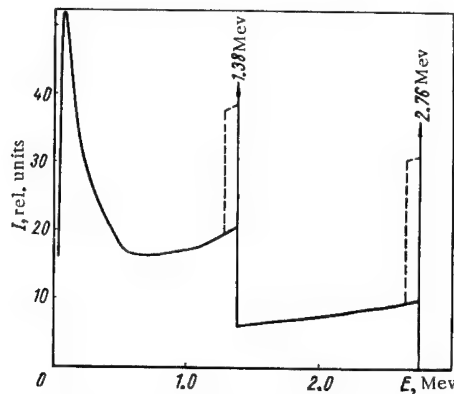


FIGURE 38. Differential spectrum of gamma emission in air above three-dimensional source having Na²⁴ isotopes distributed uniformly throughout it.

10. Gamma field of artificial model of fallout

The calculations of gamma-emission characteristics made in the foregoing sections pertained to idealized conditions. Consequently, they involve certain simplifications and do not take into account the variety of actual conditions existing when radioactive contamination of a site takes place. We constructed an artificial model [simulation] of the surface contamination of a locality, in order to make an experimental study of the gamma-emission field.* This made possible an investigation of the intensities of the direct and scattered radiations, the spectral-angular distribution of gamma-ray quanta, and the relation between these characteristics and the concentration of surface contamination under actual conditions.

TABLE 16. Some characteristics of fallout-simulation areas

| Gamma emitter | Half-life | Energy of quanta, Mev | Mean gamma-emission energy, Mev | Quantum yield, in fractions | Diameter of modeling field, m | Side length of network square, m | Total number of sources distributed | Total activity of sources in test area, curies | Surface density of contamination | | Calculated dose rate, without taking microrelief into account, $\mu\text{r}/\text{hr}$ | |
|-------------------|------------|-----------------------|---------------------------------|-----------------------------|-------------------------------|----------------------------------|-------------------------------------|--|----------------------------------|----------------------------------|--|--------------------|
| | | | | | | | | | curies/ km^2 | Mev/(cm^2/sec) | at height of 1 m | at height of 100 m |
| Co ⁶⁰ | 5.24 years | 1.17 1.33 | 1.25 | 1.0 1.0 | 500 | 14.2 | 1000 | 5.3 | 27 | 250 | 1150 | 200 |
| Sb ¹²⁴ | 60.9 days | 2.09 1.69 0.603 | 1.03 | 0.07 0.52 1.0 | 480 | 30 | 192 | 4.84 | 26.7 | 161 | 870 | 150 |
| Cr ⁵¹ | 27.8 days | 0.32 | 0.32 | 0.09 | 500 | 35.4 | 148 | 9.0 | 46 | 4.9 | 40 | 7 |

The simulation was carried out by distributing a large number of point sources (these emitted gamma-ray quanta of various energies) uniformly over fairly large areas of the earth's surface (up to 500 m in diameter). The gamma-ray energies were so selected that their range corresponded to that of the emitters producing surface contamination from the fallout of a nuclear explosion.

Three gamma-ray emitters were selected for the simulation experiment: Co⁶⁰, Sb¹²⁴, and Cr⁵¹. Table 16 gives a brief description of these emitters, together with the corresponding dose rates above the test areas studied.

* Measurements of the gamma-emission characteristics above an artificial model of surface contamination are described in greater detail in the collection of papers: "Voprosy aerogamma-s"emki mestnosti, zagryaznennoi radioaktivnymi vypadeniyami" (Aerial Gamma-Emission Surveys of Sites Contaminated by Radioactive Fallout), Edited by Yu. A. Izrael'. — Moskva, Gidrometeoizdat (in press).

One thousand Co^{60} point sources, having a total activity of 5.3 curies, were distributed throughout area 1 (diameter 500 m). The sources were placed at the nodes of a tetragonal (arbitrary) network with squares 14.2 m on a side. To make measurements on the ground more convenient, the central source was replaced by 100 sources (each 100th as strong as the primary source) located at the nodes of a tetragonal network having squares 1.76 m on a side.

In area 2 (diameter 480 m), 192 Sb^{124} sources were placed at the nodes of a tetragonal network having squares 30 m on a side. In area 3 (diameter 500 m), 148 Cr^{51} sources were placed at the nodes of a tetragonal network having squares 35.4 m on a side. The test areas were selected on a dry steppe where the grass cover was slight. Before the sources were positioned, the areas were carefully leveled, in order to evaluate later the effect of the microrelief on the experimental results. With this in mind, the Co^{60} and Cr^{51} sources were placed in thin Dural holders, so that it was possible to mount these sources in two positions: at heights of 20 to 30 cm and at the level of the ground (as desired).

The results obtained from the measurements with the source holders 20 to 30 cm above ground were taken as a reference, corresponding to an ideally even surface (provided the slight effect of the microrelief on gamma-ray scattering by the earth's surface is neglected). The Sb^{124} sources were placed directly on the ground, at the nodes of the network.

The parameters of the gamma-emission field above the test areas were studied by means of instruments carried by an MI-4 helicopter. The helicopter had a gamma-ray roentgen meter and a gamma-ray spectrometer aboard. The latter consisted of an AI-100-1 analyzer with two scintillation detectors. The first detector consisted of an NaI (Tl) crystal 100×100 mm in size and an FEU-49 photomultiplier; its resolution was 11.5% for the gamma-emission line at 662 kev ($\text{Cs}^{137} + \text{Ba}^{137m}$). The detector was used without a shield.

The second detector consisted of an NaI (Tl) crystal 70×70 mm in size and an FEU-52 photomultiplier (11% resolution). This detector was placed in a special steel shield with walls 10 cm thick, making it possible to study the spectral-angular distribution of the gamma-ray quanta. The shield was so constructed that the gamma radiation arriving at angles of 15, 30, 45, 60, 75, and 90° (here the half-angle of opening of the cone is referred to, that is, the angle between the generatrix of the cone and an axis perpendicular to the earth's surface) could be measured. A diagram of the shield is shown in Figure 39. As noted previously, the intensities of the direct and scattered radiations were investigated over all three test areas. During the measurements, the readings of the radio altimeter and roentgen meter, and the exposure time of the gamma-emission spectrum, were recorded continuously on tape. To gather the required statistics, the helicopter made from three to eight passes over the centers of the test areas, at speeds of 40 to 60 km/hr (against the wind, to reduce the relative velocity). Flights with the spectrometer having the 100×100 mm crystal were made: over area 1 (Co^{60}) at heights of 5, 10, 20, 30, 50, 80, 110, 150, 200, and 250 m; over area 2 (Sb^{124}) at heights of 5, 10, 20, 30, 50, 80, 110, and 150 m; and over area 3 (Cr^{51}) at heights of 5, 10, 20, 30, 50, 80, 110, and 150 m.

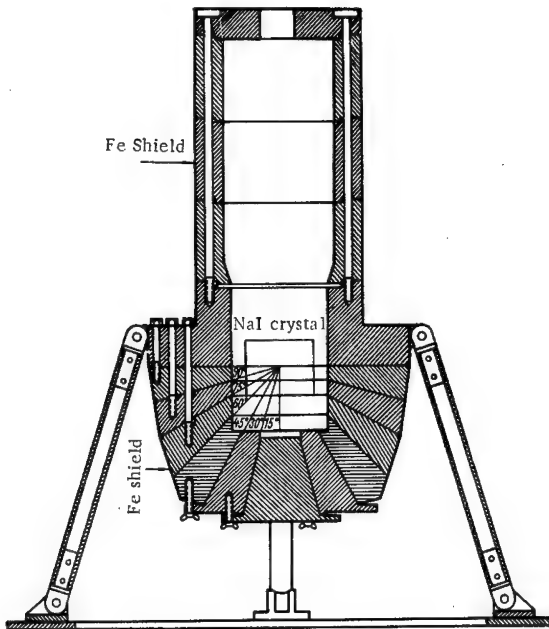


FIGURE 39. Shield used to measure spectral-angular characteristics of gamma emission.

Table 17 lists some ratios of the energy intensities from an isotropic disk-shaped plane source ($R = 250$ m) and an infinite plane source, at various heights. These results were obtained by interpolating the data in /9/ and by using the formulas of /163/ for the emission of Co^{60} ($E_{av} = 1.25$ Mev). The heights quoted are in meters of standard atmosphere (ISA). The table also includes the ratios calculated just for the component of unscattered radiation.

TABLE 17. Ratio of energy intensities from finite and infinite sources

| Height above center of field, m | Ratio of energy intensity from disk with $R = 250$ m to intensity from infinite plane source | |
|------------------------------------|---|----------------------|
| | for sum of direct and scattered radiations | for direct radiation |
| 20 | 0.95 | 0.96 |
| 30 | 0.9 | — |
| 50 | 0.85 | 0.92 |
| 70 | 0.8 | — |
| 110 | 0.75 | 0.82 |
| 150 | 0.62 | 0.76 |
| 200 | 0.53 | 0.72 |
| 250 | 0.45 | 0.62 |

It was found experimentally /176/ that a 600-meter tetragonal network is not a good enough approximation of an infinite source for heights $> 150\text{m}$, at energies of 1.25 Mev (Co^{60}) or above. With respect to the fields produced by us ($R = 250\text{m}$), Table 17 shows that for heights above 100m the scattered and unscattered components may both be more than 20 to 25% too low, in comparison with the radiation from an infinite plane source. However, for heights below 50m this error is less than 15%. The errors in measuring the direct radiation are always lower than those for the total intensity.

It should be noted that the finiteness of the field introduces errors making the results too low (that is, the intensities of both the direct and scattered radiations are low, albeit not by the same amount). Consequently, in a working model, the spectrum at great heights will be enriched in its unscattered component in comparison with an infinite plane source.

However, the variation of the ratio between the intensities of the direct and scattered radiations, due to the finiteness of the test areas, has almost no effect on the shape of the scattered-radiation spectrum. This follows from the theoretical calculations in /172/ for the spectra above an infinite isotropic plane emitter with an initial energy $E_0 = 1\text{ Mev}$, which showed that the shape of the scattered-radiation spectrum essentially does not change beginning at heights $H = 50\text{m}$ ISA. It was also concluded /9/ that the relative spectral distribution of scattered radiation established at distances of 2 to $4\mu h$ from a plane source varies little when there is a further increase of μh .

All the foregoing goes to show that, with certain reservations, the results can be interpreted using the spectra obtained at all the heights indicated. Since the shapes of the spectra are not affected, it is only necessary to introduce appropriate corrections for the intensities of the direct and scattered radiations.

When measurements are made from a helicopter flying over the test area, a "fringe effect" is observed as the helicopter moves away from the center, that is, there is a distortion of the field as the edge of the test area is approached. However, in order to gather enough statistics, and at the same time not to make too many passes, which leads to additional instrument error, the measurements made during each pass should be as protracted as possible.

A coefficient K , representing the ratio between the dose rate above any point on an isotropic emitting disk and the dose rate above the center of the disk, was calculated in /6/, the height of the detector being the same in both cases. In /6/, K was calculated for the emission of Co^{60} and for various values of μR_0 , d/R_0 , and h/R_0 , where μ is the linear attenuation coefficient for gamma rays, R_0 is the disk radius, d is the distance from the center of the disk to the projection of the detector onto the disk plane, and h is the height of the detector. The nature of the variation of K will be governed by the nature of the variation of the dose rate above a disk-shaped isotropic source. When K (for $\mu R_0 = 1.78$) is plotted as a function of d/R_0 (for $d \leq R_0$) for $H = 60\text{m}$ ($H/R_0 \approx 0.25$) and $H = 250\text{m}$ ($H/R_0 = 1.0$), the fringe effect is found to distort the dose rate at distances $d < 0.8 R_0$ by, on the average, less than 10% for $H = 60\text{m}$ and less than 15% for $H = 250\text{m}$. In the measurements over the test areas these conditions were satisfied. The spectrum was taken only for periods when the intensity, as recorded

on the automatic recorder, was essentially constant. Under these conditions, the exposure time for a single pass was about 30 or 40 seconds, given a helicopter ground speed of 40 or 50 km/hr.

The measurements at a height of 5 m were made with the helicopter hovering over the center of the test area. By landing in the center of the field of Co^{60} sources, it was possible to obtain recordings for a detector height of only 1 m. For heights less than $H = 10$ m above the test area for Co^{60} and less than 20 to 30 m above the test areas for Sb^{124} and Cr^{51} , the field nonuniformity due to the discontinuity of the emitters (discrete sources) begins to have an effect.

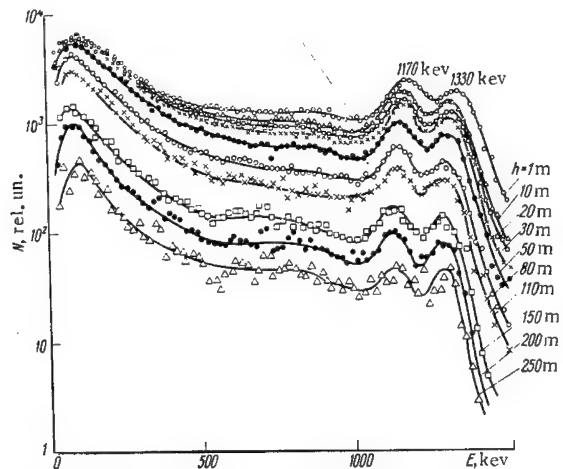


FIGURE 40. Measured gamma-emission spectra over test area simulating Co^{60} contamination of ground (isotropic detector).

The effect which the discreteness of the sources has on the dose rate at a height $H = 1$ m was checked experimentally for all three test areas, using a portable radiometer. The ratio between the dose rate directly above a source and the dose rate at the center of an elementary square of the network was 23.7 for Co^{60} , while for Sb^{124} it was 83.5. In order to reduce the nonuniformity of the field, a central region with 100 times as many point sources in it was created in the Co^{60} test area. The helicopter landed in the middle of this smaller region, in order to make measurements on the ground. Consequently, the hovering at $H = 5$ m above the field of Co^{60} sources was also carried out under conditions of satisfactory uniformity. At higher altitudes the nonuniformity of the field was sharply reduced, until, at a height equal to the distance between sources, it was practically nonexistent.

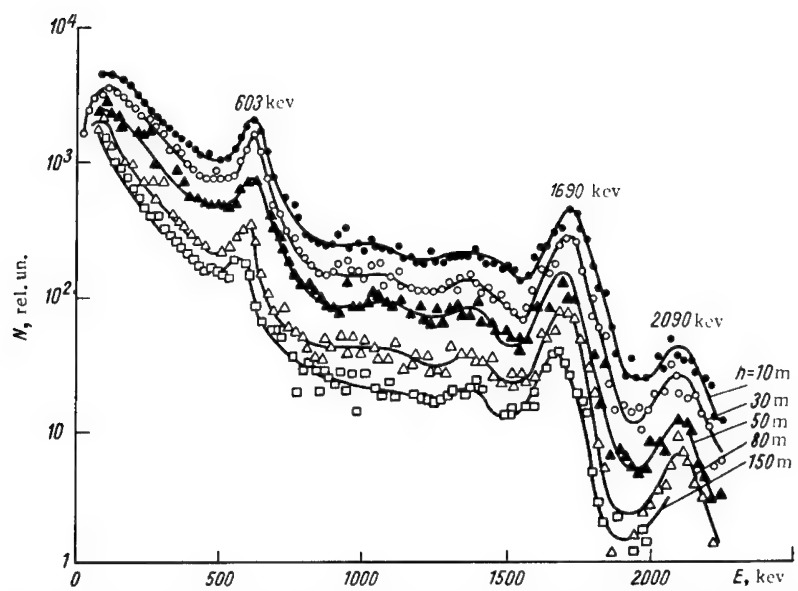


FIGURE 41. Measured gamma-emission spectra over test area simulating Sb¹²⁴ contamination of ground (isotropic detector).

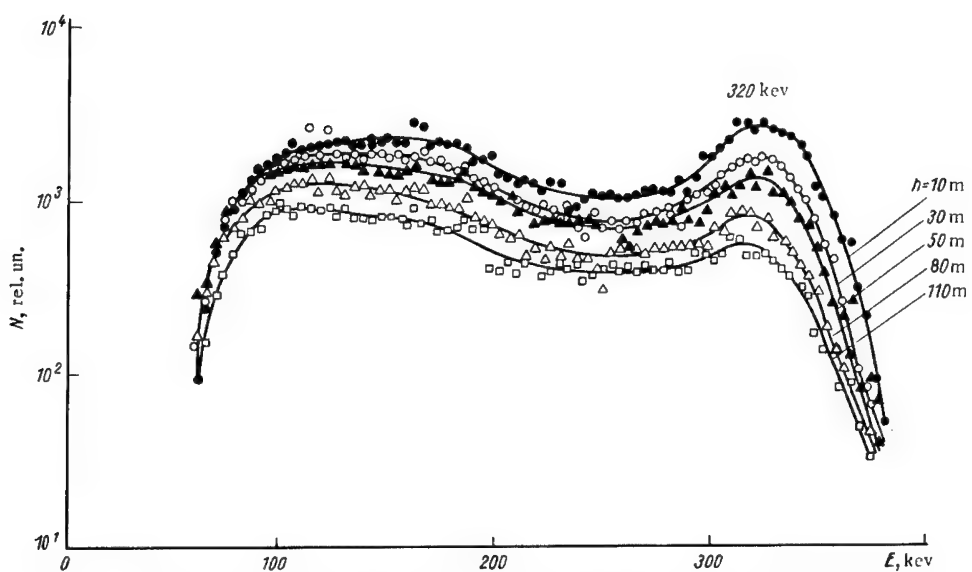


FIGURE 42. Measured gamma-emission spectra over test area simulating Cr⁵¹ contamination of ground (isotropic detector).

The foregoing must be taken into account when analyzing and interpreting spectra obtained using isotropic scintillation detectors with NaI(Tl) crystals 100×100 mm and 70×70 mm in size, above test areas with Co⁶⁰, Sb¹²⁴, and Cr⁵¹ sources. Some such spectra are shown in Figures 40 through 42. The gamma-emission spectra over the Co⁶⁰ test area are plotted in Figure 40 (for h from 1 to 250 m), the spectra over the Sb¹²⁴ test area are plotted in Figure 41 (for h from 10 to 150 m), and the spectra over the Cr⁵¹ test area are plotted in Figure 42 (for h from 10 to 110 m); for all these a 100×100 mm crystal was used.

The lines of Co⁶⁰ (1.17 and 1.33 Mev), Sb¹²⁴ (0.603, 1.69, and 2.09 Mev), and Cr⁵¹ (0.32 Mev) show up quite clearly on the spectra obtained at different heights above the three test areas. At higher altitudes the peaks corresponding to the unscattered radiation are smaller, and there is a slight shift of the peaks toward lower energies (or, more precisely, toward lower amplitudes). The scattered radiation makes a very significant contribution on all the spectra. Above heights of 30 to 50 m, the shape of the part of the spectrum corresponding to the scattered radiation changes only very slightly, but the contribution of the scattered radiation to the total increases monotonically with height. The maximum of the scattered-radiation peak lies in the vicinity of 80 kev. These data show satisfactory agreement with the results of similar measurements made for Co⁶⁰ in /176, 177/.

TABLE 18. Diameters (in m) of portions of earth's surface included in zone of direct detector visibility

| Half-angle of cone op- ening, deg | Height, m | | | | | |
|---|-----------|----|-----|-----|-----|-----|
| | 1 | 10 | 30 | 70 | 150 | 200 |
| 15 | 0.5 | 5 | 15 | 35 | 75 | 100 |
| 30 | 1.2 | 12 | 36 | 84 | 180 | 240 |
| 60 | 3.4 | 34 | 102 | 238 | 510 | 680 |

The spectral-angular distribution of gamma radiation above an isotropic plane source was studied for the same test areas using a detector with an NaI(Tl) crystal 70×70 mm in size. This detector was placed inside a special steel shield having detachable conical collars with their axes oriented perpendicular to the ground (see Figure 39). Using this shield, it was possible to study the gamma radiation arriving at angles θ of 15, 30, 45, 60, 75, and 90° (half-angles of opening).

All the remarks made with respect to studying the spectral composition of radiations using isotropic detectors essentially pertain to shielded detectors as well. Fringe effects and the effects of the finiteness of the test areas are less important during spectral-angular measurements, while the nonuniformity of the contamination is especially significant (in such measurements the radiation is collected from a smaller area).

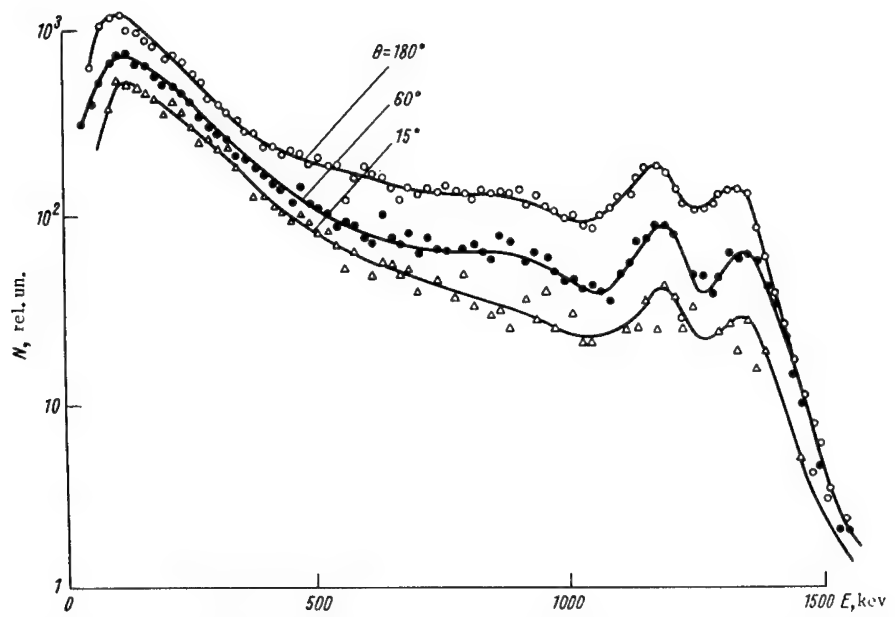


FIGURE 43. Measured gamma-emission spectra over Co^{60} area at height of 30 m (shielded detector).

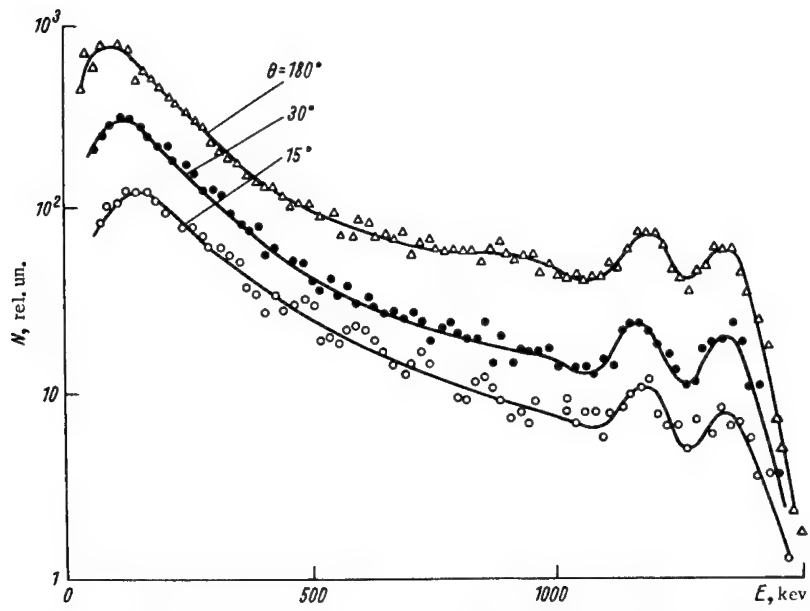


FIGURE 44. Measured gamma-emission spectra over Co^{60} area at height of 70 m (shielded detector).

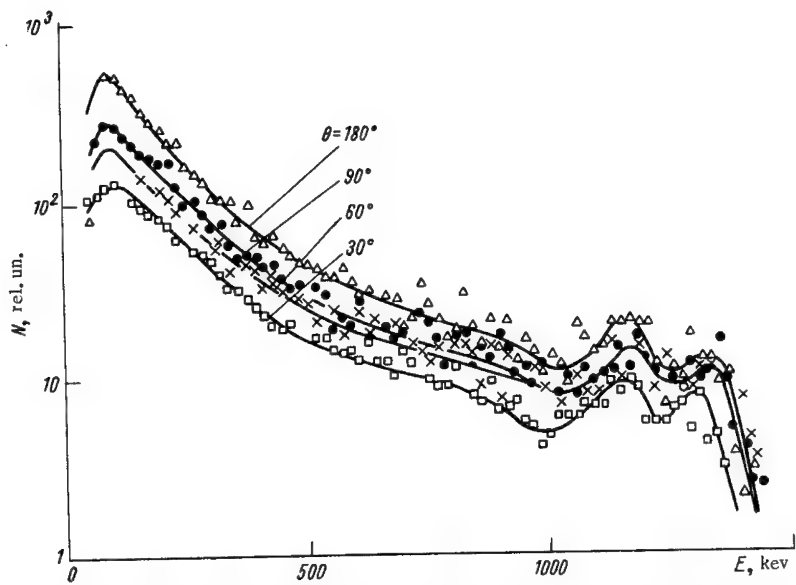


FIGURE 45. Measured gamma-emission spectra over Co^{60} area at height of 150 m (shielded detector).

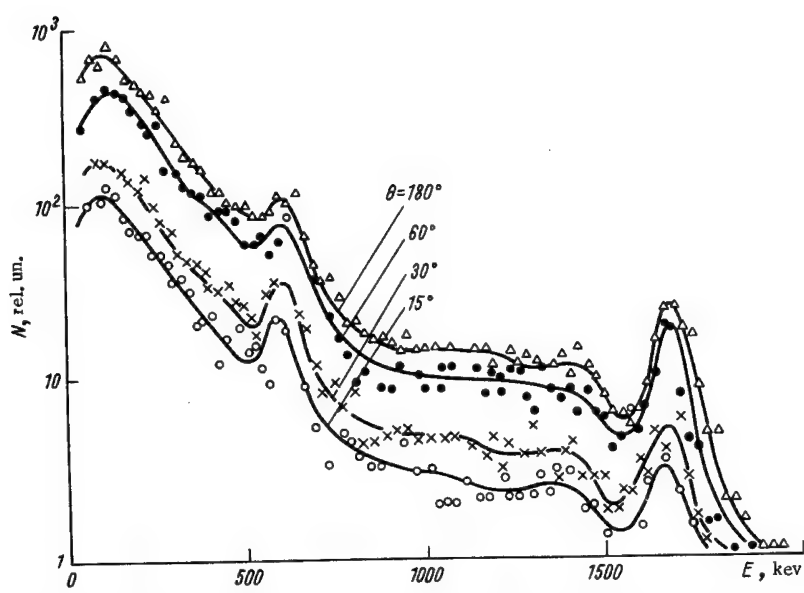


FIGURE 46. Measured gamma-emission spectra over Sb^{124} area at height of 70 m (shielded detector).

Table 18 lists the diameters of the portions of the earth's surface included in the zone of direct visibility of the detector for different opening angles of the shield and for different measurement heights. The measurements were made over a wide range of angles and heights in order to ensure that more than four point sources would be within the zone of direct visibility in the field plane simultaneously. Thus the intensity of unscattered radiation did not fluctuate by more than 30% as the number of sources within the angle of view varied (the case of four point sources corresponds to an angle of 60° for flight at a height $H = 10\text{ m}$ above a Co^{60} field).

The intensity of the radiation incident upon the detector, during the measurements with a shield, was low. Accordingly, the background radiation was carefully taken into account. This background was due to contamination by the helicopter instrument panel and also due to the emission of natural radioactive isotopes in the ground and air. The intensity and spectrum of the background radiation were obtained for all the angles and heights studied.

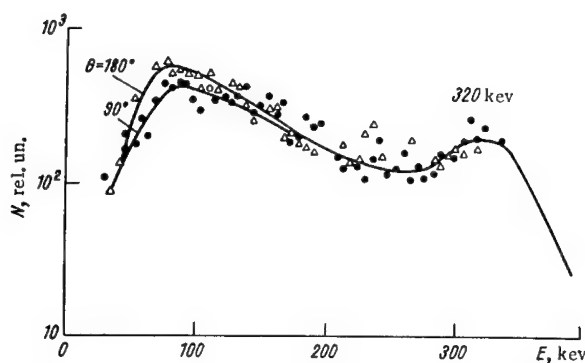


FIGURE 47. Measured gamma-emission spectra over Cr^{51} area at height of 70 m (shielded detector).

Figures 43 through 47 show the differential spectra for measurements with different solid angles, at various heights above the test areas (excluding background). The data in Figures 43 through 45 show the spectral-angular distributions of gamma quanta over the Co^{60} area at heights of 30 m (for angles of opening $\theta = 15, 60$, and 180°), * 70 m ($\theta = 15, 30$ and 180°), and 150 m ($\theta = 30, 60, 90$, and 180°). Figure 46 shows the spectra above the Sb^{154} area at a height of 70 m ($\theta = 15, 30, 60$, and 180°). Finally, Figure 47 shows the spectra above the Cr^{51} area at a height of 70 m ($\theta = 90$ and 180°). It is evident from these figures that as θ is reduced the contribution of the scattered radiation becomes somewhat less, while at the same time the peaks of the direct radiation become more pronounced.

The effect of microrelief on the intensity and the shape of the spectrum was studied using a shielded detector with an NaI (Tl) crystal 70 × 70 mm in size, at heights $H = 1, 10$, and 30 m above the Co^{60} test area, and at

* $\theta = 180^\circ$ corresponds to measurement without a shield.

heights of 10 and 30 m above the Cr⁵¹ test area for two source positions. These measurements showed that the microrelief has no effect at heights ≥ 10 m.

11. Interpretation of experimental data obtained with artificial model

During the recording of gamma-ray quanta with energies of interest, various processes take place which affect the shape of the spectrum. Because of these processes (photoelectric effect, Compton interaction, pair production), the measured spectrum will have a shape differing from that of the true spectrum at the point of measurement.

The spectrum measured with the instruments is known /147/ to be related in a complex way to the spectrum of the gamma radiation incident upon the crystal. The observed pulse-amplitude distribution may be written as

$$N(E', \mu_0 r) = \int_0^{E_0} k(E', E) J(\mu_0 r, E_0, E) dE, \quad (75)$$

where μ_0 is the attenuation coefficient for gamma radiation with an energy E_0 in the medium (air); $k(E', E)$ is the response function for the detector; $J(\mu_0 r, E_0, E)$ is the spectral function of the incident radiation at a distance r from the source; and $k(E', E)dE$ is the probability that gamma radiation of energy E will produce a pulse with an amplitude between E' and $E'+dE'$ (the amplitudes being expressed in units of energy). By solving (75) for $J(\mu_0 r, E_0, E)$, it is possible to use the measured spectrum to reconstruct the spectral composition of the radiation incident upon the crystal.

It is also known (provided secondary processes in the detector are neglected) that

$$\begin{aligned} k(E', E) = & \int_0^{\infty} g(E', \xi) \left[\frac{\mu_c(E)}{\mu_t(E)} P(\xi, E) + \right. \\ & \left. + \frac{\mu_p(E)}{\mu_t(E)} \delta(\xi - E) \right] \epsilon(E) d\xi. \end{aligned} \quad (76)$$

In this formula $g(E', \xi)$ is the Gaussian distribution, so normalized that its integral is equal to unity; $\mu_c(E)$, $\mu_p(E)$, and $\mu_t(E)$ are the Compton, photoelectric, and total absorption coefficients for gamma-ray quanta of energy E in the crystal; $P(\xi, E)$ is the probability that, after interacting with a gamma-ray quantum of energy E , an electron will acquire an energy between ξ and $\xi+d\xi$; δ is the delta function; and $\epsilon(E)$ is the detector effectiveness at an energy E (in this equation the effect of pair production is neglected).

If the effects of multiple scattering in the crystal are taken into account, then certain changes must be made inside the square brackets in (76): the first term must be replaced by $L(\xi, E)$, the probability that a gamma-ray

quantum of energy E will impart an energy between ξ and $\xi + d\xi$; and the second term must be replaced by $p(\xi, E)\delta(\xi - E)$, where $p(\xi, E)$ is the probability that a gamma-ray quantum of energy E will be picked up by the detector.

Equation (75) can be rewritten approximately in the form of a matrix equation:

$$N(E_i, \mu_0 r) = \Delta E \sum_{j=1}^m R(E_i, E_j) f(E_j, \mu_0 r), \quad (77)$$

where $E_{j+1} - E_j = \Delta E \equiv \Delta E$, and $f(E_j, \mu_0 r)$ is the value of J in the interval ΔE . Similarly,

$$E_{i+1} - E_i = \Delta E_i \equiv \Delta E.$$

Matrix $R(E_i, E_j)$ can be found from (76) by replacing E' and E by E_i and E_j , respectively, so that $R(E_i, E_j)$ becomes a square matrix. Then,

$$f(E_j, \mu_0 r) = \Delta E \sum_{i=1}^m N(E_i, \mu_0 r) R^{-1}(E_i, E_j), \quad (78)$$

where $R^{-1}(E_i, E_j)$ is the inverse of matrix $R(E_i, E_j)$. The desired function in the energy range $E_j \pm \frac{\Delta E}{2}$ is

$$J(\mu_0 r, E_0, E) = \frac{f(E_j, \mu_0 r)}{\Delta E}.$$

In practice, the approximate determination of $f(E_j, \mu_0 r)$ involves a solution of m linear equations with m unknowns.

The function $R(E_i, E_j)$ is expressed as a triangular numerical matrix, in such a way that its horizontal row is the distribution of pulses (divided into $E_j/\Delta E$ intervals) caused by gamma radiation of energy $E_j \pm \frac{\Delta E}{2}$. The matrix is normalized for the effectiveness of the crystal, that is, the sum of the elements of each matrix row is $e(E_j)$. The matrix is constructed using the results of measurements with monochromatic emission sources and of calculations made, for example, by the method of trial and error.

A matrix similar to the one described in /182/ was used to analyze the measured spectra obtained over the test areas. To make the analysis more convenient, coordinates of E' were used in this matrix. The direct matrix is given in Table 19 (up to $E = 2.89$ Mev, that is, $(1.7)^2$). This matrix was constructed for an NaI (Tl) crystal 70×70 mm in size. The results of measurements for the following sources were used to construct the matrix: Ce^{141} ($E = 0.145$ Mev); Hg^{203} (0.28 Mev); Cr^{51} (0.32 Mev); Ce^{137} (0.66 Mev); Nb^{95} (0.765 Mev); Mn^{54} (0.84 Mev); Zn^{95} (1.12 Mev); Co^{60} ($E_{av} = 1.25$ Mev); Na^{24} (1.38 and 2.76 Mev). In addition, individual gamma-emission spectra for calibrated isotopes /183/ were used.

During the measurements sources were placed from 10 to 20 cm from the end face of the crystal, on the crystal axis. In contrast to the similar procedure described in /182/, the sources and crystal were not shielded. It was assumed that in this way the measurement conditions would be close to those obtaining during the measurements over the test areas (that is,

scattering by the helicopter body was taken into account to some extent). Accordingly, the sum of each row of our matrix was somewhat larger than $e(E_j)$, since the diagonal elements of the matrix were normalized for the photoelectric effect. The inverse of the matrix described above is given in Table 20.

TABLE 19. Direct matrix for spectrometer with NaI (Tl) crystal 70 x 70 mm in size*

| $E_i^{1/2}$, Mev $^{1/2}$ | 0.1 | 0.2 | 0.3 | 0.4 | 0.5 | 0.6 | 0.7 | 0.8 | 0.9 | 1.0 | 1.1 | 1.2 | 1.3 | 1.4 |
|----------------------------|------|------|-----|-----|-----|-----|-----|-----|-----|-----|-----|-----|-----|-----|
| $E_j^{1/2}$, Mev $^{1/2}$ | | | | | | | | | | | | | | |
| 0.1 | 1000 | | | | | | | | | | | | | |
| 0.2 | 0 | 1000 | | | | | | | | | | | | |
| 0.3 | 12 | 38 | 990 | | | | | | | | | | | |
| 0.4 | 14 | 43 | 70 | 960 | | | | | | | | | | |
| 0.5 | 15 | 47 | 70 | 113 | 920 | | | | | | | | | |
| 0.6 | 15 | 46 | 74 | 108 | 220 | 866 | | | | | | | | |
| 0.7 | 15 | 44 | 73 | 104 | 135 | 163 | 682 | | | | | | | |
| 0.8 | 14 | 41 | 69 | 101 | 126 | 136 | 118 | 535 | | | | | | |
| 0.9 | 13 | 39 | 64 | 91 | 120 | 126 | 130 | 88 | 412 | | | | | |
| 1.0 | 11 | 33 | 54 | 75 | 99 | 114 | 111 | 119 | 24 | 382 | | | | |
| 1.1 | 9 | 28 | 44 | 59 | 75 | 93 | 94 | 96 | 114 | 89 | 308 | | | |
| 1.2 | 8 | 22 | 37 | 50 | 65 | 77 | 78 | 83 | 92 | 116 | 88 | 269 | | |
| 1.3 | 7 | 19 | 33 | 51 | 56 | 67 | 79 | 79 | 76 | 93 | 114 | 97 | 239 | |
| 1.4 | 6 | 19 | 31 | 43 | 52 | 62 | 72 | 79 | 81 | 75 | 90 | 114 | 101 | 209 |

* All figures in table are to be multiplied by 10^{-3} .

TABLE 20. Inverse matrix for spectrometer with NaI (Tl) crystal 70 x 70 mm in size*

| $E_i^{1/2}$, Mev $^{1/2}$ | 0.1 | 0.2 | 0.3 | 0.4 | 0.5 | 0.6 | 0.7 | 0.8 | 0.9 | 1.0 | 1.1 | 1.2 | 1.3 | 1. |
|----------------------------|------|------|------|------|------|------|------|------|------|------|-------|-------|-------|------|
| $E_j^{1/2}$, Mev $^{1/2}$ | | | | | | | | | | | | | | |
| 0.1 | 1000 | | | | | | | | | | | | | |
| 0.2 | 0 | 1000 | | | | | | | | | | | | |
| 0.3 | -12 | -38 | 1010 | | | | | | | | | | | |
| 0.4 | -14 | -42 | -74 | 1042 | | | | | | | | | | |
| 0.5 | -14 | -43 | -68 | -128 | 1087 | | | | | | | | | |
| 0.6 | -11 | -34 | -60 | -98 | -276 | 1155 | | | | | | | | |
| 0.7 | -13 | -37 | -69 | -110 | -150 | -276 | 1470 | | | | | | | |
| 0.8 | -13 | -36 | -70 | -118 | -153 | -232 | -325 | 1870 | | | | | | |
| 0.9 | -12 | -37 | -66 | -103 | -152 | -216 | -395 | -401 | 2430 | | | | | |
| 1.0 | -9 | -27 | -46 | -67 | -99 | -179 | -301 | -558 | -149 | 2620 | | | | |
| 1.1 | -3 | -13 | -15 | -11 | -3 | -61 | -114 | -272 | -854 | -756 | 3250 | | | |
| 1.2 | -2 | +2 | -2 | +1 | 0 | -9 | -21 | -110 | -504 | -883 | -1063 | 3720 | | |
| 1.3 | 0 | +6 | +2 | -26 | +12 | +14 | -73 | -100 | -104 | -302 | -1118 | -1512 | 4180 | |
| 1.4 | 2 | -4 | -1 | +10 | +11 | +12 | -27 | -127 | -196 | +14 | -276 | -1295 | -2020 | 4780 |

* All figures in table are to be multiplied by 10^{-3} .

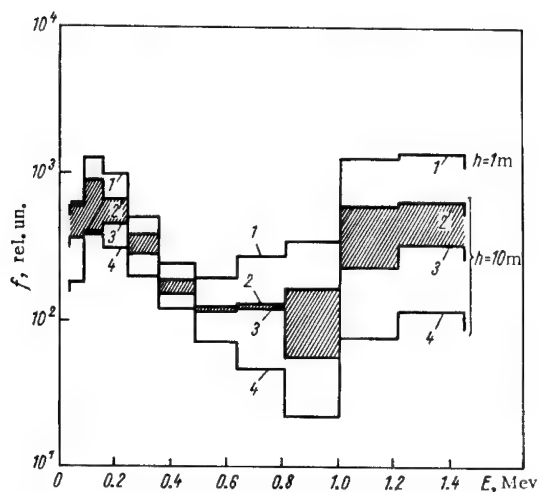


FIGURE 48. True gamma-emission spectrum above Co^{60}
test area: at height of 1 m, with measuring angle $\theta = 180^\circ$
(curve 1); at height of 10 m, with measuring angles
 $\theta = 30^\circ$ (curve 4), 60° (curve 3), and 180° (curve 2).
Shaded region shows difference for transition from $\theta = 60^\circ$
to $\theta = 180^\circ$.

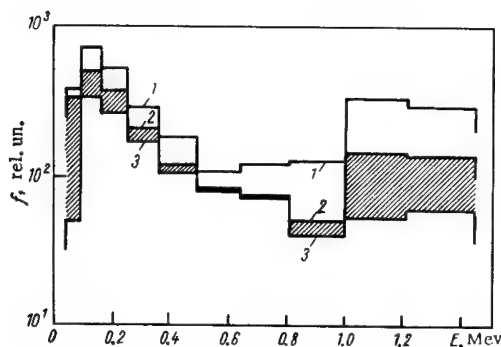


FIGURE 49. True gamma-emission spectrum above Co^{60}
test area at height of 30 m, with measuring angles
 $\theta = 180^\circ$ (curve 1), 60° (curve 2), and 15° (curve 3).
Shaded region shows difference for transition from
 $\theta = 15^\circ$ to $\theta = 60^\circ$.

The experimentally measured spectra were analyzed as follows. First, the spectrum was broken up into the same intervals as the matrix. Then, the area under the curve S_i was determined for each interval (in pulses per second) and multiplied successively by all the numbers in the j th column of the inverse matrix. The sum of the products was equal to the number of gamma-ray quanta in this energy interval which were incident on the crystal.

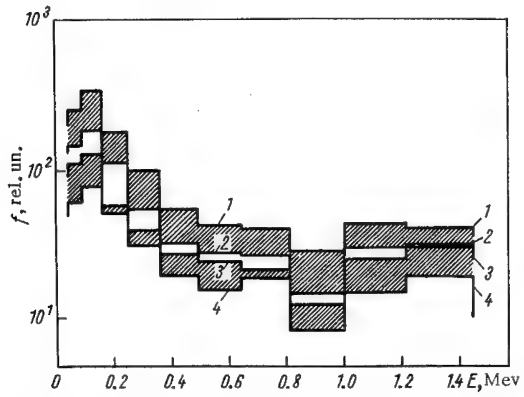


FIGURE 50. True gamma-emission spectrum above Co^{60} test area at height of 70 m, with measuring angles $\theta = 180^\circ$ (curve 1), 60° (curve 2), 30° (curve 3), and 15° (curve 4). Shaded region shows difference for transition from $\theta = 15^\circ$ to $\theta = 30^\circ$ and from $\theta = 60^\circ$ to $\theta = 180^\circ$.

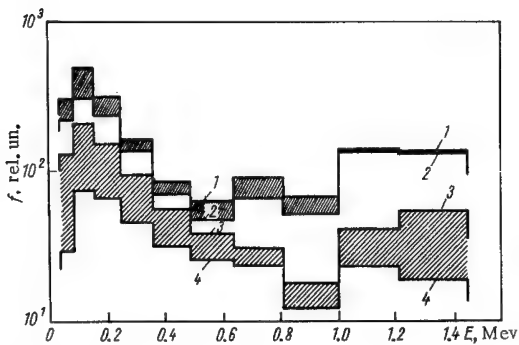


FIGURE 51. True gamma-emission spectrum above Co^{60} test area at height of 150 m, with measuring angles of $\theta = 180^\circ$ (curve 1), 90° (curve 2), 60° (curve 3), and 30° (curve 4). Shaded region shows difference for transition from $\theta = 30^\circ$ to $\theta = 60^\circ$ and from $\theta = 90^\circ$ to $\theta = 180^\circ$.

Figures 48 through 51 show the true gamma-emission spectra,* obtained in the above-described way, over the test area with the Co^{60} sources; different curves correspond to different heights. Figure 48 gives the spectra at heights of 1 m ($\theta = 180^\circ$, curve 1) and 10 m ($\theta = 15, 60$, and 180° ; curves 4, 3, and 2, respectively); Figure 49, for a height of 30 m

* The figures give the rate of arrival f of gamma-ray quanta at the point of measurement, as a function of the energy of the radiation (the diagrams are normalized for a unit interval of energy).

($\theta = 15, 60$, and 180°); Figure 50, for a height of 70 m ($\theta = 15, 30, 60$, and 180°); Figure 51, for a height of 150 m ($\theta = 30, 60, 90$, and 180°).

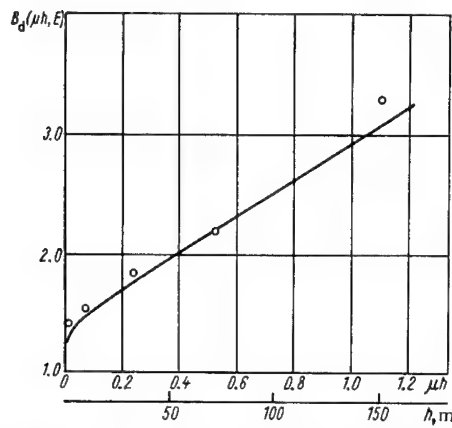


FIGURE 52. Dosage accumulation factor over Co⁶⁰ test area, as function of height.

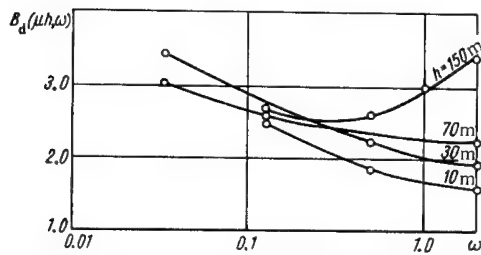


FIGURE 53. Dosage accumulation factor for radiation arriving at angle $\omega = 1 - \cos \theta$ (Co⁶⁰ test area) for various heights, as function of angle ω .

It is evident from the figures that, as the measuring angle is increased, the contributions of both the unscattered component and the scattered radiation increase by a small amount. When the flight altitude is increased, the contribution of the scattered radiation becomes greater.

Figure 52 shows the dosage accumulation factor $B_d (\mu_0 h)$ as a function of height over the Co⁶⁰ test area. The solid curve was computed using the formula

$$B_d(\mu_0 h) = \frac{G(\mu_0 h)}{E_1(\mu_0 h)}$$

(cf. formula (56)), and the data points give the values of $B_d(\mu_0 h)$ obtained using the formula

$$B_d(\mu_0 h) = \frac{\int_0^{E_0} \sigma_a(E) [J_0(\mu_0 h, E_0) + J_s(\mu_0 h, E_0, E)] dE}{\sigma_a(E_0) J_0(\mu_0 h, E_0) dE},$$

where J_0 and J_s are the energy intensities of the unscattered and scattered gamma radiations, respectively, at a height h . These intensities are determined on the basis of the experimentally found true spectra for $\theta = 180^\circ$ (Figures 48 through 51). There is good agreement between the theoretical and experimental results, as Figure 52 shows.

Figure 53 shows $B_d(\mu h, \omega)$ for Co^{60} (at $h = 10, 30, 70$, and 150m), as a function of $\omega = 1 - \cos \theta$. These curves were obtained using the same formula, but with J_0 and J replaced by the energy intensities of the unscattered and scattered radiations, $J_0(\mu_0 h, E_0, \omega)$ and $J'(\mu_0 h, E_0, E, \omega)$, arriving at an angle ω and determined on the basis of the measured spectra (Figures 48 through 51) for $\theta = 15, 30, 60, 90$, and 180° . For heights of 10 to 70m the error in the values obtained is placed at 30%, and for a height of 150m it is somewhat higher.

The data in this section serve as a supplement to the information on the characteristics of the gamma-emission field of an isotropic plane source, especially as regards the angular distribution of the gamma radiation, for which information is very limited.

Chapter III

GAMMA FIELDS OVER CONTAMINATED REGIONS

The gamma-ray field above a region contaminated with radioactive isotopes differs from the field of an idealized isotropic plane source in an infinite air medium. This difference is caused by the following factors /163/:

- 1) the effect of the underlying-surface material, which differs from air in its density and atomic makeup;
- 2) the presence of irregularities in the underlying surface;
- 3) the presence of a vegetation cover;
- 4) variations of the air density with temperature, pressure, and humidity under actual conditions. Let us now consider the effects which these factors have on the gamma-ray field over a contaminated locality under natural conditions. The source is assumed to be a surface source.

12. Effect of actual underlying surface

In the preceding chapter it was noted that the gamma-emission field of a plane source is not distorted by an underlying surface with a high density and with Z_{eff} close to that of water or air. For instance, the gamma-ray field over an ice surface contaminated with radioactive products is identical to the field for the idealized model.

However, as a rule, radioactive products fall out onto land, which has an effective atomic number somewhat different from Z_{eff} for water or air. Soil with an average composition of elements (Clarke composition) has $Z_{\text{eff}} \approx 13.0$, a value close to that of aluminum /167/. The atomic number of ordinary concrete /184/ is around 13.4, that is, it is practically the same as Z_{eff} for aluminum and soil.*

Data exist which indicate that a difference in the atomic number of the underlying-surface material (be it land or water) exerts practically no effect on the structure of the gamma-ray field. These data are as follows:

- a) the curves of the spectral distribution $J(E_0, E)$ of the scattered gamma radiation are practically identical for aluminum and water, the initial energies being the same /141/;
- b) in the case of an isotropic point source the energy albedos (for energies from 0.2 to 2.0 Mev) for water and concrete are very close in value (difference less than 15%) /184/. It is also noted in /184/ that the dosage albedo and energy albedo have absolute values which are almost the same (difference less than 10%);

* Here the values of Z_{eff} are for $E < 2.5$ to 3.0 Mev /12/.

c) experiments /153-155/ made with a point source at an "earth-air" interface confirm the calculations in /156/ for a "water-air" interface.

To gain more evidence, we studied the field of an isotropic point source (Co^{60} , $E_{av}=1.25 \text{ Mev}$) above water, soil, and concrete /163/. The fields were measured with a roentgen meter having a low "relative-response curve."* The height above the water or ground (or concrete) was $h=1$ to 10m, for distances R up to 120m and $l=0$ (see formula (50)).

In order to eliminate the effect of ground microroughnesses, source heights r from 10 to 15 cm were used (in the calculations it could be assumed that $r=0$), while R varied from 0 to 120m for water, from 0 to 40m for soil, and from 40 to 300m for concrete. For the measurements with R from 0 to 10m, the source activity was about 13 mcuries; for R from 10 to 40m, it was about 80 mcuries; for R above 40m, it was 1.2 curies (Co^{60}).

When analyzing the experimental data, we took into account the points mentioned earlier and assumed that Z_{eff} is the same for soil and concrete /167, 184/. Thus our task was to find the difference between the effects on the gamma-ray field of an underlying water surface and a soil or concrete surface.

Table 21 lists some dose rates measured over water, soil, and concrete. The ratio $P_{c,s}/P_{H_2O}$ of the dose rate over soil (concrete) to the dose rate over water is plotted in Figure 54 as a function of distance R , for h from 1 to 10m, for a point source. Within the limits of error of the measurements (about 10%), this ratio can be taken as unity, for the indicated h .

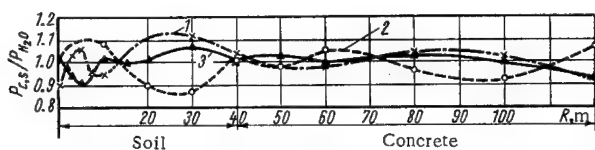


FIGURE 54. Ratio of dose rates (Co^{60} point source) over soil (concrete) and water, as function of distance:

1) $h=1 \text{ m}$; 2) $h=5 \text{ m}$; 3) $h=10 \text{ m}$.

Using Table 21 and the experimental curves in Figure 54, we can now find the ratio of the dose rates over isotropic plane sources located above soil (concrete) and water, using the formula

$$\frac{P_{c,s}^s}{P_{H_2O}^s} = \frac{\int_0^\infty [P_{c,s}(R)] R dR}{\int_0^\infty [P_{H_2O}(R)] R dR}. \quad (79)$$

* [Figure 65 below shows the relative-response curves for various types of detectors.]

TABLE 21. Measured dose rates, in $\mu\text{r/hr}$, at different heights h above water, soil, and concrete surfaces for various distances R from source

| R , m | $h = 1.0$ m | | | $h = 5.0$ m | | | $h = 10$ m | | | Statistical error of meas- urements, % |
|---------|-------------|--------|----------|-------------|----------|-------|------------|-------|------|--|
| | soil | water | soil | water | soil | water | soil | water | soil | |
| 0 | 13,900 | 14,300 | 700 | 755 | — | — | — | — | — | 3 |
| 2.0 | 3,200 | 3,260 | 600 | 600 | — | — | — | — | — | — |
| 5.0 | 310 | 760 | 360 | 390 | — | — | — | — | — | 4 |
| 10 | 190 | 180 | 150 | 145 | — | — | — | — | — | — |
| 10 | 1,020 | 1,150 | 920* | 910 | 640 | 640 | 590 | 590 | — | — |
| 20 | 270 | 245 | 280 | 280 | 210 | 210 | 230 | 230 | 8 | 8 |
| 30 | 123 | 110 | 125 | 120 | 105 | 105 | 120 | 120 | — | — |
| 40 | 68* | 58 | 68* | 57 | 60* | 60* | 60 | 60 | — | — |
| | | | concrete | water | concrete | water | concrete | water | | |
| 40 | 975 | 910 | 975 | 965 | 955 | 965 | 965 | 965 | — | — |
| 50 | 565 | 580 | 605 | 580 | 565 | 580 | 580 | 580 | — | — |
| 60 | 330 | 335 | 350 | 352 | 385 | 385 | 365 | 365 | — | — |
| 70 | 255* | 270 | 270* | 275 | 265* | 265* | 280 | 280 | — | — |
| 80 | 195 | 185 | 195 | 185 | 195 | 195 | 200 | 200 | — | — |
| 90* | 135 | 135 | 140 | 140 | 145 | 145 | 155 | 155 | 12 | 12 |
| 100 | 105 | 105 | 110 | 110 | 105 | 105 | 120 | 120 | — | — |
| 110* | 75 | 85 | 80 | 85 | 90 | 90 | 90 | 90 | — | — |
| 120 | 65 | 70 | 65 | 70 | 75 | 75 | 70 | 70 | 15 | 15 |

* Obtained by interpolation.

We insert numerical values from Table 21 into (79) and replace the upper integration limit by 120 m, since for $E = 1.25$ Mev and $h = 5$ m about 80% of the dose rate (from an infinite source) comes from within a circle 120 m in radius (for $h = 1$ m, this percentage is more than 85%). Accordingly, we obtain

$$P_{c,s}^s/P_{H_2O}^s = 0.97 \text{ (for } h = 10 \text{ m)}$$

$$P_{c,s}^s/P_{H_2O}^s = 0.93 \text{ (for } h = 5 \text{ m)}$$

$$P_{c,s}^s/P_{H_2O}^s = 0.96 \text{ (for } h = 1 \text{ m)}$$

Thus, to an accuracy within the limits of measurement error, this ratio can be taken as unity.

Consequently, theoretical calculations and simulation experiments both show that the difference between the atomic numbers of soil (concrete), on the one hand, and water, on the other, has essentially no effect on the gamma-ray dose rate in air from an isotropic plane source located at the interface between these media.

Real contamination cannot be attributed to an ideally smooth plane source, since the earth's surface always has irregularities in it (microrelief), and these may affect the structure of the gamma-ray field. Let us consider the microrelief-caused dose-rate variations at heights where the effects of individual irregularities may be neglected (that is, at heights more than four or five times greater than the heights of individual microrelief protrusions).

Microrelief here refers to nonuniformity of the surface, the individual relief elements only taking up very small spaces (from tenths of a m^2 to tens of m^2) and having heights less than a meter /185/ (frequently only from 5 to 20 cm). Some types of microrelief are: small prominences, mounds, hillocks, caved-in areas, small shallow depressions, minute hollows, shallow water holes, etc.

The effects which irregularities in the earth's surface have on the gamma-ray field of a radioactive fallout were discussed in /4, 108/, and /155, 186, 187/ are devoted to this subject. To calculate the dose rate in an open field, it was recommended in /108/ (without justification) to multiply the dose rate for an ideal surface by 0.7. In the opinion of the authors of /4/, the soil unevenness can be simulated satisfactorily by means of concretic protuberances with triangular cross sections of equal height and base. Calculations showed that for a height of 1 m above the ground the correction factors, taking into account shielding by such protuberances (with base lengths from 0 to 10 cm), varied considerably, from 1 to 4.34. However, since it was not stipulated in /4/ which form of microrelief corresponds to a given value of the correction factor, these factors cannot be utilized in practice.

In /155, 186/ we described a means of evaluating quantitatively the effect of microrelief on the dose rate over a surface source of gamma

rays. The effect of microrelief on gamma-ray propagation in the atmospheric layer near the earth was assumed to be mainly due to shielding of the radiation by small soil protuberances. Thus the radiation arriving at the observation point from various regions, which in the following will be called "shaded" regions, is interfered with.

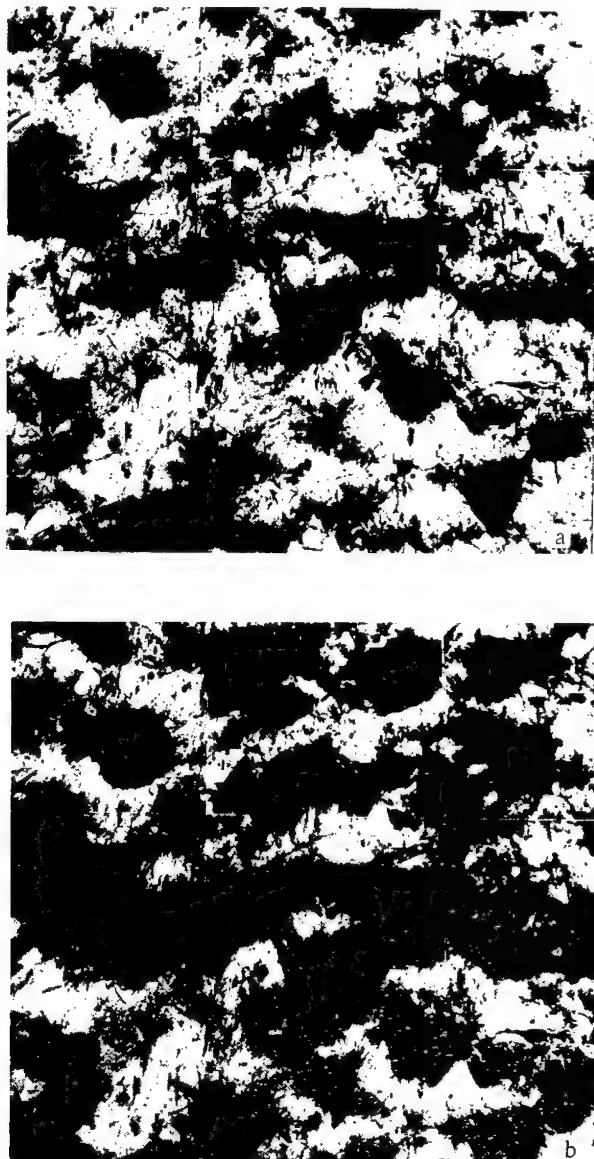


FIGURE 55. Photos of microrelief in swampy meadowland, for illumination angles from 15 to 20° (a) and from 10 to 15° (b).

Let us assume that the sizes of the "exposed" and "shaded" regions are equal to the area of their projections onto a plane at ground level. An area element dS located a distance R from the projection of the observation point is considered. We designate as β the angle between the plane of the earth's surface and the line joining area dS and the observation point, that is, $\beta = \cot^{-1} R/h$, where h is the height of the observation point.

The part of area dS which is shaded by microprotuberances of the earth's surface is called dS_s , and the ratio dS_s/dS is designated as α ; the exposed part is $\delta = 1 - \alpha$. In order to obtain a quantitative evaluation of the microrelief effect on gamma-ray propagation, let us determine the dependence of α on angle β . This dependence can be determined by means of a direct study of the given type of microrelief.

Different types of microrelief, in various regions of the Soviet Union, were studied /186/:

- a) level, grassy, unworked meadowland (two regions with combined area of about $10,000 \text{ m}^2$) in the Arkhangel'sk district;
- b) a level forest glade (two regions with area of more than 1000 m^2) in the Yaroslavl district;
- c) a swampy meadow (area of several tens of m^2) in the Yaroslavl district;
- d) a region of arid steppe (area of more than 5000 m^2) in Kazakhstan;
- e) plowed field at the period of ripening and harvesting of grain (area of about 1000 m^2) in the Yaroslavl district.

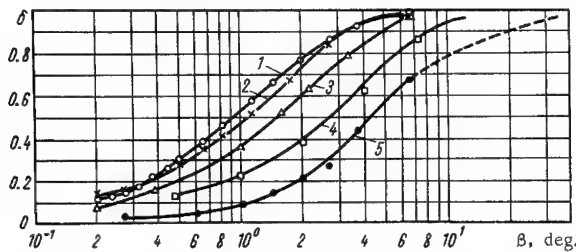


FIGURE 56. Fraction δ of exposed part of test area, as function of angle of illumination for various types of microrelief:

- 1) meadow; 2) glade (very even parts); 3) very even part of arid steppe; 4) arid steppe; 5) plowed field.

The microrelief studies in these districts were carried out in two ways: by careful leveling and by systematic photography from heights of 2 to 2.5 m at night, with illumination from a point source of light at an angle β . The size of the region and the position of the light source were so selected that the variation of β in the region was small. The dependence $\alpha(\beta)$ was established from the leveling data. Function $\alpha(\beta)$ was also determined by calculating the area of the shaded regions on the photographs for the various kinds of microrelief. The results obtained from the leveling and the photography agreed well with one another.

Photographs of part of a swampy meadow where the vegetation cover has been destroyed are presented in Figure 55. The angles of illumination are from 15 to 20° in Figure 55a, and from 10 to 15° in Figure 55b. These photos were taken from a height of 2 m. It is easy to determine from the photo that in the first case $\alpha \approx 0.35$. Function $\delta(\beta)$ is plotted in Figure 56 for various kinds of microrelief.

It can be shown that for a surface source the dose rate dP^s from an area element dS' , visible from the observation point at the same solid angle as dS and lying at an angle ω to the horizontal, will be equal to dP^s , provided the variation of the distance from the observation point to the test area may be neglected (dP^s is the dose rate from a test area dS lying in the horizontal plane).

The dose rate $dP_{\text{mcr}}^s(\beta)$ from an area element dS of an isotropic plane source, in the presence of microrelief, may be expressed as

$$dP_{\text{mcr}}^s(\beta) = \delta(\beta) dP_0^s + dP_{\text{scat}}^s, \quad (80)$$

where dP_0^s and dP_{scat}^s are the contribution to the total dose rate dP^s of the unscattered and scattered radiation. Here

$$dP_{\text{scat}}^s = dP^s - \frac{k\sigma_0 e^{-\mu r} dS}{4\pi r^2} \quad (81)$$

(notation same as in formula (51)).

The factor taking into account the effect of microrelief on the emission of area element dS (or of a point source located in this area) will be designated as $\psi^*(\beta)$:

$$\psi^*(\beta) = \frac{dP_{\text{mcr}}^s(\beta)}{dP^s}. \quad (82)$$

Now, from formulas (51) and (80) through (82), taking into account the influence of the underlying surface, we find that

$$\psi^*(\beta) = 1 - \frac{\alpha(\beta)}{K_u B_d(r, E)}. \quad (83)$$

A similar method is described in /187/, where a correction function $F_r(\cos \theta)$ is introduced ($\theta = \frac{\pi}{2} - \beta$) to allow for the effect of the microrelief.

However, no particulars concerning the microrelief and no numerical values of $F_r(\cos \theta)$ are given in /187/. To simplify the integration over the entire plane of the dose rates from the area elements (taking into account the effect of microrelief), a suggestion was made in /187/ to use the angular dose-rate distribution $I(h, \cos \theta)$ above an isotropic plane source, values of which were given in /6/ for various heights. The use of $I(h, \cos \theta)$, a function which also includes the scattered (in all directions) radiation, in conjunction with $F_r(\cos \theta)$ is justified in /187/ by the smallness of the contribution of the scattered radiation to the dose rate for small heights. For example, for $h = 1$ m this contribution does not exceed 20%.

If the function $\psi(\beta)$ introduced above is used to calculate the effect of the microrelief, then a correction factor $\eta(h)$ is obtained. This quantity, which allows for the effect of ground irregularities on the gamma-ray dose rate from the surface as a whole, may be expressed as

$$\eta(h) = \frac{\int_{-1}^{+1} I(h, \cos \theta) \psi^*(\cos \theta) d(\cos \theta)}{\int_{-1}^{+1} I(h, \cos \theta) d(\cos \theta)} \quad (84)$$

(here $\psi'(\cos \theta) = \psi(\beta)$; for $\cos \theta < 0$ it is assumed that $\psi'(\cos \theta) = 1$).

An analogous correction factor $\xi(h)$ for the intensity of unscattered radiation is given by the formula

$$\xi(h) = \frac{\int_0^{+1} p(h, \cos \theta) \delta'(\cos \theta) d(\cos \theta)}{\int_0^{+1} p(h, \cos \theta) d(\cos \theta)} \quad (85)$$

(here $\delta'(\cos \theta) = \delta(\beta)$, with $\delta(\beta)$ taken from /186/, where

$$p(h, \cos \theta) \approx \sec \theta e^{-\mu h \sec \theta}, \quad (86)$$

and the integration is from 0 to +1, since the unscattered radiation enters only from the lower half-space.

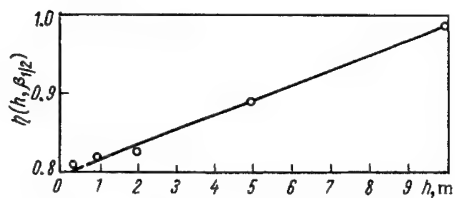


FIGURE 57. Correction factor $\eta(h)$ allowing for effect of microrelief on gamma-ray dose rate above plane (for even, unworked region, $\beta_{1/2} = 1^\circ$), as function of height.

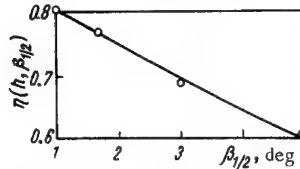


FIGURE 58. Correction factor $\eta(h, \beta_{1/2})$ as function of $\beta_{1/2}$ (that is, for different types of microrelief), for $h = 1$ m.

The data for $\eta(h)$, calculated using formula (84) for $0.1 \leq h \leq 10$ m, are plotted in Figure 57, for an even, unworked test area ($\beta_{1/2} = 1^\circ$). Figure 58 shows $\eta(h, \beta_{1/2})$ as a function of the type of microrelief (at a height of 1 m), as characterized by the angle of "half shading" $\beta_{1/2}$ (here $\delta(\beta) = 0.5$). Table 22 lists the values of $\beta_{1/2}$ for the most common types of microrelief. The values of η were calculated for gamma-ray quanta with $E = 1.25$ Mev and for the values of $\beta_{1/2}$ indicated by points in Figure 58. The deviation of the values of $\eta(h)$ for $E = 0.7$ Mev from those in the figures is only slight; for example, for $h = 1$ m and for even, unworked ground, it does not exceed 5%.

Simulation experiments were carried out in two areas of the above-described unworked land /155, 186/, in order to check the foregoing calculations.

Surface contamination was simulated by point sources of gamma rays, located close to one another. At different distances R from the observation point, along an arc subtending an angle of about 10° , 49 Co^{60} sources ($E_{av} = 1.25$ Mev) were distributed (uniformly) over the ground. The activity of each of these sources was from 3 to 7 mcuries, giving a total activity of around 200 mcuries. The sources were made in the shape of needles and

filaments, 10 to 15 mm in length and 0.5 to 3 mm in diameter. The measurements were made using a roentgen meter with a gamma-ray collector consisting of an organic scintillator and a photomultiplier; the collector had a low relative-response curve [see Figure 65 below]. Measurements were made at heights of 0.3 to 3 m and at distances of 10 to 80 m from the sources. The function $[P_{mcr}^s(\beta)]_c$ was determined experimentally by the described method. The values of P^s were also found experimentally; to do this, the same sources were placed at heights of 10 to 15 cm over the same areas on the ground, thereby eliminating shielding by the tiny protuberances on the earth's surface which make up the micro-relief. These results were taken to be typical for an ideally even surface. In this case the slight effect of the microrelief on the dose rate due to shielding of the scattered gamma radiation was neglected. For $R < 50$ m, the relative rms error in the dose rate did not exceed 10 or 15%, and for $50 \leq R \leq 100$ m it was from 25 to 35%.

TABLE 22. Quantities $\beta_{1/2}$ and Δh , characterizing shielding property of roughness of ground, for different kinds of microrelief

| Type of microrelief | $\beta_{1/2}$, deg /155/ | Δh , m (η for $h = 1$ m in parentheses), according to data of: | | | | |
|--|------------------------------|--|----------|------------|-------|---------------|
| | | /155/ | /187/ | /180/ | /179/ | /8, 108, 188/ |
| Very even unworked grassy land (meadow, glade) | 1.0 | 3.0–3.5 (0.81) | — | — | — | — |
| Very even arid steppe | 1.7 | 5.5 (0.77) | — | — | — | — |
| Even bottom of dry lake | — | — | — | 6.0 (0.67) | — | — |
| Even graveled area | — | — | — | 3–6 | — | — |
| Dry steppe | 3.0 | 8.8 (0.69) | 12 (0.5) | 12 (0.54) | 3.5 | (0.7) |
| Plowed field | 5.0 | 12 (0.60) | — | (0.58) | — | — |
| Plowed field with garden beds | — | — | — | (0.45) | — | — |

The values of $\psi^s(\beta)_c = [P_{mcr}^s(\beta)]_c/P_c^s$ were then compared with the calculated values $\psi^s(\beta)_c$ determined using formula (83). Coefficients K_u were taken from /156/, and values of $B_d(r, E)$ were taken from /139/. Table 23 lists the results of these experiments and calculations, together with the differences $\Delta\psi^s$ between the two sets of values. Of 33 measurements of ψ_c^s , in 32 cases the experimental value was within $\pm 20\%$ of ψ_c^s . The difference was as high as +30% in only one case ($R = 15$ m, $h = 0.7$ m).

Function ψ also depends on r , but for unworked land in the ranges $R = 10$ to 80 m and $h = 0.3$ to 3.0 m, we have

$$\psi_1^s \left(\arccot \frac{R_1}{h_1} \right) \approx \psi_2^s \left(\arccot \frac{R_2}{h_2} \right), \quad (87)$$

if $R_1/h_1 = R_2/h_2$.

TABLE 23. Comparison of calculated and experimental values of $\psi^s(\beta)$

| h , m | R , m | β° | α | $\frac{1}{K_u B(r, E)}$ | ψ_c^s | ψ_e^s | $\Delta\psi^s$, % |
|---------|---------|---------------|----------|-------------------------|------------|------------|--------------------|
| 0.3 | 15 | 1°10' | 0.41 | 0.77 | 0.67 | 0.68 | -2 |
| | 20 | 51' | 0.53 | 0.76 | 0.60 | 0.67 | -11 |
| | 30 | 35' | 0.69 | 0.74 | 0.47 | 0.42 | +12 |
| | 40 | 26' | 0.74 | 0.74 | 0.45 | 0.40 | +12 |
| | 50 | 22' | 0.79 | 0.73 | 0.41 | 0.40 | +3 |
| | 60 | 18' | 0.83 | 0.72 | 0.40 | 0.44 | -10 |
| | 70 | 16' | 0.85 | 0.70 | 0.40 | 0.47 | -18 |
| 0.7 | 10 | 3°50' | 0.06 | 0.79 | 0.93 | 0.90 | +4 |
| | 15 | 2°40' | 0.15 | 0.77 | 0.88 | 0.68 | +30 |
| | 20 | 2°00' | 0.23 | 0.76 | 0.82 | 0.80 | +2 |
| | 30 | 1°22' | 0.36 | 0.74 | 0.73 | 0.71 | -3 |
| | 40 | 1°02' | 0.49 | 0.74 | 0.64 | 0.71 | -11 |
| | 50 | 48' | 0.53 | 0.73 | 0.61 | 0.61 | 0 |
| | 60 | 42' | 0.60 | 0.72 | 0.57 | 0.60 | -5 |
| | 70 | 35' | 0.69 | 0.70 | 0.62 | 0.62 | -19 |
| 1.0 | 80 | 30' | 0.71 | 0.69 | 0.51 | 0.61 | -20 |
| | 10 | 7° | 0.00 | 0.79 | 1.00 | 0.94 | +6 |
| | 15 | 4° | 0.06 | 0.77 | 0.95 | 0.87 | +9 |
| | 20 | 2°50' | 0.14 | 0.76 | 0.89 | 0.89 | 0 |
| | 30 | 1°50' | 0.25 | 0.74 | 0.81 | 0.80 | +1 |
| | 40 | 1°26' | 0.34 | 0.74 | 0.75 | 0.78 | -4 |
| | 50 | 1°08' | 0.43 | 0.73 | 0.69 | 0.78 | -18 |
| 2.0 | 20 | 7° | 0.00 | 0.76 | 1.00 | 0.93 | +7 |
| | 30 | 3°40' | 0.08 | 0.74 | 0.94 | 0.80 | +17 |
| | 40 | 2°50' | 0.13 | 0.74 | 0.91 | 0.87 | +5 |
| | 50 | 2°30' | 0.17 | 0.73 | 0.88 | 0.88 | 0 |
| | 60 | 1°57' | 0.23 | 0.72 | 0.83 | 0.86 | -4 |
| | 70 | 1°43' | 0.28 | 0.70 | 0.80 | 0.75 | +7 |
| | 30 | 7° | 0.00 | 0.74 | 1.00 | 1.00 | 0 |
| 3.0 | 40 | 6°30' | 0.01 | 0.74 | 1.00 | 0.86 | +14 |
| | 50 | 3°30' | 0.10 | 0.73 | 0.93 | 0.93 | 0 |
| | 60 | 2°50' | 0.14 | 0.72 | 0.90 | 0.93 | -6 |
| | 70 | 2°30' | 0.17 | 0.70 | 0.88 | 0.89 | -1 |

Figure 59 shows $\psi^s(\beta)$ for a piece of unworked land (data points indicate experimental values) and for a plowed field, for a gamma-ray energy $E = 1.25$ Mev. For the unworked land $\psi^s(\beta)$ is expressed by a straight line, when plotted on a semilog graph. For heights from 0.3 to 3.0 m and distances from 10 to 35 m, $\psi^s(\beta)$ for a plowed field is also expressed by a straight line on a semilog graph. However, for higher R the plot of $\psi^s(\beta)$ deviates from this line. The dashed line indicates $\psi^s(\beta)$ for a plowed field at $h = 1$ m and $40 \leq R \leq 100$ m.

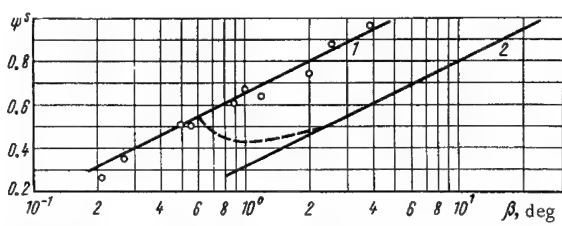
FIGURE 59. Function $\psi^s(\beta)$ for unworked land (1) and for a plowed field (2).

Figure 60 shows the results of the two series of measurements (one allowing for microrelief and one not), for various heights h , in the form of curves showing $R P_e(R)/P_e(R=0)$ as a function of R . For a given value of R the difference caused by the presence of microrelief increases with a decrease in h . For $h = 10\text{ m}$, for instance, the presence or absence of microrelief has practically no effect on $P_e(R)$. Accordingly, the results for a height of 10 m are not shown in the figure.

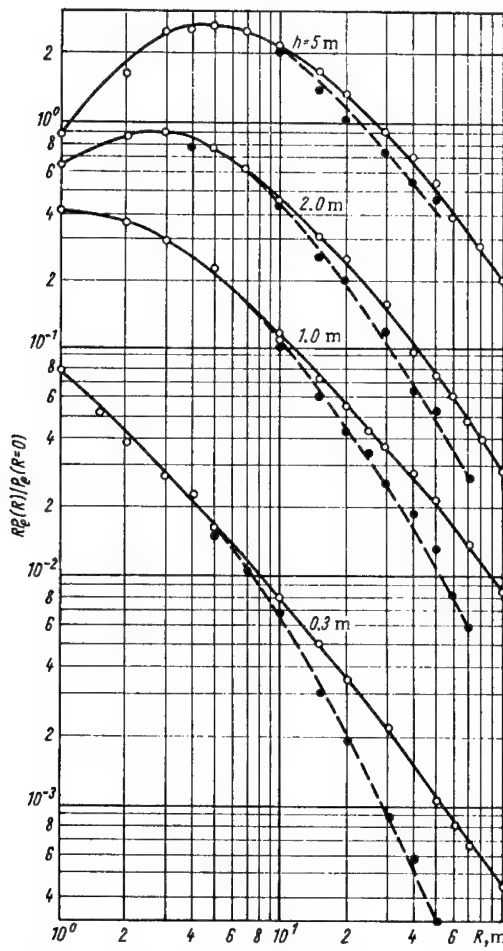


FIGURE 60. Experimentally determined ratio $R P_e(R)/P_e(R=0)$ as function of R , for point source (Co^{50}), allowing for microrelief (dashed curves) and not allowing for it (solid curves).

In Figure 57 the values of $\eta_e(h)$ for $\beta_{1/2} = 1^\circ$, calculated using the formula

$$\eta_e(h) = \frac{\int_0^{100m} RP_e^{mcr}(h, R) dR}{\int_0^{100m} RP_e(h, R) dR}, \quad (88)$$

were shown as data points, where $P_e^{mcr}(h, R)$ and $P_e(h, R)$ are the experimentally found dose rates at points (h, R) , in the presence of microrelief and in the absence of it, respectively. The values of $RP_e(h, R)/P_e(R=0)$ plotted in Figure 60 were used in the application of (88). As Figure 57 shows, there is a good fit between the calculated data and the results obtained in the simulation experiments.

In all our discussions we have neglected the variation in the distance from the observation point to the emitting areas, caused by the presence of the microrelief elements. Let us calculate the variation in the gamma-ray field due to this factor. We now designate as η_1 the quantity η when this distance variation is not taken into account (in this case the emission plane lies at the level of the base of a microprotuberance).

If the emission plane lies at the level of the tops of the microprotuberances, then the factor taking into account the influence of microrelief is

$$\eta_2 = \frac{P_{mcr}^s(h-h')}{P^s(h)}, \quad (89)$$

where h' is the height of the microprotuberance elements. Obviously, the η_{ac} of this factor will be somewhere between η_1 and η_2 :

$$\eta_1 < \eta_{ac} < \eta_2.$$

Calculations of $P_{mcr}^s(h-h')/P^s(h)$ for $h = 1\text{ m}$ and $h' \leq 0.2h$ indicated that η_2 does not differ from η_1 for a surface source by more than 5%, for a gamma-ray energy of 1.25 Mev / 185/.

The dose rate above a surface source can be calculated approximately allowing for soil unevenness, using the formulas for the dose rate above an ideally even contaminated surface. However, then some effective Δh characteristic of the given type of microrelief must be added to the measurement height:

$$P_{mcr}(h) = P(h + \Delta h). \quad (90)$$

Table 22 listed some values of Δh and η (for $h = 1\text{ m}$) for the most common types of microrelief, according to the data of various studies.

In practice, the following values of the correction factors may be used: 0.75 to 0.8 for very even land; 0.7 for steppe; 0.5 to 0.6 for plowed land (for $h = 1\text{ m}$).

In approximate calculations of the dose rate, it is also possible to use the formula for a directional plane source. Thus, in the presence of microrelief, the contamination concentration σ_{mcr} of the locality can be assumed to be equal to $\sigma \cos^n \theta$, where σ is the surface contamination

concentration of an ideal surface, and θ is the angle between a normal to the surface and the direction of an element of the emitting surface. In this case for an unworked even area $n \approx 0.2 / 155/$.

The surface contamination of a locality subsequent to the fallout from a nuclear explosion lasts only for a relatively short time. Gradually (over a period of weeks or months) the radioactive isotopes penetrate into the soil to a depth of several centimeters. Thus, a three-dimensional radiation source is created, with a concentration diminishing with depth (see Section 3 of Chapter I). In this case the influence of the microrelief will be less than for surface contamination. When the contamination of the soil is uniform to a depth exceeding several gamma-ray mean free paths, the microrelief has virtually no effect /186/. For contamination to a depth of several centimeters, the effect is somewhat less than for surface contamination /155/.

It is logical to assume that the dose rate and the gamma-ray intensity over contaminated ground will vary simultaneously with the spectral-angular gamma-ray distribution, due to the effect of irregularities in the underlying surface. Thus the shape of the spectrum of the scattered radiation should

vary only comparatively slightly, in view of the substantial contribution to it of multiply scattered gamma-ray quanta. The intensity of the unscattered gamma-ray quanta will vary considerably, however. Accordingly, the angular distributions of the gamma-ray dose rate (or intensity) should vary appreciably about some values ω close to (but greater than) zero.

Some experimental data on the angular dose-rate distributions at a height of 1 m over contaminated regions of various types are plotted in Figure 61: the even bed of a dry lake (curve 3); an arid steppe /180/ (curve 4); and very even unworked grassy land (curve 2, calculated on the basis of /155/).

These experimental distributions correspond to "effective" measuring heights (in the absence of microrelief) of: 6 m in the first case, 12 m in the second case, and 3 m in the third case, which values are practically the same as the values of Δh given in Table 22.

The figure also shows the curve of $I(h, \cos \theta)$ for $h = 1$ m in the absence of microrelief (curve 1). As was assumed, the angular distribution is distorted considerably for values of $\omega = \cos \theta$ close to zero ($0 \leq \omega \leq 0.1 - 0.2$).

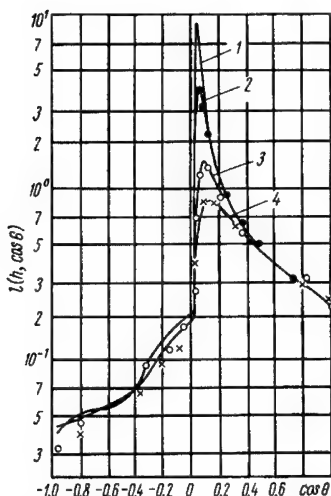


FIGURE 61. Angular dose-rate distribution at height of 1 m over contaminated locality.

13. Effects of vegetation and weather conditions

The gamma-ray field over a contaminated region covered by grass or forest differs from the field of an area in which there is no vegetation. This difference is due to the shielding effect of the biomass covering the contaminated ground /189/. When radioactive products fall out onto a forest cover, a considerable part of the radioactivity is retained by the treetops. Thus a three-dimensional source is produced, with a distribution of radioactive material that depends on the shape and density of the treetops, the fullness of the forest, the kind of forest, the time of year, and the weather conditions. Secondary transport of the radioactive particles by the wind, and especially by the rain, eventually rids the treetops of their contamination. Consequently, a radiation source which is almost an isotropic plane source (or a three-dimensional source, due to contamination of the upper soil layer) is created on the ground under the trees.

First let us consider the shielding effect of a forest, with respect to the gamma emission of a surface source. It is assumed that there are no fundamental differences between the effects on the gamma-ray field of a grass cover, a scrub growth, or a stand of trees. In the following only a forest cover will be referred to, but it is easy enough to extend the conclusions obtained (with certain reservations) to include a grass cover or scrub growth.

The absorbing properties of a forest are determined by the spatial distribution of the biomass, by its quantity, and also by its atomic makeup /189/. The amount of biomass in a forest, calculated per unit area, depends (for a given type of forest) on its conditions of growth (quality and yield), fullness, and age /190/.

TABLE 24. Amounts of biomass, for various kinds of forests, in g/cm²

| Types of trees | Age, years | Index of quality and yield | | |
|----------------------------|------------|----------------------------|---------------|------------|
| | | better (Ia, I) | average (III) | poorer (V) |
| Spruce, pine, oak | 40 | 3.4— 4.2 (4.5)* | 1.5— 2.2 | — |
| | 60 | 5.6— 6.7 (8.1) | 3.3— 3.8 | 1.75 |
| | 100 | 9.4— 10.0 (13.2) | 6.2— 6.6 | 3.80 |
| | 120— 160 | 12.0— 13.7 (15.0) | 7.4— 9.6 | — |
| Birch, aspen, linden | 40 | 2.9— 3.7 | 1.5— 1.8 | — |
| | 60 | 4.5— 5.4 | 2.3— 2.7 | — |
| | 100 | 6.0— 7.4 | 2.7— 3.6 | — |

* Values in parentheses are for spruce forests.

Table 24 lists the amounts [surface densities] $q(t)$ of biomass at the ground for the most common types of forests in the Soviet Union. General tables giving forest growth characteristics /191/ were used to calculate $q(t)$, the amount of biomass being given in m³ per hectare. In these tables the contribution of brushwood and leaves to the total amount of wood, which amounts to from 5 to 20% /190, 192/, is already taken into account. Data

on the specific weights ρ_0 of forests were taken from /193/. Values of $q(t)$ for various types of forests can be found approximately using the formulas given in /194/.

Since ρ_0 undergoes seasonal fluctuations associated with variations in the moisture content of the wood, leaves, or needles, there will be corresponding seasonal fluctuations of $q(t)$ within a range of 10 to 20%.

The distribution of q over the height from the ground surface up to some level $Z \leq h$, where h is the average tree height, is mainly determined by the shape of the trunk. The latter is close to a circular truncated cone with a height h and with diameters d_0 (at ground level) and $d(h)$ (at a height h). Thus, the amount of biomass of the trunk from $Z=0$ to Z will be /189/

$$q_{tr} = \frac{\pi}{6} [2\beta^2 Z^3 - 3\beta d_0 Z^2 + 1.5 d_0^2 Z^3], \quad (91)$$

where

$$\beta = \frac{|d_0 - d(h)|}{h}.$$

For forests of average age $\beta = 0.01$ to 0.02 and $d(h) \ll d_0$. The amount of biomass in the forest litter usually does not exceed 1.0 to 1.5 g/cm^2 and constitutes no more than 10 to 20% of the total biomass of the forest.

The biomass of a forest is distributed nonuniformly in space. In many instances the twigs, leaves, needles, and forest litter may be represented schematically as homogeneous horizontal layers. However, it is much less probable that this can be done for the biomass of the trunks, which is the factor determining the anisotropy of the forest cover as an absorbing medium.

The average number of trunks n per unit area is a monotonically decreasing function of the age of the forest. After a very long time n diminishes, as a result of self-culling of the forest /194/. Some factual data on tree quantities are given in /190/. The fluctuations of n apparently satisfy the Poisson distribution.

Now let us consider the second factor determining the absorptive capacity of a forest, namely its atomic makeup. The main chemical compounds going to make up absolutely dry wood are: cellulose, lignin, resins, and acetic acid (together with small admixtures of inorganic compounds). Accordingly, the basic atoms present are: carbon ($\sim 49\%$), oxygen ($\sim 44\%$), and hydrogen ($\sim 6\%$) /195/. Thus the effective atomic number for dry wood turns out to be very close to that for water. The effective atomic number will therefore be virtually independent of the moisture content of the wood.

Consequently, the electron densities N_e for absolutely dry wood or wet wood will differ little from one another and will be close to N_e for water. For instance, for absolutely dry wood $N_e = 3.23 \cdot 10^{23}$ electrons/g, for freshly cut wood (100% moisture content) $N_e = 3.30 \cdot 10^{23}$ electrons/g, and for water $N_e = 3.35 \cdot 10^{23}$ electrons/g /189/. Taking the foregoing into account, we may consider the absorptive capacities of a forest biomass and water to be identical in the range of gamma-ray energies from 0.1 to 3.0 Mev.

If the initial gamma-ray energy E_0 is assumed to be in this range, then the entire complex of absorbing materials (soil, forest biomass, atmospheric air) may be considered as an air-equivalent medium. The error in dose

rate caused by the use of these approximations will not exceed 5 or 10%.

The dose rate and intensity of the primary gamma radiation will be calculated assuming that the degrees of gamma-ray attenuation are the same in both homogeneous and inhomogeneous air-equivalent media, provided that

$$\mu_{\text{hom}} r_{\text{hom}} = \sum_{i=1}^n \mu_i r_i, \quad (92)$$

where μ_{hom} and μ_i are the linear gamma-ray attenuation coefficients in a homogeneous medium and in the i th homogeneous portion of an inhomogeneous medium, respectively; r_{hom} is the distance from the measuring point to the source, for a homogeneous medium; and r_i is the gamma-ray path length in the i th portion of an inhomogeneous medium (along the shortest route) /163/.

In order to check the applicability of the foregoing assumption in a forest region, we carried out a simulation experiment in the Arkhangel'sk district, in a region of mixed forest. The composition of the forest was given by the formula 6S2B2As, Al, * and the forest was around 100 years old (quality-and-yield index of IV). The overall fullness of the forest in the part studied was close to unity, and the average amount of biomass (neglecting fallout and root systems) was 2.26 g/cm^2 . The biomass was evaluated by a direct count of the trees in the region, together with a determination of their heights, diameters, and specific weights and a subsequent calculation of the reserves of the forest taking into account the shapes of the tree trunks. The biomass in different squares of the region was evaluated analogously, according to layers (according to height).

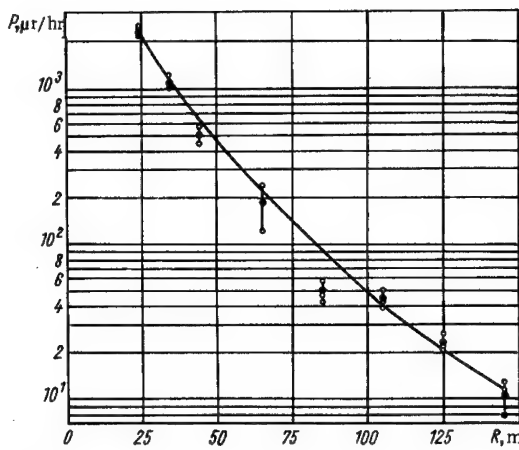


FIGURE 62. Calculated and experimental dose rates from point source in forest region. Symbol O indicates individual measurement; symbol ● indicates average value. Curve corresponds to calculated values.

* [That is, 6 spruce, 2 birch, 2 aspen, alder.]

A point source (Co^{60}) with an activity of 1.2 curies was placed at a height of 0.5 m above the ground, in order to eliminate shielding by soil irregularities. The measurements were made with a gamma-ray detector having a low relative-response curve [see Figure 65 below], at various distances R between the projections of the source and measuring point onto the earth's surface (up to 145 m) for a height $1 \leq H \leq 10$ m. For each value of R and H measurements were made at three points, divided from one another along the horizontal by 2 m. Figure 62 shows the calculated and experimental values /163/ of the dose rate from this source, for $25 \leq R \leq 145$ m and $H = 1$ m.

The dose rate was calculated using formula (46), on the assumption that

$$\mu r = \mu_1 \sqrt{R^2 + H^2} + \frac{\mu_2}{\rho_0} p_i,$$

where μ_1 and μ_2 are the linear attenuation coefficients in air and in a forest, respectively; p_i is the amount of biomass on the line joining the source and the measuring point; and ρ_0 is the specific weight of the wood. Coefficient K_{u} , allowing for the effect of the underlying surface, is here taken as unity, because the density ratio for the underlying forest litter and the forest is only from 25 to 40, considerably less than the density ratio for an underlying ground surface and air, which is of the order of 1200 to 1500. Inspection of Figure 62 shows good agreement between the calculated and experimental dose rates.

In order to calculate the dose rate from an entire surface having a forest cover, we assume that the absorbing medium consists of two uniform layers: a layer of air, with a mass essentially equal to the mass of the air layer between the ground and the measuring point, and a layer of wood (that is, the anisotropy of the forest is neglected). The thickness of these layers, expressed in gamma-ray mean free paths, are $\mu_1 H$ for the air and $\mu_2 q/\rho_0$ for the wood.

Therefore, the dose rate over a surface source covered by a forest, at a height $H \leq h$ (where h is the height of the trees), may be written as

$$P(l) = \frac{k \sigma_a}{2} \left[E_1(l) + \frac{e^{-l}}{7E^{2.4}} (1 + 7E^{2.4} + l) \right], \quad (93)$$

where $l = \mu_1 H + \frac{\mu_2 q}{\rho_0}$.

The coefficient expressing the shielding effect of the forest cover, relative to the dose rate, is

$$f_p(q) = \frac{P(\mu_1 H)}{P \left[\mu_1 H + \frac{\mu_2 q}{\rho_0} \right]}. \quad (94)$$

For a forest with a fullness α less than 1.0, the amount of biomass q_α will be

$$q_\alpha = \alpha q_{1.0} \quad (95)$$

(some values of $q_{1.0}$ were given in Table 24).

An analysis of (94) makes it clear that in the height range $50 \leq H \leq 300$ m coefficients f_p are practically independent of H . Table 25 lists some values of f_p for an infinite surface source, for forests of various types, quality-and-yield indexes, and ages (gamma-ray energy $E = 0.7$ Mev). The shielding coefficients depend mainly on the quality-and-yield index N and on the forest age t .

It is evident from Table 25 that a forest cover does shield the gamma emission from contaminated ground; however, this shielding is in general only slight. The shielding coefficients for the most common types of mature forests of average quality and yield are only from 1.3 to 1.6. These coefficients reach values of 2.0 to 2.5 just for centenarian forests of better quality and yield.

TABLE 25. Coefficients for shielding of gamma-ray dose rate by forest cover

| Types of trees | Age, years | Index of quality and yield | | |
|----------------------------|------------|----------------------------|---------------|------------|
| | | better (Ia, I) | average (III) | poorer (V) |
| Spruce, pine, oak | 40 | 1.30—1.40 (1.42)* | 1.13—1.20 | — |
| | 60 | 1.50—1.65 (1.80) | 1.30—1.35 | 1.17 |
| | 100 | 2.00—2.10 (2.55) | 1.60—1.65 | 1.35 |
| | 120—160 | 2.4—2.70 (2.95) | 1.73—2.05 | — |
| Birch, aspen, linden | 40 | 1.25—1.33 | 1.13—1.15 | — |
| | 60 | 1.42—1.48 | 1.21—1.24 | — |
| | 100 | 1.55—1.73 | 1.24—1.33 | — |

* Values in parentheses are for spruce forests.

All the above formulas were derived for measuring heights H exceeding the height h of the forest. In order to calculate the shielding effect of the forest for $H < h$, the amount of biomass contained in the layer between the ground and the height H must be substituted into formulas (93) and (94).

It is quite clear that the biomass of the treetops (twigs, needles, and leaves) may be assumed to be uniformly distributed. Thus, the gamma-ray absorption in this part of the biomass can be described quite satisfactorily using formula (94). However, most of the forest's biomass (for trees of average age, from 80 to 90%) is contained in the tree trunks and does not form a homogeneous layer.

According to the data of /189, 196/, the effect of the anisotropy of the forest material can be neglected in calculations of the gamma-ray dose rate from surface contamination, measured at heights exceeding the height of the forest (for fullness factors close to 1.0).

The calculations of the gamma-ray characteristics over an isotropic plane source (and also over an actual contaminated site) were carried out assuming a homogeneous atmosphere at standard pressure and temperature. Thus the atmospheric density ρ_0 was taken to be constant with height, having the value $\rho_0 = 1.293$ g/l (for $t = 0^\circ\text{C}$ and a pressure of 760 mm Hg).

In this section the effects of temperature t , pressure p , and air humidity and precipitation (water content W) on the gamma-ray field in a real atmosphere will be considered. The air above the earth's surface can be

assumed with sufficient accuracy to be a layered medium (at distances comparable to the mean free paths of gamma-ray quanta). Thus the air density ρ can be assumed to vary just with the altitude h . Accordingly, all the calculations of the gamma-ray field in a real atmosphere will be made for a stratified absorbing medium.

The air density is a function of the pressure p , the temperature t , and the water content W :

$$\rho(p, t, W) = \frac{\rho_0}{1 + \alpha t_v} \cdot \frac{p}{1013.2}, \quad (96)$$

where ρ_0 is the density of dry air at 0°C and a pressure of 1013.2 mbars; p is the pressure in mbars (1.0 mm Hg = 1.35 mbars); $\alpha = 1/273.2 \text{ deg}^{-1}$; and t_v is the virtual temperature, taking into account air humidity. The virtual temperature is defined as the temperature at which dry air would have the same density as the given wet air does at temperature t and pressure p :

$$t_v = t \left(1 + 0.378 \frac{e}{p} \right), \quad (97)$$

where e is the elasticity of water vapor. The virtual temperature is somewhat higher than t . The difference $t_v - t = \Delta t_v$ reaches a maximum for saturated air; it is from 1 to 3° for $6 \leq t \leq 23^\circ$ and from 3 to 5° for $23 \leq t \leq 30^\circ$.

The pressure variation with the height h is described adequately /197/ by the barometric formula

$$p(h) = p_0 \exp \left[-\frac{h}{7996(1 + \alpha t_{vm})} \right], \quad (98)$$

where h is the height above sea level, t_{vm} is the mean virtual temperature in layer h , and p_0 is the sea-level pressure.

The temperature gradient in the layer near the earth is comparatively small (0.2 to 1.0 deg/100m) /197/, and as an average it can be taken to be 0.5 deg/100 m. In addition, the virtual temperature does not vary much from the temperature t of dry air (at ground level or at a height h). Therefore, for heights $h \leq 500$ m we can set $t_{vm} = t$ in practical calculations. Now it is easy to find the relationship between a height h_{hom} in a homogeneous atmosphere (that is, an atmosphere having a constant density $\rho_0 = 1.293 \text{ g/l}$) and a height h in a real atmosphere. We may write

$$\int_{h_0}^{h_0+h} \rho(h_0 + h) dh = \rho_0 h_{hom} \quad (99)$$

$$h_{hom} = 7996 \left\{ \exp \left[-\frac{h_0}{7996(1 + \alpha t)} \right] - \exp \left[-\frac{h_0 + h}{7996(1 + \alpha t)} \right] \right\}, \quad (100)$$

where h_0 is the height in m above sea level of the ground under the point of measurement.

Figure 63 shows h_{hom} as a function of h for various temperatures (from -30 to +40°C) at sea level ($h_0 = 0$) and also for various heights above sea level ($h_0 = 0$ to 4000 m) at $t = 0^\circ$.

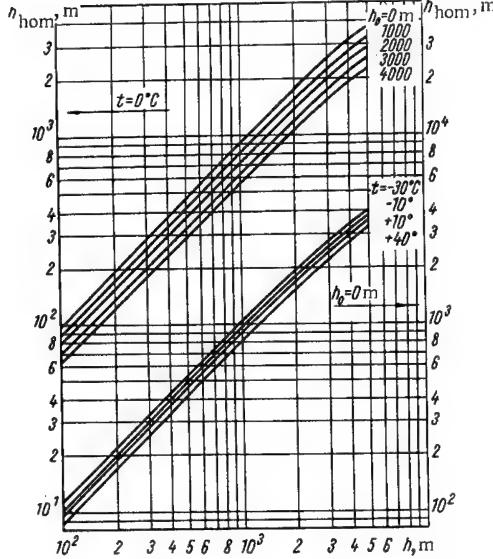


FIGURE 63. Relationship between heights of homogeneous and real atmospheres.

Consequently, the height conversion factors over a contaminated region depend on the height above sea level of the underlying surface, the air temperature, the water content (humidity, amount of moisture in droplets of clouds, mist, and precipitation), and the weather, since the pressure varies with the weather. In short, these factors are a function of the pressure, temperature, and humidity of the air. The pressure variation with height (according to the barometric formula) for a standard atmosphere also affects the value of the conversion factors.

Using the barometric formula, it is easy to demonstrate that for the standard atmosphere the conversion factor for the dose rate, from a height of 200m down to ground level, will only differ from the conversion factor calculated

for a homogeneous atmosphere by less than 2% (if the intensity of unscattered gamma radiation is less than 4%). At lower altitudes this difference will be even less. Variations in the temperature t , pressure p , and humidity W of the air will have a more significant effect on the values of the conversion factors.

The conversion factors $K_{h(t, p, W)}[H(t, p, W)]$ corresponding to actual conditions are given by the formula

$$K_{h(t, p, W)}[H(t, p, W)] = K_{h_0}(H_0), \quad (101)$$

where

$$h_0 = h(t, p, W) \frac{p(t, p, W)}{p_0} \quad \text{and} \quad H_0 = H(t, p, W) \frac{p(t, p, W)}{p_0}$$

and $K_{h_0}(H_0)$ is the conversion factor for a homogeneous atmosphere.

Figure 64 shows the relative variation of conversion factors $K_H(h)$ for a homogeneous atmosphere, with changes in air temperature, pressure, and humidity, for the dose rates at $H=100, 200$, and 300m (curves 1, 2, and 3, respectively). The figure shows the curves for $q = \frac{K_H(h)_{hom}}{K_H(h)_{real}}$ as a function of t, p and $W / 163/$.

It is clear from Figure 64 that $K_H(h)$ for the dose rate varies only slightly with a change in the water content of the air (from 1.0 g/m^3 for dense fog to 4 g/m^3 for a downpour). A temperature change from -30 to $+30^\circ$ varies $K_H(1)$ by $\sim 20\%$, and a 50 mm Hg drop or rise in pressure

varies it by $\sim 5\%$. The variation of this factor for the intensity of the primary gamma radiation is even greater. Hence, for measurements of $P(h)$ and $J(h)$ from an aircraft, air pressure and temperature have to be taken into account. When the measurements are made in mountainous regions, where the earth's surface is greatly elevated above sea level, changes in pressure are even more significant.

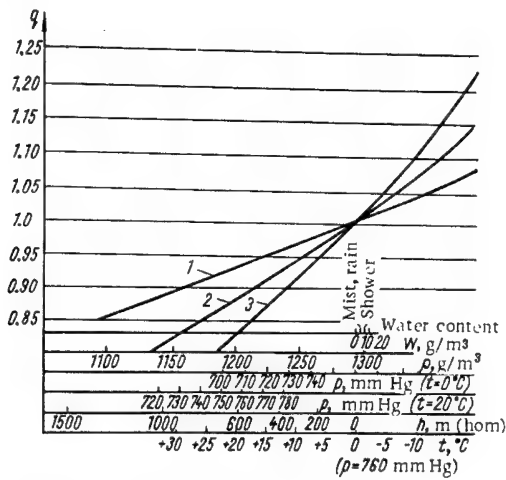


FIGURE 64. Relative variation of conversion factors $K_H(h)$ for homogeneous atmosphere, with changes in air temperature, pressure, and humidity at $H = 100$ m (curve 1), 200 m (curve 2), and 300 m (curve 3).

14. Determination of surface density of contamination according to measured gamma-ray dose rate

The dependences of the gamma-ray dose rate on the height above a surface contaminated with gamma-ray emitters of different energies (including fission fragments) were described in Section 7. Then, in Sections 12 and 13, the effects of actual conditions on the nature of these relations were considered. Using the findings of those sections, it is now easy to pass from the dose rate $P(h)$ measured at some height h (for instance, using an aircraft) to the dose rate P_H at the earth's surface (at a height $H = 1$ m):

$$P_H = P(h) K_h(H) \epsilon_u(h) \epsilon_f(h) \epsilon_p(h) \epsilon_r(h) \epsilon_w(h), \quad (102)$$

where $K_h(H)$ is the height conversion factor for conversion from height h to height H for an ideally even surface and a standard atmosphere; $\epsilon_i(h)$ is a correction factor taking into account the effect of actual conditions; $\epsilon_u(h)$ corrects for the unevenness of the earth's surface; $\epsilon_f(h)$ corrects for the vegetation (chiefly forest) cover; $\epsilon_p(h)$ corrects for air pressure; $\epsilon_r(h)$ corrects for air temperature; and $\epsilon_w(h)$ corrects for air humidity.

As demonstrated earlier, the quantity $K_H(h)^*$ for $1 \leq H$ and $h \leq 200$ m varies only slightly with primary gamma-ray energy in the energy range for emission from nuclear-explosion products. The average values of this quantity were given in Table 13. The values of $1/\epsilon_u(h) = \eta(h)$ given in Section 12 for $h > 10$ m were practically unity. For $h = 1$ m, in most cases $1/\epsilon_u(h) \approx 0.7$. The values of $\epsilon_p(h)$ and $\epsilon_r(h)$ determined in Section 13 for $h < 200$ m were close to unity (they deviated by less than 10 to 15%), and the values of $\epsilon_w(h)$ found there were almost always 1.0. Values of $\epsilon_f(h)$ were also given in Section 13.

In Section 7, together with the data on $P(h)$, the relation between the dose rate and the surface density of contamination σ was described. This made it possible to determine σ (in units of energy) in terms of measured values of $P(h)$. It follows from formula (55) that

$$\sigma = \frac{2P(h)}{k\sigma_a G(h)}. \quad (103)$$

The scatter of the values of $f(h, E) = \sigma_a(E)G(h, E)$ for energies from 0.255 to 2 Mev** is negligible (12 to 20%) up to heights of 200 m. However, at greater heights this scatter increases sharply, reaching a factor of 10 for $h = 1000$ m.

It follows from the results in Section 7 that the surface gamma-ray concentration σ , expressed in energy units, can be found from the measured gamma-ray dose rate $P(h)$ at a height $h = 200$ m, even if the spectral composition of the gamma radiation is unknown (in the indicated energy range). For this, formula (103) is used, with the accuracy given above.

An analogous conclusion may be drawn on the basis of simulation experiments for gamma-ray sources with energies of 0.411, 1.25, and 2.8 Mev (see /7, 9/). Ground-level measurements of the surface density of contamination σ are usually employed in experimental evaluations of the coefficient relating σ and $P(h)$ in formula (103).

Let us derive a formula which will give us the indicated coefficient solely from measurements of the dose rate at various heights. We begin from the law of conservation of energy and from the fact that the dose rate is proportional to the absorbed energy over a wide energy range for the primary and scattered gamma rays. The energy for the production of a single ion pair in air is practically constant and is equal to 34 ev /198/. Now we can write /163, 199/

$$\frac{1}{\rho_0} \int_0^\infty P(h) \rho(h) dh = \frac{k\sigma}{2}, \quad (104)$$

where $\rho(h)$ and ρ_0 are the air densities at a height h and at ground level.

Equation (104) signifies that half the gamma-ray energy emitted by an isotropic plane source is absorbed in the matter of the upper half-space (the air). Almost all the gamma-ray absorption takes place in the

* $K_H(h) = 1/K_h(H)$.

** For $E = 0.255$ Mev the value of $f(h, E)$ was obtained by numerical integration, using formula (56), of the tabulated values of the dosage factor.

atmospheric layer near the earth (up to a height of several hundred meters), where the variation in air density is only slight. Thus formula (104) can be written approximately as

$$\int_0^{\infty} P(h) dh = \frac{k\sigma}{2}. \quad (105)$$

Function $P(h)$ can be written as

$$P(h) = P_H K_H(h), \quad (106)$$

where P_H is the dose rate at some fixed height H , and $K_H(h)$ is the height conversion factor for conversion from height H to height h .

From (105) and (106) we obtain

$$\sigma = \frac{2}{k} \int_0^{\infty} P(h) dh = \frac{2P_H}{k} \int_0^{\infty} K_H(h) dh. \quad (107)$$

In order to determine the numerical value of the coefficient relating σ and P_H in formula (107), it is sufficient just to know function $P(h)$ above the emitting surface. Equation (105) can be obtained by integrating formula (53) over the height*:

$$\begin{aligned} \int_0^{\infty} P(h) dh &= \frac{k\sigma_a}{2} \left\{ \int_0^{\infty} E_1(\mu h) dh + \left(1 + \frac{1}{7E^{2.4}} \right) \int_0^{\infty} e^{-\mu h} dh + \right. \\ &\quad \left. + \frac{1}{7E^{2.4}} \int_0^{\infty} \mu h e^{-\mu h} dh \right\} = \frac{k\sigma_a}{\mu} \left(1 + \frac{1}{7E^{2.4}} \right) \approx \frac{k\sigma_a}{2}, \end{aligned} \quad (108)$$

since $2\sigma_a (1 + 1/7E^{2.4})/\mu$ is practically unity for energies from 0.5 to 2 Mev, Formula (107) can be rewritten as

$$\sigma = L_H P_H, \quad (109)$$

where

$$L_H = \frac{2}{k} \int_0^{\infty} K_H(h) dh. \quad (110)$$

The scatter of the values of L_H calculated for various energies E between 0.09 and 3.0 Mev is a minimum for heights H from 100 to 150 m. Therefore, heights in this range are optimum for determining σ from $P(h)$ when the spectral composition of the primary gamma radiation is unknown.

* Some error will be introduced here, since an approximate expression for the factor allowing for multiple gamma-ray scattering was used in the derivation of (53).

For $H = 100$ m

$$L_H = 1.2 \cdot 10^6 \frac{\text{Mev}}{(\text{cm}^2 \cdot \text{sec})} \Big/ \frac{\text{r}}{\text{hr}}$$

and

$$M_H = \int_0^\infty K_H(h) dh = 318 \text{ m} (\pm 7\%).$$

Table 26 lists some values of M_H obtained from an analysis of various results for $H = 100$ m.

TABLE 26. $M_H = \int_0^\infty K_H(h) dh$ corresponding to different sets of data

| Method used | Reference | M_H , in m |
|--|-----------|-------------------|
| Calculation, for E from 0.09 to 3 Mev | /163/ | 318 ($\pm 7\%$) |
| Calculation | /8/ | 323 |
| Simulation experiments, for E from 0.41 to 2.8 Mev | /7,9/ | 340 ($\pm 3\%$) |

For $H = 1$ m, we have $L_H = 2.1 \cdot 10^5 \frac{\text{Mev}}{(\text{cm}^2 \cdot \text{sec})} \Big/ \frac{\text{r}}{\text{hr}}$ and $M_H = 55$ m (for an ideally even surface)/163/. The relations obtained above can be used to determine the total amount of matter in the contaminated region of interest.

If 1 mcurie of gamma-active matter with an energy of 0.95 Mev/disintegration is distributed uniformly over 2.59 km^2 (1 square mile) of an ideally even plane surface, then according to /21/ the dose rate 1 m above the ground will be 6.8 r/hr. One hour after a 1-kt explosion the total activity of the fission products amounts to 550 mcuries. Therefore, if all the debris of a kiloton blast is distributed over 2.59 km^2 , the dose rate at a height of 1 m will be 3700 r/hr (or 0.7 of this, taking into account the microrelief). If this same matter is spread over only 1 km^2 , the dose rate will be 9700 r/hr (sometimes this level of contamination is referred to as $9700 \text{ r} \cdot \text{km}^2/\text{hr} \cdot \text{kt}$). Consequently, a surface density of contamination equal to $2.10^5 \frac{\text{Mev}}{(\text{cm}^2 \cdot \text{sec})} \Big/ \frac{\text{r}}{\text{hr}}$ will correspond to a dose rate of 1 r/hr at a height of 1 m, a value which is very close to the one obtained earlier /163/.

If the distribution of radioactive products is not uniform, but of varying concentration (as in the case in the near wake of a nuclear explosion), then the integration for the matter in the region /188/ can be carried out using the formula

$$J = \int_{S_1}^{S_2} P_H dS, \quad (111)$$

where S_1 and S_2 are the areas bounded by the isolines of the maximum and minimum dose rates, the integration being over the areas included between

adjacent isolines; and P_H is the dose rate at some specified height. It is most convenient to express the above integral in units of $r \cdot \text{km}^2/\text{hr}$, which were related earlier to the activity of the nuclear-explosion products. Therefore, this method requires a knowledge of the coefficient given above (17.6 r/hr at a height of 1 m for $1 \text{ mcurie}/\text{km}^2$, without allowing for micro-relief).

By measuring the dose rates at various heights above a contaminated region, the total amount of matter A (in units of energy) in any previously selected area can be directly determined. Let us assume that approximately half the energy emitted as gamma rays by a surface source is absorbed in air per unit time. Then, we can write

$$A = 2c \int_h \int_s P dS dh = 2c \int_s P_H dS \int_h K_H(h) dh, \quad (112)$$

where c depends on the units used.

If the integration is carried out over the wake, where R is the distance along the axis and l is the distance transverse to the axis, then

$$A = 2c \int_R \int_l P_H(R, l) dR dl \int_h K_H(h) dh. \quad (113)$$

It is convenient to express A in $\text{r} \cdot \text{km}^3$ or in Mev/sec . One $\text{r} \cdot \text{km}^3/\text{hr}$ indicates the energy absorption (release) rate in 1 km^3 of air, at every point of which the dose rate is 1 r/hr . It can be shown that $1 \text{ r} \cdot \text{km}^3/\text{hr} = 19.6 \cdot 10^{15} \text{ Mev/sec}$.

Obviously, if the dose rate at a height of 1 m over an ideally even surface (uniform contamination) is 1 r hr , then the energy emitted from an area of 1 km^2 will be $A = 0.11 \text{ r} \cdot \text{km}^3/\text{hr}$ (from $M(H=1 \text{ m}) = \int_h K_1(h) dh = 0.055 \text{ km}$) or $\sim 2.0 \cdot 10^5 \text{ Mev}/(\text{cm}^2 \cdot \text{sec})$.

Therefore, once the gamma-ray dose rate over a contaminated region has been determined at some specific height H (for example, once the dose rate at a height of 1 m has been measured), it is easy to calculate the total amount of matter (in energy units) in the region of interest, provided the variation of the dose rate with height is known. In such calculations the effects of actual conditions must be taken into account, by introducing the appropriate corrections. In practice, all the corrections indicated above should be used when determining the final value of M_H . For example, for $H = 1 \text{ m}$ a value of $M_H = 80 \text{ m}$ is obtained when the effect of microrelief is taken into account.

It is especially convenient to calculate the amount of matter in energy units when determining the fraction of the fallout material (of all the radioactive material produced) in a certain portion of the explosion wake (or in the entire wake). This is because the amount of matter (in Mev per second) produced during fission of a given type is a well-known quantity, for any moment of time after the blast (see Section 1). The fractions of the total matter in the wakes of the "Danny Boy" /188-200/, "Bravo" /21/, and other explosions were determined in just this way.

If the average release of gamma-ray energy (in $\text{Mev/disintegration}$) is known, as in the above example, then the activity of the gamma-emitting matter (in curies) can be calculated from the amount of matter expressed

in energy units. The volume concentration of contamination is related to the dose rate above a three-dimensional source of uniform concentration as follows:

$$\sigma_v = N_H P_H. \quad (114)$$

This expression is analogous to the one for a plane source. Let us now find N_H for the case when $Z=\infty$ and $\psi_0 = \pi/2$. First $P^v(h, \pi/2, \infty)$ is integrated over height from 0 to ∞ :

$$\begin{aligned} \int_0^\infty P^v(h) dh &= \frac{k\sigma_v \sigma_a}{2\mu_0} \left[\frac{1}{\mu} E_3(0) + \frac{1}{\mu} \left(1 + \frac{2}{7E^{2.4}} \right) + \right. \\ &\quad \left. + \frac{1}{7\mu E^{2.4}} \right] = \frac{k\sigma_v \sigma_a}{2\mu_0 \mu} \cdot \frac{3}{2} \left(1 + \frac{2}{7E^{2.4}} \right), \end{aligned} \quad (115)$$

where

$$E_3(x) = \int_0^\infty E_2(t) dt.$$

For energies from 0.5 to 2.0 Mev, the function

$$G(E) = \frac{3}{2} \cdot \frac{\sigma_a}{\mu} \left(1 + \frac{2}{7E^{2.4}} \right)$$

is equal to unity, with an accuracy of 10 to 25%. For this same energy range, and with the same accuracy,

$$\int_0^\infty P^v(h) dh = \frac{k\sigma_v}{2\mu_0}. \quad (116)$$

Consequently, by analogy with formula (107), we can write

$$\sigma_v = \frac{2\mu_0 P_H}{k} \int_0^\infty K_H^v(h) dh. \quad (117)$$

Therefore, for a three-dimensional source,

$$N_H = \frac{2\mu_0}{k} \int_0^\infty K_H^v(h) dh. \quad (118)$$

Just as in the case of the quantity N_H for a plane source, the scatter of the values of L_H for a three-dimensional source, for various energies (from 0.6 to 2.0 Mev), is a minimum for heights from 100 to 150 m. For $H = 100$ m*

$$N_H \cong \mu_0 L_H \cong \mu_0 1.2 \cdot 10^6 \frac{\text{Mev}}{(\text{cm}^2 \cdot \text{sec})} \Big/ \frac{\text{hr}}{\text{hr}} \quad (119)$$

* In contrast to a plane source, to determine σ_v for a three-dimensional source, it is not enough just to know $P^v(h)$. It is also necessary to know μ_0 , that is, the energy of the primary gamma emission.

(with an accuracy of 10%) and

$$U_{H=100\text{ m}} = \int_0^{\infty} K_{100}^v(h) dh \approx 300 - 320 \text{ m.}$$

In all the foregoing formulas σ_v was expressed in units of energy. The volume concentration of contamination can be determined in disint/(sec·cm³) or curies/cm³ only when the isotopic composition of the radioactive material making up the three-dimensional source is known.

If the activity of a three-dimensional source diminishes exponentially with depth, then the volume density of contamination σ_{v_0} in the surface layer of the soil may be found from the measured dose rate $P^r(h)$, using formula (72) (for known composition of contamination and penetration coefficient).

On the basis of these data, we can now determine the stock (total amount) q of a given isotope or group of isotopes per unit area (or in the region of interest as a whole):

$$q = \int_0^{\infty} \sigma_{v_0} e^{-mz} dz = \frac{\sigma_{v_0}}{m}. \quad (120)$$

In addition to the errors related to the effects of actual conditions, it is very important to correct the readings for instrument errors of various types. The principal errors associated with dosimetric analysis and measurements in air (gamma-ray surveys with aircraft) are as follows:

1. Errors due to instrument inertia;
2. Errors related to the gamma-ray collector not being air-equivalent;
3. Errors due to anisotropy of the radiation detector (as a result of the detector geometry, or of nonuniform shielding by the aircraft and the instrument case).

Let us consider each of these types of errors individually.

1. If the instrument has a large time constant, distortion may be introduced during measurements of the gamma-ray field in a region with sizable contamination gradients. The error introduced by the time constant τ of the instrument can be corrected /201/ using the formula

$$P_{act} = P_{ms} + \tau \frac{dP_{ms}}{dt}, \quad (121)$$

provided the variation with time is exponential, where P_{act} and P_{ms} are the actual and measured dose rates, respectively.

However, for most surveys of radioactively contaminated areas, these errors are not great. This is because the dose-rate variations during a fraction of a second (that is, during a time comparable to the time constant of the instrument) are negligible (less than 5 or 10% of the measured values) for flight speeds from 50 to 80 m/sec. The smallness of these variations is due to the large extent of the regions of radioactive contamination.

2. In order to measure accurately the dose rate (in r/hr) in the air over a site contaminated by radioactive products, the gamma-ray collector should

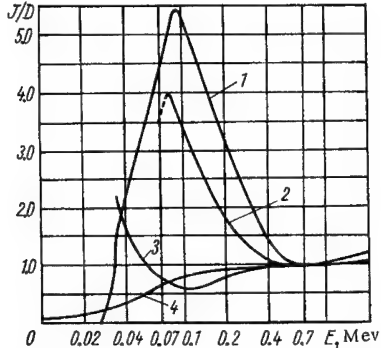


FIGURE 65. Relative-response curves for most common radiation detectors:

- 1) NaI (Tl) crystal 25 × 25 mm in size;
- 2) counter with copper cathode;
- 3) Sakharov counter;
- 4) organic crystal.

be made of an air-equivalent material having the same effective atomic number as air (for $E \leq 2.5$ Mev, Z_{eff} for air is 7.64 /12/). An example of a good air-equivalent gamma-ray collector is a thimble chamber with walls of lucite, bakelite, graphite, etc.

However, for most of the gamma-ray detectors used in practice, the ratio of the detector readings (J) to the readings of an air-equivalent detector (D) varies with the gamma-ray energy. This makes it very difficult to obtain accurate dosimetric measurements when the spectral composition of the radiation is not known.

Figure 65 shows the ratio J/D as a function of the gamma-ray energy (the relative-response curve of the detector) for the most common types of radiation detectors. The curves are normalized arbitrarily to unity for $E = 0.6$ Mev, where

photoelectric effect and pair production are virtually absent.

Curves 4 and 1, corresponding to organic and inorganic crystals, were plotted using the data of /12/, the quantity J being proportional to the current at the output of the scintillation counter. Curve 2, for a Geiger counter with a copper cathode, was plotted from data in /202/, and curve 3, for a Sakharov counter (type 400-SBM-2, with a special case), was plotted using data in /203/. For the counters, J refers to the counting rate, and the ratio J/D is also normalized to unity for an energy of 0.6 Mev.

It is evident from Figure 65 that, of all the radiation detectors considered, the ones closest to being air-equivalent over a wide energy range are an organic scintillating crystal of small dimensions and the Sakharov counter, which was developed specially for dosimetric purposes.

In order to evaluate the measurement errors caused by the detector not being air-equivalent, it is necessary to know the spectral composition of the gamma radiation at the height of the measurements. The latter composition will differ considerably from the primary spectral makeup of the mixture of radioactive isotopes making a large contribution to the scattered radiation.

Let us assume that the relative-response curve $\frac{J}{D}(E) = \xi(E)$ of the gamma-ray detector (see Figure 65) and the spectral composition of the gamma radiation over a surface are known. Then it is easy to determine the ratio of the readings of an instrument with such a detector to the readings of an air-equivalent instrument at a point over the contaminated surface:

$$\chi^s(h, E_0) = \frac{\int_0^{E_0} [J(\mu_0 h, E_0, E)] \cdot \xi(E) \sigma_a(E) dE}{\int_0^{E_0} [J(\mu_0 h, E_0, E)] \cdot \sigma_a(E) dE}, \quad (122)$$

where $J(\mu_0 h, E_0, E)$ is the spectral composition of the gamma radiation at a height h (including both scattered and unscattered gamma rays), and $\sigma_a(E)$ is the absorption coefficient for an energy E in air.

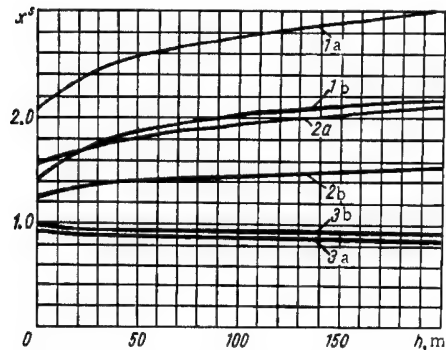


FIGURE 66. Correction factor for detector that is not air-equivalent, as function of height, for dose-rate measurements above isotropic plane source. Curves pertain to different detectors:

- 1) NaI (Tl) crystal; 2) Geiger counter with copper cathode; 3) organic crystal; curves a correspond to $E_0 = 0.5$ Mev and curves b to 1.0 Mev.

Curves of $\chi^*(h, E_0)$ for organic and inorganic crystals 25 mm thick are shown in Figure 66, together with curves for a Geiger counter with a copper cathode. The curves pertain to different heights above an isotropic plane source and to energies E of 0.5 and 1 Mev. For the organic crystal the curves of $\chi^*(h, E)$ for heights from 1 to 200 m stay close to unity.

Using the data of Figure 65, formula (122) can be employed to calculate χ^* for the different kinds of radiation detectors at various heights above a surface contaminated with fission products, for some hours after an explosion. The values calculated in this way for an organic crystal or a Geiger counter with a copper cathode turn out to be close to the values for $E = 1$ Mev.

Let us designate as $\omega(h)$ the ratio between height conversion factors $K_1(h)$ determined for air-equivalent radiation detectors and detectors that are not air-equivalent:

$$\omega(h) = \frac{[K_1(h)]_{\text{not air}}}{[K_1(h)]_{\text{air}}} \quad (123)$$

Figure 67 shows this ratio ω as a function of height, for the different types of radiation detectors (for $E = 1$ Mev).

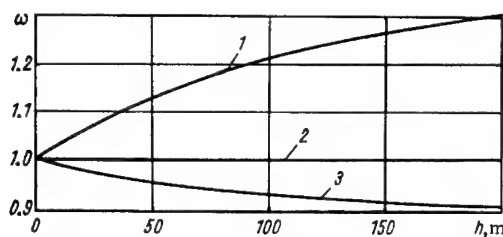


FIGURE 67. Ratio of height conversion factors for detectors that are not air-equivalent to factors for air-equivalent detectors, as function of height:

- 1) for Geiger counter with copper cathode; 2) for air-equivalent detector; 3) for organic crystal 25 mm thick.

Naturally, corrections must also be introduced for detectors which are not air-equivalent when determining the total amount of matter in a contaminated region. These corrections may be found as follows. The total amount of matter is first computed using formula (113), from the data obtained with an instrument having a radiation collector which is not air-equivalent. Obviously, the measured values

$$P(h)_{ms} \text{ and } (L_H)_{ms} = \int_0^{\infty} [K_H(h)]_{ms} dh$$

will differ from the actual values $P(h)$ and L_H . For example, for $H=1\text{ m}$ and an ideally even surface, an instrument with copper-cathode Geiger counters gives the value $E=64\text{ m}$ for $L_H=0.8\text{ Mev}$ (instead of the value of 55 m for an air-equivalent detector).

Let us designate as A_{ms} the value calculated with formula (113). The true value A can be found using the relation

$$A = A_{ms} \cdot \frac{L_H}{\chi^s(H, E) \frac{2}{k} \int_0^{\infty} K_H(h) \frac{\omega(h)}{\omega(H)} dh}, \quad (124)$$

where $\chi^s(H, E)$ and $\omega(h)$ are determined from Figures 66 and 67. For example, for an instrument with copper-cathode Geiger counters, for $H=1\text{ m}$ and $E=1.0\text{ Mev}$, we obtain $\chi^s \approx 1.4$ and $A \approx 0.62 A_{ms}$, while for an organic crystal (such as stilbene) $\chi^s \approx 1.0$ and $A \approx A_{ms}$.

3. Finally, let us consider the errors related to nonuniform shielding of the radiation detector by the aircraft (or by other shields). For this, it is necessary to know the spectral-angular characteristics of the gamma-ray field at the point of measurement, as well as the amount the body of the aircraft (and the instrument cases) shield the detector for various energies and directions.

We designate as $F(\mu_0 h, E_0, E, \theta, \varphi)$ the gamma-ray distribution over an isotropic plane source, as a function of the directions and energies. Function $\Phi(E, \theta, \varphi)$ represents the shielding by the aircraft (in polar coordinates). Function $J(\mu_0 h, E_0, E)$ is the spectral distribution of gamma-ray intensity. The ratio of the readings of a real (air-equivalent) instrument mounted on an aircraft to the readings of an ideal instrument with an isotropic air-equivalent detector may now be expressed as

$$\frac{J_{anis}}{J_{is}} = \frac{\int_0^{E_0} \int_0^{2\pi} \int_0^{\pi} \sigma_a(E) F(\mu_0 h, E_0, E, \theta, \varphi) \Phi(E, \theta, \varphi) dE d\varphi d\theta}{\int_0^{E_0} \sigma_a(E) [J(\mu_0 h, E_0, E)] dE}. \quad (125)$$

Angle φ is reckoned in a plane parallel to the earth's surface, and angle θ in a plane perpendicular to this.

As an example, let us make a rough estimate of J_{anis}/J_{is} for optimum mounting of a detector aboard one of the largest cargo aircraft which can be used for air surveys of gamma radiation (the IL-14). The optimum mounting position (from the point of view of minimum radiation shielding by the aircraft) is assumed to be in the rear of the fuselage, with a 20 to 30 cm detector opening in the hull of the aircraft, via a small port.

A direction of $\varphi = 0^\circ$ is assumed to be the same as the direction of flight, and $\theta = 0^\circ$ is in the direction of a normal to the earth's surface. For simplicity, we write

$$\Phi(E, \theta, \varphi) = e^{-\mu(E)r(\theta, \varphi)} \quad (126)$$

(that is, effects of multiple scattering in the aircraft body will be neglected), $\mu(E)$ is the linear attenuation coefficient for gamma rays of energy E in the airframe, and $r(\theta, \varphi)$ is the linear effective shielding thickness in direction (θ, φ) .

Figure 68 shows a plot of $r(\theta, \varphi)$ as a polar stereographic projection for the IL-14 aircraft (for the upper hemisphere, with $\theta \geq \pi/2$). Lines of equal effective shielding thickness (isolines) are shown in mm aluminum. For $\theta < \pi/2$, $r(\theta, \varphi) = 0$. The data in the graph were calculated after careful measurements of the corresponding shields on drawings of the aircraft. The calculations were made for a primary gamma-ray energy $E_0 = 1$ Mev and for heights h of 1 and 125 m.

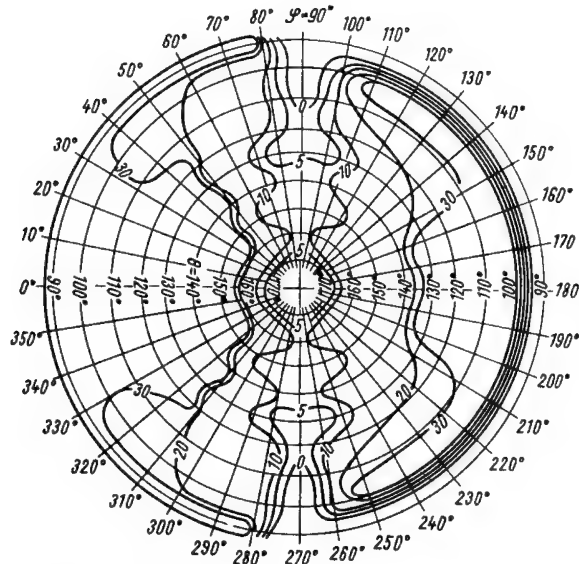


FIGURE 68. Effective shielding thickness in IL-14 aircraft, as function of direction (θ, φ) , for upper hemisphere (in mm aluminum).

The spectral-angular distribution $F(\mu_0 h, E_0, E, \omega)$ over an isotropic plane source is described in /169/, and for $\mu_0 h = 1$ and $E_0 = 1$ Mev function F was plotted back in Figure 30. Values of this function for $E = 0.3$ Mev are found by extrapolating the available data. For $E = 0.1$ Mev the gamma-ray distribution is assumed to be isotropic in space at the point of measurement.

The overall shielding coefficients $\frac{J_{\text{anis}}}{J_{\text{is}}} (h)$ obtained in this way are:

0.95 for $h = 1$ m, and 0.89 for $h = 125$ m. The calculations show that for heights from 1 to 100 m the shielding by the aircraft decreases the readings of the instrument by no more than 10 or 12% (during the calculations, in cases of doubt the conditions corresponding to higher shielding effects were always chosen). The error in determining the height conversion factors will be even less.

Consequently, in gamma-ray surveys over a contaminated area (using aircraft), the most important source of error is the fact that the detector of the roentgen meter is not air-equivalent.

In conclusion, let us note the main advantages (and disadvantages) of making gamma-ray surveys using aircraft, in comparison with other means of measuring the radioactive contamination of a locality. The chief advantage of this method is the high rate at which information is gathered from an extended territory. Other definite advantages are the averaging of the data from each measurement over an area several hundred meters in radius, and the absence of microrelief effects.

The optimum height for an air survey is from 100 to 150 m, since the variation of the dose rate with the primary gamma-ray energy is a minimum for these heights. The disadvantages of a survey using an aircraft are: relative complexity, the necessity for continuous monitoring of flight altitude, and the need to correct the measurements for pressure and temperature changes and for instrument errors.

15. Determination of surface density of contamination by individual isotopes, according to gamma emission in air

A detailed study of the characteristics of the gamma-ray field of an isotropic plane source (the field over a contaminated area) provides data on the surface contamination by individual isotopes σ_i , as well as data on the overall surface contamination σ_s . Such information may be very useful, especially if values of σ_i are obtained together with values of σ_s . Then, it is possible to determine the contribution to the total contaminations of the gamma-emitter isotopes which present the greatest biological hazards (such as I^{131} and Cs^{137}). The contributions of most of these isotopes to the total contamination cannot be determined by theoretical calculations alone, since these isotopes undergo considerable fractionation (see Section 3), and the error in the calculations may be greater than an order of magnitude.

Data on contamination of the earth's surface by radioactive fallout may be obtained by collecting a great number of samples and then analyzing them in the laboratory using scintillation spectrometers or radiochemical methods [39, 200]. However, this method is laborious and time-consuming, and it always leaves some doubt as to whether the samples collected are representative for the area in question. The doubt arises because the area of the sampled surface is, as a rule, a fraction of a square meter, while the sample is supposed to represent a region several thousand square meters in size. Radioactive fallout particles are distributed nonuniformly

over an area /179/. In addition, individual parts of the soil and vegetation accumulate entire fission fragments and individual isotopes differently /130/. Thus it is clear why averaging the measurements over a large territory is so important.

Contamination measurements using a scintillation spectrometer mounted aboard a plane or helicopter do not have these shortcomings. Such measurements are operational, since during a short period an air survey can cover an area of several thousand km². A particularly valuable aspect of an air survey is the averaging of the data over the flight-path region for the time of spectrum exposure. However, a disadvantage of this method is the need to introduce a greater number of corrections than in the case of laboratory analyses. Another disadvantage is the impossibility of obtaining reliable data on isotopes having their fundamental gamma-emission lines at energies below 300 kev (for example, Ce¹⁴¹, Ce¹⁴⁴, etc.), for a mixture of fission products of any age.

The described method is justified in cases where there is a need for determining rapidly the nature and degree of contamination created by a transient source. Examples of such cases are the reactor accident at Windscale /183/ and determinations of contamination characteristics for surface /100/ and underground /100, 188/ nuclear explosions detonated in the USA.

The measuring equipment mounted on the plane or helicopter is approximately the same as the complex described back in Section 10. The main practical problem to be solved by airborne gamma-ray spectrometry is to determine the surface density of contamination by individual isotopes. For this, a single-valued relationship must be found between the measured gamma-ray spectra, obtained with an isotropic or shielded detector at a flight altitude h , and the characteristics of the contamination of the site.

The measured spectrum (the distribution of pulse amplitudes at the analyzer output) is related to the true differential spectrum of the gamma rays incident on the detector by the Fredholm integral equation /147/ (see formula (75) in Section 11). The true spectrum of the gamma rays over a plane source consists of an unscattered component, which produces Gaussian peaks in the measured spectrum, and also a continuous distribution caused by Compton scattering of gamma rays in air.

When the contamination of a site is due to several gamma-ray emitters, it is difficult to separate their continuous distributions, in both the measured and true spectra. At the same time, the photopeaks in the measured spectra, corresponding to the unscattered component, are as a rule readily resolvable. Therefore, for quantitative studies, the photopeaks are the most useful parts of the measured spectra.

The true spectrum of the gamma rays incident upon the detector (number of gamma-ray quanta in the energy interval) is

$$J(\mu_0 h, E_0, E) = J_0(\mu_0 h, E_0) \delta(E - E_0) + J_s(\mu_0 h, E_0, E). \quad (127)$$

In this formula the spectrum is divided into a component of gamma rays scattered in the air $J_s(\mu h, E_0, E)$ and an unscattered component $J_0(\mu_0 h, E_0)$.

The integral

$$\begin{aligned} \int_0^{E_0} J(\mu_0 h, E_0, E) dE &= J_0(\mu_0 h, E_0) + \\ &+ \int_0^{E_0} J_s(\mu_0 h, E_0, E) dE \end{aligned} \quad (128)$$

indicates the total number of quanta incident upon the detector. Now let us substitute the values for $k(E', E)$ from Section 11 and the values for $J(\mu_0 h, E_0, E)$ from formula (127) into equation (75). A photopeak in the measured spectrum is then described by the formula

$$\begin{aligned} S_{ph}(\mu_0 h, E_0, E') &= \int_0^{E_0} [J_0(\mu_0 h, E_0) \delta(E - E_0) \times \\ &\times \int_0^{\infty} g(E', \xi) P(E) \delta(\xi - E) e(E) d\xi] dE \end{aligned} \quad (129)$$

or

$$S_{ph}(\mu_0 h, E_0, E') = g(E', E_0) \eta(E_0) J_0(\mu_0 h, E_0), \quad (130)$$

where $g(E', E_0)$ is a Gaussian distribution about the energy E_0 , normalized in such a way that

$$\int_0^{\infty} g(E', E_0) dE' = 1;$$

and $\eta(E_0)$ is the photoeffectiveness of the spectrometer for a gamma-ray energy E_0 , equal to the product of the total effectiveness times the photocontribution.

One of the multiplying factors in formula (130) is the intensity of unscattered gamma-ray quanta incident upon the crystal, a quantity depending on the distance from the source. The number of quanta incident upon the crystal will be affected considerably by the size, shape, and position of the crystal.

NaI(Tl) and CsI(Tl) crystals are almost always made in the shape of cylinders. When they are used on planes or helicopters, the crystals are mounted so that their end faces are parallel to the earth's surface. Let us designate as J_u^{\parallel} the number of unscattered gamma-ray quanta (direct gamma rays) per unit time that intersect a unit area lying parallel to an infinite isotropic plane source at a height h . The medium is assumed to be homogeneous (air, in our case). It is not difficult to show that

$$J_u^{\parallel} = \frac{N_0}{2} E_2(\mu_0 h), \quad (131)$$

where N_0 is the number of gamma-ray quanta of energy E_0 emitted by a unit area of the isotropic source (per unit time).

Similarly, it can be shown that the number J_u^{\perp} of unscattered gamma-ray quanta per unit time passing into one side of a unit area lying perpendicular to the source is

$$J_u^{\perp} = \frac{N_0}{2\pi} \int_{\mu_0 h}^{\infty} \frac{e^{-u}}{u^2} \sqrt{u^2 - \mu_0^2 h^2} du. \quad (132)$$

Let us designate the end face of the crystal as S_e and the lateral face as S_l . The contamination from the isotropic plane source is due to a gamma-ray emitter with an energy E_0 , and the contamination density is N_0 . Then, the number J_u of unscattered gamma-ray quanta passing through the lower end face and lateral face of the crystal will be

$$J_u = \frac{N_0 S_e}{2} E_2(\mu_0 h) + \frac{N_0 S_l}{2\pi} \int_{\mu_0 h}^{\infty} \frac{e^{-u}}{u^2} \sqrt{u^2 - \mu_0^2 h^2} du. \quad (133)$$

The conversion from the formula for an area perpendicular to the emitting surface to the lateral side of a cylinder follows a definite law. This is because the side can be replaced by the lateral surface of a parallelepiped whose base is a polygon with a number of sides approaching infinity. The intensity of the radiation incident upon each face of this parallelepiped is determined by formula (132).

Formula (133) can be used to find the ratio of the effect of unscattered gamma rays on a cylindrical detector to the corresponding effect on an isotropic (spherical) detector.* If the diameter of the cylinder equals its height, while the volumes of the cylindrical and spherical detectors are the same, the ratio of the effects will be

$$\begin{aligned} \frac{J_c}{J_{sp}} &= \frac{\frac{J_e + J_l}{J_{sp}}}{\frac{0.79 E_2(\mu_0 h) + 0.5}{E_1(\mu_0 h)}} = \\ &= \frac{0.79 E_2(\mu_0 h) + 0.5}{E_1(\mu_0 h)} \int_{\mu_0 h}^{\infty} \frac{e^{-u} \sqrt{u^2 - \mu_0^2 h^2}}{u^2} du. \end{aligned} \quad (134)$$

A curve showing J_c/J_{sp} as a function of the height μh is plotted in Figure 69 (curve 1). The same figure shows J_e/J_{sp} (curve 2) and J_l/J_{sp} (curve 3) as functions of μh . The ratio J_c/J_{sp} is seen to be close to unity, especially for $\mu h > 0.5$ (it is around 0.9). Consequently, the fundamental equation relating the density of surface contamination N_0 to the photopeak intensity S ($\mu_0 h, E_0$) in the spectrogram, at a height h in air, can be written as

$$\begin{aligned} S(\mu_0 h, E_0) &= \eta(E_0) \left[\frac{S_e}{2} E_2(\mu_0 h) + \right. \\ &\quad \left. + \frac{S_l}{2\pi} \int_{\mu_0 h}^{\infty} \frac{e^{-u} \sqrt{u^2 - \mu_0^2 h^2}}{u^2} du \right] N_0. \end{aligned} \quad (135)$$

* Assuming the spherical and cylindrical detectors are equally effective in recording gamma rays.

Equation (135) shows the result of solving the direct problem, namely calculating the counting rate in the photopeak of a measured gamma-ray spectrum from the known density N_0 of surface contamination of a locality (in units of quanta/(cm².sec)) and the gamma-emission energy E_0 of the source.

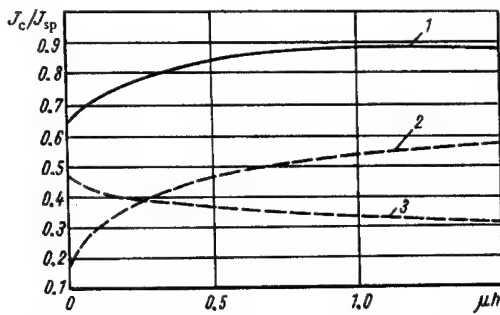


FIGURE 69. Ratio of effects of cylindrical and spherical scintillation crystals of equal volume, as function of height above plane radiation source.

However, the main practical problem in gamma-ray spectrometry, for studies of radioactive contamination using aircraft, is the reverse problem, that is, to determine the density of the surface contamination σ_i by individual isotopes (in curies/km²), from the measured gamma-ray spectrum obtained at a flight altitude h .

For an isotropic (unshielded) detector, the surface density of contamination σ_i is given by the formula

$$\sigma_i = \frac{S(\mu_0 h, E_0) F(h, h_0, E_0)}{K_i E_0 K(h_0, E_0)}, \quad (136)$$

where $S(\mu_0 h, E_0)$ is the counting rate in a photopeak with an energy E_0 (photopeak "intensity"), in a spectrogram obtained at flight altitude h ; $F(h, h_0, E_0)$ is the coefficient of reduction of the photopeak intensity $S(\mu_0 h, E_0)$ to a height $h=h_0$, K_{iE_0} is the quantum yield of the gamma-emission line with an energy E_0 , for the i th isotope; $K(h_0, E_0)$ is a coefficient representing the ratio between the intensity of a photopeak with energy E_0 at height h_0 and the density of surface contamination by an isotope having a gamma-emission line at energy E_0 and a quantum yield of unity.

The photopeak intensity $S(\mu_0 h, E_0)$ can be found directly from an analysis of the measured spectrum. It is equal to the ratio between the photopeak area on the spectrogram and the exposure time of the gamma-emission spectrum; this intensity is usually measured in pulses per second.

The quantum yield K_{iE_0} for a given gamma-emission line has a subscript i , indicating that the photopeak at E_0 on the spectrogram pertains to the i th isotope. Identifying the lines is a complicated operation,

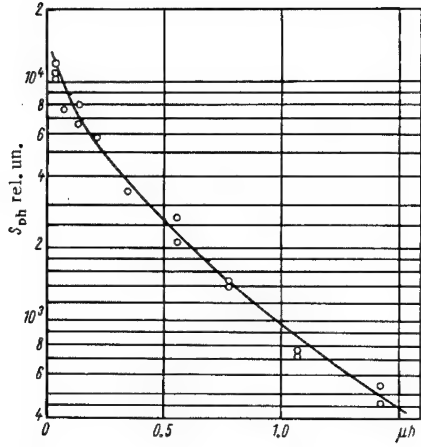


FIGURE 70. Photopeak intensity (at 1330 kev), as function of height.

closely related to the concept of the "age" of a mixture of fragments (see Sections 1 and 4). For unidentified gamma emitters the contamination density σ_i (in curies per km^2) can be determined only if the quantum yield K_{iE_0} is accurately known.

Coefficient $K(h_0, E_0)$ can be determined from measurements over a contaminated surface or over an area simulating a contaminated locality. The coefficient for converting the photopeak intensity $S(\mu_0 h, E_0)$ to the "standard" height $h = h_0$ will be equal to the ratio between the photopeak intensities at heights h_0 and h :

$$F(h, h_0, E_0) = \frac{S(\mu_0 h_0, E_0)}{S(\mu_0 h, E_0)}. \quad (137)$$

In practice, coefficient $F(h, h_0, E)$ is found from the experimentally determined curve for the photopeak intensity as a function of height [see Figure 70]. This curve is obtained as follows. Successive runs are made by the aircraft at different heights over the same part of the contaminated site. Simultaneous recordings are made of the gamma-emission spectrum and the gamma-ray intensity (dose rate) between specified reference points, the flight altitude being recorded as well. It is advisable for the flight path to be chosen over an area where the radiation-intensity gradient along the flight path is small (this is always possible in practice).

Figure 70 shows data points for the photopeak intensity at an energy of 1330 kev, as a function of height. The radiation detector was isotropic, with an NaI(Tl) crystal 100 × 100 mm in size. The calculated curve for $E_1(\mu h)$ is also shown. The good fit between the experimental and calculated data indicates that when necessary the calculated curve can be used.

The standard height h_0 is selected sufficiently arbitrarily that the error introduced into the measurement results may be kept minimal. Thus, this height must be so chosen that the true flight altitude during the survey is close to the standard height; consequently, $F(h, h_0, E_0)$ should be close to unity. For $h > h_0$, we have $F > 1$; conversely, for $h < h_0$, we have $F < 1$.

It follows from equation (136) that calibration coefficient $K(h_0, E_0)$ may be written as

$$K(h_0, E_0) = \frac{S(\mu_0 h_0, E_0) F(h, h_0, E_0)}{\sigma_i K_{iE_0}}, \quad (138)$$

and for the standard height

$$K(h_0, E_0) = \frac{S(\mu_0 h_0, E_0)}{\sigma_i K_{iE_0}}. \quad (139)$$

Here, if the contamination density σ_i is in curies/ km^2 and the photopeak intensity is in pulses/sec, coefficient $K(h_0, E_0)$ will be in $\text{pulse} \cdot \text{km}^2 / (\text{curie} \cdot \text{sec})$.

As noted previously, to determine $K(h_0, E_0)$ experimentally, we must have an infinite isotropic plane source with a precisely known contamination density. With respect to this, flights with a spectrometer mounted aboard a helicopter are useful. The flights are made over artificially contaminated areas, such as the ones described in Section 10. The values of $K(h_0, E_0)$ so obtained are calculated using formula (139).

Appendix

GAMMA EMISSIONS OF PRINCIPAL FISSION-FRAGMENT ISOTOPES

The gamma emission of a mixture of fission products at any time after the fission may be characterized by an energy value related to the quantum yield per unit time (the energy intensity of the gamma emission) or by the number of gamma-ray quanta emitted during the time interval in question (the numerical intensity of the gamma emission).*

Some other important characteristics of the gamma emission of a mixture of fission products or of any individual gamma emitter are: the mean gamma-emission energy \bar{E}_γ , the total quantum yield per disintegration \bar{K}_γ , and the gamma-emission intensity per disintegration $I_\gamma = \bar{E}_\gamma \bar{K}_\gamma$. In order to calculate these quantities for an entire isotope mixture, data on the gamma emissions of the individual isotopes making up the mixture are necessary. The most interesting such data are the energies and the absolute quantum yields of the gamma-emission lines.

The table in this appendix lists the differential and integral gamma-emission characteristics for the principal fission-fragment isotopes. The differential quantities given are the energies $E_{\gamma i}$ and the quantum yields $K_{\gamma i}$ for individual gamma-emission lines of the isotope in question, together with the product of these, the differential intensity of the i th gamma-emission line $I_{\gamma i} = E_{\gamma i} K_{\gamma i}$.

The integral gamma-emission characteristics for the isotopes were calculated as follows: the gamma-emission intensity of an isotope having n emission lines in one disintegration is

$$I_\gamma = \sum_{i=1}^n E_{\gamma i} K_{\gamma i} = \sum_{i=1}^n I_{\gamma i}; \quad (\text{A.1})$$

the total quantum yield is

$$\bar{K}_\gamma = \sum_{i=1}^n K_{\gamma i}; \quad (\text{A.2})$$

* The number of gamma-ray quanta also includes the X rays (K component) emitted by the excited atom shell after the nuclear transformations.

and the mean gamma-emission energy of the isotope is

$$\bar{E}_\gamma = \frac{I_\gamma}{K_\gamma} . \quad (\text{A.3})$$

The table gives the parameter for 125 isotopes. Each of these /49/ contributes at least 0.1% of the total gamma activity of the entire mixture, over some period of time beginning 1 hour to 100 years after fission (the mixture referred to is the unfractionated mixture of fission-fragment isotopes).

The table can also be used to calculate and construct differential gamma-ray spectra for the entire range of ages indicated. In addition, the table [see column 9] contains data on the reliability of results obtained from such calculations, since these are related to the reliability of the data on the decay schemes for individual isotopes.

Column 1 of the table lists the isotope with its mass number. The position of the isotope in the table is governed by the value of the mass number (lower mass numbers first). Column 2 gives the half-lives, taken from /201 a/ for isotopes with $A < 100$ [where A is the mass number] and from /202 a/ for $A \geq 100$.

The energies of the gamma-ray quanta are given in column 3. In this column are also shown the lines corresponding to mean energies of the X-ray K component, for isotopes having significant internal-conversion coefficients for the K shell. The mean K -component energies for these isotopes were taken from /203 a/, and these entries in the table are indicated by the symbol X_K . For some isotopes possessing many gamma-emission lines, quantum energies corresponding to quantum yields less than 1/50 of the yields of the predominant lines of the isotope are not included.

Column 4 lists the quantum yields for the gamma-emission lines. The quantum yield $K_{\gamma i}$ is the number of gamma-ray quanta leaving the shell of the daughter atom during one decay of a parent nucleus. This definition is given here because, in most general studies of decay schemes /166, 201 a, 202 a, 204, 207/, the numbers of nuclear gamma transitions with a given energy for one nuclear decay are given, instead of the quantum yields. Consequently, for those isotopes having nuclear transitions with experimentally determined conversion coefficients for the K and L shells, we calculated the quantum yields of the K component of the gamma-emission X rays.

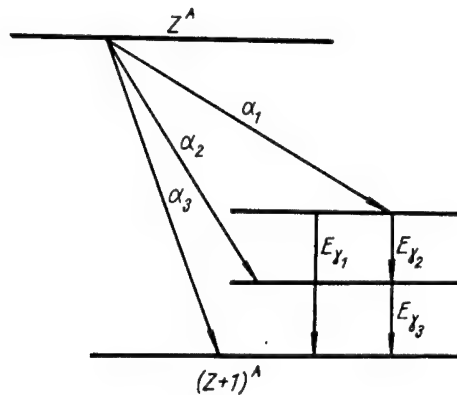
The following formulas are used to convert from the number of nuclear gamma transitions $n_{\gamma i}$ to the quantum yields:

$$K_{\gamma i} = \frac{n_{\gamma i}}{1 + \alpha_{Ki} \frac{\beta_i}{\beta_i + 1}} ; \quad (\text{A.4})$$

$$K_{X_K} = \sum_i K_{\gamma i} W_{Ki} \alpha_{Ki}, \quad (\text{A.5})$$

where β_i is the ratio of the conversion coefficient for the K shell to the sum of the conversion coefficients for the L and M shells; α_{Ki} is the internal-conversion

coefficient for the given gamma transition for the K shell (if α_{K_i} for the gamma transition is known, but not β_i , then the latter is assumed to be unity); and W_K is the fluorescence yield for the K shell, that is, the relative probability that occupation of a free site in the K shell will be accompanied by the emission of X rays. The values of W_K used were taken from /203a/.



Beta-decay scheme for nucleus Z^A .

Sometimes absolute numbers of beta transitions, but only relative numbers of the nuclear gamma transitions, were given in the literature. In such cases the absolute magnitudes of the quantum yields for the gamma-emission lines were calculated on the basis of knowledge of both these quantities from successive equations. Let us illustrate this by an example.

The decay scheme of a nucleus Z^A (see figure) has known absolute numbers of beta transitions to excited and ground levels of the daughter nucleus $(Z+1)^A$; these coefficients α_1 , α_2 , and α_3 are given in percent, so that $\alpha_1 + \alpha_2 + \alpha_3 = 100\%$.

It is also known that the relative numbers of nuclear gamma transitions are equal, that is, $n_{\gamma_1} : n_{\gamma_2} : n_{\gamma_3} = \beta_1 : \beta_2 : \beta_3$. On the basis of these data, together with the transition scheme, we can write two equations:

$$K_1(\beta_1 + \beta_2) = 0.01\alpha_1; \quad (\text{A.6})$$

$$K_2\beta_3 = 0.01\alpha_2 + K_1\beta_2. \quad (\text{A.7})$$

The unknown quantities in these equations are the proportionality coefficients K_1 and K_2 . If the data on the beta and gamma transitions are inconsistent, then the following relation must be satisfied:

$$K_1 = K_2 \equiv K. \quad (\text{A.8})$$

From this it is evident that the absolute numbers of gamma transitions, expressed in fractions, are:

$$\begin{aligned} n_{\gamma_1} &= K\beta_1; \\ n_{\gamma_2} &= K\beta_2; \\ n_{\gamma_3} &= K\beta_3. \end{aligned} \quad (\text{A.9})$$

The numbers of gamma transitions found using formulas (A.9), including the conversion coefficients, were calculated using formula (A.4) for the values of the quantum yields, which were also taken to be true.

The accuracies of the relative quantum yields given in the literature or calculated by us were checked for 45 isotopes. To do this, the areas of photopeaks in the measured spectra obtained in /208/ were compared. These spectra were taken with a gamma-ray spectrometer having an NaI(Tl) crystal 102×102 mm in size, the resolution of the spectrometer being 9.5%. The criterion for this check was satisfaction of the relation

$$K_{\gamma_1}:K_{\gamma_2}:K_{\gamma_3} \dots = \frac{S_1}{\eta_1} : \frac{S_2}{\eta_2} : \frac{S_3}{\eta_3} \dots \quad (\text{A.10})$$

where S_1 , S_2 , and S_3 are the photopeak areas in relative units, taken from /208/; and η_1 , η_2 , and η_3 are the photoeffectivenesses for a crystal 100×100 mm in size, taken from /183/. All the isotopes for which the accuracies of the relative yields were checked in this way have the number /208/ in column 10.

Column 5 of the table gives the products of the corresponding quantities in columns 3 and 4, that is, the differential intensities of the individual gamma-emission lines (in Mev/disint). Column 6 lists the sums of the differential intensities of all the lines for each isotope, that is, the gamma-emission intensity of the isotope (in Mev/disint).

Column 7 gives the sums of the total numbers of gamma-ray quanta and X_K rays emitted by the isotope in one nuclear disintegration. Column 8 lists the mean gamma-ray energies for each isotope.

Column 9 shows the degree of reliability of the data cited, according to data on the reliabilities of the quantum yields. The letters in this column indicate the following: A means that the quantum energies and the absolute quantum yields (or the absolute number of gamma transitions) are given in the literature; B means that the gamma-ray energies, the absolute numbers of beta particles per disintegration, and the relative numbers of gamma transitions are given in the literature; and C means that the gamma-ray energies and quantum yields are either unknown or are only relative to the number of gamma transitions, which have no relation to the absolute numbers of beta particles. Finally, column 10 lists the references used.

Differential and integral gamma-emission characteristics for principal fission-fragment isotopes

| Isotope | Half-life | Energy of quanta E_{γ} , Mev | Quantum yield disint $^{-1}$ | Differential intensity I_{γ_i} , Mev/disint | Gamma-emission intensity of isotope per disintegration I_{γ_i} , Mev/disint | Total quantum yield of isotope \bar{K}_{γ} , disint $^{-1}$ | Mean gamma-emission energy of isotope \bar{E}_{γ} , Mev | Reliability | References |
|-------------------|------------|---|--|--|--|--|--|-------------|----------------|
| Se ⁸³ | 25 min | 0.95 0.176 0.061 0.04 | No data | | | | | C | 201a |
| Br ⁸³ | 2.3 hr | 0.051 | 0.035 | 0.0018 | 0.0018 | 0.035 | 0.051 | B | 166, 201a, 209 |
| Kr ^{83m} | 114 min | 0.033 0.009 | Very low *1 | | | | | B | 166, 201a, 209 |
| Br ⁸⁴ | 31.8 min | 3.93 3.28 3.03 2.82 2.47 2.17 2.05 1.9 1.74 1.57 1.47 1.21 1.01 0.88 0.81 0.74 0.61 0.52 0.47 0.43 0.35 0.27 | 0.14 0.034 0.045 0.023 0.09 0.023 0.023 0.20 0.023 0.011 0.023 0.046 0.11 0.56 0.10 0.039 0.028 0.034 0.011 0.028 0.017 0.0060 0.006 | 0.55 0.11 0.14 0.065 0.22 0.050 0.047 0.38 0.040 0.017 0.034 0.056 0.11 0.49 0.081 0.029 0.017 0.018 0.0052 0.012 0.0060 0.0016 | | 1.61 | 1.54 | B | 201a |
| Kr ^{85m} | 4.36 hr | 0.305 0.149 | 0.14 0.74 | 0.043 0.11 | 0.15 | 0.88 | 0.17 | B | 201a |
| Kr ⁸⁵ | 10.3 years | 0.517 | ~0.0065 | 0.0034 | 0.0034 | 0.0065 | 0.52 | B | 166, 201a, 208 |
| Kr ⁸⁷ | 78 min | 2.57 2.05 0.85 0.403 | 0.21 0.04 0.11 0.91 | 0.54 0.082 0.094 0.37 | 1.08 | 1.27 | 0.85 | B | 201a |
| Kr ⁸⁸ | 2.8 hr | 2.4 1.55 0.85 0.36 0.191 0.166 0.028 | 0.35 0.14 0.23 0.049 0.35 0.07 0.07 | 0.84 0.22 0.20 0.018 0.067 0.012 0.002 | 1.35 | 1.26 | 1.07 | B | 201a, 209 |
| Rb ⁸⁸ | 17.8 min | 4.87 3.68 3.52 3.24 3.01 2.68 2.11 1.85 | 0.0029 0.0008 0.0023 0.0029 0.0029 0.023 0.0093 0.207 | 0.014 0.003 0.0081 0.0094 0.0087 0.062 0.020 0.38 | 0.64 | 0.39 | 1.63 | B | 201a, 209 |

| Isotope | Half-life | Energy of quanta E_{γ_i} , Mev | Quantum yield disint $^{-1}$ | Differential intensity I_{γ_i} , Mev/disint | Gamma-emission intensity of isotope per disintegration I_{γ_i} , Mev/disint | Total quantum yield of isotope \bar{K}_{γ_i} , disint $^{-1}$ | Mean gamma-emission energy of isotope \bar{E}_{γ_i} , Mev | Reliability | References |
|-------------------|-----------|---------------------------------------|------------------------------|--|--|--|--|-------------|--------------------------|
| Rb ⁸⁹ | 15.4 min | 1.39 | 0.012 | 0.017 | | B | 201a, 209 | | |
| | | 0.908 | 0.13 | 0.12 | | | | | |
| | | 3.52 | 0.022 | 0.077 | | | | | |
| | | 2.75 | 0.027 | 0.074 | | | | | |
| | | 2.59 | 0.13 | 0.34 | | | | | |
| | | 2.20 | 0.14 | 0.31 | | | | | |
| | | 1.55 | 0.037 | 0.057 | | | | | |
| Sr ⁸⁹ | 50.5 days | 0.915 | ~0.0001 | 0.0001 | 0.0001 | 0.0001 | 0.915 | A | 166, 201a |
| Sr ⁹⁰ | 28 years | No gamma emission | | | | | | A | 166, 201a |
| Y ⁸⁹ | 64.2 hr | 1.734 | ~0.0002 | 0.00035 | 0.00035 | 0.0002 | 1.734 | A | 166, 201a |
| Sr ⁹¹ | hr | 1.413 | 0.07* ^a | 0.099 | | B | 201a, 208 | | |
| | | 1.025 | 0.30 | 0.31 | | | | | |
| | | 0.93 | 0.03 | 0.028 | | | | | |
| | | 0.748 | 0.29 | 0.22 | | | | | |
| | | 0.645 | 0.14 (0.08) | 0.090 | | | | | |
| Y ^{91m} | 50.3 min | 0.551 | 0.94 | 0.52 | 0.52 | 0.94 | 0.551 | B | 166, 201a, 209 |
| Y ⁹¹ | 57.5 days | 1.19 | 0.002 | 0.0024 | 0.0024 | 0.002 | 1.19 | A | 166, 201a, 208 |
| Sr ⁹² | 2.6 hr | 1.37 | 0.90 | 1.23 | | B | 201a, 208 | | |
| | | 0.44 | 0.04 | 0.018 | | | | | |
| | | 0.23 | 0.035 | 0.0080 | | | | | |
| Y ⁹² | 3.6 hr | 2.4 | 0.002 | 0.0048 | | B | 201a, 210 | | |
| | | 1.9 | 0.01 | 0.019 | | | | | |
| | | 1.45 | 0.10 | 0.14 | | | | | |
| | | 0.94 | 0.19 | 0.18 | | | | | |
| | | 0.48 | 0.11 | 0.053 | | | | | |
| Sr ⁹³ | 8.2 min | 0.21 | 0.10 | 0.021 | 0.42 | 0.51 | 0.82 | C | 166, 201a, 209 |
| | | No data | | | | | | | |
| Y ⁹³ | 10.4 hr | 2.14 | 0.009 | 0.019 | | B | 166, 201a | 201a | |
| | | 1.88 | 0.022 | 0.041 | | | | | |
| | | 1.40 | 0.010 | 0.014 | | | | | |
| | | 1.15 | 0.005 | 0.0058 | | | | | |
| | | 0.94 | 0.036 | 0.034 | | | | | |
| | | 0.68 | 0.015 | 0.010 | | | | | |
| | | 0.455 | 0.003 | 0.0014 | | | | | |
| Y ⁹⁴ | 16.5 min | 0.265 | 0.097 | 0.026 | | C | 166, 201a, 209 | | |
| | | No data | | | | | | | |
| Y ⁹⁵ | 10.5 min | " " | | | | C | 166, 201a, 209 | | |
| | | | | | | | | | |
| Zr ⁹⁵ | 65 days | 0.757 | 0.43 | 0.32 | 0.72 | 0.98 | 0.74 | A | 166, 201a, 209, 211 |
| Nb ^{95m} | 90 hr | 0.724 | 0.55 | 0.40 | | B | 166, 201a, 209, 211 | | |
| | | 0.231 | Very low * ^a | | | | | | |
| Nb ⁹⁵ | 35 days | 0.768 | 1.0 | 0.768 | 0.768 | 1.0 | 0.768 | A | 166, 201a, 208, 209, 211 |
| Zr ⁹⁷ | 17 hr | 1.05 | 0.012 | 0.013 | 0.020 | 0.018 | 1.11 | B | 208, 212 |
| | | 1.15 | 0.006 | 0.0069 | | | | | |
| Nb ^{97m} | 60 sec | 0.75 | 1.0 | 0.75 | 0.75 | 1.0 | 0.75 | A | 166, 201a, 208, 212 |

| Isotope | Half-life | Energy of quanta E_{γ_i} , Mev | Quantum yield κ_i , disint $^{-1}$ | Differential intensity I_i , Mev/disint | Gamma-emission intensity of isotope per disintegration I_γ , Mev/disint | Total quantum yield of isotope $\bar{\kappa}_\gamma$, disint $^{-1}$ | Mean gamma-emission energy of isotope \bar{E}_γ , Mev | Reliability | References |
|--------------------|-----------|---|---|---|--|---|--|-------------|----------------------------------|
| Nb ⁹⁷ | 72.1 min | 0.664 | 0.99 | 0.66 | 0.66 | 0.99 | 0.66 | A | 166, 201a, 208 |
| Mo ⁹⁹ | 66.5 hr | 0.74 0.37 0.18 0.142 | 0.14 0.01 0.04 0.063 | 0.104 0.0037 0.0072 0.0089 | 0.12 | 0.25 | 0.48 | A | 166, 201a, 208, 209, 213, 214 |
| Tc ^{99m} | 6.04 hr | 0.14 0.018 [X _K] | 0.84 0.038 | 0.12 0.00068 | 0.12 | 0.88 | 0.14 | A | 166, 201a, 208, 209, 213, 214 |
| Mo ¹⁰¹ | 14.6 min | 0.704 0.590 0.510 0.080 | 0.054 0.045 0.06 0.10 | 0.038 0.026 0.031 0.008 | 0.10 | 0.25 | 0.40 | B | 201a, 202a, 208 |
| Tc ¹⁰¹ | 14 min | 0.545 0.307 0.130 | 0.076 0.95 0.024 | 0.041 0.29 0.0031 | 0.34 | 1.05 | 0.32 | B | 201a, 202a, 208 |
| Mo ¹⁰² | 11.5 min | No data | | | | | | C | 201a, 202a, 209 |
| Tc ¹⁰² | 5 sec | " " | | | | | | C | 201a, 202a, 209 |
| Ru ¹⁰³ | 39.4 days | 0.61 0.56 0.495 | 0.06 0.005 0.90 | 0.037 0.0028 0.44 | 0.48 | 0.96 | 0.50 | A | 201a, 202a, 208 |
| Rh ^{103m} | 56 min | 0.02 | 0.065 | 0.0013 | 0.0013 | 0.065 | 0.020 | B | 201a, 202a, 208 |
| Ru ¹⁰⁵ | 4.5 hr | 0.97 0.87 0.725 0.67 0.475 0.400 0.317 0.260 | 0.053 0.058 0.51 0.19 0.25 0.035 0.075 0.035 | 0.051 0.050 0.37 0.13 0.120 0.014 0.024 0.0091 | | | | B | 201a, 202a, 208 |
| Rh ^{105m} | 45 sec | 0.13 0.020 [X _K] | 0.17 0.45 | 0.029 0.009 | 0.031 | 0.62 | 0.050 | B | 201a, 202a, 208 |
| Rh ¹⁰⁵ | 36.5 hr | 0.31 | 0.1 | 0.031 | 0.031 | 0.1 | 0.31 | A | 201a, 208 |
| Ru ¹⁰⁶ | 366 days | No gamma emission | | | | | | A | 201a, 202a |
| Rh ¹⁰⁶ | 30 sec | 1.05*3 0.87 0.624 0.513 | 0.015 0.0043 0.11 0.25 | 0.016 0.0037 0.069 0.13 | | | | A | 201a, 202a, 208, 215 |
| Rh ¹⁰⁷ | 21.7 min | 0.68 0.57 0.385 0.305 | 0.025 0.013 0.15 0.84 | 0.017 0.0074 0.058 0.26 | 0.22 | 0.38 | 0.58 | B | 201a, 202a |
| Pd ¹⁰⁹ | 13.5 hr | 0.77 0.64 0.412 0.314 | 0.0002 0.0002 0.0002 0.0002 | 0.0002 0.0001 0.0001 0.0001 | 0.0005 | 0.0008 | 0.62 | A | 201a, 202a, 209 |
| Ag ^{109m} | 41.3 sec | 0.088 0.022 [X _K] | 0.037 0.35 | 0.0032 0.0077 | 0.011 | 0.39 | 0.028 | B | 202a, 208, 209 |

| Isotope | Half-life | Energy of quanta E_{γ_i} , Mev | Quantum yield disint ⁻¹ | Differential intensity I_{γ_i} , Mev/disint | Gamma-emission intensity of isotope per disintegration Mev/disint | Total quantum yield of isotope K_i , disint ⁻¹ | Mean gamma-emission energy of isotope E_{γ} , Mev | Reliability | References |
|--------------------|-------------|--|--|--|---|---|--|-------------|-------------------------|
| Ag ¹¹¹ | 7.6 days | 0.340 0.247 0.023 [X_K] | 0.08 0.01 0.01 | 0.027 0.0025 0.00023 | 0.030 | 0.10 | 0.3 | A | 201a, 208, 209 |
| Pd ¹¹¹ | 22 min | No data | | | | | | C | 201a, 202a |
| Pd ¹¹² | 21 hr | 0.019 | Very low | | | | | B | 201a, 202a |
| Ag ¹¹² | 3.2 hr | 2.83 2.54 2.11 1.83 1.62 1.39 1.090 0.615 | 0.011 0.019 0.062 0.031 0.062 0.10 0.023 0.77 | 0.031 0.048 0.13 0.057 0.10 0.14 0.025 0.47 | | | | B | 202a, 208 |
| Ag ¹¹³ | 5.3 hr | 0.67 0.58 0.30 0.27 0.12 | No data | | 1.00 | 1.08 | 0.92 | C | 201a, 202a, 209 |
| Ag ¹¹⁵ | 21.1 min | 0.138 0.227 | 0.18 0.91*4 | 0.025 0.21 | 0.24 | 1.09 | 0.22 | B | 202a |
| Cd ^{115m} | 43 days | 1.29 0.94 0.49 | 0.01 0.023 0.003 | 0.0129 0.022 0.0015 | 0.036 | 0.036 | 1.0 | B | 201a, 202a, 208, 209 |
| Cd ¹¹⁵ | 53 hr | 0.523 0.49 0.26 0.23 | 0.25 0.12 0.019 0.006 | 0.13 0.059 0.0049 0.0014 | | | | B | 202a, 208 |
| In ^{115m} | 4.5 hr | 0.335 0.024 [X_K] | 0.47 0.32 | 0.16 0.0077 | 0.20 | 0.40 | 0.50 | | |
| Cd ^{117m} | 3.0 hr | 2.25 1.97 1.53 1.27 0.281 0.267 | No data | | | 0.79 | 0.21 | B | 202a, 208 |
| Cd ¹¹⁷ | 50 min | 0.425 | No data | | | | | C | 201a, 202a, 209 |
| In ^{117m} | 1.93 hr | 0.311 0.161 0.024 [X_K] | 0.096 0.21 0.10 | 0.030 0.034 0.0024 | 0.066 | 0.41 | 0.16 | B | 201a, 202a |
| In ¹¹⁷ | 1.1 hr | 0.565 0.161 0.024 [X_K] | 1.0 0.87 0.09 | 0.56 0.14 0.0022 | 0.71 | 1.96 | 0.36 | B | 201a, 202a, 209 |
| In ¹¹⁹ | 17.5 min *5 | No data | | | | | | C | 201a, 202a, 209 |
| Sn ¹²¹ | 28.2 hr | No gamma emission | | | | | | A | 201a, 202a |
| Sn ¹²³ | 40 min | 0.153 0.027 [X_K] | 0.84 0.16 | 0.13 0.0043 | 0.13 | 1.0 | 0.13 | B | 201a, 202a, 209 |

| Isotope | Half-life | Energy of quanta E_{ν_i} , Mev | Quantum yield disint ⁻¹ | Differential intensity $I_{ii} \cdot$ Mev/disint | Gamma-emission intensity of isotope per disintegration $I_{\gamma} \cdot$ Mev/disint | Total quantum yield of isotope $K_{\gamma} \cdot$ disint ⁻¹ | Mean gamma-emission energy of isotope $E_{\gamma} \cdot$ Mev | Reliability | References |
|--|------------------------|--|--|---|--|--|--|-------------|------------------------------------|
| Sn ¹²⁵ | 9.7 days | 1.96 1.41 1.07 0.90 0.81 0.47 0.34 | 0.009 0.002 0.038 0.012 0.011 0.004 0.0028 | 0.018 0.0028 0.041 0.011 0.0089 0.0019 0.0095 | | | | B | 202a, 209 |
| Sb ¹²⁶ | 2.6 years | 0.637 0.595 0.463 0.427 0.377 0.175 | 0.067 0.255 0.09 0.29 0.011 0.055 | 0.043 0.15 0.042 0.12 0.0041 0.0096 | 0.084 | 0.079 | 1.06 | B | 202a, 208 |
| Te ^{125m} | 58 days | 0.110 0.036 0.028 [X _K] | 0.072 0.0034 1.34 | 0.0079 0.00012 0.038 | 0.37 | 0.77 | 0.48 | B | 202a, 208 |
| Sb ^{126m} | 6.2 days | 1.35 1.10 0.90 0.69 0.42 | 0.01 0.05 ^{*6} 0.10 1.0 0.26 | No data | 0.046 | 1.42 | 0.032 | C | 201a, 202a, 209 |
| Sb ¹²⁶ | 18.8 min ^{*7} | 0.65 0.42 | No data | | | | | C | 201a, 202a, 209 |
| Sn ¹²⁷ | 2.05 hr | No data | | | | | | C | 201a, 202a, 209 |
| Sb ¹²⁷ | 88 hr | 0.772 0.463 0.310 0.248 0.060 | 0.22 0.49 0.054 0.13 0.03 | 0.17 0.23 0.017 0.032 0.0018 | 0.45 | 0.92 | 0.49 | B | 201a, 202a |
| Te ^{127m} | 105 days | 0.665 0.089 0.059 0.028 [X _K] | 0.00013 0.001 0.005 0.36 | 0.000086 0.000089 0.00030 0.010 | 0.01 | 0.37 | 0.028 | B | 201a, 202a |
| Te ¹²⁷ | 9.35 hr | 0.418 0.360 0.059 | 0.008 0.001 0.0005 | 0.0033 0.00036 0.000030 | 0.0037 | 0.0095 | 0.39 | A | 201a, 202a |
| Sn ¹²⁸ | 65 min | No data | | | | | | C | 201a, 202a, 209 |
| Sb ^{128m} | 10 min | 0.75 0.32 | No data | | | | | C | 201a, 202a |
| Sb ¹²⁹ | 4.6 hr | 0.79 0.534 0.308 0.165 | No data | | | | | C | 201a, 202a, 209 |
| Te ^{129m} | 41 days | 0.028 [X _K] | 0.27 | 0.0076 | 0.0076 | 0.27 | 0.028 | C | 201a, 202a |
| Te ¹²⁹ | 74 min | 1.09 0.74 0.46 | 0.10 0.04 0.15 | 0.11 0.030 0.069 | 0.21 | 0.29 | 0.72 | B | 201a, 202a, 209 |
| Sh ¹³⁰ Sb ¹³¹ | 33 min 23 min | No data " " | | | | | | C C | 201a, 202a, 209 201a, 202a, 209 |

| Isotope | Half-life | Energy of quanta E_{γ_i} , Mev | Quantum yield disint ⁻¹ | Differential intensity I_{γ_i} , Mev/disint | Gamma-ray emission intensity of isotope per disintegration I_{γ_i} , Mev/disint | Total quantum yield of isotope K_{γ_i} , disint ⁻¹ | Mean gamma-ray emission energy of isotope \bar{E}_{γ_i} , Mev | Reliability | References |
|--------------------|-----------|---|---|---|--|--|--|-------------|------------------------------|
| Te ^{131m} | 30 hr | 2.0 1.92 1.65 1.22 1.14 1.08 0.92 0.85 0.78 0.335 0.200 0.100 0.80 0.029 [X _K] | 0.046 0.025 0.030 0.20 0.27 0.06 0.14 0.5 1.0 0.18 0.08 0.032 0.014 0.17 | 0.092 0.048 0.050 0.24 0.31 0.065 0.13 0.42 0.78 0.060 0.016 0.0032 0.011 0.0048 | | | | B | 201a, 202a |
| Te ¹³¹ | 24.8 min | 0.94 0.604 0.445 0.147 0.029 [X _K] | 0.25 0.072 0.22 0.34 0.075 | 0.24 0.043 0.098 0.050 0.0021 | 2.23 | 2.75 | 0.81 | B | 201a, 202a |
| I ¹³¹ | 8.06 days | 0.722 0.637 0.364 0.284 0.080 0.030 [X _K] | 0.01 0.093 0.8 0.065 0.023 0.05 | 0.0072 0.059 0.29 0.018 0.0018 0.0015 | | 0.96 | 0.45 | A | 201a, 202a, 208, 209, 216 |
| Te ¹³² | 77.7 hr | 0.23 0.053 0.029 [X _K] | 0.91 0.16 0.82 | 0.21 0.0085 0.024 | 0.38 | 1.04 | 0.36 | B | 202a, 208 |
| I ¹³² | 2.29 hr | 1.45 1.39 1.29 1.14 0.953 0.775 0.72 0.67 0.640 0.620 0.515 | 0.014 0.054 0.031 0.051 0.20 0.83 0.065 1.0 0.210 0.10 0.2 | 0.020 0.075 0.040 0.058 0.19 0.64 0.047 0.67 0.13 0.062 0.10 | 0.24 | 1.89 | 0.13 | B | 202a, 208 217, 218 |
| Te ^{133m} | 50 min | No data | | | 2.03 | 2.76 | 0.74 | C | 201a, 202a |
| Te ¹³³ | 2 min | 1.0 0.6 | 0.7* ^a 1.0 | 0.7 0.6 | 1.3 | 1.7 | 0.76 | C | 201a, 202a |
| I ¹³³ | 20.9 hr | 1.3 1.24 1.05 0.87 0.71 0.53 | 0.04 0.02 0.01 0.09 0.02 1.0 | 0.052 0.025 0.010 0.078 0.014 0.53 | | | | B | 202a, 209 |
| Xe ^{133m} | 2.2 days | 0.232 0.030 [X _K] | 0.18 0.69 | 0.042 0.021 | 0.063 | 0.87 | 0.072 | B | 201a, 202a, 209 |

| Isotope | Half-life | Energy of quanta E_{γ_i} , Mev | Quantum yield disint $^{-1}$ | Differential intensity I_{γ_i} , Mev/disint | Gamma-emission intensity of isotope per disintegration I_{γ_i} , Mev/disint | Total quantum yield of isotope $\bar{\kappa}_{\gamma_i}$, disint $^{-1}$ | Mean gamma-emission energy of isotope E_{γ_i} , Mev | Reliability | References | |
|--------------------|-----------|---|--|--|--|---|--|-------------|----------------------|----------------------|
| Xe ¹³³ | 5.65 days | 0.160 0.081 0.031 [X _K] | 0.016 0.36 0.49 | 0.0026 0.029 0.015 | | | | B | 201a, 202a, 209 | |
| Te ¹³⁴ | 42 min | No data | | | 0.047 | 0.87 | 0.05 | C | 201a, 202a | |
| I ¹³⁴ | 54 min | 1.79 1.62 1.47 1.15 1.07 1.00 0.89 0.848 0.76 0.69 0.61 0.53 0.41 | 0.066 0.049 0.036 0.10 0.18 0.07 0.74 1.0 0.055 0.073 0.20 0.084 0.082 | 0.12 0.079 0.053 0.12 0.19 0.07 0.66 0.85 0.042 0.050 0.12 0.044 0.034 | | | | B | 202a, 209 | |
| I ¹³⁵ | 6.75 hr | 1.8 1.72 1.46 1.28 1.14 1.04 0.86 0.42 | 0.11 0.19 0.12 0.34 0.37 0.09 0.11 0.069 | 0.20 0.33 0.18 0.44 0.42 0.094 0.095 0.029 | | 2.74 | 0.89 | B | 201a, 202a | |
| Xe ^{135m} | 15.8 min | 0.53 0.031 [X _K] | 0.8 0.15 | 0.42 0.0046 | 1.77 | 1.40 | 1.27 | B | 201a, 202a, 209 | |
| Xe ¹³⁵ | 9.13 hr | 0.604 0.360 0.250 0.031 [X _K] | 0.03 0.001 0.91 0.044 | 0.018 0.00036 0.23 0.0014 | | 0.95 | 0.45 | B | 202a, 208, 209 | |
| Cs ¹³⁷ | 30 years | No gamma emission | | | | | | A | 201a, 202a | |
| Ba ^{137m} | 2.57 min | 0.661 0.033 [X _K] | 0.89 0.072 | 0.59 0.0024 | | 0.96 | 0.61 | B | 201a, 202a, 208, 209 | |
| Xe ¹³⁸ | 17 min | 2.01 1.78 0.51 0.42 | No data | | | | | C | 201a, 202a | |
| Cs ¹³⁸ | 32.5 min | 3.34 2.63 2.21 1.43 1.01 0.87 0.55 0.46 0.41 0.23 0.19 0.14 | 0.005 0.09 0.18 0.73 0.25 0.015 0.015 0.23 0.03 0.12 0.01 0.056 | 0.017 0.24 0.40 1.04 0.25 0.013 0.0082 0.10 0.012 0.028 0.0019 0.0078 | | 2.12 | 1.73 | 1.22 | B | 201a, 202a, 208, 209 |

| Isotope | Half-life | Energy of quanta E_{γ_i} , Mev | Quantum yield disint $^{-1}$ | Differential intensity I_{γ_i} , Mev/disint | Gamma-ray emission intensity of isotope per disintegration I_{γ_i} , Mev/disint | Total quantum yield of isotope K_{γ_i} , disint $^{-1}$ | Mean gamma-ray emission energy of isotope \bar{E}_{γ_i} , Mev | Reliability | References |
|-------------------|-----------|--|---|--|--|--|--|-------------|-----------------|
| Cs ¹³⁸ | 9.5 min | No data | | | | | | | |
| Ba ¹³⁹ | 82.9 min | 1.43 0.163 0.034 [X _K] | 0.003 0.23 0.049 | 0.0043 0.037 0.0017 | | | | | |
| Ba ¹⁴⁰ | 12.8 days | 0.537 0.430 0.304 0.162 0.0296 | 0.25 0.055 0.040 0.073 0.15 | 0.13 0.024 0.012 0.012 0.0044 | 0.043 | 0.28 | 0.15 | B | 202a, 208, 209 |
| La ¹⁴⁰ | 40.2 hr | 2.52 1.597 0.923 0.868 0.815 0.748 0.491 0.323 | 0.035 0.95 0.091 0.05 0.186 0.043 0.40 0.20 | 0.088 1.52 0.084 0.043 0.15 0.032 0.20 0.065 | 0.18 | 0.57 | 0.32 | B | 201a, 202a, 208 |
| Ba ¹⁴¹ | 18.3 min | 0.61 0.46 0.37 0.28 0.19 0.125 | 15* ^a 20 40 45 100 25 | | 2.18 | 1.96 | 1.11 | | |
| La ¹⁴¹ | 3.85 hr | 1.37 | 0.025 | 0.034 | 0.034 | 0.025 | 1.37 | B | 202a, 209 |
| Ce ¹⁴¹ | 32.5 days | 0.145 0.037 [X _K] | 0.47 0.15 | 0.068 0.0056 | 0.074 | 0.62 | 0.12 | B | 201a, 202a, 208 |
| Ba ¹⁴² | 11 min | 1.68 1.36 1.20 1.08 0.97 0.89 0.08 | 0.3* ^a 0.3 3.5 1.0 1.5 4.0 3.0 | | | | | C | 202a |
| La ¹⁴² | 77 min | 3.65 3.30 3.00 2.57 2.40 2.08 1.92 1.75 1.54 1.03 0.90 0.64 | 0.012 0.007 0.04 0.03 0.11 0.03 0.06 0.025 0.04 0.06 0.12 0.55 | 0.044 0.023 0.120 0.077 0.26 0.062 0.12 0.044 0.062 0.063 0.11 0.35 | | | | A | 202a, 209 |
| La ¹⁴³ | 14 min | 2.85 2.56 2.46 2.22 1.98 | 0.15* ^a 0.27 0.13 0.06 0.35 | | 1.33 | 1.08 | 1.23 | C | 202a |

| Isotope | Half-life | Energy of quanta E_{γ_i} , Mev | Quantum yield disint $^{-1}$ | Differential intensity I_{γ_i} , Mev/disint | Gamma-emission intensity of isotope per disintegration I_{γ_i} , Mev/disint | Total quantum yield of isotope K_{γ_i} , disint $^{-1}$ | Mean gamma-emission energy of isotope E_{γ_i} , Mev | Reliability | References |
|-------------------|------------|---|---|---|---|---|--|-------------|---------------------|
| Ce ¹⁴³ | 33.4 hr | 1.70 1.58 1.17 1.07 0.915 0.80 0.62 0.44 | 0.19 0.28 0.57 0.26 0.08 0.44 1.00 0.13 | | | | | | |
| Pr ¹⁴³ | 13.6 days | 0.72 0.66 0.493 0.29 0.057 0.037 [X _K] | 0.08 0.08 0.02 0.43 0.063 0.70 | 0.058 0.053 0.0099 0.12 0.0036 0.026 | 0.27 | 1.37 | 0.20 | B | 201a, 202a, 208 |
| Ce ¹⁴⁴ | 284 days | No gamma emission 0.134 0.08 0.036 [X _K] | 0.150 0.016 0.13 | 0.020 0.0013 0.0047 | 0.026 | 0.296 | 0.088 | B | 202a, 208, 220 |
| Pr ¹⁴⁴ | 17.3 min | 2.18 1.49 0.695 | 0.0068 0.0029 0.0149 | 0.015 0.0043 0.010 | 0.026 | 0.025 | 1.16 | A | 202a, 208 |
| Pr ¹⁴⁵ | 5.98 hr | Low quantum yields | | | 0.029 | 0.025 | | B | 201a, 202a |
| Ce ¹⁴⁶ | 13.9 min | 0.32 0.27 0.22 0.142 0.110 | 0.65 0.078 0.32 0.27 0.13 | 0.21 0.021 0.070 0.038 0.014 | 0.353 | 1.45 | 0.24 | B | 202a |
| Pr ¹⁴⁶ | 24 min | 1.49 0.75 0.74 0.46 | 0.33 0.11 0.11 1.0 | 0.49 0.082 0.081 0.46 | 1.11 | 1.55 | 0.72 | B C | 202a 201a, 202a] |
| Pr ¹⁴⁷ | 1.95 min | No data | | | | | | | |
| Nd ¹⁴⁷ | 11.3 days | 0.69 0.533 0.442 0.413 0.400 0.322 0.277 0.091 | 0.01 0.125 0.020 0.007 0.016 0.032 0.014 0.282 | 0.0069 0.067 0.0088 0.0029 0.0064 0.010 0.0039 0.026 | | | | A | 202a, 208 |
| Pm ¹⁴⁷ | 2.64 years | 0.039 [X _K] | 0.335 | 0.013 | 0.14 | 0.84 | 0.17 | A | 201a, 202a |
| Nd ¹⁴⁹ | 1.8 hr | 0.65 0.538 0.424 0.326 0.266 0.211 0.155 | 91** 78 68 3.7 53 180 22 | 0.0000034 0.0000041 0.0000041 0.0000034 0.0000034 0.0000041 0.0000041 | 0.0000041 0.0000041 0.0000041 0.0000041 0.0000041 0.0000041 0.0000041 | 0.0000034 0.0000034 0.0000034 0.0000034 0.0000034 0.0000034 0.0000034 | 0.121 | C | 202a, 208 |

| Isotope | Half-life | Energy of quanta E_{γ_i} , Mev | Quantum yield disint $^{-1}$ | Differential intensity I_{γ_i} , Mev/disint | Gamma-emission intensity of isotope per disintegration I_{γ_i} , Mev/disint | Total quantum yield of isotope K_{γ_i} , disint $^{-1}$ | Mean gamma-emission energy of isotope \bar{E}_{γ_i} , Mev | Reliability | References |
|-------------------|------------|---------------------------------------|------------------------------|--|--|--|--|-------------|---------------------|
| Pm ¹⁴⁹ | 53.1 hr | 0.114 | 143 | | | | | | |
| | | 0.081 | 4 | | | | | | |
| | | 0.038 [X _K] | 220 | | | | | | |
| | | 0.85 | 0.006 | 0.0051 | | | | | |
| Nd ¹⁵¹ | 12 min | 0.58 | 0.003 | 0.0017 | | | | | |
| | | 0.285 | 0.075 | 0.021 | 0.028 | 0.084 | 0.34 | A | 202a, 209 |
| | | 2.17 | 0.0033 | 0.0072 | | | | | |
| | | 1.75 | 0.015 | 0.026 | | | | | |
| | | 1.29 | 0.018 | 0.023 | | | | | |
| | | 1.17 | 0.078 | 0.091 | | | | | |
| | | 0.735 | 0.056 | 0.041 | | | | | |
| | | 0.595 | 0.056 | 0.033 | | | | | |
| | | 0.434 | 0.078 | 0.034 | | | | | |
| | | 0.426 | 0.078 | 0.033 | | | | | |
| | | 0.318 | 0.056 | 0.018 | | | | | |
| | | 0.305 | 0.078 | 0.024 | | | | | |
| | | 0.256 | 0.294 | 0.075 | | | | | |
| | | 0.175 | 0.078 | 0.014 | | | | | |
| | | 0.139 | 0.294 | 0.041 | | | | | |
| Pm ¹⁵¹ | 28.4 hr | 0.117 | 0.54 | 0.063 | | | | B | 202a, 209 |
| | | 0.107 | 0.215 | 0.023 | | | | | |
| | | 0.715 | 0.035 | 0.025 | | | | | |
| | | 0.645 | 0.015 | 0.0097 | | | | | |
| | | 0.44 | 0.042 | 0.018 | | | | | |
| | | 0.34 | 0.15 | 0.051 | | | | | |
| | | 0.275 | 0.042 | 0.012 | | | | | |
| | | 0.24 | 0.036 | 0.0086 | | | | | |
| | | 0.165 | 0.086 | 0.014 | | | | | |
| | | 0.10 | 0.049 | 0.0049 | | | | | |
| | | 0.065 | 0.03 | 0.0020 | | | | | |
| | | 0.041 [X _K] | 0.32 | 0.013 | 0.16 | 0.805 | 0.20 | | |
| Sm ¹⁵¹ | 93 years | 0.175 | 0.0053 | 0.00093 | | | | B | 209 |
| | | 0.155 | 0.0106 | 0.0016 | 0.0026 | 0.016 | 0.16 | | |
| Sm ¹⁵³ | 47.1 hr | 0.103 | 0.34 | 0.035 | | | | B | 202a, 208, 219, 222 |
| | | 0.07 | 0.052 | 0.0036 | 0.063 | 0.96 | 0.066 | | |
| | | 0.042 [X _K] | 0.57 | 0.024 | | | | | |
| Sm ¹⁵⁵ | 21.9 min | 0.246 | 0.063 | 0.016 | | | | A | 202a, 209 |
| | | 0.141 | 0.0104 | 0.0015 | 0.103 | 0.99 | 0.104 | | |
| | | 0.105 | 0.74 | 0.078 | | | | | |
| | | 0.042 [X _K] | 0.18 | 0.0076 | | | | | |
| Eu ¹⁵⁵ | 1.81 years | 0.105 | 0.16 | 0.017 | | | | B | 202a, 208 |
| | | 0.086 | 0.32 | 0.028 | 0.054 | 0.69 | 0.078 | | |
| | | 0.044 [X _K] | 0.21 | 0.0093 | | | | C | 201a, 202a, 209 |
| Sm ¹⁵⁶ | 10 hr | No data | | | | | | | |
| Eu ¹⁵⁶ | 14 days | 2.184 | 0.064 | 0.14 | | | | A | 202a, 223 |
| | | 2.098 | 0.036 | 0.076 | | | | | |
| | | 2.026 | 0.029 | 0.059 | | | | | |
| | | 1.966 | 0.053 | 0.104 | | | | | |
| | | 1.937 | 0.023 | 0.045 | | | | | |
| | | 1.877 | 0.022 | 0.041 | | | | | |
| | | 1.366 | 0.015 | 0.020 | | | | | |

| Isotope | Half-life | Energy of quanta E_{γ_i} , Mev | Quantum yield disint^{-1} | Differential intensity I_{γ_i} , Mev/disint | Gamma-emission intensity of isotope per disintegration K_{γ} , Mev/disint | Total quantum yield of isotope K_{γ} , Mev/disint ¹ | Mean gamma-emission energy of isotope \bar{E}_{γ} , Mev | Reliability | References |
|---------|-----------|--|--|--|--|---|--|-------------|------------|
| | | 1.242 1.231 1.154 1.153 1.065 0.961 0.867 0.812 0.72 0.646 0.60 0.199 0.089 0.044 [X_K] | 0.061 0.092 0.056 0.057 0.061 0.028 0.015 0.092 0.056 0.065 0.015 0.007 0.084 0.108 | 0.076 0.113 0.065 0.066 0.065 0.025 0.013 0.075 0.040 0.042 0.009 0.001 0.008 0.004 | | 1.09 | 1.04 | 1.05 | |

*¹ Isotopes with "very low" in column 4 have parameters close to those of isotopes listed as having "no gamma emission." These isotopes thus have "B" in column 9.

*² According to data of /208/, for the $E_{\gamma} = 0.645$ Mev line, $K_{\gamma} = 0.08$.

*³ Quantum yields for 1.05-Mev and 0.87-Mev lines taken, according to data of /208/, from comparison with $K_{\gamma} = 0.25$ for line with $E_{\gamma} = 0.513$ Mev.

*⁴ Low reliability of quantum-yield value.

*⁵ Half-life of In¹¹⁹ uncertain.

*⁶ Only relative number of gamma transitions known.

*⁷ Half-life of Sb¹²⁶ uncertain.

*⁸ Reliability of data very low ("C" in column 9).

REFERENCES

1. FEDOROV, E.K. (Editor). Meteorologiya i atomnaya energiya (Meteorology and Atomic Energy).—Moskva, IL. 1959 [Russian translation from English].
2. LAVRENCHIK, V. N. Global'noe vypadenie produktov yadernykh vzryvov (Global Fallout of Nuclear-Explosion Products).—Moskva, Atomizdat. 1965.
3. KAROL', I. L. et al (Editors). Radioaktivnye izotopy v atmosfere i ikh ispol'zovanie v meteorologii (Radioactive Isotopes in the Atmosphere and Their Use in Meteorology).—Moskva, Atomizdat. 1965.
4. SHVEDOV, V.P. and S.I. SHIROKOV (Editors). Radioaktivnye zagryazneniya vneshnei sredy (Radioactive Contamination of the Environment).—Moskva, Gosatomizdat. 1962.
5. PETROV, R. V., V.N. PRAVETSKII, et al. Zashchita ot radioaktivnykh osadkov (Shelter from Radioactive Fallout).—Moskva, Medgiz. 1963.
6. SPENSER, L. V. Zashchita ot gamma-izlucheniya radioaktivnykh vypadenii (Protection from Gamma Emission of Radioactive Fall-out).—Moskva, Atomizdat. 1965.
7. LEIPUNSKII, O.I. Gamma-izluchenie atomnogo vzryva (The Gamma Radiation of an Atomic Blast).—Moskva, Atomizdat. 1959.
8. Deistvie yadernogo oruzhiya (The Effects of Nuclear Weapons).—Moskva, Voenizdat. 1963.
9. LEIPUNSKII, O.I. et al. Rasprostranenie gamma-kvantov v veshchestve (Propagation of Gamma Rays in Matter).—Moskva, Fizmatgiz. 1960.
10. FANO, U. et al. Perenos gamma-izlucheniya (The Transfer of Gamma Emission).—Moskva, Gosatomizdat. 1963.
11. AGLINTSEV, K.K. Dozimetriya ioniziruyushchikh izluchenii (The Dosimetry of Ionizing Radiations).—Moskva, Gostekhizdat. 1957.
12. HINE, G. and G. L. BROWNELL (Editors). Radiation Dosimetry.—New York, Academic Press. 1956.
13. SIEGBAHN, K. (Editor). Beta and Gamma-Ray Spectroscopy.—Amsterdam, North Holland Publishing Co. 1955.
14. STOLYAROVA, E. L. Prikladnaya spektrometriya ioniziruyushchikh izluchenii (Applied Spectrometry of Ionizing Radiations), Edited by G. D. Latyshev.—Moskva, Atomizdat. 1964.
15. VYAZEMSKII, V.O. et al. Stsintillyatsionnyi metod v radiometrii (The Scintillation Method in Radiometry).—Moskva, Gosatomizdat. 1961.
16. Yadernye vzryvy (Nuclear Explosions).—Moskva, IL. 1958.
17. EMEL'YANOV, V.S. (Editor). Atomnaya energiya (kratkaya entsiklopediya) (Atomic Energy (A Short Encyclopedia)).—Moskva, Bol'shaya Sovetskaya Entsiklopediya. 1958.

18. Atomnaya energiya (novye dannye) (Atomic Energy (Recent Data)).— Moskva, IL. 1954.
19. Hearings before the Special Subcommittee on Atomic Energy, Congress of the United States, 86th Congress, First Session on Fallout from Nuclear Weapons Tests. Vols. 1, 2, 3. US Govt. Print. Off. Wash., 1959.
20. TELEGADAS, Y. Announced Nuclear Detonations, US, UK, USSR.— Ibid, Vol. 3, p. 2517.
21. The Effects of Nuclear Weapons, USAEC, Wash., 1963.
22. HARDY, E. et al. AEC Health and Safety Laboratory, HASL-142, p. 218, 1964.
23. YAMPOL'SKII, P. A. Neitrony atomnogo vzryva (Neutrons from an Atomic Explosion).— Moskva, Gosatomizdat. 1961.
24. GOLDSTEIN, H. Fundamental Aspects of Reactor Shielding.— Addison-Wesley. 1959.
25. BETHE, H. A.— Bull. Atom. Sci., 6, No. 4, 99. 1950.
26. RIDENOUR, L.— Bull. Atom. Sci., 6, No. 4, 105. 1950.
27. RIDENOUR, L. N.— Sci. Amer., 182, 11. 1950.
28. GOL'DANSKII, V. I. and E. I. LEIKIN. Prevrashchenie atomnykh yader (Transformations of Atomic Nuclei).— Moskva, Izdatel'stvo AN SSSR. 1958.
29. PERFILOV, N. A. Fizika deleniya atomnykh yader. Prilozhenie No. 1 k "Atomnoi energii" (The Physics of Nuclear Fission. Appendix No. 1 to "Atomic Energy").— Moskva, Atomizdat. 1957.
30. ZYSIN, Yu. A. et al. Vykhody produktov deleniya i ikh raspredelenie po massam. Spravochnik (Fission-Product Yields and Their Mass Distribution. Handbook).— Moskva, Gosatomizdat. 1963.
31. ROTBLAT, J. — Atom. Sci. J., 4, No. 4, 224. 1955.
32. Atom. Sci. J., 5, No. 549. 1955.
33. LAPP, R. E. — Bull. Atom. Sci., 11, 45, 206. 1955.
34. LIBBY, W. F. — Bull. Atom. Sci., 11, No. 7, 256. 1955.
35. COCROFT, J. — Nature, 175, 873. 1955.
36. MAGATA, N. Ya. — Genshiryoku Kogyi, 9, No. 8, 13. 1963.
37. DREVINSKY, P. J. et al.— J. Geophys. Res., 69, No. 8, 1457. 1964.
38. SCHUMANN, G., and M. STOEPPLER.— J. Geophys. Res., 68, No. 13, 3827. 1963.
39. LANE, W. B. Some Radiochemical and Physical Measurements of Debris from an Underground Nuclear Explosion.— NRDL-PNE-229F. Project Sedan. Aug. 1962. NSA, 17, 23551.
40. ESSINGTON, et al.— Health Phys., 11, No. 8, 689. 1965.
41. BATZEL, R. E.— J. Geophys. Res., 65, No. 9, 2897. 1960.
42. MOSTOVAYA, G. A.— Atomnaya Energiya, 10, No. 4, 372. 1961.
43. Fizika deleniya atomnykh yader (The Physics of Nuclear Fission), A Collection of Articles.— Moskva, Gosatomizdat. 1962.
44. WAY, K. and E. WIGNER.— Phys. Rev., 70, 115. 1946; 73, 1318. 1948.
45. HUNTER, H. F. and N. E. BALLOU.— Nucleonics, 9, No. 5, C-2. 1951.
46. MALÝ, J. et al.— Czechos J. Phys. 7, No. 1, 45. 1957.
47. LOW, K. and R. BJÖRNERTEDT.— Arkiv fys., 13, 85. 1958.
48. BJÖRNERTEDT, R.— Arkiv fys., 16, 293. 1959.
49. GRECHUSHKINA, M. P. Tablitsy sostava produktov mgnovenennogo deleniya U²³⁵, U²³⁸ i Pu²³⁹ (Tables of Product Compositions for Instantaneous Fission of U²³⁵, U²³⁸, and Pu²³⁹).— Moskva, Atomizdat. 1964.

50. KATCOFF, S.— Nucleonics, No. 11, 163. 1960.
51. LEVOCHKIN, F. K. and Yu. L. SOKOLOV.— Atomnaya Energiya, 10, No. 4, 403. 1961.
52. PERKINS, J. F. and R. W. KING.— Nucl. Sci. Eng., 3, 726. 1958.
53. HELMS, A. T. and I. W. COPPER.— Health Phys., 1, 427. 1959.
54. PEIRSON, D. H.— Brit. J. Appl. Phys., 11, 346. 1960.
55. MATHER, R. L.— In "The Shorter-Term Biological Hazards of a Fallout Field. AEC — Symposium," 1956, p. 35.
56. LAPP, R. E.— Bull. Atom. Sci., 15, No. 5, 181. 1959.
57. ARNOLD, E. P.— Nucl. Sci. Eng., 3, 707. 1958.
58. GHIORSO, A. et al.— Phys. Rev., 99, 1048. 1955.
59. FIELDS, P. R. et al.— Phys. Rev., 102, 180. 1956.
60. CAMERON, A. G.— Canad. J. Phys., 37, 322. 1959.
61. J. Fac. Sci. Niigata Univ. Ser., 1, 2, 107. 1960.
62. NISHIWAKI, J.— Atom. Sci. J., 4, No. 2, 97. 1954.
63. NISHIWAKI, J.— Atom. Sci. J., 4, No. 5, 279. 1959.
64. KNAPP, H. A.— In "Hearings before the Special Subcommittee on Atomic Energy, Congress of the United States, 86th Congress, First Session on Fallout from Nuclear Weapons Tests." Vol. 3, Appendix A., US Govt. Print. Off. Wash., 1959, p. 1969.
65. DUNHAM, C. L.— Ibid. Vol. 1, p. 10.
66. MAMURO, T. and T. MATSUNAMI.— Annual Report. Radiation Center Osaka, Prefect, 5, 23. 1965.
67. SALTER, L. P. et al.— Science, 148, No. 3672, 954. 1965.
68. KRIEGER, H. L. and D. GROCHE.— Science, 131, No. 3392, 40. 1960.
69. KRIEGER, H. L.— Health Phys., 11, No. 7. 653. 1965.
70. STROM, P. O. et al.— Science, 128, 417. 1958.
71. WEISS, H. V. and W. H. SHIPMAN.— Science, 125, 695. 1957.
72. STRAUB, C. P.— In "Hearings before the Special Subcommittee on Atomic Energy, Congress of the United States, 86th Congress, First Session on Fallout from Nuclear Weapons Tests." Vol. 2. Appendix A., US Govt. Print. Off. Wash., 1959, p. 963.
73. Research in the Effects and Influences of the Nuclear Bomb Test Explosions.— Publication by Japan Society for the Promotion of Science. Yeno — Tokyo. 1956.
74. CERRAI, E. et al.— Rend. Ist. Iomhardo sci. e lettere. Cl. Sci. mat. e natur., B98, 197. 1964.
75. GACLIONE, P. et al.— Nature, 204, No. 4964, 1215. 1964.
76. GUSTAFSON, P. F. et al.— Nature, 203, No. 4944, 470. 1964.
77. SHIPMAN, W. H. et al.— Science, 126, 971. 1957.
78. JOHNSON, J. E. et al.— Health Phys., 12, No. 1, 37. 1966.
79. SLYMOUR, A.— In "Hearings before the Special Subcommittee on Atomic Energy, Congress of the United States, 86th Congress, First Session on Fallout from Nuclear Weapons Tests." Vol. 3. Appendix A., US Govt. Print. Off. Wash., 1959, p. 1976.
80. GODT, K. I.— Atomkernenergie, 6, H. 7/8, 318. 1961.
81. KALKSTEIN, M.— Science, 137, No. 3531, 645. 1962.
82. KURCHATOV, B. V. et al.— Atomnaya Energiya, 13, No. 6, 576. 1962.
83. KAURANEN, P.— J. Geophys. Res., 69, No. 23, 5075. 1964.

84. Report of Scientific Committee of United Nations Organization on the Effects of Atomic Radiation, A/5216, 19 April 1962, Vol. II, Appendix F [Russian Version].
85. JUNGE, C.E. Air Chemistry and Radioactivity.— New York, Academic Press, 1963.
86. SALTER, L. P.— In "Radioactive Fallout from Nuclear Weapons Tests." Ed. A. W. Klement. USAEC. 1965, p. 409.
87. HASL-140. 1963, p. 166.
88. KALKSTEIN, et al.— In "Radioactive Fallout from Nuclear Weapons Tests." Ed. A. W. Klement. USAEC. 1965, p. 405.
89. RUSSEL, S.I. and R. V. GRIFFITH.— HASL-142, 1964, p. 306.
90. HAGEMANN, F. T.— Monthly Catalog, U.S. Govt. Publ., No. 845, 8547. 1965.
91. NYDAL, R.— Fra fys. verden, 26, 51. 1964.
92. NYDAL, R. et al.— Nature, 206, No. 4988. 1029. 1965.
93. NYDAL, R.— Nature, 200, No. 4903, 212. 1963.
94. Atom Sci.J., 3, No. 5, 292. 1954.
95. NISHITA, H.— Health Phys., 11, No. 12, 1527. 1965.
96. GARKUSHA, I. F. Pochvovedenie (Soil Science).— Moskva—Leningrad, Sel'khozgiz. 1954.
97. ALEKIN, O. A. Gidrokhimiya (Chemical Hydrology).— Leningrad, Gidrometeoizdat. 1952.
98. STOREBÖ, P. B. On Particle Formation in Nuclear Bomb Debris. 13th Session of UNSCEAR, Discussion of Meteorological Problems with WMO Experts. 1964.
99. FREILING, E. C.— In "Radioactive Fallout from Nuclear Weapons Tests. I. TID-7632," Wash., 1962, p. 25.
100. ANDERSON, A. D.— J. Meteorol., 18, No. 4. 431. 1961.
101. ADAMS, C. E. et al.— Geochim. et cosmochim. acta, 18, No. 1/2, 42. 1960.
102. STEWART, K.— Trans. Faraday Soc., 52, 161. 1956.
103. FREILING, E. C.— In "Radioactive Fallout from Nuclear Weapons Tests, I. TID-7636," Wash., 1962, p. 47.
104. IZRAEL', Kh. and A. KREBS (Editors). Yadernaya geofizika (Nuclear Geophysics).— Moskva, Mir. 1964.
105. ZUBKIN, A. S. and V. A. MEDVEDEV. Chto takoe radioaktivnoe zarazhenie i sposoby zashchity ot nego (Radioactive Contamination and Means of Protection from It).— Moskva, Atomizdat. 1963.
106. LARSON, K. H. Radioecology, Edited by V. Schultz. p. 21.— London, Chapman and Hall. 1963.
107. NIFONTOV, B. I. et al. Podzemnye yadernye vzryvy (Underground Nuclear Explosions).— Moskva, Atomizdat. 1965.
108. KELLOGG, W. W. et al.— J. Meteorol., 14, No. 1, 1. 1957.
109. PETROV, V. N. and A. Ya. PRESSMAN.— Doklady AN SSSR, 146, No. 1, 86. 1962.
110. MACHTA, L. and K.M. NAGLER. In "The Shorter-Term Biological Hazards of a Fallout Field, AES-Symposium," 1956, p. 3.
111. EDVARSON, K. et al.— Nature, 184, No. 4701, 1771. 1959.
112. MAMURO, T. et al.— Nature, 197, No. 4871, 964. 1963.

113. MAMURO, T. et al.— Health Phys. 11, 199. 1965.
114. GAZIEV, Ya. I. et al.— Atomnaya Energiya, 18, No. 5, 535. 1965.
115. COOK, C. S. et al.— Nature, 187, No. 4743, 1100. 1960.
116. KERN, W.— Nukleonik, 2, 203. 1960.
117. SCHEIDLING, J. A.— Staub, 20, No. 5, 139. 1960.
118. RAJEWSKY et al.— Atompraxis, 8, 237. 1962.
119. SITTKUS, A.— Naturwissenschaften, 46, 12, 399. 1959.
120. MAY, R. and A. SCHNEIDER.— Atomkernenergie, 4, 1, 28. 1959.
121. FREILING, E. C.— Science, 133, No. 3469, 1991. 1961.
122. MARTELL, E. A.— Science, 129, No. 3357, 1197. 1959.
123. GRECHUSHKINA, M. P. and Yu. A. IZRAEL'.— In Sbornik: Radioaktivnye Izotopy v Atmosfere i ikh Ispol'zovanie v Meteorologii, p. 1964, Moskva, Atomizdat. 1965.
124. WAHL, A. C. et al.— Phys. Rev., 126, No. 3, 1112. 1962.
125. IZRAEL', Yu. A.— Doklady AN SSSR, 161, No. 2, 343. 1965.
126. KALKSTEIN et al.— Natural Aerosols and Nuclear Debris Studies Progress. Report II. GRD Res. Notes (A/Ac 82/G/L 350), No. 24, Nov., 1959.
127. STOREBÖ, P. B.— J. Meteorol., 16, No. 6, 600. 1960.
128. STOREBÖ, P. B.— Tellus, 12, No. 3, 293. 1960.
129. BRYANT, E. A. et al.— Science, 132, No. 3423, 327. 1960.
130. ALEKSAKHIN, R. M. Radioaktivnoe zagryaznenie pochvy i rastenii (Radioactive Contamination of Plants and Soil).— Moskva, Izdatel'stvo AN SSSR. 1963.
131. GRAHAM, E. R.— Science, 129, No. 3358, 1276. 1959.
132. LINDSTEN, C. et al.— J. Amer. Water Works Assoc., 53, No. 3, 256. 1961.
133. HASP. High Altitude Sampling Program, Defense Atomic Support Agency, Wash., Rep. 5398. 1961.
134. VON HALTER, I. et al.— Atomkernenergie, H. 7/8, 295. 1965.
135. BYKHOVSKII, A. V. et al. (Editors). Radioaktivnye chastitsy v atmosfere (Radioactive Particles in the Atmosphere), A Collection of Articles.— Moskva, Gosatomizdat. 1963.
136. BENSON, P. et al.— In "Radioactive Fallout from Nuclear Weapons Tests" Ed. A. W. Klement. USAEC, 1965, p. 108.
137. MALAKHOV, S. G. and K. P. MAKHON'KO.— Atomnaya Energiya, 16, No. 6, 530. 1964.
138. FANO, U.— Nucleonics, 11, No. 8, 8. 1953.
139. GOLDSTEIN, H. Fundamental Aspects of Reactor Shielding.— Addison-Wesley. 1959.
140. ROCKWELL, T. (Editor). Reactor Shielding Design Manual.— New Jersey, Von Nostrand. 1956.
141. GOLDSTEIN, H. and J. WILKINS. Calculations of the Penetration of Gamma Rays.— NYO-3075, 1954.
142. BERGER, M. J. — T. Res. Nat. Bur. Standards, 55, No. 6, 343. 1955.
143. GALISHEV, V. S. et al.— Uspekhi Fiz. Nauk, 61, 161. 1957.
144. NELIPA, N. F. Vvedenie v teoriyu mnogokratnogo rasseyaniya chastits (Introduction to the Theory of Multiple Scattering of Particles).— Moskva, Atomizdat. 1960.

-
145. IZRAEL', Yu.A.— Atomnaya Energiya, 14, No. 3, 317. 1963.
146. GORSHKOV, G. V. Gamma-izluchenie radioaktivnykh tel i elementy zashchity ot izlucheniya (Gamma Emission of Radioactive Substances and the Elements of Radiation Protection).— Moskva, Izdatel'stvo AN SSSR. 1959.
147. THEUS, R. B. et al.— J. Appl. Phys., 26, 294. 1955.
148. VAN DILLA and G. J. HINE.— Nucleonics, 10, No. 7, 54. 1952.
149. BIBERGAL', A. V. et al.— Atomnaya Energiya, 7, No. 3, 244. 1959.
150. WHITE, G. R.— Phys. Rev., 80, No. 2, 154. 1950.
151. SAKHAROV, V. N.— Atomnaya Energiya, 3, No. 7, 57. 1957.
152. TSYPIN, S. G. et al.— Atomnaya Energiya, 1, 71. 1956.
153. SOOLE, B. W.— Proc. Roy. Soc. A230, 343. 1955.
154. LEIPUNSKII, O. I. and V. N. SAKHAROV.— Atomnaya Energiya, 6, No. 5, 585. 1959.
155. IZRAEL', Yu.A.— Atomnaya Energiya, 17, No. 2, 137. 1964.
156. BERGER, M. J.— J. App. Phys., 28, No. 12, 1502. 1957.
157. CHILTON, A. B.— Nucleonics, 23, No. 8, 119. 1965.
158. HOLLAND, J. Z. Proceedings of the International Conference on the Peaceful Uses of Atomic Energy, Geneva. 1955.
159. SCHAAERSCHMIDT, A. — Nucl. Instr. Methods, 27, No. 3, 311. 1964.
160. SAKHAROV, V. N. et al. — Atomnaya Energiya, 7, No. 3, 266. 1959.
161. KIMEL', L. R.— In Sbornik: Voprosy fiziki zashchity reaktorov, Edited by D. L. Broder, p. 217, Moskva, Gosatomizdat. 1963.
162. KOVALEV, E. E. and D. P. OSANOV.— Atomnaya Energiya, 2, No. 6, 555. 1957.
163. IZRAEL', Yu. A.— Izvestiya AN SSSR, Seriya Geofizicheskaya, No. 7, 1103. 1964.
164. BRUES, A. M. et al.— In "Hearings before the Special Subcommittee on Atomic Energy, Congress of the United States, 86th Congress, First Session on Fallout from Nuclear Weapons Tests," Vol. 3., Appendix A, 1959, p. 1400.
165. PEIRSON, D. H. and L. SALMON.— Nature, 184, 1678. 1959.
166. DZHELEPOV, B. S. and L. K. PEKER. Skhemy raspada radioaktivnykh yader (Decay Schemes of Radioactive Nuclei).— Moskva, Izdatel'-stvo AN SSSR. 1958.
167. KOGAN, R. M.— Izvestiya AN SSSR, Seriya Geofizicheskaya, No. 7, 988. 1959.
168. MALAKHOV, S. G. et al.— Atomnaya Energiya, 19, No. 1, 28. 1965.
169. BERGER, M. J.— J. Appl. Phys., 26, 1504. 1955.
170. VOROB'EV, V. A.— Atomnaya Energiya, 19, No. 1, 69. 1964.
171. BORG, D. C.— In "The Shorter-Term Biological Hazards of a Fallout Field, AEC Symposium," 1956, p. 39.
172. KOGAN, R. M. and Sh. D. FRIDMAN.— Izvestiya AN SSSR, Seriya Geofizicheskaya, No. 4, 530. 1960.
173. DE VRIES, T. W.— Trans. Amer. Nucl. Soc., 7, 320. 1964.
174. FRENCH, R. L.— Health Phys., 11, No. 5, 369. 1965.
175. HAYWOOD, F. E.— Health Phys., 11, No. 3. 185. 1965.
176. DAVIS, F. J. and P. W. REINHARDT.— Health Phys., 8, No. 3, 233. 1962.

177. IZRAEL', Yu. A. et al.— Atomnaya Energiya, 19, No. 2, 199. 1965.
178. IONOV, V. A.— Atomnaya Energiya, 19, No. 4, 397. 1965.
179. MATHER, R. L. et al.— Health Phys., 8, No. 3, 245. 1962.
180. HUDDLESTON, C. M. et al.— Health Phys. 11, No. 6, 537. 1965.
181. BULASHEVICH, Yu. P.— Trudy Gorno-Geologicheskogo Instituta, Ural'skii Filial AN SSSR, No. 30, 146. 1957.
182. HUBBELL, J. H.— Rev. Scient. Instrum., 29, No. 1, 65. 1958.
183. VARTANOV, N. A. and P. S. SAMOILOV. Prakticheskie metody stsintillyatsionnoi gamma-spektrometrii (Practical Methods of Scintillation Gamma-Ray Spectrometry).— Moskva, Atomizdat. 1964.
184. BERGER, M. J. and D. J. RASO.— Radiation Res., 12, No. 1, 20. 1960.
185. SADOVNIKOV, I. F. Pochvennye issledovaniya i sostavlenie pochvennykh kart (Soil Studies and the Construction of Soil Maps).— Moskva, Sel'khozgiz. 1954.
186. IZRAEL', Yu. A.— Izvestiya AN SSSR, Seriya Geofizicheskaya, No. 5, 818. 1963.
187. EISENHAUER.— Health Phys. 9, 8, 503. 1963.
188. NORDYKE, M. D. and W. WRAY.— J. Geophys. Res., 69, No. 4. 675. 1964.
189. IZRAEL', Yu. A. et al.— Izvestiya AN SSSR, Seriya Geofizicheskaya, No. 8, 1126. 1962.
190. TYURIN, A. V. Taksatsiya lesa (Forest Valuation).— Moskva, Goslestekhizdat. 1945.
191. TRETYAKOV, N. V. et al. Spravochnik taksatora (Forest-Appraiser's Handbook).— Moskva, Goslesbumizdat. 1962.
192. MOLCHANOV, A. A. Sosnovyi les i vлага (Pine Forests and Moisture).— Moskva, Izdatel'stvo AN SSSR. 1953.
193. Polevoi spravochnik taksatora (Forest Appraiser's Field Manual).— Moskva, Goslesbumizdat. 1954.
194. KHLIMI, C. F. Teoreticheskaya biogeofizika lesa (Theoretical Biogeophysics of Forests).— Moskva, Izdatel'stvo AN SSSR. 1957.
195. Yadernye reaktory. 1. Fizika yadernykh reaktorov (Nuclear Reactors. 1. The Physics of Nuclear Reactors).— Moskva, IL. 1956.
196. MATVEEV, A. V. Voprosy rudnoi geofiziki (Problems in Mining Geophysics), No. 3, p. 185.— Moskva, Gosgeoltekhizdat. 1961.
197. KHORGIAN, A. Kh. Fizika atmosfery (Physics of the Atmosphere).— Moskva, Fizmatgiz. 1958.
198. SIVINTSEV, Yu. V.— Atomnaya Energiya, 9, No. 1, 39. 1960.
199. KOGAN, R. M.— In: Sbornik Rabot po Nekotorym Voprosam Dozimetrii i Radiometrii Ioniziruyushchikh Izluchenii, Edited by Yu. V. Sivintsev, No. 2, p. 36, Moskva, Gosatomizdat. 1961.
200. BONNER, N. and I. MISKEL.— Science, 150, No. 3695, 489. 1965.
201. PEIRSON, D. H. and E. FRANKLIN.— Brit. J. Appl. Phys., 2, No. 10, 281. 1951.
- 201a. STROMINGER, D. et al.— Rev. Mod. Phys., 30, No. 2, pt. 2, 585. 1958.
202. SINCLAIR, W. K.— Nucleonics, 7, No. 6, 21. 1950.
- 202a. DZHELEPOV, B. S. et al. Skhemy raspada radioaktivnykh yader (Decay Schemes of Radioactive Nuclei).— Moskva, Izdatel'stvo AN SSSR. 1966.
203. SAKHAROV, V. N.— Atomnaya Energiya, 3, No. 7, 61. 1957.

-
- 203a. VAPSTRA, A. Kh. et al. Tablitsy po yadernoi spektroskopii (Nuclear-Spectroscopy Tables).— Moskva, Gosatomizdat. 1960.
204. BERGEL'SON, B. R. and G. A. ZORIKOEV. Spravochnik po zashchite ot izlucheniya protyazhennykh istochnikov (Handbook on Protection from Radiation of Extended Sources).— Moskva, Atomizdat. 1956.
205. KUNZ, W. and SCHINTLMEISTER. Tabellen der Atomkerne.— Berlin. Bd. I. 1958; Bd. II. 1959.
206. Nucl. Data Sheets, National Academy of Sciences. Washington, National Research Council, 1958—1961.
207. AJZENBERG-SELOVE F. and T. LAURITSEN. — Nucl. Phys., 11, 1. 1959.
208. GRONTHAMEL, C. E. Applied Gamma-Ray Spectrometry.— Pergamon Press. 1960.
209. GUSEV, N. G. et al. Radioaktivnye izotopy kak gamma-izluchateli (Radioactive Isotopes as Gamma-Ray Emitters).— Moskva, Atomizdat. 1964.
210. Phys. Rev., 127, 3. 1962.
211. VOINOVA et al.— Izvestiya AN SSSR, Seriya Fizicheskaya, No. 7, 24. 1960.
212. Zhurnal Eksperimental'noi i Teoreticheskoi Fiziki, 43, No. 6. 2056. 1962.
213. ESTULIN, I. V. et al.— Zhurnal Eksperimental'noi i Teoreticheskoi Fiziki, 35, 71. 1958.
214. J. Phys. et Radium, 22, No. 5, 249. 1961.
215. Nucl. Phys., 29, No. 4, 657. 1962.
216. Nucl. Phys., 31, No. 3, 456. 1962.
217. DEVARÉ, H. G.— Nucl. Phys., 28, No. 1, 148. 1961.
218. ROBINSON, R. et al.— Phys. Rev., 122, No. 6. 1863. 1961.
219. DEVARÉ, H. G.— Nucl. Phys., 15, No. 4. 653. 1960.
220. GEIGER, J. S. et al.— Nucl. Phys., 28, No. 3. 387. 1961.
221. J. Phys. et Radium, 22, No. 10, 655. 1961.
222. SUTER, E. et al.— Nucl. Phys., 29, No. 1. 33. 1962.
223. Proc. Indian Acad. In., A52, No. 4, 157. 1960.

SUBJECT INDEX

A

Absorption of gamma rays, 48
Absorptive capacity of forest, 102
Accident, Windscale reactor, 120
Accumulation of energy of scattered radiation, 48, 49
Accumulation factor, 52 ff dosage, 49, 52 ff, 86, 87

Activity distribution, 24 induced, correction factors, 16 in exposed ground, 15 ff in underlying surface, 14, 15 total, density function, 35 high-melting products, 35

Age mixture, 5 of radioisotope fallout, 38 samples, 39 — 45

Agreement, Moscow, v

Air density, 106
Air equivalent detector, 115 ff correction for detector which is not air equivalent, 116 water as, 50

Air survey, optimum height for, 119 temperature, 106

Airborne gamma-ray spectrometry, 120
Aircraft

disadvantages of survey using, 119 shielding thickness in, 118

Albedo, 88

dosage, 88
energy, 88

Anisotropic detector, errors due to, 114, 117 ff

Ashes, Bikini, 13
Artificially contaminated areas, 71 ff, 125
Atmospheres, homogeneous and real, 107
Atomic bomb, 1
Attenuation coefficient, gamma-emission energy, 67
Attenuation of gamma-rays, 47 ff, 103
Availability of isotope, biological, 37

B

Barometric formula, 106
Beta activities of fission products, 5
Beta decay, 3
Beta-decay scheme, 128
Beta transitions, 128
Bikini ashes, 13
Biological availability of isotope, 37
Biomass in forests, 101 ff of trunk, 102

Bomb atomic, 1 "fission-fusion," 1 "fission-fusion-fission," 2, 13 hydrogen, 1 nominal, 1 thermonuclear, 1

"Bravo" test, 13, 22, 66, 112

C

Calibration coefficient, 124
Chain mass, high-melting elements, 31 radioactive, 3

Clarke composition, 88
 Cloud
 mushroom, height of, 23
 time of ascent of, 24
 Coagulation, 18, 19
 Composition, Clarke, 88
 Compton scattering, 47, 120
 Concrete, 88
 Condensation, 18, 19
 Contaminated areas, artificial, 71 ff, 125
 Contaminated locality, dose-rate
 distribution over, 100
 regions, 88 ff
 Contamination
 of soil, 25
 surface, 67
 surface density of, 109, 110, 119 ff,
 123
 uniform, 67
 volume, 69, 70
 volume concentration of, 113, 114
 Conversion coefficients, 127
 Conversion factors, height, 58, 59, 107,
 108
 Correction factors, dose-rate, 55 ff, 62
 of photopeak, 124
 for detector which is not air-equi-
 valent, 116
 ground irregularities, 94 ff
 microrelief, 95 ff
 Correlation for fractionation of
 isotopes, 29
 Counter
 Geiger, 115, 117
 Sakharov, 115
 Crystal effect vs. height above source,
 122, 123
 Crystals, NaI(Tl) and CsI(Tl), 121

 D
 "Danny Boy" explosion, 112
 Decay, beta, 3
 Decay scheme, beta, 128

 Detector
 air-equivalent, 115 ff
 anisotropic, errors due to, 114, 117 ff
 isotropic, 122, 123
 response function for, 81
 scintillation, 72
 shielded, 80
 spherical, 122
 total number of quanta incident upon, 121
 Detector visibility, direct, 77
 Displacement of particles, horizontal, 24
 Distribution
 function, 48
 Gaussian, 121
 of activity, 24
 Distribution of emission
 angular, 63 ff
 spectral, 63 ff
 fallout, 21
 gamma emission from isotropic plane
 source, 63 ff
 yields in mass chain, 30
 Distribution over contaminated locality,
 angular, 100
 Poisson, 102
 pulse-amplitude, 81
 spectral-angular, 48
 Dosage
 accumulation factor, 49, 52 ff, 86, 87
 albedo, 88
 factors for isotropic plane source, 60
 water, 50, 51
 Dose rate, 25
 at height h, 108, 110
 Dose-rate correction factor, 55 ff, 62
 distribution over contaminated
 locality, 100
 for isotropic plane source, 57 ff
 point source, 50
 for three-dimensional source, 68, 69
 Dose rate in presence of microrelief, 94
 over forest, 104
 Dose-rate ratio vs. distance, 63, 89, 90
 Dose rates in forest, 103
 Dosimetry, errors in, 114 ff

E

Effect

- fringe, 74
- photoelectric, 47

Emmission, microrelief effect on, 94

Energies

- mean gamma-ray, 129 ff
- of gamma-ray quanta, 127 ff

Energy accumulation of scattered radiation, 48, 49

- albedo, 88
- density, 17

Energy flux, gamma-ray, 48

- intensities from finite and infinite sources, 73

Errors due to anisotropic detectors, 114, 117 ff

- detector that is not air-equivalent, 114 ff, 119
- instrument inertia, 114
- in dosimetry, 114 ff

Explosion

- "Bravo", 13
- "Danny Boy," 112
- thermonuclear, 12

"Exposed" regions, 93

F

Fallout

- artificial model of, 71 ff
- "dry," 20
- dynamic model, 24
- global (world-wide), 20
- intermediate, 20
- local, 20
 - D-model of, 24
- mathematical model of, 21 ff
- particles, 19
- processes leading to, 26
- radioactive, 18
 - categories of, 20

restricted, 20

- simulation areas, 71
- stratospheric, 20
- tropospheric, 20

Fireball, 17 ff

- size, 18

Fireball temperature, time variation of, 18

- time to reach melting point in, 28

Fission event, 1

Fission products, beta activities of, 5

Flight altitude, 86

Forest, absorptive capacity of, 102

Forest cover, shielding effect of, 104, 105

- dose rates, 103 ff
- litter, 102

Forests, biomass in, 101 ff

Fractionation coefficients vs. particle size, 36

- of isotopes, 28 ff
- of products of nuclear explosion, 27

Fredholm integral equation, 120

Fringe effect, 74

G

Gamma emission above three-dimensional source, 70

- average energy of, 9
- average quantum yield of, 9
- dose rate of, 48

Gamma emission from isotropic plane source, distribution of, 63

Gamma-emission intensity, numerical, 9

- line spectrum of, 10 ff

- fission products, 7

- of fission-fragment isotopes, 126 ff

- spectra above simulating area, 84, 85

- of samples, 39 -45

Gamma emission, variation with time, 8

- field of three-dimensional source, 67 ff

Gamma quanta, angular distribution of, 64

- radiation above isotropic plane

- source, 62

- ray absorption, 48

Gamma-ray attenuation, degree of, 103
 factor, 50
 collector, 96

Gamma-ray concentration, surface, 109

Gamma-ray energies, mean, 129 ff
 energy flux, 48
 intensity, 48

Gamma-ray quanta
 energies of, 127 ff
 numerical intensity of, 8
 total numbers of, 129 ff
 unscattered, 122
 roentgen meter, 72
 spectrometer, 72

Gamma-ray spectrometry, 38
 airborne, 120

Gamma-ray spectrum, photopeak of, 122 ff

Gamma rays, true spectrum of, 120

Gamma transitions, 127 ff

Gauss's law (distribution of yields in mass chain), 30

Gaussian distribution, 121

Geiger counter, 115, 117

Ground irregularities, correction for, 94 ff

Interface
 earth-air, 89
 water-air, 89

Ion pair production, 109

Isodose contours in wake of nuclear explosion, 22

Isotope
 biological availability of, 37
 fractionation, 28, 29
 mean gamma-emission energy of, 127

Isotopes
 fission-fragment, gamma emissions of, 126 ff
 gamma-emitting, 2
 stock of, 114
 total amount of, 114

Isotropic plane source, 57 ff
 distribution of gamma emission from, 63
 dosage factors for, 60
 dose rate for, 57 ff
 gamma radiation above, 62

Isotropic point source, dose rate for, 50

J, K

H

"Jangle-U" test, 25
King function, 67

Half-lives, 127 ff

"Hardtack" tests, 14

Height conversion factors, 58, 59, 107, 108
 for detectors that are not air-equivalent, 116

Height for air surveys, optimum, 119

Helicopter, 72 ff
 spectrometer aboard, 120, 125

Hot particles, 43

Hydrogen bomb, 1

L

Law, Gauss's, 30
Raoult's, 33

Line spectra of gamma emission, 10 ff

Lines, differential intensities of, 129 ff

Lithium deuteride, 2

M

Instrument inertia, 114

I

Mass chain, 29 ff
 high-melting elements in, 31

Matter in the region, 111
 total amount of, 112, 117

| | |
|---|--|
| Melting point in fireball, time to reach the, 28 | Point source |
| Microrelief, 91 ff | isotropic, 49 |
| correction for, 95 ff | dose rate, 50 |
| dose rate in presence of, 94 | Poisson distribution, 102 |
| effect on emission, 94, 97 ff | Processes leading to fallout, 26 |
| shielding by, 96 | Pulse-amplitude distribution, 81 |
| Mixture activity, time change in, 4 age, 5 | |
| Model of fallout | Q |
| artificial, 71 ff | Quanta energies of gamma-ray, 127 ff |
| mathematical, 21 ff | Quanta incident upon detector, total |
| Model of local fallout, dynamic, 24 | number of, 121 |
| Monte-Carlo method, 52, 53, 55 | sums of total numbers of gamma-ray, 129 ff |
| Moscow agreement, v | Quantum yield |
| Mushroom cloud, 23 | of gamma-emission line, 123, 124 |
| | total, 126 |
| P | Quantum yields |
| Pair production | relative, 129 |
| electron-positron, 47 | reliability of, 129 ff |
| single ion, 109 | |
| Particle ascent, 23 | R |
| Particle size, fractionation coefficients vs., 36 | Radiation |
| Particle velocity, vertical, 23 | "hard", 10 |
| Particles, horizontal displacement of hot, 43 | "soft", 10 |
| Penetration coefficients for soil, 44, 46 | spectral function of incident, 81, 82 |
| Photoeffectiveness of spectrometer, 121 | unscattered, intensity of, 70 |
| Photoelectric effect, 47 | Radioactive chain, 3 |
| Photopeak conversion coefficient, 124 | Raoult law, 33 |
| intensity vs. height, 124 | Rayleigh scattering, 47 |
| of gamma-ray spectrum, 122 ff | Reaction threshold, 13 |
| Plane, scintillation spectrometer aboard, 120 | Reactor accident, Windscale, 120 |
| Plane source | Reliability of quantum yields, 129 ff |
| isotropic, 57 ff | Response curve, relative, 89, 96, 104, 115 |
| distribution of gamma emission, 63 | function for detector, 81 |
| dosage factors, 60 | Roentgen meter, 89, 96 |
| dose rate, 57 ff | gamma-ray, 72 |
| gamma radiation, 62 | |
| Plowed field, 97 | S |
| | Sakharov counter, 115 |

Sampling, 38
 Scattered radiation, accumulation of energy of, 48, 49
 Scattering
 coherent, 47
 Compton, 47, 120
 Rayleigh, 47
 Scintillation detectors, 72
 gamma-ray spectrometer, 45
 spectrometry, 38
 spectrometer aboard a plane or helicopter, 120
 Seawater, 16
 "Sedan" test, 42, 44
 "Shaded" regions, 92
 Shield, 72, 73
 Shielding by forest cover, 104, 105
 microrelief, 96
 Shielding by soil irregularities, elimination of, 104
 coefficients, 119
 thickness in aircraft, 118
 Simulating area, spectra over, 76 ff
 Simulation of fallout, 71 ff
 "Small Boy" test, 66
 Soil
 contamination, 25
 penetration coefficients for, 44, 46
 Source
 isotropic plane, 57 ff
 isotropic plane, distribution of gamma emission from, 63
 isotropic plane, dosage factors, 60
 isotropic plane, dose rate, 57 ff
 isotropic plane, gamma radiation above, 62
 isotropic point, 49 ff
 isotropic point, dose rate, 50
 three-dimensional, 67 ff
 three-dimensional, dose rate, 68, 69
 Sources, finite and infinite, energy intensities for, 73
 Spectra, line, 10 ff
 Spectral function of incident radiation, 81, 82
 Spectrometer, airborne, 120, 125
 direct matrix for, 83
 gamma-ray, 72
 inverse matrix for, 83
 photoeffectiveness of, 121
 scintillation gamma-ray, 45
 Spectrometry
 airborne gamma-ray, 120
 scintillation gamma-ray, 38
 Spectrum of gamma emission above three-dimensional source, 70
 Spectrum of gamma-rays
 photopeak of, 122 ff
 true, 120
 T
 "Teapot" test, 65, 66
 Test
 "Bravo", 13, 22, 66, 112
 "Danny Boy", 112
 "Jangle-U", 25
 "Sedan", 42, 44
 "Small Boy", 66
 Tests, "Hardtack", 14
 Thermonuclear bomb, 1
 explosion, 12
 Three-dimensional source, 67 ff
 dose rate for, 68, 69
 spectrum of gamma emission above, 70
 Threshold, reaction, 13
 Time change in mixture activity, 4
 constant of instrument, 114
 of ascent of cloud, 24
 Tracers, 14
 Transitions
 beta, 128
 nuclear gamma, 127, 128
 "Trigger", 1

U, V

- Unscattered radiation, intensity of, 70, 73
Velocity, vertical particle, 23
- W
- Water as air equivalent, 50
dosage factors for, 50, 51, 54
Windscale reactor accident, 120

Y

- Yield of fission-product, 14
Yield of fragment isotopes, cumulative, 6
quantum, 127
average, 10
relative, 129
reliability of, 129 ff
total, 126